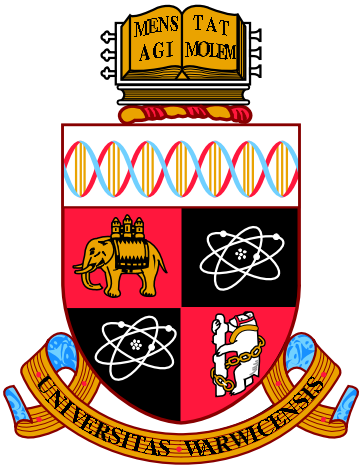

The Cartography Of Cell Motion

by

Richard Anthony Tyson

Thesis

Submitted to the University of Warwick
for the degree of

Doctor of Philosophy

Department of Systems Biology

December 2011

THE UNIVERSITY OF
WARWICK

Contents

List of Tables

List of Figures

Acknowledgments

I wish to thank the following people without whom this thesis could not have been completed.

First and foremost, I offer my sincerest gratitude to my supervisor Till Bretschneider, who's time, knowledge, and guidance was pivotal in all work presented herein, and also to Kurt Anderson who made the wet side of this project possible.

Many thanks to Ireen König, Margaret O'Prey, Michael Carnell, for teaching me the intricacies of confocal microscopy, and all things *Dictyostelium*. Much gratitude to David Epstein for his probing mind and development of key ideas for the creation of ECMM. My foremost collaborators, Wayne Croft, Eleni Panousopoulou, Jeremy Green, Evgeny Zatulovskiy and Robert Kay all played vital parts. Evgeny Zatulovskiy in particular has proved himself a hard working and talented scientist, producing quality data for analysis.

Many thanks to my group colleagues Mike Downey, Chengjin Du, Sarah Cosgriff, and Ingrid Tigges for input, discussion, and software testing. My advisory committee; Dr Graham Ladds, Silvester Czanner, Keith Vance, and Markus Kirkilionis. The Systems Biology DTC staff, past and present, and DTC directors Vicky Buchanan Wollaston and Alison Rodger. The 2007 DTC cohort, and now firm friends, Richard Hickman, Wayne Croft, Steven Kiddle, Heather Riley, Max Joseph, Matt Bano, Elizabeth Widman, Robert Gardner, Polly Downton, Darren Braddick, and Carl Blakey, who sadly is no longer with us.

Finally, I could not have gotten as far as I have without the support of my family, Clive, Janice, Justin, Mark, and my partner Bryony.

This list is far from exhaustive, so I wish to thank those people not mentioned who's contributions have not been forgotten.

The implementation and distribution of QuimP is made possible by the excellent, and free image processing tool, ImageJ. This thesis was typeset with LaTeX 2ε[1].

[1] LaTeX 2ε is an extension of LaTeX. LaTeX is a collection of macros for TeX. TeX is a trademark of the American Mathematical Society. The style package *warwickthesis* was used.

Declarations

This thesis is presented in accordance with the regulations for the degree of Doctor of Philosophy. It has been composed by myself and has not been submitted in any previous application for any degree. The work in this thesis has been undertaken by myself except where otherwise stated.

Abstract

Cell motility plays an important role throughout biology, the polymerisation of actin being fundamental in producing protrusive force. However, it is increasingly apparent that intracellular pressure, arising from myosin-II contraction, is a co-driver of motility. In its extreme form, pressure manifests itself as hemispherical protrusions, referred to as blebs, where membrane is torn from the underlying cortex. Although many components and signalling pathways have been identified, we lack a complete model of motility, particularly of the regulation and mechanics of blebbing. Advances in microscopy are continually improving the quality of time series image data, but the absence of high-throughput tools for extracting quantitative numbers remains an analysis bottle-neck.

We develop the next generation of the successful QuimP software designed for automated analysis of motile cells, producing quantitative spatio-temporal maps of protein distributions and changes in cell morphology. Key to QuimP's new functionality, we present the Electrostatic Contour Migration Method (ECMM) that provides high resolution tracking of local deformation with better uniformity and efficiency than rival methods. Photobleaching experiments are used to give insight into the accuracy and limitations of *in silico* membrane tracking algorithms. We employ ECMM to build an automated protrusion tracking method (ECMM-APT) sensitive not only to pseudopodia, but also the complex characteristics of high speed blebs.

QuimP is applied to characterising the protrusive behaviour of *Dictyostelium*, induced to bleb by imaging under agar. We show blebs are characterised by distinct speed-displacement distributions, can reach speeds of $4.9\,\mu m/\,\mathrm{sec}$, and preferentially form at the flanks during chemotaxis. Significantly, blebs emerge from flat to concave membrane regions suggesting curvature is a major determinant of bleb location, size, and speed. We hypothesise that actin driven pseudopodia at the leading edge induce changes in curvature and therefore membrane tension, positive curvature inhibiting blebbing at the very front, and negative curvature enhancing blebbing at the sides. This possibly provides the necessary space for rear advancement. Furthermore, bleb kymographs reveal a retrograde shift of the cortex at the point of bleb expansion, suggesting inward contractive forces acting on the cortex even at concave regions. Strains deficient in phospholipid signalling show impaired chemotaxis and blebbing.

Finally, we present further applications of QuimP, for example, we conclusively show that dishevelled is not polarised during *Xenopus* gastrulation, contrary to hypotheses in the literature.

Resulting Publications and those in Preparation

- Tyson, R.A, Epstein, D.B, Anderson, K.I and Bretschneider, T. (2010) *High Resolution Tracking of Cell Membrane Dynamics in Moving Cells: an Electrifying Approach.* Mathematical Modelling of Natural Phenomena, Vol. 5, No. 1, pp. 34-55.
- E Zatulovskiy, R A Tyson, T Bretschneider, R R Kay. *Working title: Blebbing is an important driver of Dictyostelium discoideum chemotaxis.* In preparation.
- E Panousopoulou, R A Tyson, T Bretschneider, J B A Green. *Working title: Dsh intracellular localisation in convergent extension is not a marker of polarity.* In preparation.

Oral and Posters Presentations

- Invited oral presentation. Actin 2009, Bristol.
- Poster presented. 10th International Conference on Systems Biology, Edinburgh, 2010.
- Poster presented. Actin 2010, Bristol.

The QuimP11 Software

The QuimP software package is provided on the accompanying CD, but can also be downloaded at:
`http://go.warwick.ac.uk/quimp`

Abbreviations

ABD	Actin Binding Domain.
ABP	Actin Binding Protein.
ADF	Actin Depolymerising Factor.
ADP	Adenosine Di Phosphate.
Akt/PKB	Serine/threonine protein kinase, otherwise known as protein kinase B.
AMP	Adenosine monophosphate.
ARP	Actin Related Protein.
ATP	Adenosine tri phosphate.
cAMP	Cyclic adenosine monophosphate.
cGMP	Cyclic guanosine monophosphate.
cARs	Cyclic Adenosine monophosphate receptor.
CRAC	Cytosolic regulator of adenylyl cyclase.
CT	Computational time.
DP	Decimal position. A decimal value in the range $[0, 1)$ representing the position of a marker on a length normalised cell outline.
DIC	Differential Interference Contrast Microscopy.
Dsh	Dishevelled.

Dex Rhodamine Dextran.

DTT Dithiothreitol

ECMM Electrostatic Contour Migration Method. Our computer algorithm for mapping one cell outline to another.

ERM Ezrin-radixin-moesin.

F-actin Filamentous-actin.

FN Failed node.

FSM Fluorescent speckle microscopy.

Fi Frame interval. Time interval (*seconds*) between frames in an image sequence.

FRAP Fluorescence recovery after photobleaching.

Gbp cGMP-binding protein.

G-protein Guanine nucleotide-binding proteins.

GMP Guanosine monophosphate.

GTP Guanosine triphosphate.

GTPase Guanosine triphosphate kinase.

ID Identifier. An integer label for tracking markers.

IKK Inhibitor Kappa B Kinase: phosphorylation and ubiquitination of the IκB proteins.

LEGI Local excitation & global inhibition.

M2 Melanoma cell line.

MHC Myosin heavy chain.

MLC Myosin light chain.

mlcE Myosin essential light chain.

mlcR Myosin regulatory light chain.

MO Marker origin. A decimal value in the range $[0, 1)$, representing the position a marker originated from on the outline at the previous frame.

MRC Medical Research Council.

NF-κB Nuclear factor kappa-light-chain-enhancer of activated B cells

NPF Nucleation promoting factor

ODE Ordinary differential equation.

PCP Planar cell polarity.

PDE Partial differential equation.

PH domain Pleckstrin homology domain.

PKB Protein kinase B.

PR Protrusion rate.

PTEN Phosphatase and tensin homolog.

QuimP Quantitative Imaging of Membrane Proteins. Title given to the software developed by Dr. T.Bretschneider.

Rac1A Rac-related C3 botulinum toxin substrate 1.

Ras RAt sarcoma.

RasGEFs Ras guanine nucleotide exchange factors.

RITC-Dx Rhodamine-B-isothiocyanate-dextran.

SD Standard deviation.

sGC Soluble guanylyl cyclase.

STM Spatio-temporal map.

Xdsh *Xenopus* Dishevelled.

Chapter 1

Introduction

1.1 Eukaryotic Cell Motility

Motility in eukaryotes is vital for many biological processes, for example, orchestrating embryogenesis, targeting epithelial cells to wounds, the inflammatory response, and organisation of brain neurones [Ilic et al., 1995; Kim et al., 1998; Frangogiannis et al., 2002; Rakic et al., 1994]. Mis-regulation can result in inflammatory diseases, osteoporosis, multiple sclerosis, and mental retardation [Dellas and Loskutoff, 2005]. Motility is tightly linked with metastasis; mutations in components for directional sensing are frequent in human cancers [Iijima and Devreotes, 2002; Chalhoub and Baker, 2009].

Early models of eukaryotic motility were based on observations in plants and fungi. They each rely on close control of cell osmolarity, membrane tension, and hydrostatic pressure to produce the driving force for processes such as growth, stomatal oscillations, and spore dissemination [Proseus et al., 2000; Fischer et al., 2004]. Similar processes were thought important in motility of plasmodial slime moulds.

The importance of regulating intracellular pressure took a back seat given the advances made in the study of actin and its role in driving motility [Tilney, 1975]. Actin is a globular monomer capable of polymerising into dense, branched networks of semi-flexible filaments. Filamentous-actin (F-actin) is a major component of the cell cytoskeleton, providing structural rigidity, but it is the rapid assembly and disassembly of filaments which is considered the dominant mechanism in providing force to deform the plasma membrane [Pollard and Borisy, 2003]. Actin allows cells to co-ordinate and locally regulate cellular protrusions for both random and directed movement in the form of cell crawling, a process of which plants and fungi are incapable.

However, it is becoming increasingly clear that actin polymerisation is not the sole means of locomotion in crawling cells, particularly in natural environments, such as

soil or densely packed tissues, which impose greater resistance. Blebbing, an alternate form of protrusion, exploits intracellular hydrostatic pressure to drive forwards patches of membrane that have become detached from the underlying supporting cortex. This produces highly distinct hemispherical protrusions that extend at high speed and leave *actin scars*, not observed in actin driven protrusions [Langridge and Kay, 2006].

We will outline the classical view of actin driven motility and the complexities of regulation in directed movement (chemotaxis) in *Dictyostelium discoideum*. We introduce blebbing within this context as a relatively poorly understood process.

1.1.1 Classical View of Actin Driven Protrusion

Cell crawling is generally considered a four step process: 1) protrusion of the leading edge; 2) substrate adherence; 3) retraction of the cell rear; 4) de-adherence [Pollard and Borisy, 2003]. Actin and myosin are key players, providing force and structural integrity. Short, branched F-actin forms a narrow layer beneath the plasma membrane called the cortex, while longer filaments (in concert with microtubules) maintain overall cell shape [Inoué and Salmon, 1995; Svitkina and Borisy, 1999]. Remodelling of F-actin networks by actin binding proteins, and motor proteins (such as myosin-II) underpins cell movement.

Actin was first isolated from smooth muscle. Actin and myosin filaments form networks for the transduction of contraction force [Aguilar and Mitchell, 2010]. The dominant myosin, myosin-II, is a hexamer containing two heavy chains (MHC) and two pairs of light chains (MLC). The C-terminals of MHC intertwine to form a filamentous tail. N-terminals form a globular head with an actin-binding domain, and is the site of ATP hydrolysis. The regulatory light chain (mlcR) binds the neck between tail and head, and its phosphorylation causes a change in angle, moving the head along the actin filament (the power stroke) and activating ATP hydrolysis to slide filaments and contract the network. The essential light chain (mlcE) likely functions to stabilise the structure and regulate contraction [Hernandez et al., 2007].

Actin filaments were seen to associate with sites of motility in non-muscle cells [Mooseker and Tilney, 1975], hence it was theorised that the sliding-filament model of muscle contraction also formed the basis for movement (as reviewed by Pollard and Weihing [1974]). However, evidence mounted for the direct contribution of force from dynamic actin filament assembly. For example, changing ratios of monomeric to F-actin during protrusion, induced polymerisation causing deformation of microvilli membrane, and creation of protrusions in liposomes resembling filopodia (slender, spike like protrusions) [Mooseker et al., 1982; Cooper, 1991]. Furthermore, cells lacking myosin (mutant or otherwise) can show unperturbed motility [Korn and Hammer, 1988]. This led to

the general acceptance that actin filaments must contact the membrane and force it outwards by polymerisation, as proposed years earlier by Tilney [1975]. It is now appreciated that actin polymerisation is employed by bacteria for intracellular *rocketing*, virus motility, and mediation of endocytosis [Tilney et al., 1992; Frischknecht et al., 1999; Kaksonen et al., 2006].

Fish keratocytes form a large, flat structure at their fronts, dense with actin, termed lamellipodia [Atilgan et al., 2006]. Organisms such as amoeba, extend more temporary protrusions termed pseudopodia. At the rear, actin and myosin form a contractile network that pulls the cell's rear along. In synchronisation with protrusion and retraction, cells form focal adhesions to the substratum, anchor points for mechanical force transmission and signalling. New adhesions are formed at the front by the clustering of membrane integrins, while rear adhesions are broken by myosin contractions and proteins involved in adhesion turn-over at the front (e.g. FAK and Src) [Ridley et al., 2003].

ATP-bound actin monomers (ATP-actin) arrange head to tail, imposing a polarity [Small et al., 1978]. Photobleaching and speckle microscopy reveal a treadmilling of monomers, in which they are rapidly added to the *barbed* end pointing towards the membrane, while dissociating from the *pointed* end [Fujiwara et al., 2002]. ATP hydrolysis is not required for polymerisation, but acts as a timer for filament disassembly [Pollard and Borisy, 2003]. The actin-related proteins 2 and 3 (Arp2/3) nucleate branched filaments at approximately 70 degrees (thought dependent on filament length) [Mullins et al., 1998; Goley and Welch, 2006], and the capping protein terminates growth by binding filament ends [Cooper and Schafer, 2000]. Two questions remain unanswered; how do filaments apply force to the membrane, and how do they grow rapidly given the slow rate of treadmilling of pure actin in vitro [Fujiwara et al., 2002].

Early models considered how single filaments apply force. The *elastic Brownian ratchet* theory suggests filaments flex away from the membrane due to thermal motion, extend, and apply force as they flex back [Hill, 1981; Mogilner and Oster, 1996]. This model agrees with the elastic properties of filaments and a branched, orthogonal actin network observed in keratocyte lamellipodium [Small et al., 1995]. However, filaments in some cases are attached to the membrane (presumably preventing growth at the barbed end) [Cameron et al., 2001], while single filament models ignore the complexities of the network and membrane curvature, and do not fit experimental data on force-velocity [McGrath et al., 2003; Upadhyaya et al., 2003; Marcy et al., 2004]. More complex theories have been proposed, such as the *End-tracking motor model* [Dickinson et al., 2004] or *elastic propulsion* [Bernheim-Groswasser et al., 2005], but none completely explain observations (reviewed by Mogilner [2006]).

Polymerisation is diffusion limited, but exceeds rates possible in steady state. In cells, the protein profilin binds monomers to accelerate association at the barbed end. Binding prevents both association to the pointed end, and spontaneous nucleation of new filaments. The pool of free monomers is maintained by ADF/cofilin severing and disassembling older ADP-actin filaments, profilin catalysing the exchange of ADP for ATP, and the capping protein limiting network density.

As a nucleator of branched filaments, Arp2/3 is a pivotal target for regulation of protrusion extension, as demonstrated by disruption having multiple detrimental effects on motility and development [Vartiainen and Machesky, 2004]. Arp2/3 requires activation by forming a complex with nucleation promoting factor (NPF) proteins, increasing the affinity for ATP, and transformation to an active confirmation (reviewed by Goley and Welch [2006]). NFPs are classified into two groups, containing multiple members, but the most well studied are the eukaryotic *class I* Wiskott-Aldrich syndrome protein (WASP), and suppressor of cyclic AMP repressor (SCAR; also called WAVE). As will be discussed in the next section, the NFP proteins are activated by upstream signal-transduction pathways that co-ordinate actin polymerisation spatially and temporally. Interestingly, Arp2/3 appears autocatalytic, increasing the rate of nucleation in proportion to the number of filaments [Pantaloni et al., 2000], aiding an explosive rate of polymerisation.

Predictably, Arp2/3 is not the lone nucleator of filaments. Formin and spire proteins nucleate linear filaments, important for filopodium formation, and represent further targets for regulation [Kovar, 2006; Baum and Kunda, 2005]. Cofilin is also tightly regulated and is thought to act synergistically with Arp2/3 to amplify polymerisation. Cofilin exposes barbed ends as it severs filaments, and therefore promotes growth of new filaments, to which Arp2/3 preferentially binds [DesMarais et al., 2005].

1.1.2 Chemotaxis in *Dictyostelium*

First observed in bacteria, chemotaxis is the process by which cells migrate along a extracellular chemical gradient. This requires sensing of the environment, determination of direction, and establishment of a front and rear (polarisation) [Insall, 2010].

Chemotaxis plays a vital role in many eukaryotes, for example, human leukocytes migrate in leukotriene gradients, produced in response to allergic reactions [Downey, 1994]. The unicellular, soil living, amoeba *Dictyostelium discoideum*, shares many of the behavioural responses and molecular components of motility with higher eukaryotes [Chen et al., 1996]. *Dictyostelium* is easily genetically manipulated for the creation of mutant libraries, and as such is considered a model organism for studying cell motility [Watts and Ashworth, 1970; King and Insall, 2009].

Dictyostelium responds to many chemoattractants (e.g. folic acid, platelet activating factor, lysophosphatidic acid) [Chen et al., 1996], the most well studied being the response to cyclic adenosine monophosphate (cAMP). When starved of food, *Dictyostelium* secretes cAMP, inducing cAMP production by neighbouring cells, and aggregation into a multicellular pseudoplasmodium (or slug) in preparation for forming a fruiting body and sporulation [Bonner, 1947; Konijn, 1972; Gerisch, 1982]. Studies using GFP labelling reveal that, in response to cAMP, molecular cytoskeletal remodellers and transduction components, such as actin, coronin, and cofilin, became asymmetrically distributed within the gradient [Gerisch et al., 1995; Kreitmeier et al., 1995; Gottwald et al., 1996; Aizawa et al., 1997; Parent et al., 1998], polarising the cell.

1.1.2.1 History of Directional Sensing

Sensing and transduction of chemoattractant signals utilise surface receptors coupled to components of G-protein linked pathways. Binding of attractants to receptors such as cAR (cAMP receptor), causes dissociation of G-proteins into $G\alpha$ and $G\beta\gamma$ subunits. Cells lacking the $G\alpha$ or unique $G\beta$ subunit are unable to respond to cAMP, as are cells lacking receptors [Kesbeke et al., 1988; Wu et al., 1995b; Chen et al., 1996]. Initially, cells were thought to process chemoattractant signals in much the same way as bacteria, responding to changes in receptor occupancy as they migrate, effectively continually sampling the local gradient [Koshland, 1977]. However, earlier work by Gerisch and Keller [1981] showed that Human granulocytes, could spontaneously extended lamellipodia towards a chemoattractant source, even when previously immobile. Furthermore, papers by Xiao et al. [1997], Servant et al. [1999] and Parent and Devreotes [1999] removed the possibility of polarisation being the result of unevenly distributed receptors, or $G\beta\gamma$, by observing even GFP signals at the membrane. Hence, cells are able to differentiate tiny differences in concentration between front and back, perhaps as little as 2%, when stationary.

A clue to how *Dictyostelium* polarises in response to cAMP came in the form of the cytosolic regulator of adenylyl cyclase (CRAC), which contains a pleckstrin homology (PH) domain. Lilly and Devreotes [1994] showed that CRAC was needed for adenylyl cyclase activation, producing cAMP during aggregation, and that it translocates to the membrane in response to cAMP [Insall et al., 1994; Lilly and Devreotes, 1995]. More significantly, using a CRAC-GFP construct, Parent et al. [1998] showed that in the absence of a gradient CRAC evenly distributes around the membrane, but restoring the gradient caused selective re-localisation of CRAC in the direction of the gradient. Furthermore, the same localisation is seen in cells unable to move (cells treated with latrunculin which prevents actin polymerisation) [Parent and Devreotes,

1999].

Similarly, other PH domain containing proteins, such as the signal transducer Akt/PKB, transiently associate with the membrane on chemoattractant stimulation [Meili et al., 1999], and many Rho family members (specifically small GTPases Rac, and cdc42), are known to mediate actin remodelling and contain PH domains. The PH domain, consisting of a bent β-sheet and a C-terminal α-helix, binds to phosphorylated inositol lipids such as phosphatidylinositol 3,4,5-trisphosphate (PtdIns(3,4,5)P_3) [Saraste and Hyvönen, 1995]. This has led to the formulation of the *local excitation-global inhibition* in which PtdIns(3,4,5)P_3 distribution acts as a cellular compass, amplifying signals from receptors.

1.1.2.2 PtdIns(3,4,5)P_3 as a Cellular Compass

In this model, local peaks in PtdIns(3,4,5)P_3 correlate with sites of new F-actin formation [Insall and Weiner, 2001] and act as binding sites for cytoskeletal remodellers and effectors, hence determining the location of pseudopodia nucleation [Parent and Devreotes, 1999]. PtdIns(3,4,5)P_3 metabolism is determined by two classes of proteins; type-1 phosphoinositide-3-kinases (PI3Ks), of which 5 are known to exist in *Dictyostelium*, that phosphorylate phosphatidylinositol 4,5-trisphosphate (PtdIns(4,5)P_2) to generate PtdIns(3,4,5)P_3 [Hoeller and Kay, 2007], and phosphatase and tensin homolog (PTEN) that catalysis the reverse reaction, generating PtdIns(4,5)P_2 [Funamoto et al., 2002]. PI3K and PTEN amplify the directional signal to form peaks in PtdIns(3,4,5)P_3 at the membrane. PI3K transiently locates to the leading edge in chemotaxing cells, while PTEN exhibits the reciprocal pattern, dissociating from the leading edge, but remaining membrane bound at the rear [Funamoto et al., 2002]. The directional signal originates at the level of receptors. Those higher in the gradient are transiently activated slightly more frequently than those further down the gradient [Janetopoulos et al., 2001]. In turn, this creates a small asymmetric distribution of dissociated G-protein subunits, subsequently amplified by PtdIns(3,4,5)P_3 metabolism (Figure 1.1).

The second part of the model hypothesises a global inhibitory response, determined by the average occupancy of receptors, that exceeds the excitatory response at the rear [Devreotes and Janetopoulos, 2003]. A candidate for this roll is the fast diffusing, cytoplasmic signalling molecule, cyclic GMP (cGMP), which is produced in response to cAMP binding. Although transiently active, cGMP is known to mediate phosphorylation of myosin-II chains [Bosgraaf et al., 2002].

However, this is one mode of movement and does not explain more recent observations. Gradients of PtdIns(3,4,5)P_3 still form in the absence of chemoattrac-

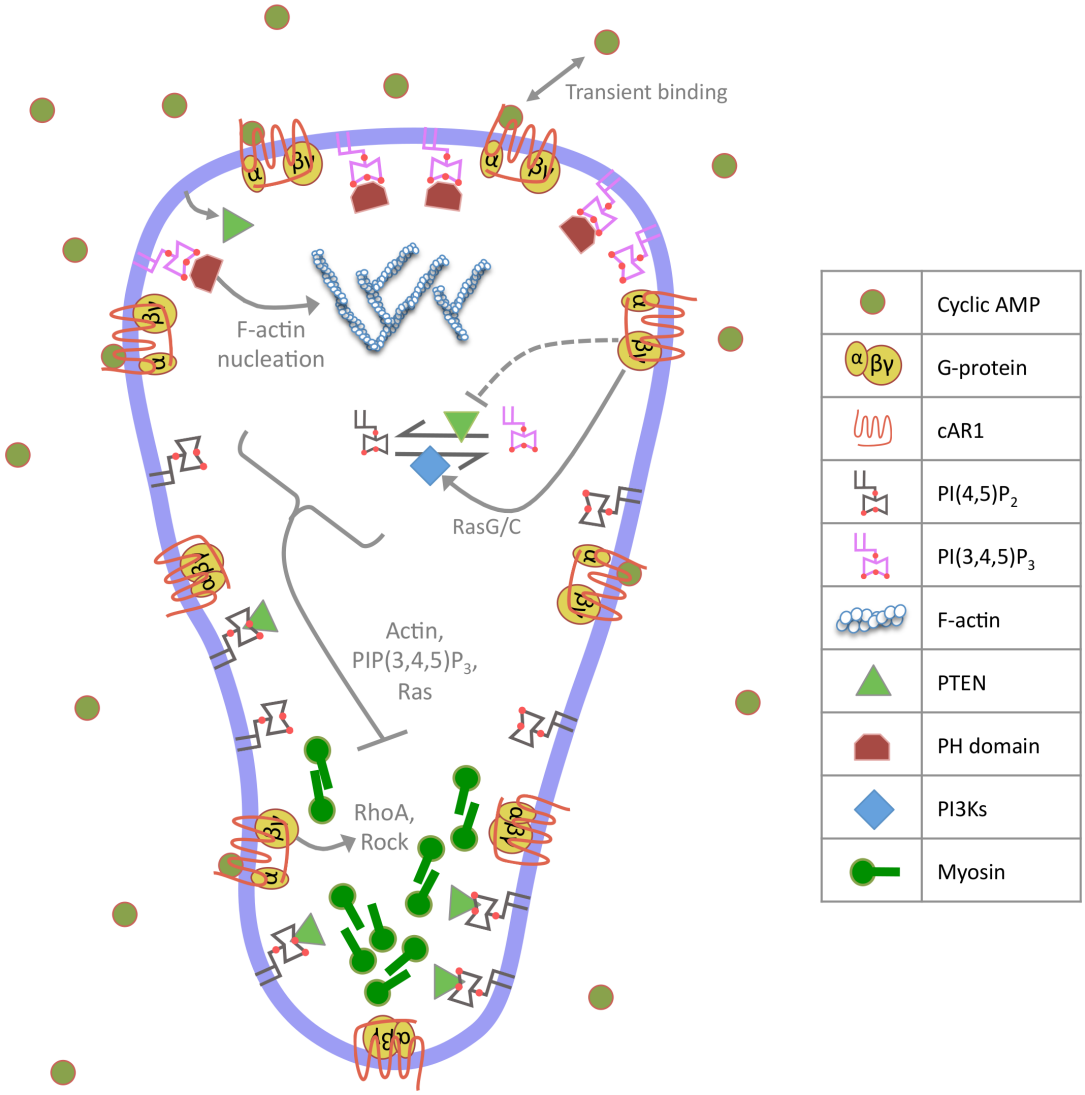

Figure 1.1: **Caricature of *Dictyostelium* polarising in response to cyclic AMP.** *Dictyostelium* response to a gradient of extracellular cyclic AMP by polarising in the direction of the source, nucleating actin-polymerisation at the front to form protrusions, and activating myosin-II to contract the rear. A cyclic AMP gradient, as small as 1% between front and back, is amplified to produce a asymmetric distribution of PtdIns(3,4,5)P_3. Transient binging of cyclic AMP to the G-couple transmembrane receptor cAR1 occurs at a greater rate at the front, producing a small asymmetric distribution of dissociated G-protein $\beta\gamma$-subunits. Subsequently, PtdIns(3,4,5)P_3 levels are increased by activation of PI3Ks (via RasG/C), and dissociation of PTEN from the membrane. F-actin nucleation and remodelling proteins are localised to the leading edge by binding of PH domains to PtdIns(3,4,5)P_3. G-protein activation at the rear is insufficient to overcome global inhibition of leading edge formation. G-protein activation of RohA and Rock at the rear promotes actomyosin formation, while actomyosin formation at the front is inhibited by actin, PtdIns(3,4,5)P_3, and Ras.

tants, and G-protein β subunit mutants, hence directing random movement [Sasaki et al., 2007]. Inhibiting F-actin formation can destroy these gradients, suggesting that peaks in PtdIns(3,4,5)P_3 can be sustained by positive feedback loops. Patches of PtdIns(3,4,5)P_3 also form spontaneously in uniform cAMP [Sasaki et al., 2007]. Furthermore, Arai et al. [2010] recently observed self-organised waves of PtdIns(3,4,5)P_3 around the cell circumference (with periodicity of $\approx$ 200s) accompanied by opposing waves of PTEN. Waves are not affected by treatment with latrunculin (inhibition of actin polymerisation), but functioning PTEN and PI3Ks are essential. Similarly, actin waves have also been observed, and assumed to be linked to the generation of random movement [Vicker, 2002; Bretschneider et al., 2004].

Sasaki et al. [2007] showed that the apparent feedback loop created by F-actin was dependent on Ras, a subfamily of the Ras small GTPase superfamily. *Dictyostelium* has 15 identified Ras proteins that function as signal transducers [Rivero and Somesh, 2002]. They can exist in either an active GTP-bound, or inactive GDP-bound state. Ras states are switched by guanine nucleotide exchange factors (RasGEFs) which are activated by G-protiens in the cAMP response, and can act on a wide range of Ras proteins [Kae et al., 2007]. Not only do both Type-I PI3Ks and PTEN contain Ras binding domains (RBD), but Ras is seen to localise to the leading edge [Sasaki et al., 2004]. Knocking out any one Ras protein has little effect on chemotaxis, but removal of the Ras proteins RasG and RacC (or RasG and the RasGEF aimless) completely abolishes chemotaxis towards cAMP [Tuxworth et al., 1997; Sasaki et al., 2004; Bolourani et al., 2006]. Hence, Ras proteins provide the link to G-protein activation during the cAMP response, but their wide range of targets also suggests involvement of Ras proteins in the absence of chemoattractants and PtdIns(3,4,5)P_3 gradients.

The role of PtdIns(3,4,5)P_3 in random migration appears to be the result of self-organising properties. Interestingly, Hoeller and Kay [2007] showed that *Dictyostelium* lacking all five PI3Ks and PTEN, which are unable to form PtdIns(3,4,5)P_3 gradients, can still undergo effective chemotaxis, although they are severely impaired without a strong gradient.

1.1.2.3 Chemotaxis In The Absence of PtdIns(3,4,5)P_3

Genetic screens of cells with inhibited PI3Ks identified phospholipase A_2 (PLA2) as acting in parallel with PI3K pathways to mediate chemotaxis [Chen et al., 2007; Haastert et al., 2007]. PLA2 metabolises arachidonic acid, but how this functions in chemotaxis is unknown. Similarly, Lee et al. [2005] showed that the target of rapamycin complex 2 (TORC2) is required for both chemotaxis and signal relay via phosphorylation of two Akt/PKB kinases, PKBA and PKBR1. The TORC2 pathway can be activated

independently of PtdIns(3,4,5)P_3 at the leading edge by RasC and the RasGEF aimless [Kamimura et al., 2008; Charest et al., 2010]. More perplexing is that knocking out PI3Ks, PLA2 and TORC2 pathways still does not obliterate chemotaxis in 7 hour starved cells [Veltman et al., 2008]. Soluble guanylyl cyclase (sGC) locates to the front and interacts with F-actin, driving chemotaxis, while its product, cGMP, re-localises to the rear and directs myosin-II contraction by activation of GbpC [Bosgraaf et al., 2005; Veltman et al., 2008].

Current observations point to parallel pathways in the chemotaxis network, each containing multiple redundant components [Chen et al., 2007]. Lipids act as universal regulators with both specific and non-specific PH domain binding [Balla, 2005]. Signal transducers, like RasGEFs, can have multiple targets, but also bind specifically, as in the case of RasC [Kae et al., 2007], and can act upstream or downstream of lipid regulation, or even completely independently. Furthermore, the motility machinery contains both feedback mechanisms and inherent self-organising properties, allowing dynamic control and random movement [Théry et al., 2006; Ji et al., 2008]. Typically, motility mechanisms respond on time scales far in excess of gene regulation and protein turnover, and therefore require complex activation and deactivation of pathways in response to signals. Signals may be chemical or mechanical forces (such as forces generated from fluid flow [Dalous et al., 2008]).

1.1.3 Cellular Blebbing: The Role of Intracellular Pressure

Trinkaus [1973] demonstrated that Fundulus deep cells were able to migrate through the tightly packed tissue of a developing embryo by expanding large, bubble like protrusions from their surface, structures referred to as blebs. The forces produced by actin polymerisation are considered to be insufficient to overcome the extracellular pressures of resistive environments, resulting in the branched F-actin network becoming deformed as opposed to producing forward motion. It appears that blebbing provides an alternative mechanism that can overcome these larger resistive forces. As such, blebbing is a key mode of migration for *Dictyostelium*. Dormann and Weijer [2006] showed its importance at the multicellular slug stage of the *Dictyostelium* life cycle, where blebbing was significantly increased over other stages.

Blebbing has been observed in numerous mammalian cell lines and processes: developmental tissues [Jaglarz and Howard, 1995; Blaser et al., 2006]; motile cancer cell lines, aiding tumour invasion [Haston and Shields, 1984; Sahai and Marshall, 2003; Yamaguchi and Condeelis, 2007; Friedl and Wolf, 2003; Wolf et al., 2003]; melanoma cell line (M2) [Charras et al., 2005]; cell spreading [Pletjushkina et al., 2001]; and apoptosis [Coleman et al., 2001]. Blebbing in all these cases is thought to derive from the same

basic mechanics, namely the induction of intracellular pressure via the contraction of the actomyosin cytoskeleton [Wessels et al., 1988; Chen et al., 1995; Maugis et al., 2010], followed by either rupture of the cortex [Paluch et al., 2005], or breakage of adhesion at the cortex-membrane interface [Dai and Sheetz, 1999].

1.1.4 Blebbing in *Dictyostelium*

Figure 1.2 shows the typical formation of blebs in *Dictyostelium* migrating under agar (courtesy of Evgeny Zatulovskiy, MRC laboratory, Cambridge). Labelling of F-actin reveals a densely fibrous actin cortex at the rear which is contracted by association with myosin-II [Torgerson and McNiven, 1998; Hagmann et al., 1999], reducing the cell's volume and increasing intracellular fluid pressure [Janson and Taylor, 1993; Charras and Paluch, 2008]. Pressure is the driving force behind blebbing, similar to the primary method of motility in plants and fungi [Charras et al., 2005], but it is the supporting actin cortex and its adherence to the plasma membrane via lipid binding that provides the structural rigidity to build pressure [Raucher et al., 2000]. The actin cortex may also act as an elastic material, storing energy from myosin contraction [Tinevez et al., 2009].

Blebbing can be inhibited by disrupting the action of myosin-II, for example, by treatment with the myosin-II ATPase blocker, blebbistatin, or disruption of the essential light chain [Cunningham, 1995; Chen et al., 1995; Cheung et al., 2002]. Further to this, *Dictyostelium* myosin-II knockouts stall in the tip-less mound developmental stage, suggesting that myosin-II has a key role in driving blebs essential for development [Carrin et al., 1996]. (However, some blebs have been shown to form independently of actomyosin contraction; necrotic blebs rely on influx of ions and water, but grow over a slow period of 10 min [Bovellan et al., 2010]).

Pressure within the cell is experienced in its majority by the plasma membrane, rather than the permeable cortex. Pressure on the membrane, coupled with cortex tension acting inwards, creates stress at the cortex-membrane interface. In *Dictyostelium*, at a critical stress level, tethers are broken at a patch of membrane leading to the expansion of a characteristic hemispherical protrusion at the surface [Keller and Eggli, 1998; Yoshida and Inouye, 2001; Keller et al., 2002] (white arrows, Figure 1.2). Bleb nucleation can also result from rupture of the cortex, as demonstrated in L929 cells by Paluch et al. [2005].

During expansion, stored energy is released as cytoplasm floods into the space between cortex and membrane, and in doing so causes further membrane to tear from the cortex, widening the bleb's base. A bleb appears to be devoid of actin during its expansion. Unlike pseudopod extension, the cortex at the site of nucleation is

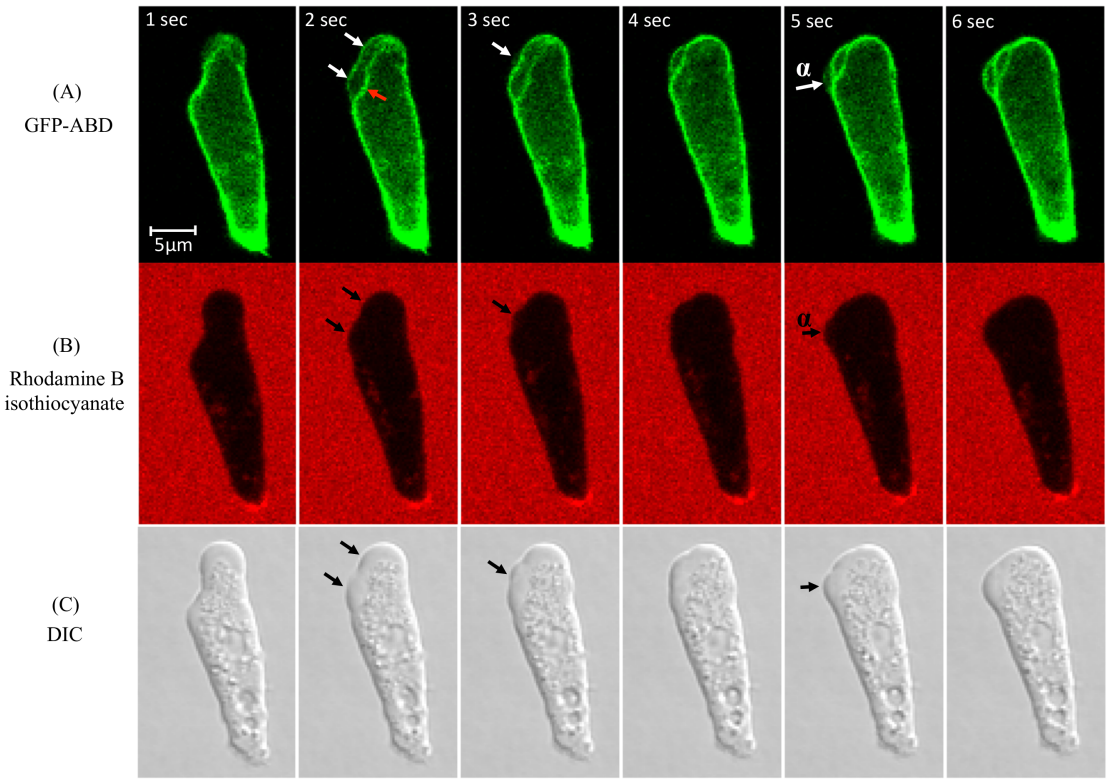

Figure 1.2: **Two channel fluorescence and DIC sequence of *Dictyostelium* induced to bleb.** Blebbing is induced by imaging under 1% agarose. The sequence depicts a series of four blebs (white arrows) over a period of 6 seconds (imaged at 2 fps). (A) GFP labelled actin binding domain. The cell rear shows a densely fibrous actin cortex, required for the build up of hydrostatic pressure via the action of myosin-II. Blebs tear from the cortex which is left visible as an actin scar for several seconds (red arrow). (B) Rhodamine B isothiocyanate negative stain improves segmentation at the site of blebs, typically devoid of actin (α). (C) DIC shows blebs to have a relatively smooth surfaced, the actin scar acting as barrier to rigid cell components and organelles.

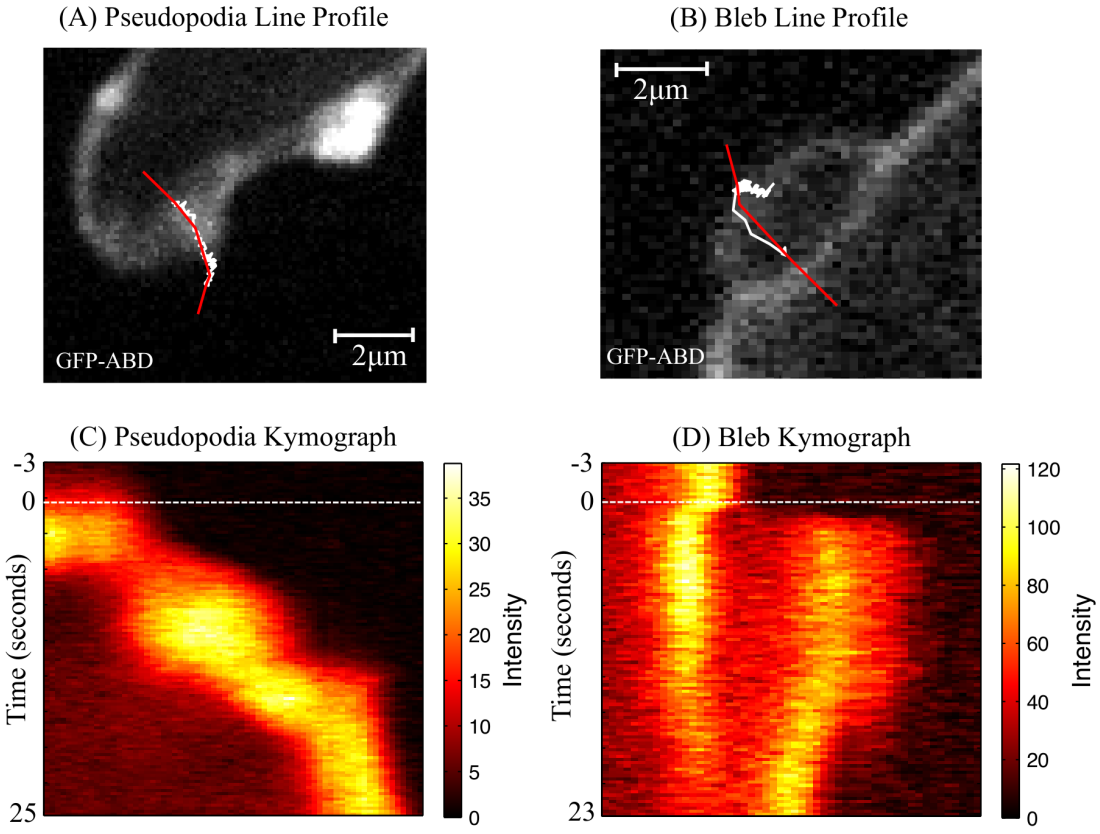

Figure 1.3: **Bleb and pseudopodia kymographs: visualising cortex dynamics.** (A) Image of an extending pseudopodia, overlaid with protrusion path (white) and kymograph line profile (red). (B) Extending bleb. Line profiles are low resolution alternatives to the protrusion paths. (C) and (D) are kymographs of sampled intensities along pseudopodia and bleb line profiles, respectively (3 seconds prior to extension and 20 seconds post extension), with time points stacked vertically. Blebs show rapid expansion (left to right) at time zero, disassembly of the actin scar, and assembly of a new cortex. A characteristic gap is left between scar and newly formed cortex, representing the absent of GFP-ABD during expansion. Pseudopodia are filled with actin, and leave no scar, and as such the map shows a very different pattern.

not immediately disassembled, appearing as an actin scar, post bleb, that is visible for several seconds (red arrow, Figure 1.2). The actin scar also appears to act as a barrier to rigid cell components and organelles, preventing them entering a growing bleb. Blebs therefore often appear smoothly textured when viewed with Differential Interference Contrast Microscopy (DIC) (Figure 1.2C). Once expansion ceases, a new cortex is built below the bleb's surface, re-instating membrane support [Keller and Eggli, 1998; Raucher et al., 2000]. Figure 1.3 compares kymographs of a bleb and actin driven pseudopodia, clearly demonstrating the contrasting characteristics of cortex dynamics. Blebs show rapid expansion and a characteristic gap between scar and newly formed cortex, representing the absence of GFP-ABD. Pseudopodia are filled with actin, and leave no scar, and as such the kymograph shows a more usual pattern of slower, continuous GFP movement.

In *Dictyostelium*, a bleb will typically expand at a speed of approximately $2\,\mu m/\,\text{sec}$, as opposed to $0.5\,\mu m/\,\text{sec}$ for pseudopodia. In other cell lines, speeds can vary hugely. Maugis et al. [2010] observed speeds of 10 to $20\,\mu m/\,\text{sec}$, with extension occurring over a few hundred milliseconds, in *Entamoeba histolytica* (a parasitic *Entamoeba*). In contrast, blebs in M2 cells expand over a period of 10 to 30 seconds [Charras et al., 2006].

It has been proposed that halting expansion is facilitated by a combination of dissipated pressure, increased membrane tension (resulting from increased curvature), and reattachment to the newly assembled cortex [Charras et al., 2006, 2008; Bovellan et al., 2010]. Intuitively, an expanding bleb increases in surface area compared to its base of nucleation, so additional membrane must be supplied, either by unfolding of membrane wrinkles or from lipid flow [Bovellan et al., 2010].

Although blebbing is typically a feature of eukaryotic cells, and is an active process, it can also be induced in Gram-negative bacteria via treatment with vancomycin, disrupting cross-linking in the peptidoglycan cell wall [Daly et al., 2011]. This suggests that all cells that possess a supported plasma-membrane have the necessary mechanics for blebbing, but eukaryotic cells show the ability to actively exploited it, including during chemotaxis.

1.1.5 Cross-links Between Blebbing and Signalling to the Cytoskeleton

The ability of *Dictyostelium* to polarise and chemotax up cAMP gradients is well documented [Bonner, 1947; Meili et al., 1999; Manahan et al., 2004; Parent, 2004; Haastert and Veltman, 2007], but questions remain as to the signalling pathways that determine the location of detachments between membrane and cortex when forming blebs, and

hence how migration by blebbing is polarised. The components and mechanism of detachment are also unclear [Charras and Paluch, 2008].

Just as localised PtdIns(3,4,5)P_3 production at the leading edge can induce Arp2/3 nucleation of filaments via NFPs, a mechanism must also exist to localise detachment of the cortex from the membrane, in order to form blebs advanced in the gradient. The ERM proteins (ezrin-radixin-moesin) have shown to be essential in tethering the membrane to the cortex by directly binding F-actin and integral membrane proteins [Bretscher et al., 2002; Charras et al., 2006]. The presence of ERM proteins, particularly ezrin, can have a marked impact on blebbing; cells expressing constitutively an active mutant of ezrin show marked decrease in blebbing; the ezrin-rich uropod-like structures of melanoma cells show inhibited blebbing [Lorentzen et al., 2011]. Interestingly, Hao et al. [2009] showed that PtdIns(4,5)P_2 plays a key role in mediating the ERM proteins, acting as a docking molecule for proteins with lipid-binding domains [Balla, 2005]. Controlling the quantities of PtdIns(4,5)P_2 at the leading edge therefore provides a mechanism by which tethering by ERM proteins can be manipulated to induce blebs. However, the density of the cortex is also suspected to play a role, possibly altering tethering, as drug-induced depolymerisation of the cortex can induce blebs, as can creating actin cytoskeleton mutants [DesMarais et al., 2004; Delorme et al., 2007; Kay et al., 2008].

Work completed at Robert Kay's group (MRC Laboratory of Molecular Biology, Cambridge), has yielded criteria for defining blebs as visualised in *Dictyostelium*, and demonstrated that the site of bleb formation can be controlled by a chemotactic gradient. Importantly, it has been established using blebbing assays under agarose, that blebbing becomes the dominant form of protrusion in resistive environments. By increasing the agarose concentration, and therefore the magnitude of resistance, *Dictyostelium* can be made to shift its mechanism of protrusion towards the much better suited blebbing. However, blebbing in *Dictyostelium* is yet to be well characterised in terms of, for example, their distribution of speeds, displacements, and frequency.

1.2 Motivation: Seeking Quantitative Data From Images

We have presented a view of cell motility as a complex and intricate set of interactions between signalling cascades, components for manipulation and remodelling of the cytoskeleton, and mechanical action of tension, pressure and actin polymerisation in deforming cells, all of which need to be co-ordinated for movement. As such, motility is highly dynamic, heavily temporally dependent, and tightly coupled process, which requires a set of appropriate tools to capture these events, so that we can begin to build

a systems level view of motility.

Blebbing provides a fitting example, requiring activation in resistive environments, polarisation in chemical gradients, induction of mechanical stress, and ordered recruitment of proteins for both assembly and disassembly of the cortex. To elucidate the mechanics we not only need data on spatial and temporal patterns of protein localisation and of cell membrane deformation, but be able to compare data across multiple experiments and between perturbed systems. Statistical descriptors are needed which can only be built using quantitative, normalised data.

Inherent redundancy of motility components, as shown by Veltman et al. [2008] and others, makes quantitative data even more important as mutants will generally show only small perturbations in phenotype. Distribution of the SCAR complex, for example, can subtly reduce protrusion persistence [Bear et al., 1998]. That said, any mutant that completely lacks the ability to migrate provides very little insight, particularly as these mutants often prove to be unhealthy and fail to undergo particular stages of development, for example $talB^-$ *Dictyostelium* cells arrest at the tight-mound stage, making them difficult to grow and study [Tsujioka et al., 2008]. Being able to identify subtle phenotypes is therefore key in screening for defective mutants.

Better understanding will arise from building models of motility for which quantitative data is essential for both construction and testing of model predictions. For example, Ji et al. [2008] constructed a spring based mechanical model of actin, built from images of actin retrograde flow, to estimate intracellular force during pseudopod expansion. They showed that actin assembly rates are not highest during fastest extension, but rather when their model predicted highest resistance to extension, suggesting a tension feedback loop. Many mathematical models of have been proposed for gradient sensing and polarisation, such as those based on the local excitation & global inhibition (LEGI) principle, or feedback and amplification, all of which require quantitative data on spatial-temporal protein localisation (reviewed by Iglesias and Devreotes [2008], Jilkine and Edelstein-Keshet [2011]). Models have been proposed that mimic patterns of protrusion, such as maintenance and splitting of pseudopodia [Insall, 2010]. Such models are made possible by using automated tools for quantifying pseudopodia extension from images, some of which we discuss in the next section, along with key principles of image analysis.

1.3 Challenges and Tools for Extracting Numbers From Images

Unravelling cell motility requires analysis of time series images to capture the spatial-temporal pattern and changes in morphology. These are attained in two or three dimensional, and often in multiple channels. Microscopy images consist of a 2D grid of integer values (pixels) representative of the brightness of the image at any one location (greyscale). Intensity may be representative of fluorescence emission (confocal microscopy), or interaction of light with passing through a sample (DIC).

The first challenge is ensuring that the measured pixel intensities are comparable both within the same image sequence and across experiments. Images may be pre-processed to normalise values, for example, removal of uneven backgrounds. Descriptors can then be extracted, and in general, the following tasks must be tackled: 1) Segmentation of an image into background pixels and cell body pixels, the boundaries forming cell outlines; 2) Tracking of cells, or particles, through a sequence by identifying its associated segmentation in each image; 3) Mapping associated outlines to measure local deformations (as performed by ECMM, and reviewed by [Xiong and Iglesias, 2010]).

In the ideal case, images would be captured at very small frame intervals to minimise displacement between frames, but imaging technology, detrimental response to light, and fluorescence bleaching forces compromises on frame rate in order to maintain image quality (particularly when imaging z-stacks). Analysis tools therefore need to adapt to image noise and missing data.

Developing automated, high-throughput tools is imperative because of the vast quantities of data available, possibly thousands of images per sequence. Many processes, such as pseudopodia, appear highly stochastic [Xiong et al., 2010], so analysing large numbers of cells is unavoidable if we want meaningful statistics. Results from manual analysis are prone to error, time consuming, and inconsistent, making comparison of data between labs impossible (even affecting analysis by the same person at different times of day).

Soll and Wessels developed the pioneering three-dimensional dynamic image analysis system (3D-DIAS) that provides a semi-automated method to quantitatively describe aspects of motility [Murray et al., 1992; Soll, 1995; Wessels et al., 1998]. Cells were semi-automatically outlined in DIC z-stack images using a complexity filter to identify in-focus regions [Soll and Voss, 1997]. Subsequent 3D reconstruction allows tracking of the centroid, and manual identification of pseudopodia. DIAS successfully quantified defective motility in *Dictyostelium* cytoskeleton mutants [Shutt et al., 1995;

Wessels et al., 1996], and later also tracked nuclei, although this required manual segmentation [Wessels et al., 1998].

This work has led to the development of new methods for extracting richer data with greater automation. Techniques are frequently borrowed from the fields of machine learning and computer vision, and applied to a variety of biological problems. For example, image-based chemical compound screening [Xia et al., 2010], classification of cancer tissues using support vector machines [Wei et al., 2005], and application of clustering, graph cut, and neural networks for tissue segmentation in medical imaging [Shen et al., 2005; Vicente et al., 2008]. Commercial software for these approaches is very expensive, but free software is available. *CellProfiler* can perform cell segmentation, but also supervised machine learning for high-throughput identification of cell phenotypes [Carpenter et al., 2006; Jones et al., 2009]. The Danuser Lab also provides a number of programs for image analysis, such as the new *plusTipTracker* [Applegate et al., 2011].

1.4 Segmentation and Tracking

The simplest approach to automated segmentation is thresholding, whereby pixels are classified by some local measure (e.g. local intensity variance), which is often coupled with pre-processing techniques to reduce noise, and post-processing to filter anomalies (reviewed by Miura [2005]). Tracking can then be performed by computing the most probable links between object outlines based upon a range of measures, such as distance, size, or intensity [Al-Kofahi et al., 2006; Downey et al., 2011], with possible improvements derived from graph theory [Bollobas, 1998; Vallotton et al., 2003] (for a review of cell tracking see Meijering et al. [2009]).

In the context of biological images, thresholding often fails to produce an accurate result because of poor signal to noise, faint boundaries, or uneven fluctuations in signal across a cell due to protein turnover or localisation (prominent in cell motility processes) [Wu et al., 1995a]. Cells in contact can easily become merged when boundaries between them are too fait.

These issues can be tackled to an extend by using local thresholding [Chan et al., 1998], but more advanced methods are available. For example, CellTracker is freely available software developed to study the translocation of NF-κB to the nucleus. A combined particle filter and active contour segments cells and nuclei, and was later updated to include a novel method based on geodesic commute distance [Du et al., 2010]. Deformable models, such as active contours, attempt to fit a closed contour to object boundaries by minimising contour energy states. They are commonly used

for segmentation of medical and biological images because of their robustness to noise, ability to transverse gaps in boundaries, and inherent tracking [Dormann et al., 2002; Zimmer et al., 2002; Ray et al., 2002; Debeir et al., 2004; Huang and Helmke, 2011] . Below, we briefly outline the ideas behind the deformable model, first proposed by Kass et al. [1988], in preparation for describing segmentation and tracking in QuimP.

1.4.1 The Deformable Model

A closed contour, or snake, is initialised around an object and *evolved* as a Lagrangian system in the form of a gradient descent algorithm, as to minimise the snake's total energy, E_{snake}

$$E_{snake} = E_{int} + E_{ext}, \tag{1.1}$$

where E_{int} results from internal forces acting to enforce smoothness constraints, while E_{ext} is composed of image derived forces designed to guide the snake to features of interest. For example, the forces contributing to E_{ext} may be computed from image intensities at any one pixel position, $\delta I(x, y)$, or the local image gradient, allowing the detection of edges. Smoothness constraints prevent *leakage* through gaps in image features, but can hinder its ability to converge into concavities (similar to plasma membrane tension being curvature dependent, affecting bleb growth [Tinevez et al., 2009]). As the snake is *evolved* the energy in the system is minimised as forces equilibrate. Once a solution is obtained, snakes can be used for initialisation at subsequent frames, hence active contours contain an inherent tracking (provided objects overlap previous solutions).

Adapted active contours have since been proposed to improve concavity detection, and to expand the limited capture range of image features normally requiring close initialisation. For example, the Gradient Vector Flow snake [Xu and Prince, 1998] and the Force Field Analysis snake [Hou and Han, 2005].

Implicit representations can be used to segment multiple cells from a single, all encompassing initialisation by the inherent ability of the contour to split and merge as objects are encountered [Dufour et al., 2005; Sarti et al., 2000]. However, objects in contact will still be segmented as single objects. To avoid this, Dufour et al. [2005] associated all objects with a separate active contour (implemented in 3D), and allowed contours to interact to maintain boundaries if objects were to touch each other. We apply this method for multi-cell segmentation in QuimP.

1.5 Tools for Mapping Cell Deformation

Global measures can be easily computed from a sequence of cell outlines. Veltman et al. [2008] used centroid trajectories to compute speed and persistence measures, demonstrating chemotaxis deficiency in PLA2 and sGC mutants. Li et al. [2011] demonstrated that if such data has great enough resolution, then *wobbling* of the perimeter centroid (which is sensitive to extension of pseudopodia) can reveal cyclic pseudopodia splitting in *Dictyostelium*. They were than able to successfully model this behaviour using a stochastic approach. However, global parameters lack the necessary detail regarding local membrane deformation, and an appropriate co-ordinate system for tracking and describing fluorescence distributions.

One approach is to overlay outlines at successive time points, and subdivide them into segments according to the points of intersection. The area of these segments will be representative of the amount of extension or retraction, as used in the DIAS system. Other methods use similar approaches, such as Edge Evolution Tracking (EET), although EET extends this concept by linking segments through time [Tsukada et al., 2008]. However, this provides only very low resolution data, justified only for very simple deformations.

Xiong et al. [2010] proposed a *skeletonisation* method to directly locate and track emerging pseudopodia. Skeletonisation is a form of morphological operation that describes a shape in terms of its main lines of axis, represented by connected lines. Extending pseudopodia produce new lines of axis, that connect to previous lines, producing an effective means to follow pseudopodia and splitting. However, the process does require *branch pruning* to remove false axes, does not (to date) include a co-ordinate system for intensity sampling, and is likely to fail in the case of small *de novo* pseudopodia or blebs, which are often small and susceptible to pruning.

Another classic approach is to use kymographs to measure rates of deformation, for example the membrane activity in human epidermal keratinocytes [Libotte et al., 2001], but such analysis is limited to single regions. Nevertheless, kymographs can be used to visualise spatial-temporal protein distribution by coupling them with an appropriate co-ordinate system. Arai et al. [2010] mapped positions on cell outlines (intensity sampling points) to angles in the plane, centred at an arbitrary position that remained fixed over the length of a sequence. The resulting maps revealed the spontaneous self organising waves of PtdIns(3,4,5)P_3 as zig-zag patterns.

Maeda et al. [2008] used a similar angular system, but also measured deformation at sampling points by computing their distance from the cell centroid. They could identify ordered patterns by computing cross-correlations between deformation and

fluorescence maps to investigate how intensity is influencing shape change. Although simple to implement, the use of an angular co-ordinate system breaks down when dealing with cell shapes containing concavities, which are very common in *Dictyostelium* during chemotaxis, and can only measure deformation in the direction of the centroid (which is not fixed over the sequence). In the case of Arai et al. [2010], treatment of cells with latrunculin and caffeine inhibited actin polymerisation and cAMP production respectively so cells were comparatively stationary and rounded, hence compliant for analysis.

We would prefer a co-ordinate system that evolves with deformation, and hence has the inherent properties of tracking points in the outline throughout a sequence. This requires a one-to-one mapping of any chosen position (or marker) on an outline at time t, (Γ_t), to a corresponding position on the preceding outline, Γ_{t+1}. Furthermore, we require a simulated marker path (as if mapped via missing intermediate data) to compute distance of marker travel, and hence local speed. Any such method would need to be computable in real time to be viable for high through-put approaches.

Mapping curves in this way is referred to as parameterisation of the curve. In the same way that a globe can be projected onto a flat surface, maintaining 90 degree angles between lines of longitude and latitude, the Riemann Mapping Theorem states that for any simply-connect domain there exists a conformal (angle-preserving) parameterisation into any other simply-connected domain [Riemann and Wilkins, 1851]. We discussed the use of Riemann mapping in Tyson et al. [2009], concluding that implementation is complex and computationally too expensive.

Spherical harmonics, another focus of surface parameterisation, has been successfully applied to 3D images of cells [Shen et al., 2009]. However, computing membrane deformation is non-trivial when deformations are large, and registration of subsequent frames difficult.

Alternatively, we can employ boundary propagation techniques, the most prominent being the Level Set Method (LSM) [Osher and Sethian, 1988]. By computing intermediate boundaries, markers can be mapped via normals towards Γ_{t+1} (demonstrated in Figure 1.4). Briefly, LSM evolves a boundary in the normal direction at all locations, which is controlled by *speed functions*. As such, LSM has been used in implicit implementations of active contours, as mentioned above. We detail LSM in Section 2.2 for the purpose of comparison with our own method, LSM being the main contender.

Machacek and Danuser [2006] employed LSM to quantify the propagation of Rac1 mediated waves of protrusion in epithelial cells. Their parallel attempts to use a mechanical method for propagation (based on virtual springs) failed in situations of

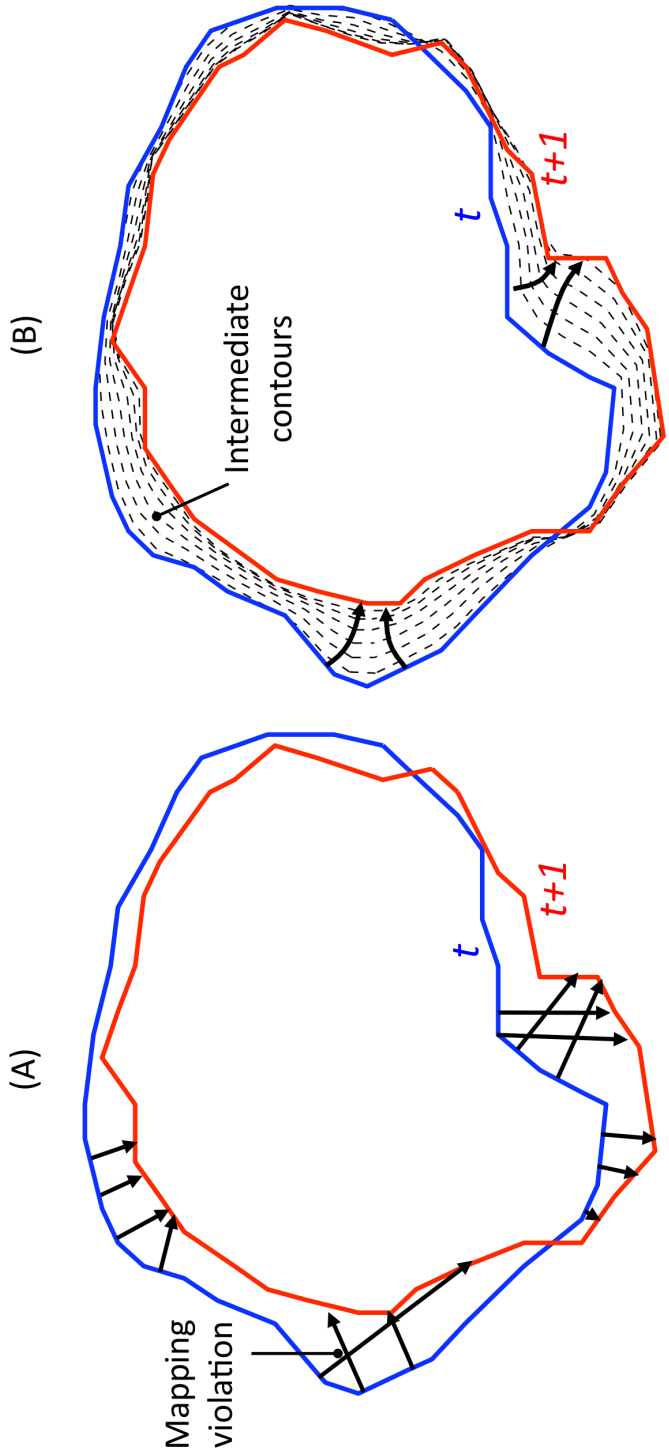

Figure 1.4: **Mapping outline Γ_t to Γ_{t+1}, via normals.** (A) Markers placed on Γ_t are mapped by following the normal direction to Γ_{t+1}. In the majority of cases, markers will cross paths effectively causing a twisting in the contour (mapping violations). (B) One solution is to create intermediate contours over which normals can be followed more reliably. This approach is employed in the level set method (LSM). Figure adapted from Tyson et al. [2009].

strong deformation. In the related problem of motility simulation, LSM is also used to propagate the cell boundary by coupling it to mechanical, or PDE based, models by defining speed functions [Yang et al., 2008; Neilson et al., 2010a]. LSM has several drawbacks for mapping and modelling, experienced by Machacek and Danuser [2006] and demonstrated in Chapter 3, centred around computational cost and achieving even marker distribution.

Unlike skeletonisation, LSM provides no inherent way to track cell extension or retraction from the mappings it produces, and to our knowledge no one has combined LSM with any such algorithm. However, previous iterations of QuimP, as outlined in the next section, include this functionality, but holds its own limitations.

1.6 Quantitative Imaging of Membrane Proteins (QuimP)

The QuimP software package was first conceived by Till Bretschneider and Thorsten Libotte in 2002 [Dormann et al., 2002], and implements an active contour method to automatically track cell position and shape over time, but crucially, to track local regions of interest during movement for correlation of sampled fluorescence with local deformations.

The QuimP active contour model implements a form of Kass snake, adapted to improve detection of weak boundaries and concave regions. A virtual, closed chain of points (nodes) are connected by contractive forces, but are also acted upon by an additional inward force, pushing nodes into concavities. Together, these forces contract the snake towards objects within the snakes boundaries. An opposing, outward force is calculated from pixel intensities within a bounding box around each node (orientated normal to the snake's surface), and is referred to as the image force. The gradient in the box determines the size of the image force, and halts nodes at edges.

Because nodes keep their positions relative to their neighbours from frame to frame, the key approach was to utilise them as a reference co-ordinate system for constructing spatio-temporal polar plots, and capturing the dynamics of membrane fluorescence as cells move. Fluorescence was measured by shrinking nodes inwards over the cortex, and recording maximal values. The resulting inner outline is then used to define the cell interior and calculate relative membrane fluorescence in the form of a ratio. This accounts for differences in expression level, photobleaching, and varying illumination between experiments.

Dormann et al. [2002] were able to show that the translocation of CRAC and Akt/PKB to the membrane occurred in response to stimulation with cAMP, and that this correlated with changes in cell elongation and dispersion (computed from fitted

Legendre-Ellipses). Furthermore, a quantitative difference was observable in the rate of association and dissociation between the two proteins, as well as periodic CRAC translocation.

Since conception, QuimP has been the analysis tool in numerous publications. The study of acto-myosin dynamics in *Dictyostelium* in response to cAMP addition, or mechanical stimulation, revealed the well known *cringe* response. F-actin is seen to rise sharply and then fall, while myosin-II accumulates only after this response [Etzrodt et al., 2006]. The reversal of polarity that occurs when switching fluid flow is characterised by global reduction in F-actin, in contrast to myosin-II which continuously redistributes [Dalous et al., 2008]. Bosgraaf et al. [2005] used myosin-II-GFP to demonstrate deficient polarisation in *Dictyostelium* mutants. QuimP has also been used to analyse the results of FRAP experiments, determining the average exchange rates of cell-cortex bound coronin to and from the cytoplasm [Bretschneider et al., 2002].

QuimP has been instrumental in studying PtdIns(4,5)P_2 and PtdIns(3,4,5)P_3 localisation in cAMP gradients. Using GFP tagged, PH domain containing proteins as reporters, Dormann et al. [2004] studied PtdIns localisation and degradation during phagocytosis and chemotaxis, revealing that different PH domains gave distinct spatio-temporal patterns in response to the same PtdIns(3,4,5)P_3 signal, enabling varied responses. Similarly, Ferguson et al. [2007] observed that PtdIns accumulation is PI3K dependent in mouse neutrophils. Bosgraaf et al. [2008] showed strong PtdIns(3,4,5)P_3 localisation in steep gradients, enhanced speed, and that PI3K mutants were poor at chemotaxing.

Although providing novel methods for studying protein dynamics, QuimP was unsuitable for quantifying local membrane deformation. QuimP2 [Bosgraaf et al., 2009] introduced the notion of signed area change to quantify membrane deformation between frames. Snake nodes are assigned unique tracking numbers, which are maintained over time. The area increase/decrease resulting from a nodes displacement quantifies deformation local to a node (this minimises the contribution of tangential movement, as opposed to using absolute distance). Data on membrane deformation could then be assembled into spatio-temporal plots, alongside fluorescence data, for the purpose of correlation.

Bosgraaf et al. [2009] applied QuimP2 to study myosin-II and F-actin distributions in response to cAMP, revealing a 40 second period in which *Dictyostelium* freezes, accompanied by global increase in F-actin and translocation of myosin-II to the membrane. F-actin levels are observed to be elevated at the site of pseudopodia extension some time in advance, suggesting the position of pseudopodia is determined earlier. At the time of extension local myosin levels are seen to decrease, suggesting that myosin

filaments block extension, and that interaction between myosin and F-actin determines both the start and end periods of an extension.

Bosgraaf and Haastert [2009c] used the output of QuimP2 to develop an automated pseudopodia tracking algorithm. By combining information on node area change and curvature, they were able to detect the start and end points of pseudopodia in *Dictyostelium*, producing data on size, lifetime, frequency, and direction. Analysis showed pseudopodia to extend normal to the surface, rather than directly towards a chemoattractant source [Haastert and Bosgraaf, 2009b], and that disruption of cGMP-mediated signalling produces a 3 times reduction in *de novo* pseudopodia nucleation [Bosgraaf and Haastert, 2009a] (due to myosin filament formation at the cell's sides [Bosgraaf et al., 2002]). Furthermore, the pseudopod tracking suggests a skating pattern of left/right splitting pseudopodia to amplify response to shallow gradients [Bosgraaf and Haastert, 2009b], and a step-turn strategy used for finding food [Haastert and Bosgraaf, 2009a]. These results have informed a stochastic model by Haastert [2010] which correctly predicted hindered chemotaxis in mutants incapable of pseudopodia splitting, and a feedback-based model by Neilson et al. [2011] where pseudopodia are driven by peaks in local activators, which then feedback to stimulate the production of inhibitors.

1.7 Limitations of the QuimP2 Software

Labelling nodes of an active contour combines segmentation and tracking of local deformations into a one step process, and as such is a significant advantage over implementing and computing additional, slower mapping techniques, like LSM. But, although nodes can be retained between frames, changes in local surface area require nodes to be added or removed to maintain node resolution, which subsequently interrupts tracking lineages and leaves gaps in deformation data. As an example, using 170 nodes to segment a cell over 160 frames will typically introduce over 2,000 new nodes, none of which are traceable to previous frames. Removal of nodes is particularly frequent as concave regions become convex, again breaking lineages. Furthermore, the positions of nodes are determined by parameters chosen to obtain a good segmentation, rather than achieve constant tracking, and do not represent a unique solution. Similarly, the resolution of the tracking is limited by the speed and numerical stability of the active contour method.

QuimP2 would significantly benefit from an independent, high resolution mapping method allowing it to match the quality of data produced by Machacek and Danuser [2006], on condition that an additional mapping step is efficient enough for high-throughput approaches. In addition, the improved data on deformation will pro-

vide new means for automated protrusion tracking algorithms that can be applied to cells exhibiting complex patterns of protrusions, including high speed blebbing.

Mapping aside, the segmentation plug-in provided by QuimP2, although effective, is relatively slow (due to implementation), non-parallel, and suffers from instability. Most importantly however, users are required to pre-set parameters and can not interact with the segmentation process. Therefore, parameter setting requires a certain amount of guess work, and corrections cannot be made manually, making segmentation somewhat laborious. QuimP2 also lacks tools for further analysis, which is a significant problem for free software intended for the benefit of the scientific community, who in general, require the flexibility to extract specific measures of interest.

1.8 Project Aim

Pseudopod formation is generally viewed in the literature as the primary mechanism of movement in *Dictyostelium*. The polymerisation of actin monomers generates force, acting to push forward the plasma membrane. It is becoming increasingly clear that this is not the sole means of locomotion, particularly in resistive environments [Kay et al., 2008]. Blebbing exploits intracellular hydrostatic pressure to drive forwards patches of membrane, producing distinct hemispherical protrusions that extend quickly, at high speed, and leave *actin scars*.

To study these mechanisms of motility we require new high-throughput techniques capable of quantifying both deformation and fluorescence of large, slowly extending pseudopodia, but also rapidly extending blebs, which are often comparatively small, short lived, and result in complex changes to membrane curvature. Hand-in-hand with this aim is the need to update the current QuimP software to handle these kinds of problems, and eliminate the limitations outline in the previous section.

To this end, we want to integrate into QuimP a new, high resolution, membrane tracking method, which does not suffer from dilation of markers (as LSM does), while being efficient enough for high-throughput analysis. We can use this method to implement an automated protrusion tracking algorithm capable of tracking blebbs. Furthermore, we aim to be able to validate the membrane tracking performed *in silico* with that of real membrane deformation in *Dictyostelium*. In collaboration with Rob Kay's group, we aim to then apply QuimP to extract quantitative data on the nature of pseudopodia and blebs in *Dictyostelium* migrating under agar.

Finally, QuimP was conceived as free software, made available to the scientific community for a variety of image analysis tasks that require automation. The new generation of QuimP should be available for free download, and contain the necessary

documentation and analysis tools.

The following chapter, *Materials and Methods*, contains diverse experimental and theoretical methods appropriate to all chapters. References to sections within *Materials and Methods* are given throughout this document, hence the reader may jump directly to Chapter 3 (page 40).

Chapter 2

Materials and Methods

2.1 Software Development Tools

QuimP was written in the Java programming language as plug-ins for ImageJ[1], image analysis software based in the Java language (created by Wayne Rasband at the National Institute of Mental Health) [Abràmoff et al., 2004].

ImageJ includes inbuilt image processing algorithms and allows cross platform distribution. QuimP was developed within Mac OSx 10.6.8 using Netbeans IDE 6.9.1, Java development kit 5, and ImageJ source code 1.45g [Computer spec: 2.4GHz Intel Core i5, 4 GB 1067 MHz DDR3 memory].

Image-preprocessing and analysis (including the use of QuimP) was performed on the Warwick Systems Biology Image Server (Linux OS) [spec: Dual Quad-Core AMD Opteron Processor 2350 2 GHz , 32 GB memory]. Fiji (1.45b), an expanded version of ImageJ (`http://fiji.sc/wiki/index.php/Fiji#`) was used for scripting ImageJ macros for image pre-processing and manipulation. Prototyping of ECMM, ECMM-APT, and analysis of QuimP output was performed using MATLAB[2] version 7.10.0.499 (R2010a). This included the use of the MATLAB products Image Processing Toolbox, Statistics Toolbox, and Curve Fitting Toolbox.

2.2 Marker Mapping Using the Level Set Method

This section describes a level set method for tracking local membrane deformations, as previously implemented by Machacek and Danuser [2006], and as overviewed by Tyson et al. [2009].

[1] `http://rsbweb.nih.gov/ij/`

[2] © 2011 The MathWorks, Inc.

We propagate the cell outline Γ_T to Γ_{T+1}, and extract a series of intermediate boundaries, Γ_t, where t is an evolutionary time step.

First, Γ_T is defined on a two dimensional cartesian grid ($\Gamma_T(x, y) \in \mathbb{R}^2$). The grid is transformed into a three dimensional surface, ϕ_T, called the *level set*, by applying a signed distance function (Figure 2.1A, B, C). The function defines z values on $\phi_T(x, y)$ equal to the distance between (x, y) and the closest point on Γ_T. The outline Γ_T is therefore defined by the zero level set

$$\Gamma_T = \{(x, y) | \phi_T(x, y) = 0\}. \tag{2.1}$$

Γ_T can be evolved uniformly by adding a constant to the signed distance function, effectively displacing ϕ_T in the z axis (Figure 2.1D). A new zero level set can then be extracted.

Similarly, ϕ_T can be propagated onto ϕ_{T+1} by controlling the speed of level set evolution via the evolution equation

$$\frac{\partial \phi(x, y, t)}{\partial t} + F(\phi_t, t)|\nabla \phi_t(x, y, t)| = 0, \tag{2.2}$$

$$\phi_{(x,y,t=0)} = \phi_{(x,y,T)}, \tag{2.3}$$

where F (the speed function) controls the speed at which the surface gradient of ϕ_t is followed (Figure 2.2). The MATLAB add-on *toolbox implementing Level Set Methods* [Mitchell, 2008] was used to provide the functionality for evolving level sets. Critically, the speed function influences the characteristics of the intermediate boundaries, and hence the propagation of normals. The simplest speed function, F_d, will move Γ_T at speeds proportional to its distance from Γ_{T+1}:

$$F_d = \phi_t - \phi_{T+1}. \tag{2.4}$$

During evolution, intermediate contours, Γ_t, are extracted as zero level sets (as in equation (2.1)). A set of virtual markers are then propagated successively between intermediate boundaries in a direction defined by the normal at the location of the marker on Γ_t, until Γ_{T+1} is reached. The computational expense of propagating markers is independent from the computation of the intermediate outlines.

2.3 Photobleaching Membrane Markers

For fluorescence imaging we use *Dictyostelium* cell lines expressing two fluorescently tagged proteins; GFP labelled cAR1 labels the entirety of the membrane and is the

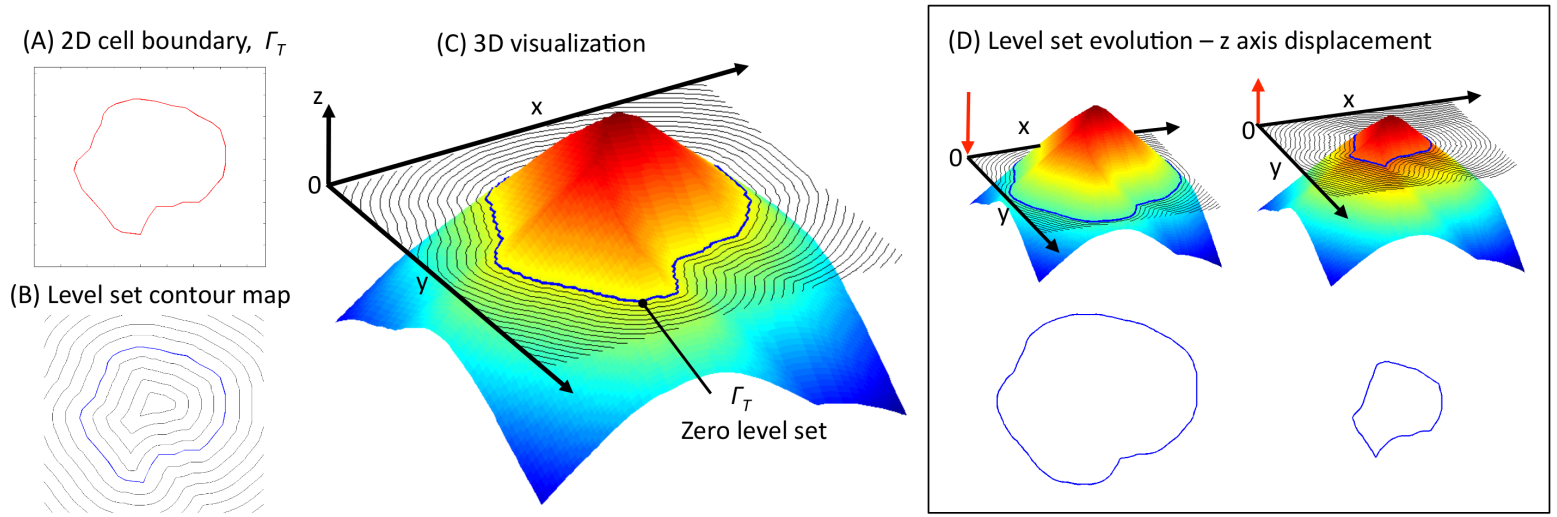

Figure 2.1: **Construction and evolution of the level set.** (A) The cell outline at time T is defined on a 2 dimensional grid ($\Gamma_T(x, y) \in \mathbb{R}^2$). (B) Γ_T is embedded into the level set ϕ_T by transformation with a signed distance function defining the distance a grid point lies from Γ_T). The contour lines depicted follow grid points of equal distance from Γ_T. (C) Mapping distance to a third co-ordinate, z, allows 3D visualisation of the level set. The outline Γ_T lies at what is referred to as the zero level set. (D) In the simplest case, the level set is displaced in the z-axis, either positively or negatively, and a new zero level sets extracted to define Γ_T. The outline Γ_T can be said to have *evolved* continuously, in the normal direction, in accordance with the level set surface. Reproduced from Tyson et al. [2009].

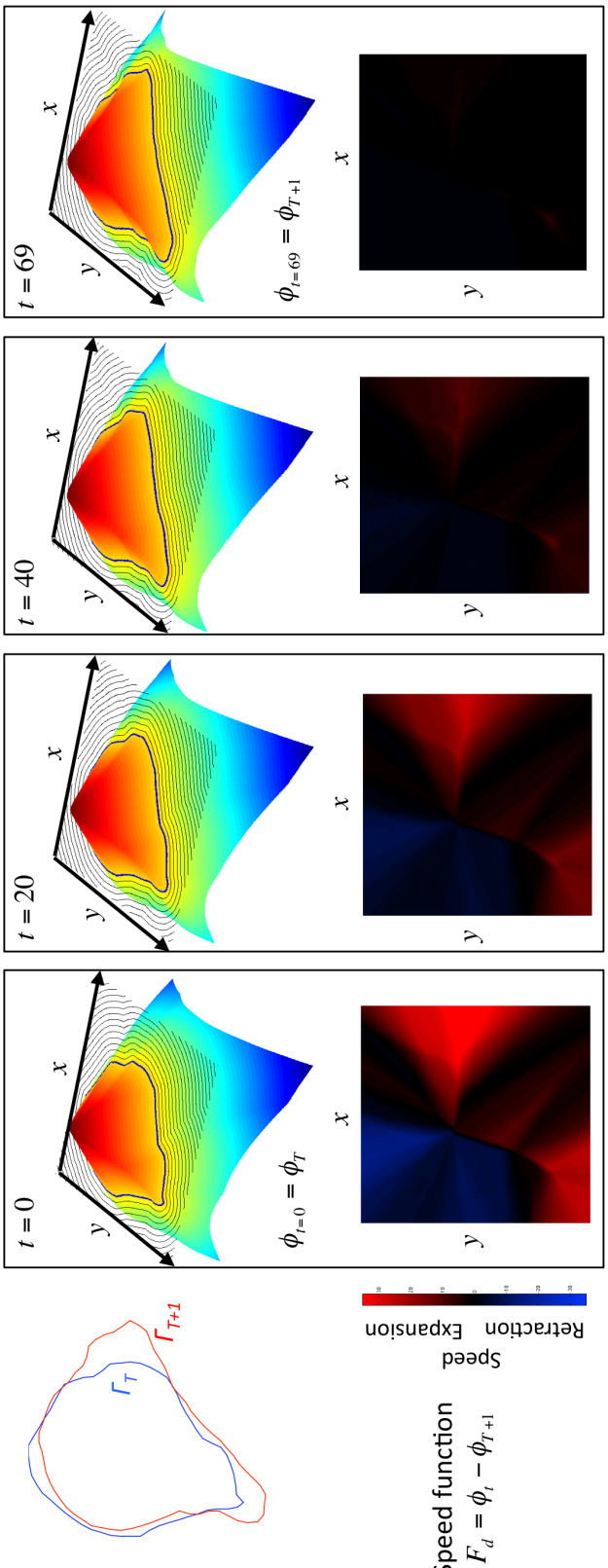

Figure 2.2: **Evolving Γ_T to converge at Γ_{T+1}.** The level set ϕ_T is propagated to ϕ_{T+1} over time steps t as in the evolution equation (Equation 2.2), until $\phi_t = \phi_{T+1}$. Vitally, the speed function F_d controls the rate of evolution across the level set and is representative of a distance map between ϕ_T and ϕ_{T+1}. As ϕ_T converges to ϕ_{T+1} the speed function is reduced to zero, halting evolution. Reproduced from Tyson et al. [2009].

target for photobleaching; RFP labelled LimE, previously shown to be an excellent labeller of F-actin [Bretschneider et al., 2004], provides a secondary signal (throughout the cytoplasm) required for segmentation by QuimP.

2.3.1 Sample Preparation

Dictyostelium lines are cultured at room temperature in 10ml FM growth medium containing $5\mu g\ ml^{-1}$ of the antibiotic G418, and $10\mu l$ hydromycin, for selection of transformed lines. Cultures are split every 2 days to maintain the exponential growth phase (cultures contain less then $4x10^6\ cells\ ml^{-1}$). For imaging, $20\mu l$ is transferred to a glass bottom dish, and $2ml$ of KK2 buffer is added if the cells are to be starved, otherwise $2ml$ of FM medium is added. Cells are allowed a minimum of 15 minutes to adhere to the glass surface, and can be optionally starved for 3-6 hours prior to imaging to promote cell movement.

2.3.2 Imaging

Cells are imaged in two channels under an Olympus FV1000 confocal microscope using a 60x oil immersion objective. Typically, images are captured at 1.6 $frames\ sec^{-1}$. Exposure to light is minimised by using low laser power, and low frame rates prior to image capture. Spots, or patterns, are bleached into the green channel (GFP labelled cAR1) for the purpose of tracking.

2.3.3 Tracking Bleach Spots

The centre of a bleach spot in a captured image is extracted by manually placing a line selection across the membrane at the spots location (performed in the image analysis software ImageJ) and fitting a Gaussian curve to the intensities sampled along this line. The peak of the Gaussian is considered to be the bleach centre. When applied to all frames of an image sequence, a bleach spots trajectory can be plotted and compared to the marker mapping outputted by ECM for a short period of time (typically 6 seconds).

2.4 QuimP Software Implementation: Methods

2.4.1 Motility and Morphological Measurements

Measurements are converted to real world units of *microns* and *seconds* unless otherwise stated.

2.4.1.1 Cell Area

$$A = \frac{1}{2}\sum_{N-1}^{i=0}(x_i y_{i+1} - x_{i+1} y_i) \tag{2.5}$$

where N is the number of nodes in the chain, x the horizontal image co-ordinate of a node and, y the vertical image co-ordinate.

2.4.1.2 Cell centroid

The cell centroid, $c_{x,y}$, is defined as the *centre of mass* of the nodes forming the cell outline:

$$c_x = \frac{1}{6A}\sum_{N-1}^{i=0}(x_i + x_{i+1})(x_i y_{i+1} - y_i x_{i+1}), \tag{2.6}$$

$$c_y = \frac{1}{6A}\sum_{N-1}^{i=0}(y_i + y_{i+1})(x_i y_{i+1} - y_i x_{i+1}), \tag{2.7}$$

2.4.1.3 Displacement

Cell displacement, DS, is defined as the Euclidean distance between a cell's starting location and current location, as determined by the cell centroid.

2.4.1.4 Distance travelled

Distance travelled, D, is the length of the path travelled by the cell centroid between $T = 0$ and T.

2.4.1.5 Persistence in direction

A cell's persistence at T, P_T, is defined as

$$P_T = DS/D, \tag{2.8}$$

hence, a cell that travels in a straight line has a persistence value of 1, whereas cells that deviate from a straight path have values less than 1.

2.4.1.6 Speed

A cell's speed at time T, S_T, is defined as

$$S_T = \frac{D_T - D_{T-1}}{FI}, \tag{2.9}$$

where FI is the frame interval (image capture rate).

2.4.1.7 Perimeter

Perimeter, P_T, is the length of the cell outline computed as the sum of the distances between nodes.

2.4.1.8 Elongation

Elongation is defined as the length of the major axis of an ellipse fitted to the cell outline. The ellipse has the same area, orientation, and centroid as the outline, hence the same moments (as computed by ImageJ [Abràmoff et al., 2004]).

2.4.1.9 Circularity

Circularity, C_T, is a measure of cell roundness:

$$C_T = 4\pi \frac{A_T}{{P_T}^2}. \tag{2.10}$$

A value of 1 indicates a perfectly round cell (cell area matches that of a circle with perimeter P_T). Values below 1 indicate reduced circularity.

2.4.2 Definition of Fluorescence Statistics

Spatial-temporal units are in *microns* and *seconds* where appropriate. Intensity values have arbitrary units depending on the bit depth of an image, or represent values normalised to a cell's mean cytoplasmic intensity.

- **Node maximal intensity:** The maximal 3×3 *pixel* average intensity recorded within the local cortical region of the node.
- **Node sample location:** X and Y image pixel co-ordinates of maximal intensity.
- **Total and mean fluorescence:** Total and mean fluorescence of pixels enclosed by the cell boundary.

- **Cortex width:** User defined width between the cell outline and inner cortex boundary. Can be altered for individual channels.
- **Cortex area:** Area of the cortical region.
- **Cytoplasmic area:** Area of the region enclosed by the inner boundary.
- **Total and mean cortical fluorescence:** Total and mean intensity of pixels within the cortical region.
- **Total and mean cytoplasmic fluorescence:** Total and mean intensity of pixels enclosed by the inner boundary.
- **Percentage cortical fluorescence:** Percentage of the cell's total fluorescence localised to the cortical region.

2.5 Blebbing Assays in Resistive Environments (Experiments by Evgeny Zatulovskiy)

2.5.1 Strains

The wild type *Dictyostelium discoideum* strain is the Kay Laboratory version of Ax2 [Watts and Ashworth, 1970], transformed with a plasmid containing the reporter construct GFP fused with the amino terminus of the *Dictyostelium* actin cross-linking protein ABP-120 (GFPABD, strain HM2231) [Pang et al., 1998]. Cells were grown at 22°C on tissue culture plates with sterile axenic medium [Watts and Ashworth, 1970], and transformed cells were selected by cultivation in medium containing 10 $\mu g/ml$ G418 antibiotic.

Three KO strains were assayed; Myosin II KO missing the essential light chain (mlcE-KO) (defective in contractile function [Chen et al., 1995]), obtained form the Dicty Stock Center [3], derivatives of the JH10 strain; Pikl gene (DDB0234212) KO encoding the PtdInsP Kinase Type 1 PI(4)P5-kinase (PI5K) (unpublished, recently created by Louise Fets, MRC laboratory, Cambridge), functioning to transform PtdIns(4)P into PtdIns(4,5)P_2 by phosphorylation at the D-5 position of the inositol ring [Yang et al., 2004]; PI3K-KO quintuple mutant in which all five type-1 phosphoinositide-3-kinase genes (pikA, pikB, pikC, pikF and pikG) have been knocked out, derived from Ax2 cells by electroporation [Hoeller and Kay, 2007].

[3] *http://dictybase.org/StockCenter/StockCenter.html*

2.5.2 Assays Under Agarose

Methods used here are adapted from those developed by Laevsky and Knecht [2001]. A thin layer of agarose gel (600 μl at 0.7% agarose in KK_2 buffer) is allowed to harden on a two-chamber Lab-Tek coverslip. A central rectangular trough 4 by 8 mm is cut into the agarose, and two further rectangles 1 by 5 mm, cut parallel either side at a distance of 6 mm. To the central trough 4 μM cAMP is added and allowed to diffuse for 40 minutes, setting up a cAMP gradient. Roughly 1×10^5 cells are placed into both the left and right troughs and allowed to settle. Cells respond to the chemotaxis gradient and do so by squeezing under the agarose gel, where they are imaged.

To enhance the contrast of the cell outline, samples were negatively stained with Rhodamine-B-isothiocyanate-dextran (RITC-Dx) added to the agarose at 0.5 mg/ml, and its emission recorded in a separate fluorescence channel. The stain acts to fluoresce the background while cells appear as shadows. Without negative staining segmentation using QuimP would rely solely on actin labelling, which in the case of blebbing is inaccurate due to the absence of actin in an emerging bleb.

2.5.3 Imaging

Images of Ax2 cells were taken using both confocal and spinning disk microscopy to provide image sequences at multiple frame rates. Confocal fluorescence and DIC image sequences were taken using the Zeiss 710 laser scanning confocal microscope (Zeiss, Germany) with a 63× oil-immersion objective and a frame interval of 500 ms (2 fps) for a period of 100 seconds.

Spinning disk microscopy was used to capture fluorescence image sequences at speeds in the range of 4-6 fps. Confocal images at 2 fps proved insufficient to capture the fastest blebs during extension, hence resulting in an underestimate of the extension speed for the fastest occurring blebs. Additionally, attaining sequences at multiple frame rates allowed us to develop a frame-rate independent method for automated protrusion tracking, eliminating possible side effects of differing frame rates on protrusion analysis.

Mutant strains were imaged using spinning disk microscopy only, and lacked GFP-ABD labelling.

2.5.4 Image Pre-Processing

Image pre-processing was done using ImageJ macros. Blank sequences of roughly 50 frames (containing no cells in the field of view) were imaged prior to each experiment to capture background illumination. Intensity fluctuations over blanks were removed by

equalising the mean intensity at all frames. Average intensity projections were created from the corrected blank frames and Gaussian convolution applied ($\sigma = 1$ *pixel*) to smooth high frequency noise (as provided by ImageJ). We refer to resulting images as background masks.

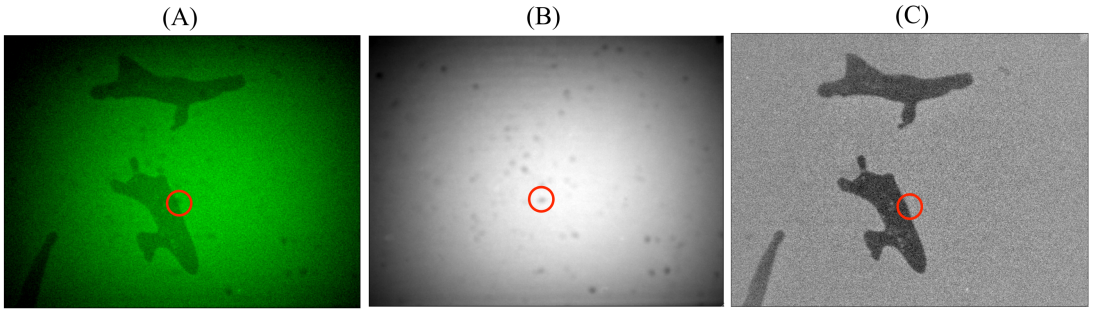

Figure 2.3: **Background correction within spinning disk microscopy images.** (A) Raw image obtained from spinning disk microscopy (frame interval = 0.22 *sec*) demonstrating uneven illumination and shadows resulting from specks in the optics. Circled is a shadow obscuring the cells true boundary. (B) Background mask generated from a z-projection of a blank image sequence. (C) Image corrected using the background mask.

Similarly, image sequences containing cells were processed to remove intensity fluctuations, as described above (sampling of mean intensity was restricted to regions containing no cells). Each frame was then background corrected by dividing image pixels by the corresponding pixels in the background mask. To improve background removal where contrast differed significantly between mask and image, contrast and brightness were matched by manipulating the distribution of pixel intensities. See Figure 2.3 for an example of background removal.

The RITC-Dx channel, used for segmentation, was inverted to produce bright cells on a dark background. In cases where background correction was inadequate to achieve an acceptable segmentation, or intracellular structures greatly interfered with the cell edge, the RITC-Dx channel was converted to a binary image using thresholding. *Holes* in the binary image were filled using ImageJ's *Fill Holes* option.

2.6 Methods for Protrusion Analsysis

2.6.1 Computing Peak Protrusion Speed

Given a motility displacement profile (see Section 6.2.5.1), we attain a noise free measurement of the gradient, during the constant speed phase, by fitting the following

generalised logistic sigmoid curve,

$$f(x) = a(1 - \exp(-\frac{x}{b}^c)) + d, \tag{2.11}$$

$$\frac{d}{dx}f(x) = \frac{ac\frac{x}{b}^{c-1}}{b\exp(\frac{x}{b})^c}. \tag{2.12}$$

Equation 2.11 allows fitting to negative values during acceleration (resulting from noise, or small contractions) by including the parameter d, and also non-symmetrical acceleration and deceleration. The generalised logistic sigmoid is real-valued and differentiable (Equation 2.12) hence the peak gradient can be determined. Fits with a *coefficient of determination* (R^2, as defined in Appendix A.6) below 0.6 are labelled as incorrect protrusions.

Over-fitting can occur when the number of available co-ordinates is below 6, typically when a protrusion is not imaged during extension due to its high speed. Fits have a high R^2 but fail to accurately represent the stationary phase leading to an over estimate of peak speed. We linearly interpolate the displacement profile to generate points mid extension, guiding the sum of squares minimisation to fit the slope correctly. This is likely to result in an underestimate of speed, but as a result of missing data and not an artefact of fitting.

2.6.2 Protrusion Rate

Given a sequence of N cell outlines, with K detected protrusions, the protrusion rate, PR ($\mu m^{-1}.s^{-1}$), is

$$PR = \frac{K}{IP}, \tag{2.13}$$

$$IP = \sum_{i=0}^{N}(T_{i+1} - T_i)\frac{P_i + P_{i+1}}{2}, \tag{2.14}$$

where i is the frame number, T is time (seconds), and P the cell perimeter (μm).

2.6.3 Generating Line Segments for Protrusion Kymographs

To obtain appropriate co-ordinates for a sampling line, L^p, protrusion paths are smoothed to remove noise using the *smooth* function provided by Curve Fitting Toolbox software (parameterised to use the *Lowess* method over a window of 10 points). To reduce the resolution of L^p (fewer line segments) co-ordinates are removed which do not signif-

icantly alter the direction. A co-ordinate p_i, is determined not to deviate from the path direction if the area of the polygon formed by $[p_i, p_{i-1}, ...p_{i-k}]$, where k is the number of co-ordinates previously determined as not deviating, is below a threshold (see Appendix A.1.1 for pseudo code). Typically, this results in L^p having 3 to 4 line segments, set to a width of $0.5\,\mu m$ over which pixels are averaged.

2.6.4 Correcting Overlapping Protrusion Tracks

Patterns of overlap can be complex to untangle. Protrusions have to be cut depending on where the overlap, or multiple overlaps, occur relative to mid-extension points. We define a set of overlap rules that, when applied to protrusions in the order of occurrence, determines where tracks are to be cut in order to satisfy the following criterion,

1. Mid-extension points cannot be removed.
2. Protrusions must not occupy the same map space within a spatial threshold of, L (μm), at the same point in time, else they are defined as overlapping.
3. Protrusions occurring earlier in time have *ownership* of map space occupied by their backward tracks, over protrusions later in time.
4. If the forward track of a protrusion, P1, overlaps completely with the backward track of a protrusion, P2, P1 and P2 share the map space, divided at the point of lowest displacement.

Additionally, protrusions can be joined end-to-end if they occur sequentially, determined by the proximity of their start and end points. See Figure 2.4 for example situations where protrusions overlap, and refer to Appendix A.1.2, Figure A.1 for a decision tree of the cutting process.

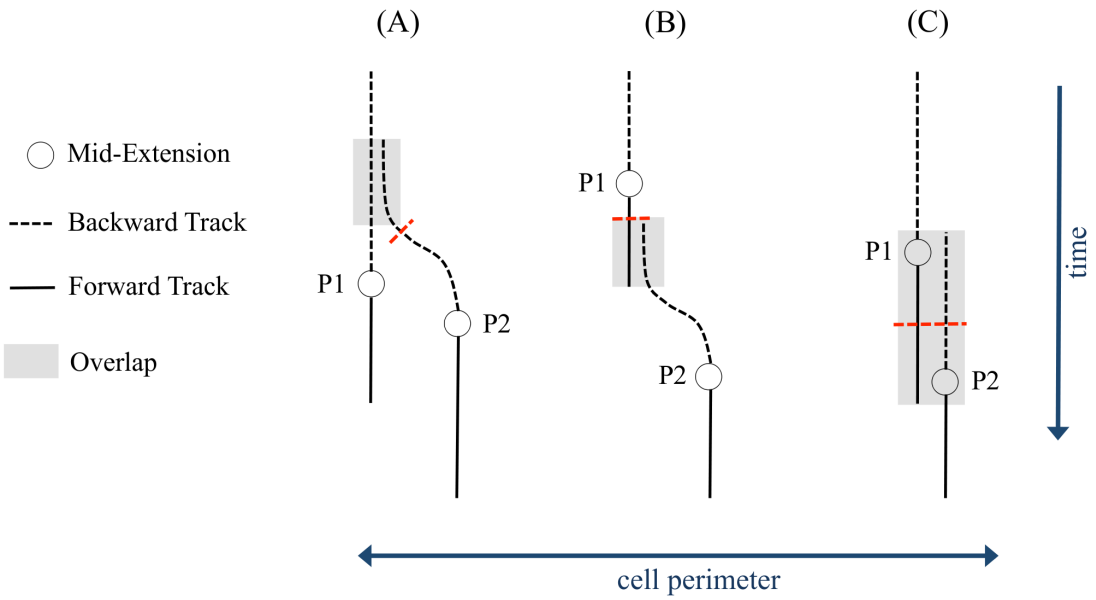

Figure 2.4: **ECMM-APT: Diagrammatic examples of correcting overlapping tracks.** Protrusions detected automatically may overlap in time and space, and require trimming. A protrusion's centre (circle) must remain intact, while traces forward through time (solid line) and backward (dashed line) may be cut to rectify overlaps (red line). Protrusions P1 and P2 may overlap in several configurations, P1 occurring earlier in time than P2. (A) P2 is cut as P1 retains priority of the overlapping area. (B) P1 is cut as P2 retains priority. (C) Overlap occurs at the mid-extension points of both P1 and P2, therefore both P1 and P2 are cut at the point of minimum displacement.

Chapter 3

Electrostatic Contour Migration Method: Tracking Cell Outlines

ECMM is founded on the creation of a fixed electrostatic field formed by placing a chain of virtual line charges, with segments of equal length, along the outlines Γ_T and Γ_{T+1}, with charges on each outline being opposing [Tyson et al., 2009]. Virtual markers placed on either outline, themselves charged, experience a force determined by the magnitude and direction of the electrostatic field at their location, causing them to migrate along field lines which flow between the outlines. A key property of electrostatic fields is that their field lines never cross, providing an ideal mechanism for mapping markers.

3.1 Calculating Electric Fields for Numerical Marker Migration

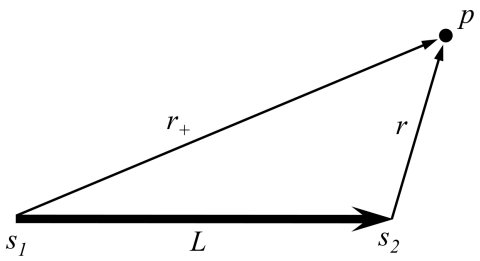

Figure 3.1: **Defining quantities for a line charge.** Adapted from Rowley [2006].

Charged chains of line segments form the electric field in which markers migrate. In Figure 3.1 the finite line L is defined in two dimensional Euclidean space by the

endpoints s_1 and s_2. The vector $\overrightarrow{r}$ points from s_2 to the field position, p, and $\overrightarrow{r_+}$ points from s_1 to p. The electric field, $\overrightarrow{E}$, at p, as described by Rowley [2006], is given by

$$\overrightarrow{E(L,\lambda)} = \frac{k\lambda}{d}(\hat{r}_+ + \hat{r}), \tag{3.1}$$

$$d = \frac{2L}{(r_+ + r)^2 - L^2}, \tag{3.2}$$

where k is the electrostatic constant, λ is the magnitude of the charge on L, $\hat{r}$ and $\hat{r}_+$ are unit vectors of $\overrightarrow{r}$ and $\overrightarrow{r_+}$ respectively.

A marker, positioned at p within an electric field, and carrying a single unit of positive charge, will experience a force, $\overrightarrow{F_p}$, equal to the sum of the forces contributed by each line of charge,

$$\overrightarrow{F_p} = \sum_{i=1}^{U} \overrightarrow{E(L_i,\lambda)} + \sum_{j=1}^{V} \overrightarrow{E(L_j,-\lambda)}, \tag{3.3}$$

where U is the number of positively charged lines and V the number of negatively charged lines. A line is assigned a positive or negative charge depending on its position relative to Γ_T and Γ_{T+1}, but also its position relative to p. Hence, a line's charge may be flipped as a marker migrates, principally to contain the marker within the bounds of the chain as described in section 3.2.1.

The force $\overrightarrow{F_m}(p,q)$ experienced by a marker m (of zero mass), at p, carrying a charge of magnitude q, is given by

$$\overrightarrow{F_m}(p,q) = \overrightarrow{F_p}.q. \tag{3.4}$$

Markers are migrated through the field numerically, using the explicit Euler method, by solving the equation

$$\overrightarrow{p_{t+1}} = p_t + \overrightarrow{F_m}(p,q).\Delta t. \tag{3.5}$$

3.2 Migrating Markers: A Simple Test Case

A cell outline, Γ, consists of a chain of connected nodes at a density of ω_N (nodes per pixel) determining the resolution of the segmentation. Markers and line charges are placed at densities independent of ω_N, and of one another, to control field complexity

and mapping resolution. Endpoints that define line charges are spaced equidistantly along the contour of Γ_T at a density of ω_L, typically equal to, or less than, ω_N. Similarly, markers are placed equidistantly along Γ_T at a density of ω_M, which is typically larger than ω_N.

In the test case depicted in Figure 3.2A, markers are individually migrated inwards from the outer outline Γ_T towards the target outline Γ_{T+1} , densities being equal ($\omega_N = \omega_L = \omega_M$). To demonstrate the mappings that occur in more complex situations, Γ_T includes a folded region. Note that no intersections exist between Γ_T and Γ_{T+1}. Depicted nodes represent line charge endpoints and also, due to equal densities, marker starting positions on Γ_T. Markers carry a positive charge and are attracted to negative charges placed on Γ_{T+1}. Positive charges on Γ_T repel markers, smoothly directing them towards Γ_{T+1} and without causing their paths to cross. Importantly, markers are unable to cross Γ_T due to repulsion. This is key to the functioning of ECMM under large deformations, especially in cases where the membrane folds over itself, if we are to avoid *twisting* in the mapping as encountered by the mechanical model of Machacek and Danuser [2006].

The speed of marker migration is controlled by the magnitude of the charges placed on the various components (but not the density of charges). It was necessary to introduce an upper limit on the maximal speed of migration, F_{max}, since very large forces can result from charges in close proximity. When forces become too large our approach becomes numerically unstable and migrating nodes may overshoot the target outline. Accuracy is determined by the numerical method (explicit Euler), and the speed of migration, both of which can be tuned for the required performance.

3.2.1 Adaptation to Line Charges and Adjustable Field Density

Previously, we described ECMM implemented with chains of point charges, as opposed to segments of line charges [Tyson et al., 2009]. Point charges allowed for simple implementation and fast computation, but sacrificed the uniformity of the electric field when in areas in proximity to Γ_T and Γ_{T+1}. As a marker approaches Γ_{T+1} its path skews towards the location of nearby point charges, resulting in the clumping together of markers, an undesirable characteristic (Figure 3.2B). Skewing/clumping becomes more severe when increasing marker resolution, as demonstrated in Figure 3.2C. This effect can be compensated for by increasing charge density, to be inline with marker density, but at high computational cost.

To remove skewing, marker migration was halted at distance threshold, d, and the marker *snapped* to the closest point on Γ_{T+1}. Snapping markers to their closest point can introduce mapping violations which must be corrected post mapping, adding

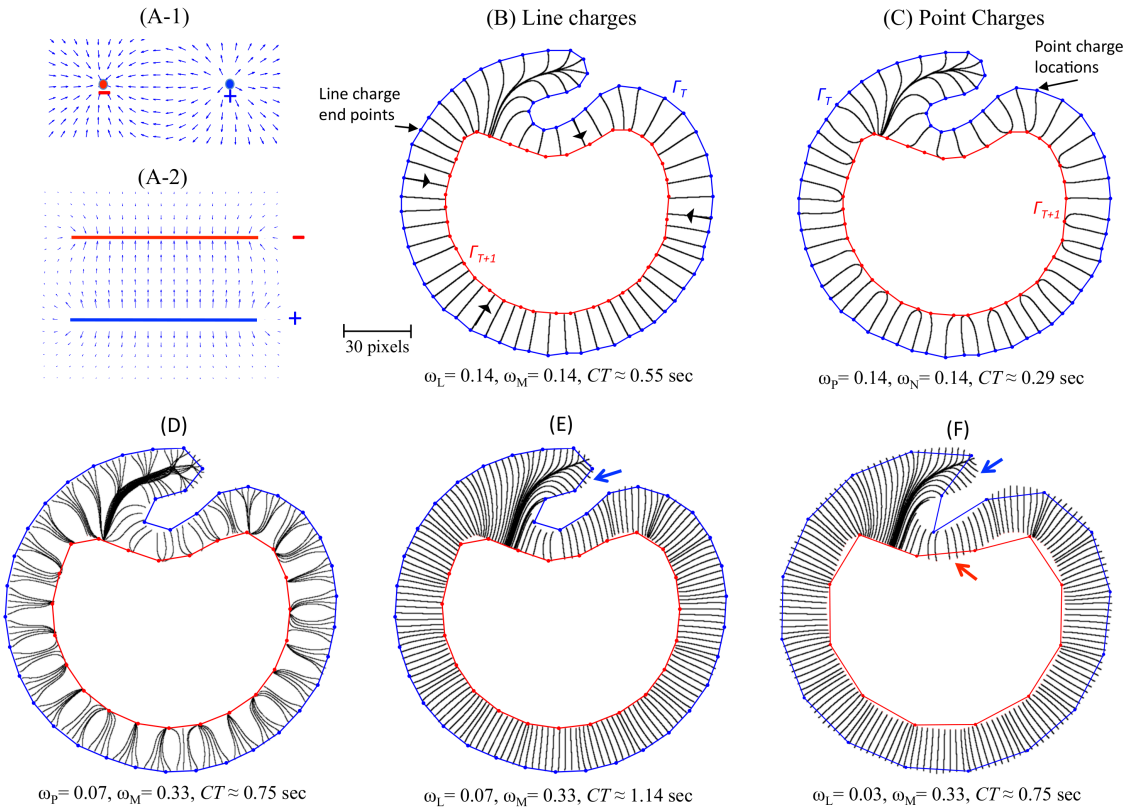

Figure 3.2: **Comparison of point charge and line charge implementation on a simple test case.** (A-1) Force field computed from positive and negative point charges. (A-2) Force field computed from line charges. (B) The outline Γ_T is mapped to Γ_{T+1}. Depicted nodes mark the endpoints of line charges that have been placed at a density $\omega_L = 0.14$ (a separation of ≈ 7 *pixels*). Markers are placed at the matching density, $\omega_M = 0.14$, and their paths of migration (as calculated by equation 3.5) are shown in black. The computational time (CT) is ≈ 0.55 *sec* (2.*d.p*). (C) Virtual point charges replace line charges at the previous location of endpoints, $\omega_P = 0.14$ (as described by Tyson et al. [2009]), $CT \approx 0.29$ *sec* (2.*d.p*). Markers are seen to skew undesirably as they approach Γ_{T+1}. (D) Marker density is increased, $\omega_M = 0.33$, resulting in severe clumping together of markers. (E) Increasing marker density when using line charges displays no skewing and therefore allows the field density to be reduced, as in (F), $\omega_L = 0.03$, saving on computation. Blue arrows indicate areas where markers have begun migration from outside the line of charges (caused by the drop in charge density). The polar nature of the charges draws markers inside. Similarly, the red arrow indicates where markers must cross the charges of Γ_{T+1}.

complexity and computation. It should also be noted that doubling the density of point charges, for example, will double the force experienced by markers, whereas a doubling of line charge endpoints will not increase forces (assuming the length of an outline remains constant when increasing line charge density). Control of numerical accuracy is therefore much simpler.

Implementing ECMM with line charges removes the effect of skewing, allowing d to become very small, acting only to compensate for numerical inaccuracy. Marker resolution can be arbitrarily increased without compromising the quality of the mapping (Figure 3.2D). Furthermore, charge density can be decreased to accelerate mapping without significant detrimental effects (Figure 3.2E).

A crucial concept for successfully migrating line charges, is the switching of a line's sign of a charge, from positive to negative, or vice versa, to attract markers that begin migration outside the bounds of charges on Γ_T (blue arrows in Figures 3.2D & E), and to repel charges towards Γ_{T+1} when entering the bounds of charges placed on Γ_{T+1} (red arrow in Figures 3.2E). Such a scheme is required simply because concave and convex regions of an outline can be *cut out* when ω_L differs from ω_M. A line's sign of charge is set by determining a marker to be inside or outside Γ_T and Γ_{T+1}, at each iteration of migration. This approach is applied to sectors as described in the next section, and we shall refer to charges that behave in this way as being *polar*.

3.3 Mapping Cell Outlines According to Intersections

Cell outlines at T and $T+1$ are overlaid on one another according to their absolute pixel position in the image sequence, and their intersection points calculated. Points of intersection compartmentalise the computation of mapping into *sectors*, closed contours made up from outline segments from the two time points (Figure 3.3A). Difficulties in defining sectors are discussed in Section 3.6. The boundary of a sector consists of an edge, Υ_T, from the cell outline at time T, and the corresponding edge, Υ_{T+1}, from the outline at $T+1$, flanked by intersection points.

Sectors are categorised according to two features, and will determine the direction of marker migration. A sector is designated as *expanding* if deformation between Υ_T and Υ_{T+1} results in an increase in cell area, and as *contracting* in the reverse case. Additionally, a sector is designated as growing if the length of Υ_T is greater than Υ_{T+1}, and as shrinking in the reverse case. This results in 4 possible categories, shown in Figure 3.3(A,C,D,E): expanding/growing, expanding/shrinking, retracting/growing and retracting/shrinking.

Each sector is considered separately for computation; that is to say the electric

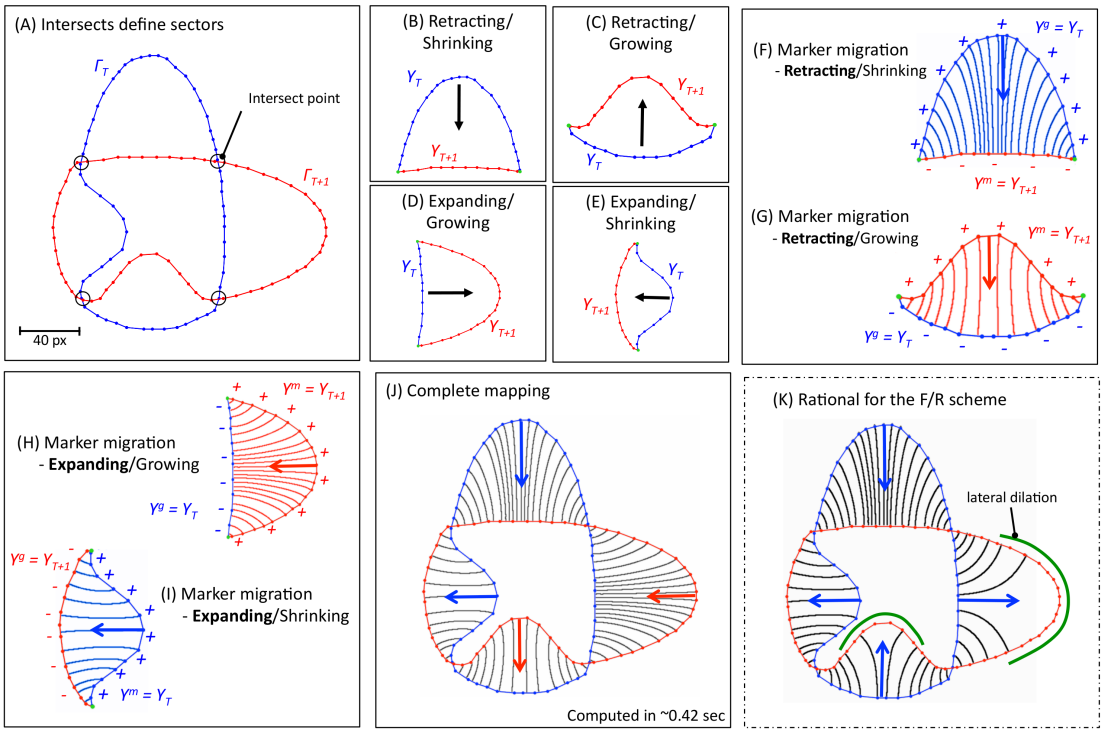

Figure 3.3: **Electrostatic Contour Migration Method (ECMM).** (A) The first step is to overlay outlines Γ_T and Γ_{T+1}, and to compute their intersects. Intersects are used to split the computation into sectors. Fixing attention on a single sector, we denote its two edges by $\Upsilon_T \subset \Gamma_T$ and $\Upsilon_{T+1} \subset \Gamma_{T+1}$. A sector is designated as expanding if it reduces cell area, and as contracting in the reverse case. Similarly, a sector is defined as growing if $\Upsilon_T \subset \Gamma_T \leq \Upsilon_{T+1} \subset \Gamma_{T+1}$, or as shrinking if $\Upsilon_T \subset \Gamma_T > \Upsilon_{T+1} \subset \Gamma_{T+1}$. The result is 4 categories of sectors, as depicted in (B) to (E). A sector's category determines the direction of migration in the forward/reverse scheme (F/R), as shown in (F) to (I). Negatively charged line segments, held fixed during the migration, are placed along the shorter of the two edges, the *target edge*, denoted by Υ^g. Positively charged line segments are placed along the longer edge, the *migrating edge*, denoted by Υ^m. Positively charged markers on Υ^m move under the influence of the subsequent electric field, advancing the edge Υ^m until within a threshold d of Υ^g. In this example the density of markers is equal to that of charges ($\omega_M = \omega_L$). (J) shows the complete mapping of virtual markers and the direction of the migration. Finally, (K) shows the rationale for the F/R scheme, without which undesirable lateral dilation occurs within growing sectors.

field for the sector is computed using only the edges Υ_T and Υ_{T+1}. This is necessary since categories of sectors are treated differently. Furthermore, restricting to these two edges reduces the complexity of the field, thus speeding execution of the code.

The technique is shown in detail in Figure 3.3. Migration of virtual markers is always directed from the longer boundary edge of a sector, termed the *migrating* edge (Υ^m), to the shorter edge, termed the *target* edge (Υ^g). This enables us to treat all sectors in a uniform manner, with Υ^m moving to Υ^g. We refer to this as the *forward/reverse (F/R) scheme* since markers are either mapped forward in time, or backward. The F/R scheme is vital to ECMM, since it avoids marker dilation, which lowers marker resolution in Υ_{T+1}. This effect is demonstrated in Figure 3.3K.

The first step in migrating markers within a sector is to place negative charges along Υ^g (at the desired density ω_L), and positive charges along Υ^m. As mentioned in section 3.1, the contribution a positive charge has to the field at distance, is less than that of a negative charge. This prevents the migrating edge heavily influencing migrating markers at distance, which could result in markers being compressed together to a point, most problematic when migrating highly convex edges.

Markers are then placed on Υ^m and allowed to migrate as described by equation 3.5. Migration is halted when a marker is within a threshold distance, d, of the closest point on Υ^g (typically $d \approx 0.4$ pixels).

Finally, migration is completed by *snapping* a marker to the closest position on Υ^g (moving a marker by roughly the size of d). Examples of the migration in the four sector categories are given in Figures 3.3B-E. Finally, Figure 3.3J shows the complete mapping between outlines Γ_T and Γ_{T+1}.

3.4 Comparison of ECMM to LSM: Elliptical Test Case

In our previous publication [Tyson et al., 2009] we tasked ECMM, and the rival LSM, with mapping virtual markers between two overlapping ellipses, one rotated 90 degrees to the other, to simulate both strong expansion in the horizontal direction, and strong retraction in the vertical direction (Figure 3.4). We show this same task here and include the mapping that results from a line charge implementation of ECMM. For details of the LSM implementation see Materials and Methods, Section 2.2 (page 27).

The major axes of ellipses are both 30 *pixels*, and level sets computation is performed by embedding the ellipses into a 240×240 grid. [Computer spec : 2.16GHz Intel core 2 duo, 2GB 667MHz DDR2 SDRAM].

Figure 3.4A shows the result of mapping using LSM and speed function given in equation (2.4) ($Computationtime(CT) \approx 21.2$ seconds). The evolution of the level

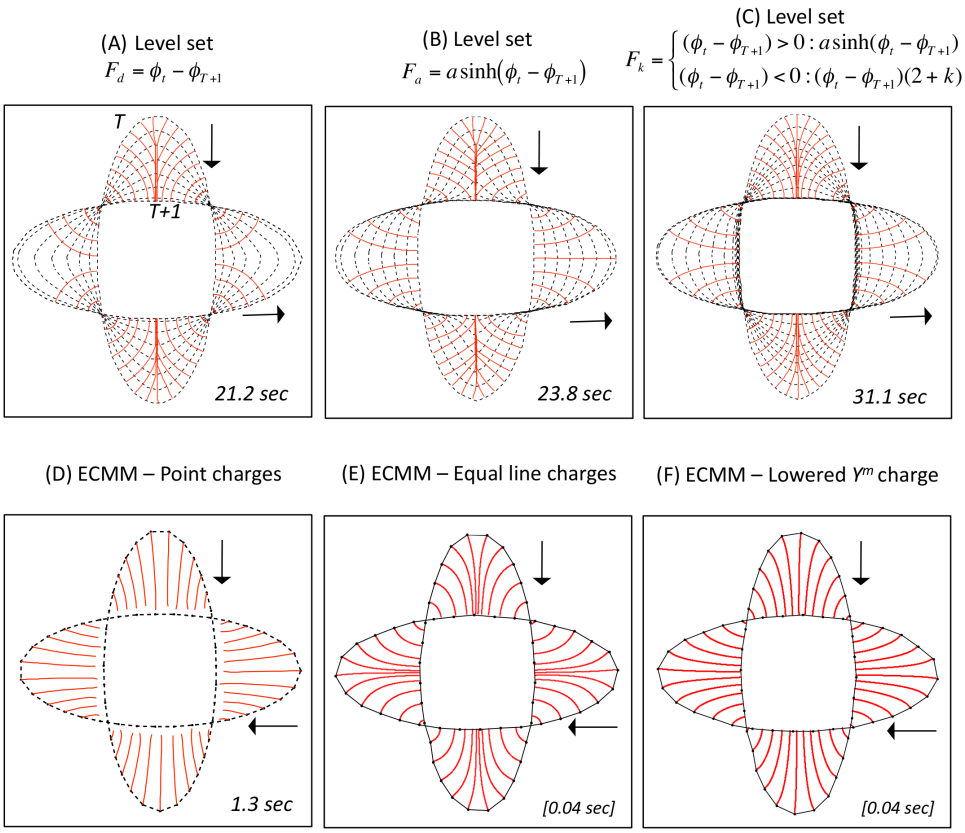

Figure 3.4: **Evaluation of ECMM and LSM using an elliptical test case.** An ellipse at T is migrated to an ellipse at $T+1$ to recreate retracting and expanding sectors. Ellipse major axis is 30 *pixels* in length. Dashed lines show the progress of the zero level set. Solid red lines show the paths of virtual markers. Arrows indicate the direction in which markers migrate. Timings are provided, in seconds, for computation. A grid size of 240×240 pixels was used for level set computation. (A) The distribution of markers undergoes severe lateral deformation during both retraction and expansion. Markers become dilated during expansion leaving unmapped regions, while congregating centrally during retraction. In this highly compressed region markers may become jumbled, crossing paths. (B) Dilation effects are reduced, but at the expense of increased central compression of markers. (C) The combined speed function reduces the central compression of markers, at the expense of slower convergence. (D) ECMM with point charges shows a distribution of markers that is identical during retraction and expansion, and markers remain equidistant with minimal lateral deformation. Satisfactory marker distribution is made possible by ECMM's F/R scheme. ECMM performs the mapping in 1.3 seconds, highlighting its relatively low computational cost. (E) ECMM with line charges allows a lower threshold d to be used, hence markers do not fall short of the target contour [Note: Timings in brackets are none comparable as implementation differs]. (F) ECMM with line charges and Υ^m charges 1/10 the magnitude of those in (E). Markers display less lateral compression. [Figure concept by Machacek and Danuser [2006], Figure 6].

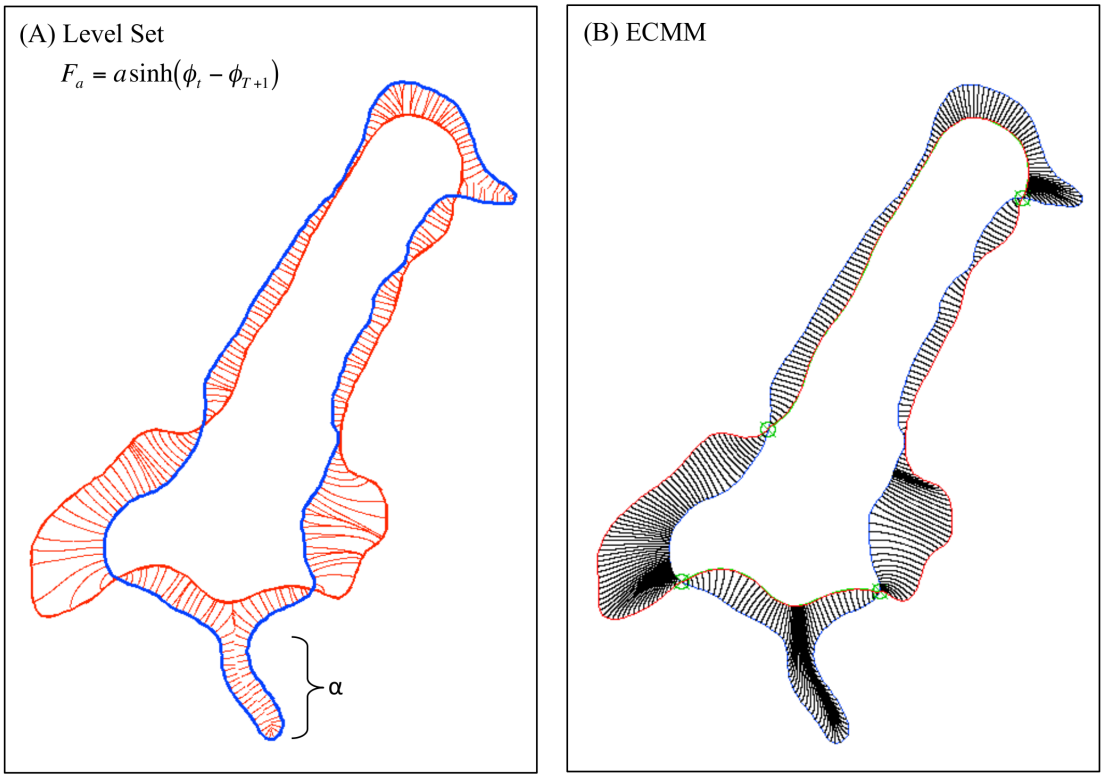

Figure 3.5: **Example cell boundary mapping with LSM and ECMM.** Blue boundary exists at time T, red at $T+1$. (A) LSM mapping shows severe marker dilation and compress, becoming more prominent in the case of larger deformation. Markers in region (α) fail to converge onto $T+1$ because the speed function in regions where boundaries run parallel becomes very small and numerically unstable at the midline. (B) ECMM produces a smooth, even mapping when faced with the same large deformations.

set is halted when the absolute size of F_d drops below a threshold value. Markers show strong lateral dilation in expanding sectors, leaving expanses of the ellipse at $T+1$ with very low spatial resolution of markers. The opposite problem is observed in retracting sectors, markers congregating centrally to a single point (and overlapping to an extent determined by the accuracy of the numerical solution), undesirably mapping the majority of the boundary to a point.

To reduce dilation and congregation of markers, Machacek and Danuser [2006] proposed two additional speed functions:

1. A dampening function (Figure 3.4B) that slows level set evolution at high speeds

$$F_a = \text{asinh}(\phi_t - \phi_{T+1}). \tag{3.6}$$

2. A combination speed function which dampens level set evolution in expanding sectors, and determines evolution speed in retracting sectors according to the curvature of the evolving contour (Figure 3.4C). Highly curved regions evolve faster so that the contour tends towards straightening, with the aim of reducing the congregation of markers,

$$F_k = \begin{cases} (\phi_t - \phi_{T+1}) > 0 : \text{asinh}(\phi_t - \phi_{T+1}) \\ (\phi_t - \phi_{T+1}) < 0 : (\phi_t - \phi_{T+1})(\epsilon + k) \end{cases}, \tag{3.7}$$

where k is a second-order finite difference approximation to the curvature gradient of the cell boundary,

$$k = \frac{\phi_{xx}\phi_y^2 - 2\phi_y\phi_x\phi_{xy} + \phi_{yy}\phi_x^2}{(\phi_x^2 + \phi_y^2)^{3/2}}. \tag{3.8}$$

Level set evolution using F_a reduces lateral dilation in expanding regions to a certain degree, but the congregating effect on markers in retracting regions is exacerbated (computational time of 23.8 seconds). The speed function F_k retains the improvements given by F_a and improves marker distribution in retracting regions, but this comes at the expense of slightly increased time until convergence ($CT \approx 31.1$ *seconds*).

Figure 3.4D and E. show the result of mapping using ECMM with point charges, and line charges respectively. The first noteworthy observation is that mappings in retracting and expanding regions are close to identical. This is because the mapping of all deformations (sectors) are computed as retractions following the F/R scheme. Secondly, the distribution of markers is very uniform throughout the mapping and therefore even marker resolution is achieved along the whole ellipse. The ECMM point

charge mapping was computed in a relatively fast time of 1.31 seconds [CT values for Figure 3.4E and F. are not comparable due to implementation in different programming languages].

Figure 3.4E was computed with equally charged Υ^g and Υ^m contours, unlike those in Figure 3.4D. With equal charges, greater lateral compression is observed in comparison to Figure 3.4F, where charges on Υ^m have been lowered to $\frac{1}{10}^{th}$ of the charge of Υ^g. Adjusting parameters, such as charge magnitude, provides a simple way of tuning ECCM without the need for complex speed functions that require greater computation.

Test cases aside, the failings of LSM become more apparent when applied to large cell deformations. In particular, long, thin membrane regions may fail to map due to numerical instability as the speed function becomes very small (Figure 3.5).

3.5 Computational Scaling

In the previous section, we showed that ECMM in comparison to a level set approach is computationally cheaper. Figure 3.6 shows how the Java implementation of ECMM scales with the density of line charges and markers.

Computation of equation (3.1) is at the centre of ECMM and explains the linear scaling of CT with both charge density and marker density. Doubling of ω_L, or ω_M, requires twice as many computations of equation (3.1) per marker, per time point. The slight deviation from linearity seen in Figure 3.6B. is due to pair wise operations on markers in post processing of the final mapping (for example, error checking).

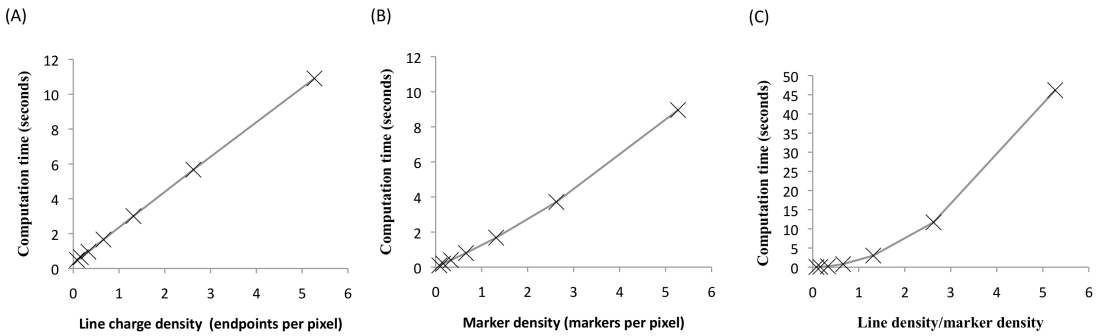

Figure 3.6: **ECMM computational scaling.** (A) Effect of increasing the density of line charges on computation time (seconds). (B) Effect of changing the mapping resolution (marker density) on computation. (C) Effect of maintaining equal charge and marker density, where the number of migrated markers matches the number of line charges.

When maintaining $\omega_L = \omega_M$, as shown in Figure 3.6, CT scales with a power of ≈ 1.97 (curve fit $CT = 1.756\omega^{1.97}$, $RMSE = 0.024$ $(2.s.f)$). It is clear that by allowing marker density to be increased independently of line charge density, power scaling of CT can be avoided while still achieving high marker resolution.

3.6 Correcting Sector Violations

We have previously described issues regarding the formation of sectors prior to the migration of nodes [Tyson et al., 2009]. Figure 3.7A shows the typical formation of sectors, each consisting of the two edges $\Upsilon_g \subset \Gamma_T$ and $\Upsilon_{T+1} \subset \Gamma_{T+1}$. A sector is said to be valid only if Υ_g and Υ_m begin and end at common intersection points, when travelling clockwise along Γ_T and Γ_{T+1}, hence forming a *closed sector*. In certain situations, defining valid sectors given all intersection points is impossible, as Υ_g and Υ_m form *open sectors*, as demonstrated by test case K in Figure 3.7B (only those labelled by an $*$ are valid sectors).

Invalid sectors are generally caused when an outline bends and intersects its previous location on both flanks. Such arrangements of intersects can become common if a cell outline is composed of many long, thin protrusions. The key to solving these cases is to disregard an intersection point if it prevents a sector from closing, as demonstrated in the two possible solutions to test case K in Figure 3.7B.S1 and B.S2.

When numerous artificial test cases are investigated it becomes apparent that multiple solutions exist for any mapping that has open sectors. Which solution is reached is determined by; 1) which intersection point is used as a starting point for defining sectors; 2) which edge, Υ_T or Υ_{T+1}, is first transversed when attempting to form a closed sector. In the majority of cases, some valid sectors will exist which can be used to help determine which intersect points should be disregarded (as for test case K). In other, rarer circumstances, no valid sectors exist, as in Figure 3.7C, and a random intersection point must be chosen to begin defining sectors.

The most appropriate solution is often subjective, but some basic measures are calculated to help determine which of the possible solutions is most appropriate. For example, if the length of Υ_T is similar to that of Υ_{T+1}, it is assumed that this forms a better sector arrangement than if the length of Υ_T and Υ_{T+1} differ hugely. In the vast majority of cases, using such a measure, along with valid sectors, allows the same solution to be chosen as would be by eye.

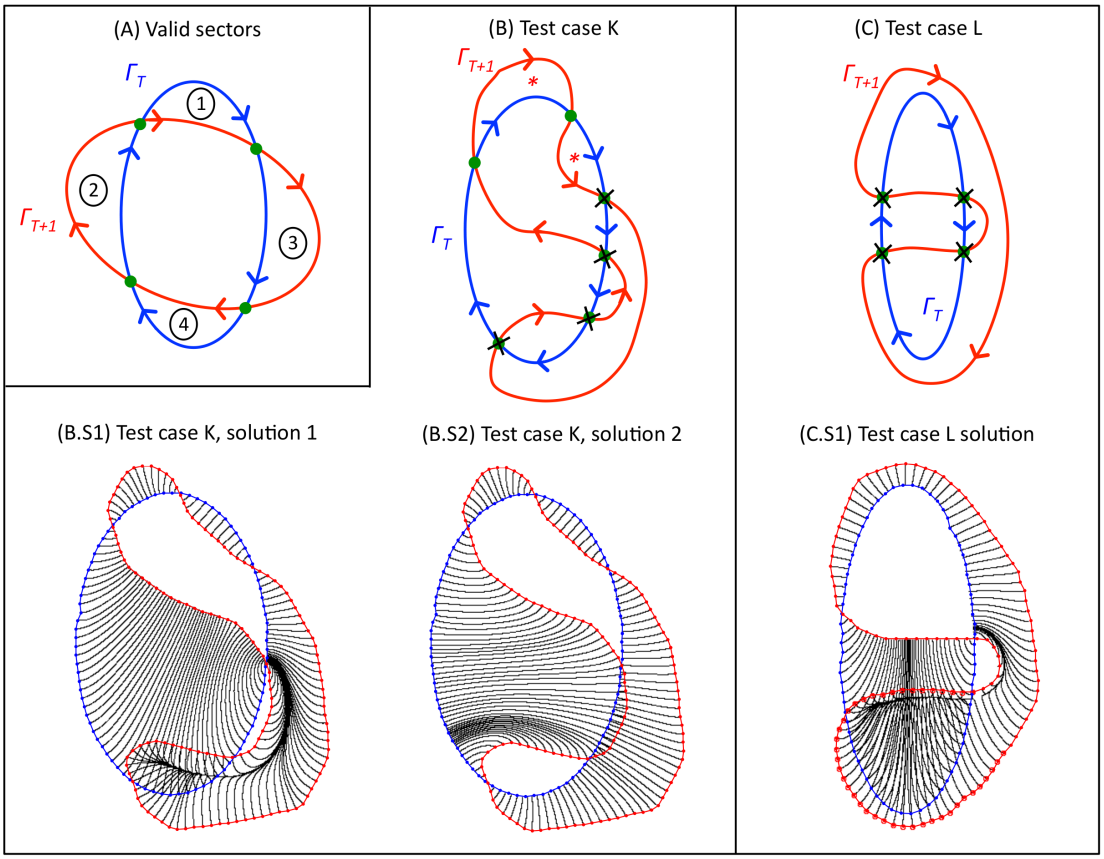

Figure 3.7: **Test cases for sector construction.** (A) In the simplest case, Γ_T and Γ_{T+1} overlap forming 4 intersection points (green dots). Arrows indicate the clockwise direction. Four sectors can be formed by following both outlines, clockwise, from one intersection point to the next. (B) A more complex case in which four intersection points (marked by crosses) cannot be used to form valid sectors and leaving multiple open sectors, although two valid sectors do exist (indicated by $*$). Two alternative solutions exist for this problem, as shown in (B.S1) and (B.S2), reachable by ignoring two of the four invalid intersection points. In this case solution (B.S2) provides the most plausible result. (C) In this example no valid sectors exist to provide a starting point for forming sectors. (C.S1) proposes one possible solution (although many nodes fail to map because of the abstract shape).

3.7 Tracking Markers throughout Sequences of Outlines

To track markers throughout 2 or more frames, markers must be identifiable, for example, at frame T and $T+10$; that is to say a marker should maintain a lineage across frames. Early versions of QuimP used a method whereby newly initialised markers were assigned an integer identifier (ID) that was maintained for as long as the marker existed. We previously adopted a similar technique for ECMM, as shown in Figure 3.8A, and adapted it to function with the F/R scheme.

When Υ_T was the migrating edge, markers travel forward in time, and simply retained their ID's. When Υ_{T+1} was migrated backwards in time, markers competed for IDs held by markers migrated in the previous frame mapping ($T-1$ to T), based on Euclidean distance. Markers that failed to inherit an ID were assigned the next available integer.

Integer ID's are far from ideal as they contain no information as to a marker's location or its place in the chain of markers. More significantly, inheritance of ID's is only a rough estimate of a markers actual mapped location, even though precise data is known. These drawbacks prevent easy insertion/deletion of markers and squanders information.

We replace IDs with a system of decimal positions (DPs), and marker origins (MOs), as demonstrated in Figure 3.8B. Outlines are normalised to length 1, and markers on Γ_T are assigned DPs in the range $(0, 1]$ according to their normalised distance from an arbitrarily chosen head marker (assigned DP$= 0$). Markers are migrated, and subsequently assigned MOs to encoded the positions from which they originated from on Γ_T. In the forward case, a marker's origin at Γ_{T+1} will be its decimal position within Γ_T. In the reverse case, an interpolated origin value is calculated from DPs on Γ_T which flank the markers landing position.

Finally, all markers mapped to Γ_{T+1} are assigned new DP values according to their position on Γ_{T+1} (again in relation to an arbitrary head marker). The result is a set of markers at each frame, each having a normalised position, indicating the proportion of distance it lies around the circumference from the origin, and an MO value, indicating from where it originated from in relation to DPs on the previous outline (Figure 3.8C).

New markers can now be introduced at any desired location, at any frame, by interpolating DP and MO values, attaining an unbroken lineage throughout the sequence. Any arbitrary position, for example DP=0.1567, can be chosen, and tracked from beginning to end, without inserting new markers (although tracks will be estimates based on linear interpolation).

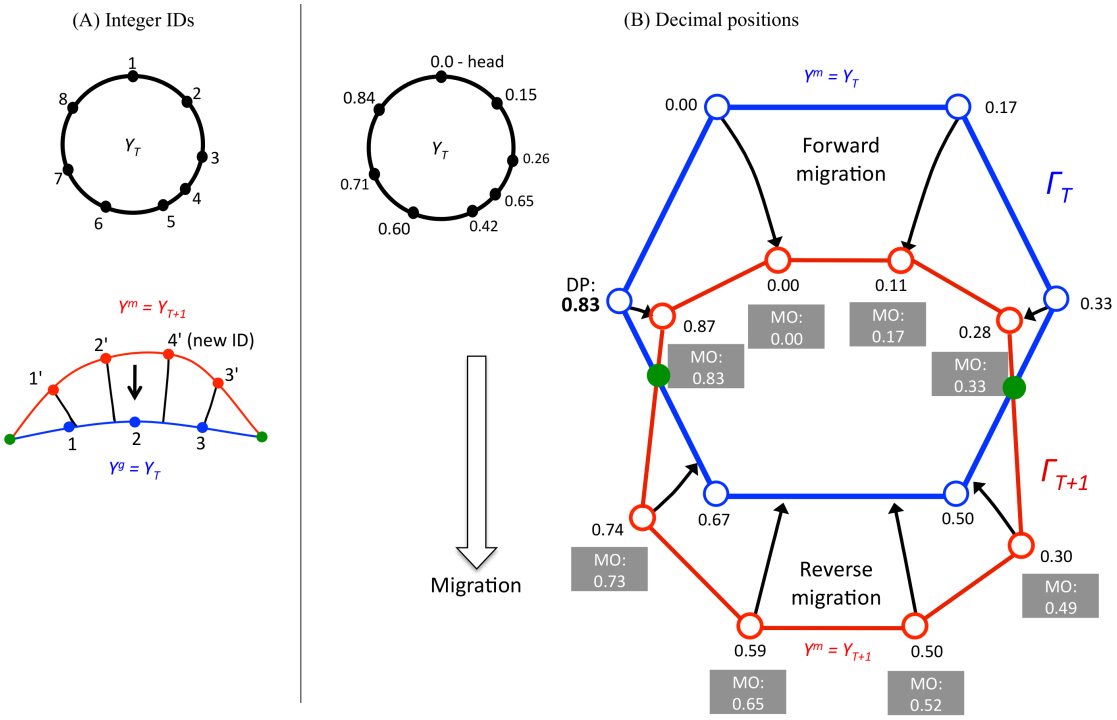

Figure 3.8: **ECMM marker tracking using decimal positions.** (A) Integer ID scheme: Markers on Γ_T are assigned integer ID's in the order they are initialised. Markers simply retain their label in cases where Υ_T is the migrating edge Υ_m (forward migration). If $\Upsilon_m = \Upsilon_{T+1}$, as depicted, markers are mapped in reverse and compete for the inheritance of marker IDs based on Euclidean distance. Markers unable to inherit an ID are assigned new IDs. (B) Decimal position scheme: Γ_T is normalised to a length of 1, and markers assigned decimal positions (DPs) in the range $(0, 1]$ indicating their position relative to a head marker. Outlines Γ_T and Γ_{T+1} represent a simplified cell migrating south. At the rear markers are migrated forward in time as $\Upsilon_m = \Upsilon_T$, and marker origins (MOs) are set equal to marker DPs. Markers are then assigned new DP values for the frame $T + 1$. At the cell front markers are migrated in reverse ($\Upsilon_m = \Upsilon_{T+1}$). On reaching Γ_T nodes are assigned MOs by interpolating DPs of markers on Γ_T.

3.8 Example ECMM Output

Figure 3.9 shows a sample sequence of 10 frames, and is representative of the typical deformations encountered during mapping (using a reduced marker resolution for illustrative purposes). The image sequence in electronic format is included on the accompanying disk (*/Chapter3/ECMM_example_mappings.tif*). In the next section we apply photobleaching experiments designed to valid marker paths computed by ECMM.

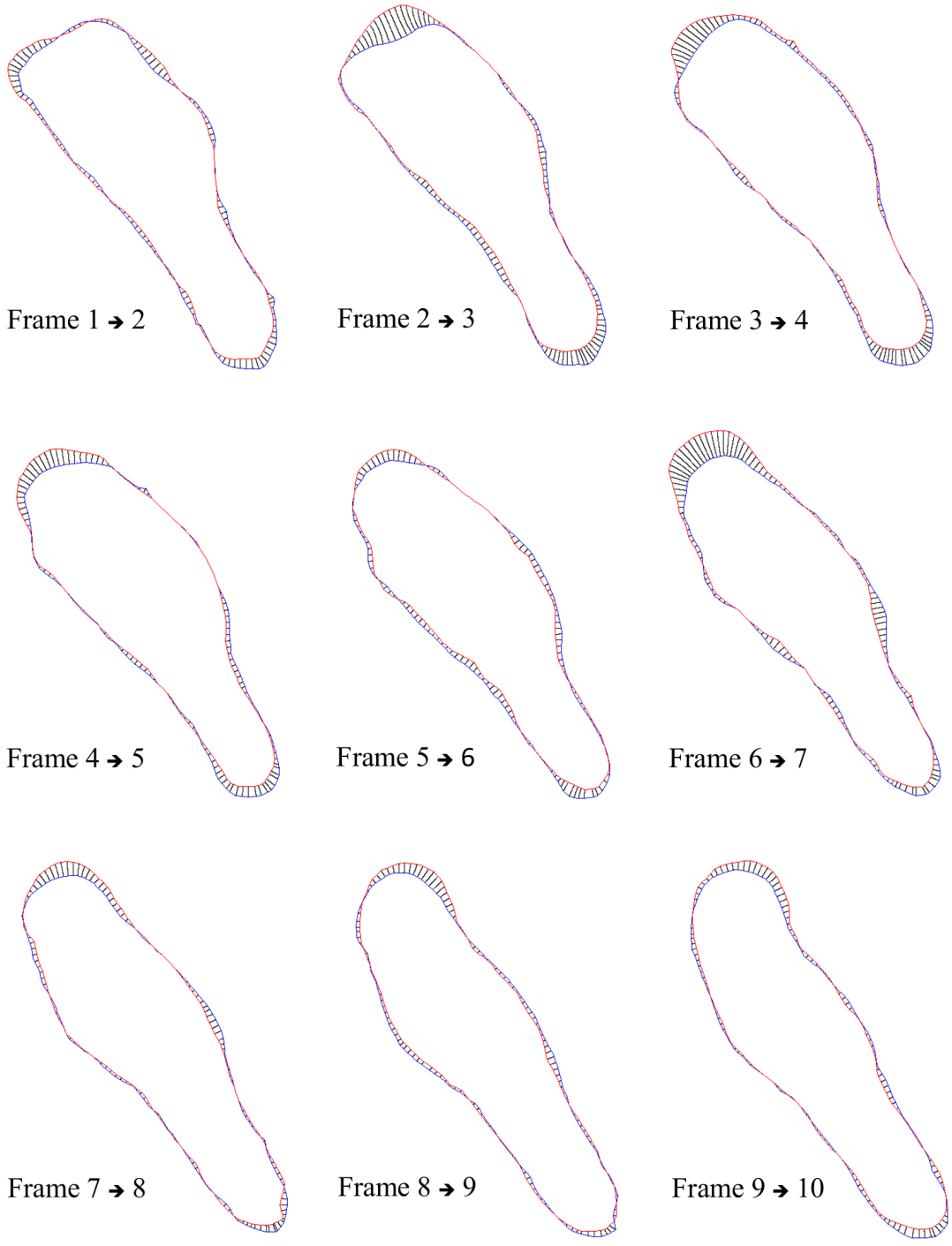

Figure 3.9: *Example ECMM sequence.* Ten consecutive frames are shown, mapped using ECMM. Red represents the outline Γ_t, and blue Γ_{t+1}. Marker paths are depicted in black. [See disk file */Chapter3/ECMM_example_mappings.tif* for the full sequence]

Chapter 4

Validating ECMM: Photobleaching of Membrane Markers

This chapter presents work completed at the Beatson Institute for Cancer Research under the supervision of Kurt Anderson, aiming to validate tracking computed by ECMM. To date, no data yet exists detailing the true deformation of local membrane regions during cell membrane retraction/expansion, particularly the nature of movement within flanking regions. We investigated the extent to which our mapping method, based on virtual electrostatic fields, can accurately describe real world membrane deformations in two dimensions and hence determine the extent to which velocity measurements output by ECMM are biologically applicable.

Markers are created in the membrane of *Dictyostelium discoideum* by photobleaching spots, as is typically conducted in FRAP experiments, into membrane labelled with GFP fused to cAR1 (GFP-cAR1). We employ fluorescence time lapse images to capture the synchronous movement of bleach spots with the cell boundary during membrane deformation and directly compare their paths to those of virtual markers (see Materials and Methods Section 2.3).

Although membrane markers are employed, which is not directly representative of the cell cortex, the membrane is tethered to the cortex and hence the bleaching of membrane proteins provides a good estimate for cortex movement. The membrane is also just as important for correlating fluorescence as it is the location of important signal transducers like PtdIns(3,4,5)P_3. Traynor and Kay [2007] performed similar experiments whereby they bleached spots on the top and underside of cAR labelled membrane of *Dictyostelium*. Although their bleach radius was relatively large, and

targeted away from the cell border, they showed that spots did not move backwards during extension, but in fact move forward with the leading edge. Backward movement of spots would be expected in the case of membrane retrograde flow, whereby lipids are added to the site of extension via the exocytic cycle, allowing membrane surface area to increase, as well as help drive protrusion [Bretscher, 1984]. Traynor and Kay [2007] showed that the exocytic cycle is active in migrating *Dictyostelium* and important in allowing surface area to match changes in shape. However, it does not seem that membrane is added at the site of extension. Because spots move forward on both the top and underside, this also rules out the possibility of rolling behaviour. For example, neutrophils roll along endothelial walls, like a sticky bead, to the sites of inflammation, hence, membrane moves forward on top and backward underneath, continually forming and breaking adhesions [Sundd et al., 2010].

We present example image sequences, spot and marker path comparisons, and demonstrate the creation of marker patterns for acquiring more informative data on membrane deformation.

4.1 Examining the Tracks of Bleached Membrane Markers

Figure 4.1. displays an example image sequence in which a spot is photo-bleached on the right flank of a protrusion. The addition of the LimE actin label aids the tracking of the cell outline in QuimP (Figure 4.1), particularly at the spot's location.

Although viable data has been gathered using photobleaching, the technique is generally too demanding for compiling a *gold standard* for validating membrane tracking methods. The example in Figure 4.1 is the result of a chance event made rare by several difficulties. Firstly, the target area is relatively small and continuously moving so the delay between placing a region of interest (ROI) within the imaging software and the bleach occurring is long enough for the cAR labelled membrane to shift out of the ROI. Secondly, due to the apparent random nature of *Dictyostelium* migration it must be predicted as to where a cell is about to produce a pseudopodium. This is helped somewhat by actin labelling providing clues as to an extensions next possible location. Furthermore, if a spot is correctly placed the bleach recovery time is such that a spot becomes untraceable after a period of 6 to 8 *sec*, hence spots cannot be bleached far in advance.

By far the most prominent difficulty, compounding those previously stated, is *Dictyostelium's* photosensitivity. Exposure to too much laser light causes the amoeba to abandon its normal behaviour and halt protrusion extension, often contracting glob-

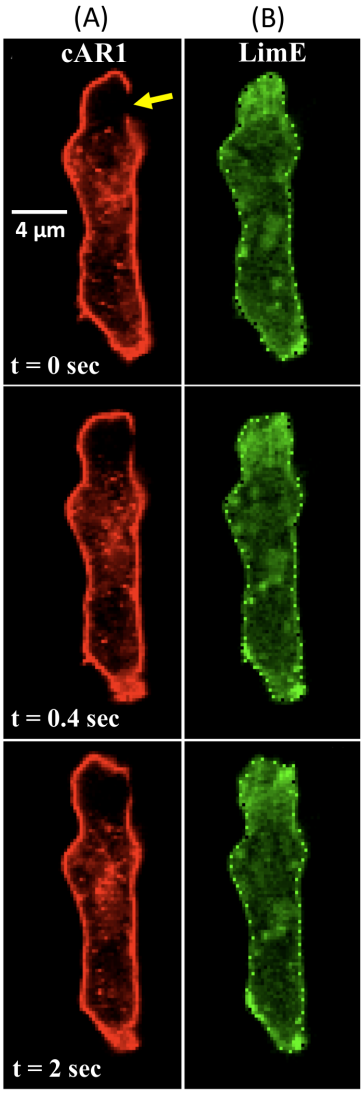

Figure 4.1: **Example photobleaching of membrane markers in *Dictyostelium*.** Time series of fluorescent images over a period of 2 seconds (frame interval of 0.43 *sec*). (A) GFP-cAR. (B) LimE (actin binding), overlaid with segmentation nodes computed by BOA (dots around the circumference). The cell is extending at its north edge. FRAP techniques were used to photo-bleach a spot (arrow) in the GFP-cAR channel, striking the right flank of the extension. Subsequently, the spot's path is traced as to track membrane deformation.

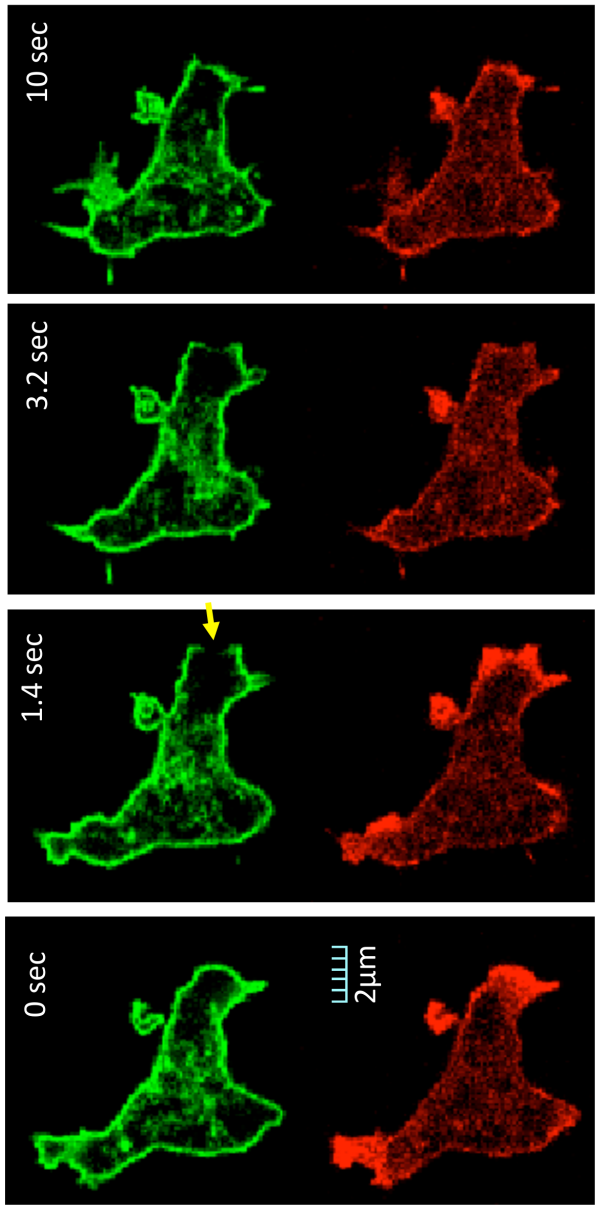

Figure 4.2: **Photo-toxicity during photobleaching.** Dual channel time lapse sequence of *Dictyostelium* demonstrating photo-toxicity during photobleaching. Channel 1 (top, green) is GFP labelled cAR membrane protein. Channel 2 (bottom, red) is RFP labelled LimE (actin binding). A line bleach is made at an expanding region (red arrow). The bleach causes the expansion to halt and a breakdown of actin is observed at the bleach point (visible after 3.2 seconds). This is followed by contraction of the region. Such a reaction prevents the analysis of extending regions, and alters the behaviour of the amoeba.

ally (balling up). This phototoxic effect is demonstrated in Figure 4.2 and is thought to result from a build up of free radicals which the cell detects and can response to [Taminato et al., 2002].

Photobleaching directly at the site of pseudopod extension caused extension to cease on all occasions, but by minimising light exposure to cells, data was obtained for some extension events. Success requires low laser power, low capture rates for image preview prior to bleaching, and large scan areas (low zoom) to avoid concentrating light onto cells. Such requirements further increase the difficulty of the task.

In the course of the experiments we attempted to counteract phototoxicity by adding the reducing agent Dithiothreitol (DTT) (at 10 mM), intended to remove free radicals. However, this had little affect, and becomes itself toxic at high concentrations. Similarly, adding the antioxidant trolox gave no improvement.

Figure 4.3. shows the results of three cases in which bleach spots have been tracked and overlaid onto the output of ECMM. Tangential membrane movement and/or displacement do indeed occur in real life membrane deformations (typically along the flanks of an extension or contraction) and the absence of tangential movement of markers in ECMM results in failure to replicate their paths. However, ECMM does provide accurate mapping at the centre point of retracting regions.

These examples highlight the difficulties in applying a purely mathematical technique for tracking membrane regions, which lacks physical aspects of visco elastic coupling required to model tangential boundary movements. Hence, ECMM is unable to mimic the tangential movement of a bleach spot along the flanks of protrusions.

4.2 Photobleaching of Membrane Patterns

Phototoxicity aside, using a single bleach spot (or indeed any single marker) provides no information on the relative movement of different regions of the membrane. An alternative approach is to bleach line patterns across the cell to serve as a reference grid as done in Figure 4.4. The deformation of the grid could then be quantified, but as would be expected, line bleaching exacerbates the phototoxic effect observed when bleaching single spots.

4.3 ECMM Accuracy and Theoretical Application

In this chapter we presented photobleaching experiments designed to re-create *real life* membrane markers in the form of bleach spots within cAR-GFP labelled membrane of *Dictyostelium*. Tracked movements of spots over time were compared with marker

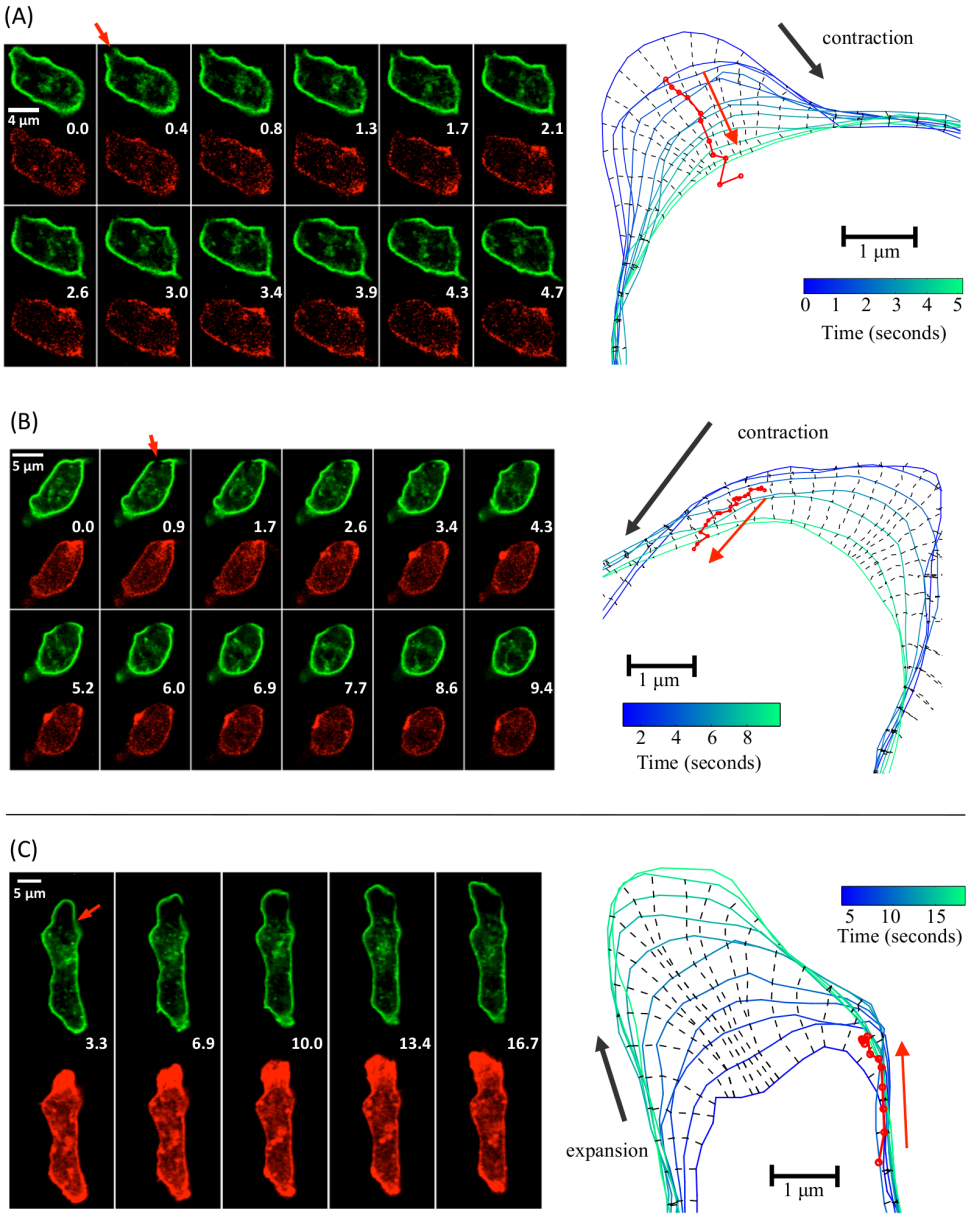

Figure 4.3: **A comparison of ECMM mappings and tracked bleach spots.** in the case of contraction. Image sequences are two channel fluorescence, cAR (green) and LimE (red). Time points are in seconds. Red arrows indicate the bleach location. Cells were segmented with QuimP, and outlines plotted as a sequence running from blue to green through time. Dashed lines represent ECMM tracking data. Bleach spots centres were located on each frame by fitting a Gaussian curve to image intensities along a manually placed line selection. Spot paths are shown in red. (A) Bleach located at the centre of a contracting region. (B) Bleach located at the flank of a contracting region. (C) Bleach located at the flank of an extending region. In B and C, the lateral movement of the spot at the flanks is not present in the mapping provided by ECMM.

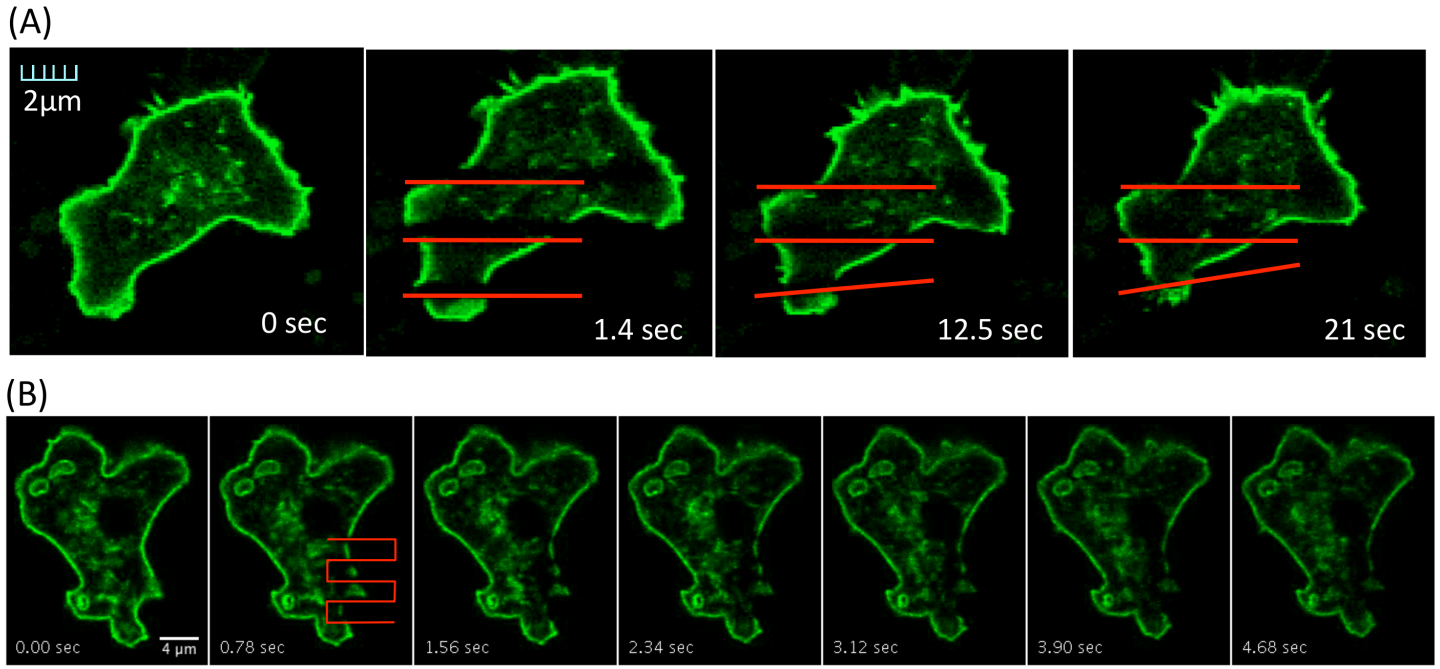

Figure 4.4: **Applying a bleach pattern to quantify movement of the membrane.** Using a single bleach spot has two disadvantages; 1) Bleaching in the desired location is, in practice, very difficult; 2) A single traceable marker provides no information on the relative movement of different regions of the membrane. A bleach pattern is instead made in the form of three straight line segments. The deformation of the bleach pattern has the potential to provide detailed insights into membrane movements during migration, but the ever increased phototoxicity, resulting from bleaching, means this approach is not viable.

tracks computed by ECMM, revealing ECMM to be an accurate estimate of membrane movement at the centre of a protrusion (typically normal to the cell surface), but which is unable to simulate tangential spot movement at a protrusion's flanks.

As demonstrated in Chapter 6, accurate tracking at centre points can provide useful measures, such as protrusion speed, where movement at the flanks is off less interest, but key to the rest of this thesis, such tracking can act as the foundation for highly sensitive, automated, protrusion tracking.

Chapter 5

Implementing the Next Generation of QuimP

QuimP was written in the Java programming language as a series of plug-ins for the popular, open source image processing tool, ImageJ (see Materials and Methods, Section 2.1). The BOA plug-in provides a supervised image segmentation algorithm, in the form of an active contour, for extracting cell outlines, and is capable of segmenting multiple cells in parallel. The resulting outlines are fed to the ECMM plug-in for boundary tracking. Cortical fluorescence intensities are sampled by the ANA plug-in in which the user defines a cortex width, and ECMM is utilised to migrate nodes across the cortex. Finally, the QAnalysis plug-in compiles spatial-temporal maps of motility, fluorescence, convexity and tracking. Figure 5.1 provides a brief overview of the software pipe line and the data produced at each stage.

In this chapter we aim to provide details of the new methods used within the QuimP plug-ins, such as the building of spatial temporal-maps, and detached from these descriptions we summarise the implementation of plug-ins within ImageJ. The reader is refereed to the QuimP Guide, on the accompanying disk (folder *QuimP_Software*), for help documentation and an example analysis (including an example of scripting in MATLAB). These files are also included with the downloadable version of QuimP at `http://go.warwick.ac.uk/quimp`.

5.1 Cell Segmentation and Global Morphological Measures: BOA Plug-in

The BOA plug-in performs two main functions; cell segmentation, and measurement of global cell statistics, such as elongation and displacement.

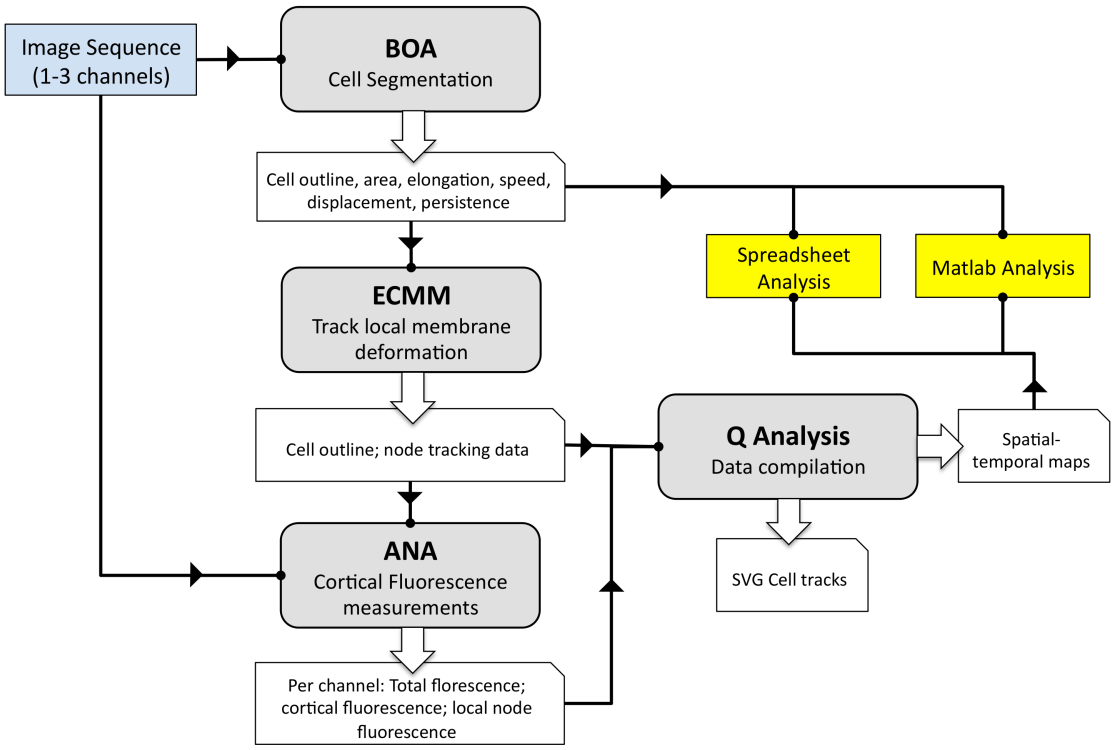

Figure 5.1: **Flow diagram outlining the software structure.** Large arrows represent data output, while thinner lines indicate the flow of data. Yellow are points of analysis.

5.1.1 The BOA Active Contour

QuimP uses multiple active contours to segment cells, and constructs an outline as a chain of nodes (Figure 5.2). The chain is manually initialised around a cell at time T (which can be any frame within a sequence) ensuring the chain does not overlap any object in the image. Nodes are acted upon by three types of forces; 1) Central forces pull nodes inwards and are required for entering concave regions; 2) Contraction forces between nodes have the overall effect of shrinking the chain, the force direction dependent on the angle between neighbouring nodes; 3) Image forces, proportional to the local contrast of the image, oppose chain contraction. Local contrast is measured within a bounding box aligned with a node's outer normal direction. In addition, the image is assigned a friction force that opposes all node movement in proportion to a node's current velocity, and allows for global tuning of node speeds.

The total force vector is computed for each node, and their positions (at sub-pixel resolution) are updated via numerical approximation (with a step size δt). As the chain approaches the cell boundary, characterised by high contrast, forces begin to balance, neutralising the internal energy of the snake below a critical threshold, and halting shrinkage of the outline. The process is repeated at $T + 1$, the snake initialised by expanding the solution snake derived at T until it encloses the cell boundary at $T + 1$. In cases where the object of interest does not leave the bounds of the original, manual initialisation the chain may be reset to this position at each frame.

During shrinkage of the snake, nodes may be added or removed to maintain minimum/maximum distances between neighbouring nodes (Figure 5.2F). Due to the numerical nature of the computation, nodes may also be removed if they cross paths with neighbouring nodes (causing a twist in the outline).

The active contour has been adapted from previous versions to be semi-supervised; solutions at any time point may be manually altered to correct segmentation in regions of poor contrast. Manually corrected solutions may be utilised for initialisation in the following frame. Additionally, multiple snakes can be initialised for parallel segmentation.

5.1.2 Multi-Cell Segmentation

Dufour et al. [2005] demonstrated segmentation of multiple cells in parallel by implementing interacting active contours. Parallel segmentation not only boosts high throughput analysis, but also improves segmentation accuracy when handling objects that come into close contact with one another.

We have employed a simple method whereby each cell is assigned an independent

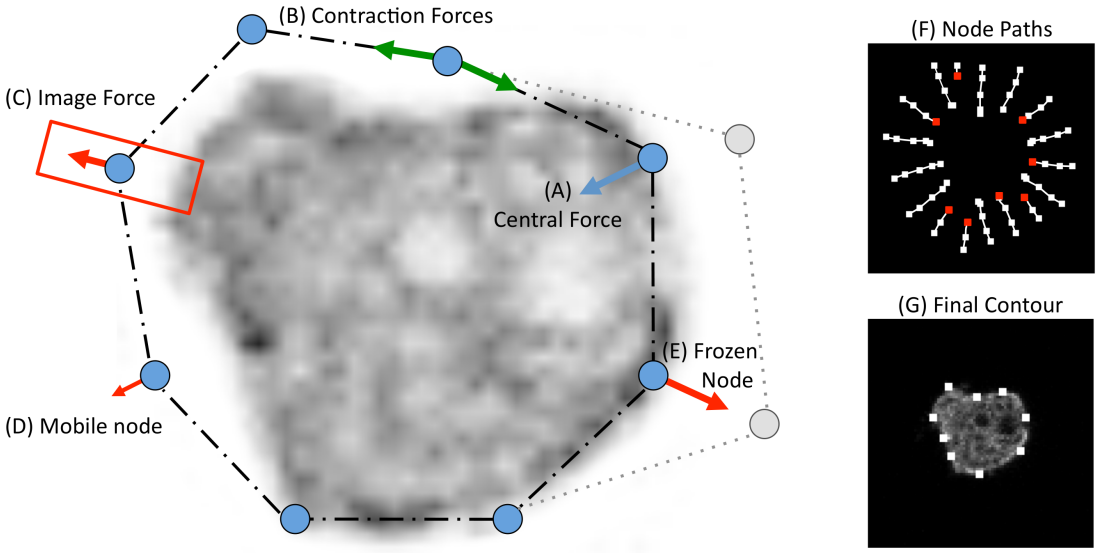

Figure 5.2: **Caricature of outline detection using active contours.** The image analysed is that of *Dictyostelium discoideum* expressing GFP-myosin II at a resolution of 5 *pixels* μm^{-1}. QuimP's active contour consists of a chain of connected nodes (a reduced number are shown here for simplicity) initialised to encircle a cell of interest. Three types of forces act on each node; (A) Central forces contribute to chain shrinking; (B) Contraction forces between neighbouring nodes shrink the chain and maintain chain integrity; (C) Image forces oppose the shrinking of the chain by a magnitude determined by the local image intensity gradient (red box) in the direction of the outer normal. When mobile, a node experiences inward forces greater than the opposing image force (D). On reaching the boundary the image force becomes sufficiently large to cancel out the other forces, halting and freezing the node (E). (F) shows the paths of nodes during contraction. Note that nodes can be added or removed (red nodes) to maintain an average distance between neighbours. (G) shows the final position of nodes. QuimP usually makes use of 100 or more nodes to extract high resolution cell outlines. Figure reproduced from Tyson et al. [2009].

active contour, initialised manually. At frame T, solutions are computed independently for each chain, as described previously, with the assumption that the user initialised chains do not overlap other nearby cells. When expanding the solutions for segmentation at $T+1$, chains within a threshold Euclidean distance interact with one another. Interacting chains are prevented from overlapping by halting expansion at locations where chains collide, and therefore preventing chains from encompassing neighbouring cells when no clear boundary is visible.

5.1.3 Motility and Morphological Measurements

The result of segmentation is a closed chain of nodes which we refer to as the cell outline. As with previous implementations of QuimP, we compute a range of motility and morphological measurements, in real world units, that provide a global view of migration. For example, perimeter length, elongation and circularity. See Material and Methods, Section 2.4.1 (page 31) for details of computation.

5.2 Tracking Cell Deformation: ECMM Plug-in

The reader is refereed to Chapter 3 for details regarding ECMM. Application of ECMM replaces nodes of the original segmentation with new nodes based on migrated markers. Marker resolution is pre-set at a density of $\omega_m = 0.5$ per pixel.

As described in Section 3.7, nodes/markers have associated decimal positions (DPs) encoding their locations on the cell outline at T, and marker origins (MOs), indicating the decimal position from where they originated on the outline at $T-1$. Node DP and MO data is used to build, and track through, spatial-temporal maps (STMs) as described in Section 5.4.1.

At this point in the analysis no data has been collected on fluorescence intensities. Fluorescence is sampled by the ANA plug-in.

5.3 Sampling Fluorescence Intensities: ANA Plug-in

Each node has an assigned speed, at each time point, as computed by ECMM, and we complement this data by assigning nodes fluorescence intensity values sampled from the local cortical region of a cell, where proteins instrumental in cell motility localise. Additionally, ANA measures whole cell fluorescence, such as average cell interior intensity, at all time points. Fluorescence data may be sampled from up to 3 channels, and be either 8-bit (256 levels of intensity) or 16-bit images ($65,536$ levels of intensity) images.

We define the cortical region as a continuous strip, of uniform thickness (decided upon by the user), located on the immediate underside of the cell outline. Nodes of the cell outline are migrated across the cortex by ECMM, adapted to simultaneously sample pixel intensities. The maximal sampled intensity is recoded for each node and optionally normalised to the average fluorescence within the cell interior. Details of the image intensity sampling are given in the following sections.

5.3.1 Defining the Cortical Region

Huang and Helmke [2011] extract line profiles across a set distance of the cortex to determine the presence of actin ruffles within 1 micron of a cell's edge, relying on robust algorithms for segmentation (and high quality images). In the vast majority of cases, segmentation accuracy will fluctuate massively depending on the image quality, and detail of data that the user aims to extract.

Several concerns must be addressed when defining the cortical region. Firstly, the cortex has a relatively loose definition in eukaryotic cells as an actin-rich layer just below the plasma membrane, the thickness varying between species and cell types [Brugués et al., 2010; Medalia et al., 2002]. Secondly, cortex thickness may become nonuniform around the cell perimeter as the cytoskeleton is dynamically reorganised in regions of contraction, or pseudopodia extension. Finally, inevitable errors in segmentation (particularly of concave structures that cannot be penetrated by active contours) causes the location of the plasma membrane not to be accurately portrayed by the outline.

As a consequence, intensities cannot be sampled at a set distance beneath the outline as this may omit key areas, and possibly result in sampling of the background. To circumvent these issues we allow the user to define a generous cortex width, known to incorporate the features of interest, and only consider the maximal intensity of fluorescence across a slice of the cortex at each nodes location.

The outer boundary of the cortex is assumed to be located at the cell outline. The inner boundary is generated by shrinking the outline by the cortex width, as demonstrated in Figure 5.3A. Shrinking is achieved by iteratively displacing nodes in the direction of the inner surface normal ($\frac{1}{20}$ pixel per iteration) (this is akin to the level set method). Nodes are removed if they come into close proximity to avoid unnecessary sub pixel resolution, and to reduce the likelihood of nodes crossing paths. It must be stressed that paths taken by nodes during shrinkage are in no way connected with the location of intensity sampling, as was the case in previous version of QuimP.

The shrinking chain is self-interacting in order to prevent edges from intersecting, and twisting the chain (red arrows, Figure 5.3A). As edges approach one another, they may intersect depending on the local width of the cell and the chosen cortex width,

and possibly leave the bounds of the cell. For example, a cortex width of 1 μm will result in intersections at the base of cell extremities less than 2 μm wide. Intersects are highly undesirable as they can cause fluorescence to be sampled outside the cell, or sampling of the same cortex region for nodes at opposite sides of the chain, and result in invalid input for ECMM (chains must not contain intersecting edges), later used for migrating nodes across the cortex.

Intersects could be removed by simply cutting the chain at the intersection point and removing the twisted region, but this would cut extremities from the chain and hinder proper sampling in those regions. Instead, intersections are prevented by freezing nodes and edges that come into close proximity. At each iteration, the perpendicular distance between all nodes and edges is calculated, and the node (and those forming the edge) are frozen if the distance falls below a threshold of 1 *pixel*.

5.3.2 Adaptation of ECMM for Intensity Sampling

ECMM is utilised to migrate markers from the cell outline, across the cortex, to the inner cortex boundary (Figure 5.3B). The outline is treated as time point T, and the inner boundary as $T+1$. As measurements are required for all nodes in the outline, node positions are used as the position of markers, that is to say, marker density matches that of node density. Unlike previous mappings computed by ECMM no intersection points exist, and so the computation is not split into sectors. This can dramatically increase computational time due to increased field complexity. To reduce computational time we lower the line charge density to 0.25 per pixel.

As markers are migrated, ECMM samples image intensity below the marker, recording a 3×3 pixel average. On completion, the maximum recorded value is assigned to the markers associated node within the cell outline. Figure 5.3C depicts the location of maximal intensity for each migrated marker.

In the unlikely event that a marker fails to map correctly (it fails to reach the inner boundary) its recorded values is replaced by an interpolated value, computed from successfully mapped neighbouring nodes.

Once complete for one channel the locations of maximal intensity can be optionally re-used for sampling from other channels. This is particularly useful if a ratio of intensities is required, as in the case presented in Section 7.3, where a ratio between a tagged protein (Dishevelled) and a cytoplasmic stain (Rhodamine Dextran) is required.

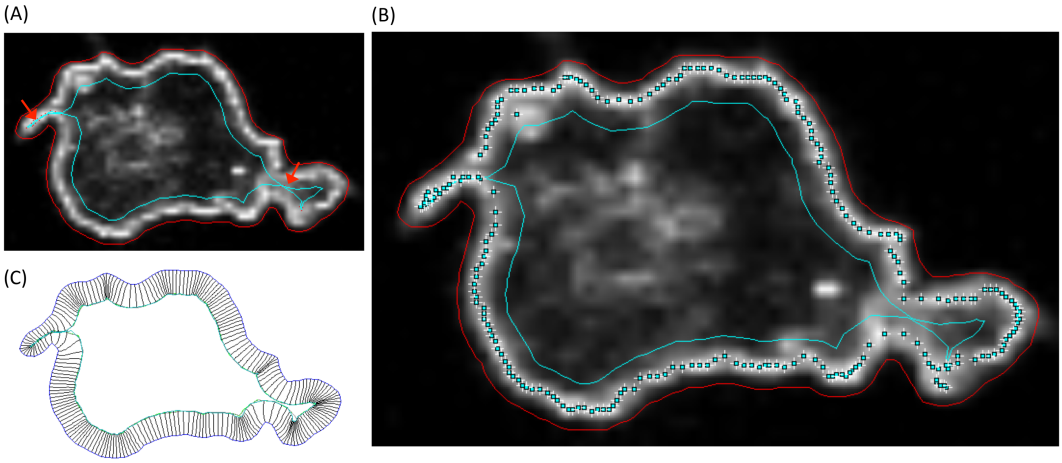

Figure 5.3: **ANA plug-in: sampling maximal fluorescence intensity within the cortex.** Image is of (*Dictyostelium* expressing a tagged membrane protein, GFP-cAR. (A) The cortical region is enclosed by the outline (red) and an inner boundary (blue). The width of this cortical region is user defined. The inner boundary is generated by shrinking the outline continuously inwards in the direction of the surface normal. The chain is self-interacting preventing edges from intersecting (twisting the chain); nodes and edges that come into close proximity are frozen. This is particularly important for preserving thin protrusions (red arrows) that may otherwise be cut from the chain resulting in erroneous intensity sampling. (B) ECMM is employed to migrate nodes of the outline inwards towards the inner boundary while simultaneously sampling pixel intensity (3×3 pixel average) along their path (density has been reduced in this example for clarity). (C) depicts the location of maximal intensity sampled along each node's path that is then assigned The maximal sampled intensities, the locations of which are depicted in (C), are assigned to nodes, and may be normalised to the average intensity measured in the cytoplasmic region of the cell. Recording only the maximal intensity counters for inaccuracy in the segmentation and determination of the cortex width. The locations of maximal intensities may be re-used for sampling within other channels.

5.3.3 Fluorescence Statistics

Statistics recorded by ANA are measured in *microns* and *seconds*, where appropriate. Intensity values have arbitrary units and can be in 8-bit, or 16-bit ranges (depending on the input image). Optionally, node intensity values, I_n, are normalised to the cell's mean cytoplasmic intensity (defined as the region within the inner boundary),

$$I_n = Node\ Intensity/Mean\ Cytoplasmic\ Intensity. \tag{5.1}$$

In the majority of cases, normalised values should be used to facilitate comparison between cells with varying levels of expression, and to account for bleaching, or differences in illumination across experiments. At every frame of an image sequence (up to three separate channels of data), fluorescence statistics are recorded, as defined in Section 2.4.2.

5.4 Compiling Data: QAnalysis Plug-in

The QAnalysis plug-in is responsible for compiling the output from BOA, ECMM and ANA, in order to create visual representation of cell motility and data for analysis. These are scalable vector graphics, or spatio-temporal maps which contain ECMM measures of membrane speed, and fluorescence data, in a comparable, consistent format.

A spatial-temporal map is a two dimensional plot in which the x-axis is representative of the cell outline, and the y-axis of time ($T = 0$ being at the top). Values encoded within the plot can represent any desired measure (for example membrane speed) at a particular time and location on the cell perimeter. A colour map can be applied to highlight areas of high/low activity, and correlations computed between maps.

5.4.1 Building Spatio-Temporal Maps

At time $T = 0$ the head node within $\Gamma_{T=0}$ (labeled with a DP=0.0) is positioned at the top left corner of the map. All other nodes forming $\Gamma_{T=0}$ are positioned along the x-axis at locations determined by their DP relative to the head node. The map is therefore cylindrical, the left and right edges being connected. Nodes are not placed at discrete map pixels, but are instead positioned at sub-pixel resolution (for example, if the chosen map resolution is 400 pixels in width, a node with PD=0.5 will be placed at 200.5 pixels along the x-axis). Map pixels are assigned values, such as fluorescence intensity, by linearly interpolating values held by the neighbouring nodes.

Nodes of Γ_T could be positioned onto a map in one of two ways. Mapping data produced by ECMM could be used to position nodes directly below their position of origin within Γ_{T-1}. This would equate to any vertical line draw down an STM representing the mapping of a single location on the cell outline, over all time points. Such an arrangement is ideal for visualising data over a short period of time, but issues arise when tracking positions for long periods, as explained in Figure 5.5. Tracked positions move towards the rear of the cell, and eventually become compressed to a point if movement is highly persistent in one direction. In turn, this would results in heavy distortion of the map along the y-axis. Figure 5.5A reveals the pattern of tracked positions at the leading edge of a cell. Positions spread sideways during expansion events, shifting to the side of the cell, where they remain stationary (in relation to the background) as the cell moves forward (indicated by arrows), and then shift to the cell's rear.

In the next section we describe how positions are tracked through STMs, and display the paths of markers as they move towards the cell's rear. For the meantime, consider an alternative approach, in which we map only a single DP vertically down the map, the head node at $T = 0$, and position the rest of the nodes relative to it, according to their own DP; that is, the left most column of pixels on an STM represent a single ECMM tracked position throughout all time points, while other pixels are representative of normalised positions on the cell outline relative to this tracked position.

Using this approach, Q-Analysis produces the following spatio-temporal maps, as for the example analysis in Figure 5.4:

- **Motility Map.** Pixels are valued according to the speed of marker migration ($\mu m/\,\mathrm{sec}$), as calculated by ECMM. Positive values represent expanding regions, negative values indicate contraction.

- **Fluorescence Map**. Pixels are valued according to the node fluorescence intensities recorded by the ANA plug-in, resulting in either 8-bit, 16-bit, or scaled intensity values (see section 5.3). A single fluorescence map is created for each recorded channel.

- **Curvature Map**. Pixels are valued according to the local curvature of the cell outline. Curvature at a node , Θ_n, is given by

$$\Theta_n = \frac{\theta_n}{180} - 1, \tag{5.2}$$

  where θ_n is the external angle between left and right neighbouring nodes. Hence,

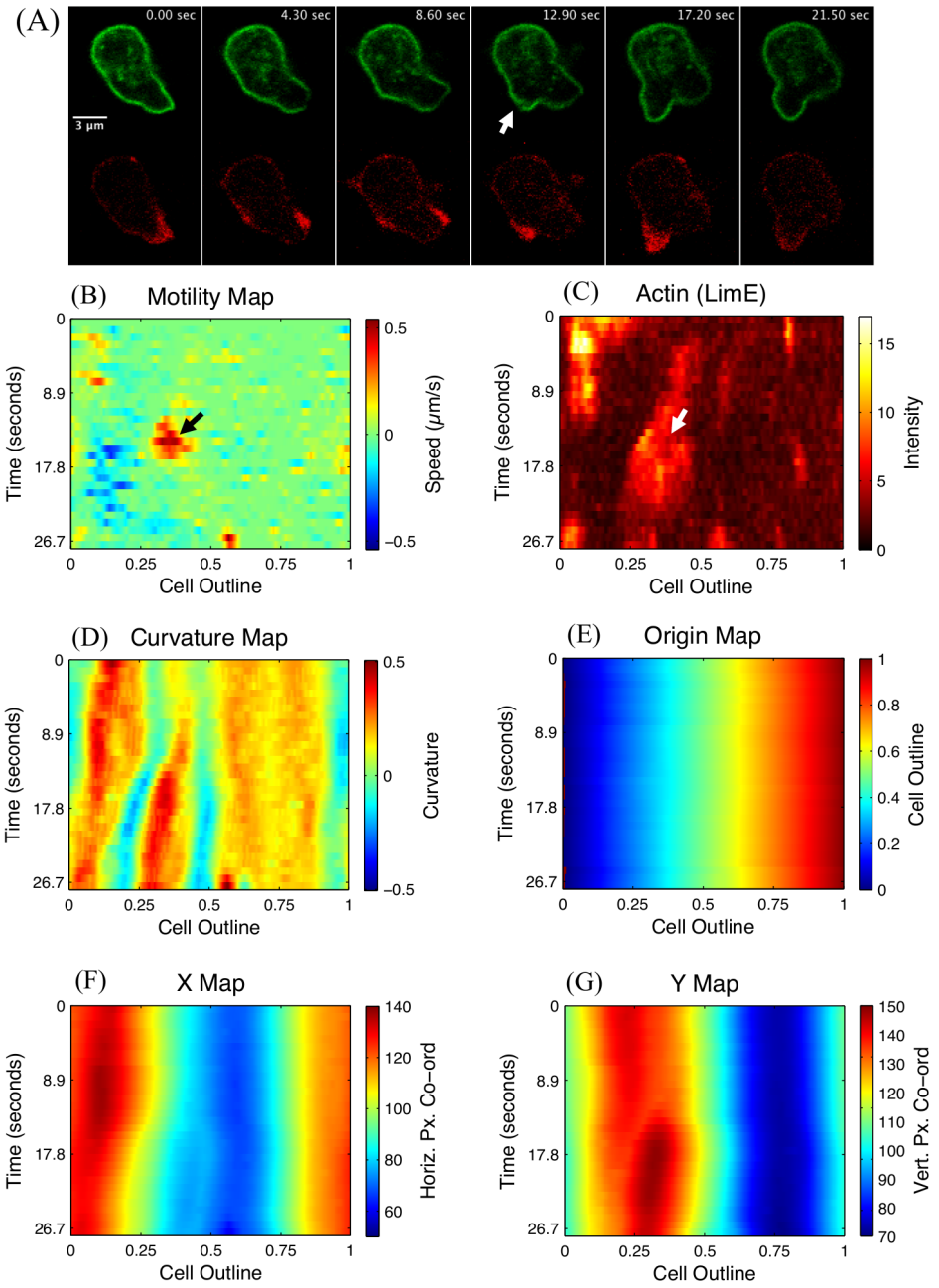

Figure 5.4: **Example QuimP output: spatio-temporal maps.** (A) Image sequence of *Dictyostelium*(1.2 fps) expressing GFP labelled cAR (green) and RFP labelled LimeE (red). Arrows indicate the location of an emerging pseudopodium. (B)-(G) Spatio-temporal maps of A. Each row contains data relating to a single frame, sampled around the normalised circumference of the cell (columns). Curvature is averaged over 1 μm. (E) Colours on the origin map indicates the position on the cell outline from which a point originated (as determined by ECMM). (F) and (G) encode the (x, y) pixel locations in A, associated with each point within the spatio-temporal maps.

curvature is encoded into the range $[-1, 1]$, where negative values represent concave membrane regions, positive values convex regions. Optionally, curvature may be averaged and/or summated over nodes spanning a user defined distance, in order to smooth over noise and visualise larger features of curvature.

- ***X* Map/*Y* Map**. Pixels of an X map are valued according to the horizontal pixel co-ordinates of nodes within the original image sequence. The Y map contains the vertical image co-ordinate (the image origin being the top left). These maps allow the corresponding image pixel location of a DP to be queried.

5.4.2 Tracking Positions through Spatio-Temporal Maps

Any chosen DP value can be tracked over a sequence of outlines (Figure 5.5A). These can be depicted directly onto STMs, drawn as described in the previous section (Figures 5.5B and C, white lines indicating the tracking of DPs from time $T = 0$). In addition to motility, or fluorescence maps, tracking DPs through STMs requires *tracking maps*. These include the *position map* and *origin map*.

The position map contains interpolated DP values, built in the same fashion as previous maps, hence it provides the position at which each pixel resides on the cell outline relative to the zero position. Pixels within the origin map contain interpolated marker origins (MO) values, and hence indicate the position at which a pixel originated from in the previous time point (the line of pixels above).

Figure 5.6 demonstrates tracking backwards through an STM, a three step process:

1. Given a map co-ordinate, (x, y), where x is a DP and y is a time point, consult the location (x, y) within the origin map to extract the MO.

2. Determine the x location of the MO within the position map at the previous time point, $y - 1$.

3. Repeat for the map co-ordinate $(x, y - 1)$ to determine x at $y - 2$.

Tracking is not limited to pixel resolution, any arbitrary location may be chosen and its origin interpolated, as is the case in Figure 5.6, keeping in mind that maps are cylindrical, so $DP = 0.98$ is closer to $DP = 0.01$ than it is to $DP = 0.94$. The same approach can be performed forward through time points.

Because outlines are essentially straight line segments, it is assumed that MO values change linearly between neighbouring markers. This is a valid assumption if the end points of line segments in Γ_T are mapped directly to end points of Γ_{T+1}. Although

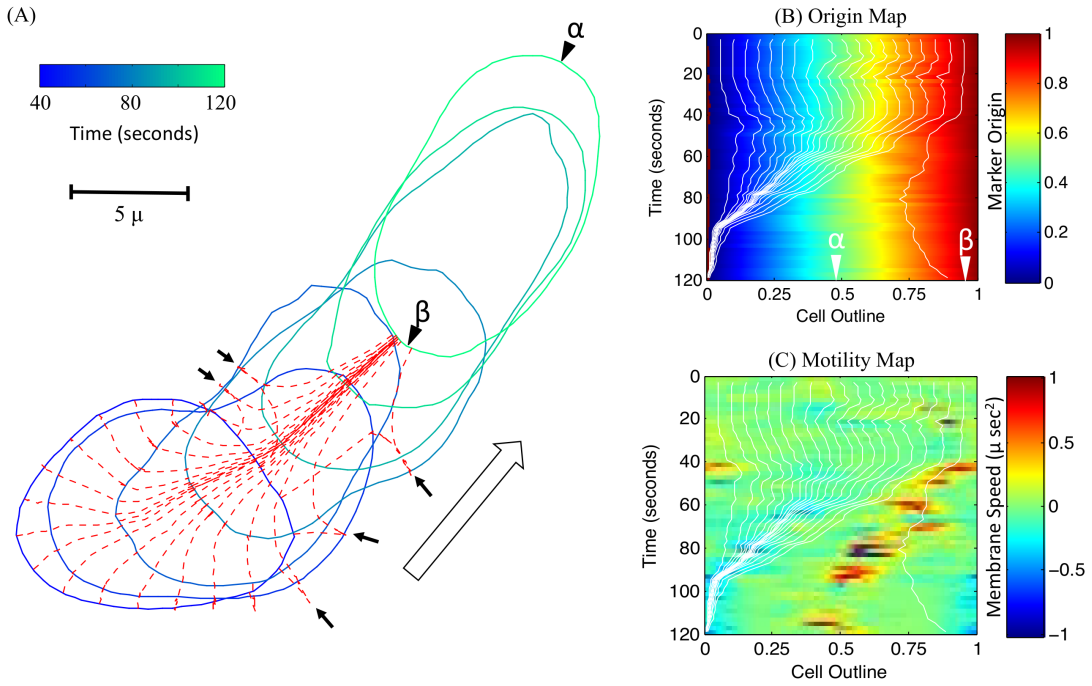

Figure 5.5: **Tracking positions through spatio-temporal maps.** (A) overlaid outlines of a migrating cell. Dashed red lines represent decimal positions (DPs) tracked from $T = 40$ seconds onwards (by ECMM). Arrows point to DPs at $T = 60$, now located at the cell's flanks. By $T = 120$, DPs are all at the cell's rear. Positions α and β mark the front and rear at $T = 120$. (B) Origin map (containing marker origins). (C) Motility map (membrane velocity). White lines trace the paths of DPs depicted in A. DP paths become conjugated to one edge, the cell's rear, hence they could not be used to construct the maps themselves (in which paths would appear as vertical, straight lines). Instead, only a single path at DP = 0 is used as a reference to which all other DPs are positioned along the horizontal.

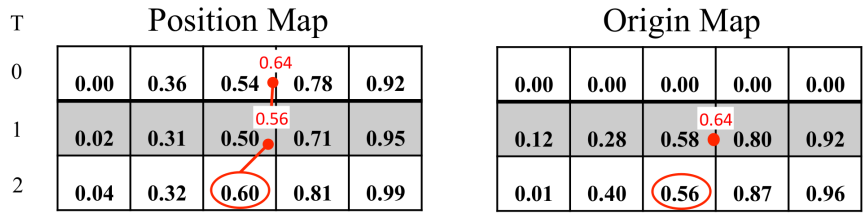

Figure 5.6: **Tracking positions backward using position and origin maps.** For an image sequence of three time points, a position map and origin map are generated with a horizontal resolution of 5 pixels. Values in both tables indicate the proportion of distance around the cell circumference from the origin. To track position 0.69 at $T = 2$, backward in time to $T = 0$: consult the origin map for the associated marker origin (MO) at $T = 2$, attaining 0.56; as a fraction, compute where 0.56 lies between flanking pixels at $T = 2$ in the position map, $((0.56 - 0.5)/(0.17 0.5)) = 0.29$; compute the *origin* of 0.56 by linearly interpolating between the corresponding pixels in the origin map, using the fraction 0.29, $0.58 + ((0.8 - 0.58) * 0.29) = 0.64$. This process may be performed iteratively, for any number of time points, for any arbitrary position, both forward and backwards in time.

this is highly unlikely, using a higher marker density will minimise the error of this approximation (as the marker density approaches infinity, errors introduced by linear interpolation become zero).

Section 5.5.4 describes two further tracking maps designed for efficient tracking within MATLAB matrices. They provide an approximation by encoding only integer matrix positions, rather than real numbers.

5.5 Software Implementation

The following section is an overview of the ImageJ software implementation of aforementioned methods. We present only key aspects of the user interface for each plug-in, and refer the reader to the QuimP Guide for full details regarding use of the software, file formats, and a walkthrough analysis (see disk file *QuimP_Software_QuimP11_Guide.pdf*). This chapter concludes with a brief description of data integration with MATLAB.

QuimP's plug-ins are designed to be run consecutively in the order presented on the QuimP bar, shown in Figure 5.7. As input, a plug-in requires only an open image and/or a QuimP parameter file (extended **.paQP*), that stores associated file paths and parameters for an analysed cell. The user may re-execute plug-ins, in any order, to make alterations, bearing in mind this will erase data recorded by plug-ins

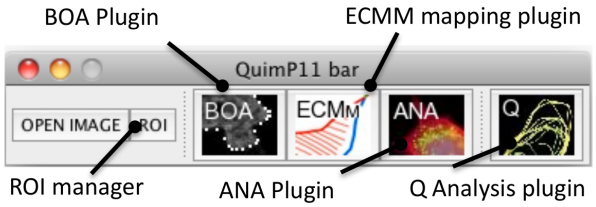

Figure 5.7: **Launching plug-ins: the QuimP bar** Plug-ins are executed from left to right, requiring an open image and/or a QuimP parameter file.

downstream.

5.5.1 The BOA Segmentation Window

Previous versions of QuimP require parameter setting prior to computing solutions for all frames of a sequence (hence, they remain fixed throughout segmentation). As a result, user interaction is heavily restricted and accurate segmentation becomes laborious.

QuimP11 uses a semi-automated approach to significantly improve user interaction, and to recover from failed segmentation. Users are able to preview segmentation results, manually correct segmentation errors, and alter parameters for individual frames, all within the BOA window (Figure 5.8). Below is a brief summary of features:

- Dynamically add and remove cells from the segmentation process, at any frame of an image stack.
- Instantly preview solutions when parameters are altered.
- View intermediate solutions (show paths)(Figure 5.8C).
- Manually edit a solution, at any frame (Figure 5.8D).
- Alter parameters for individual frames.
- Delete inaccurate solutions.
- Edit image content on the fly using ImageJs tools.
- Alter image scale and frame interval within BOA.

BOA stores cell outlines as a chain of nodes to be read by the ECMM plug-in. Outlines are inspected for self intersects and corrected if necessary.

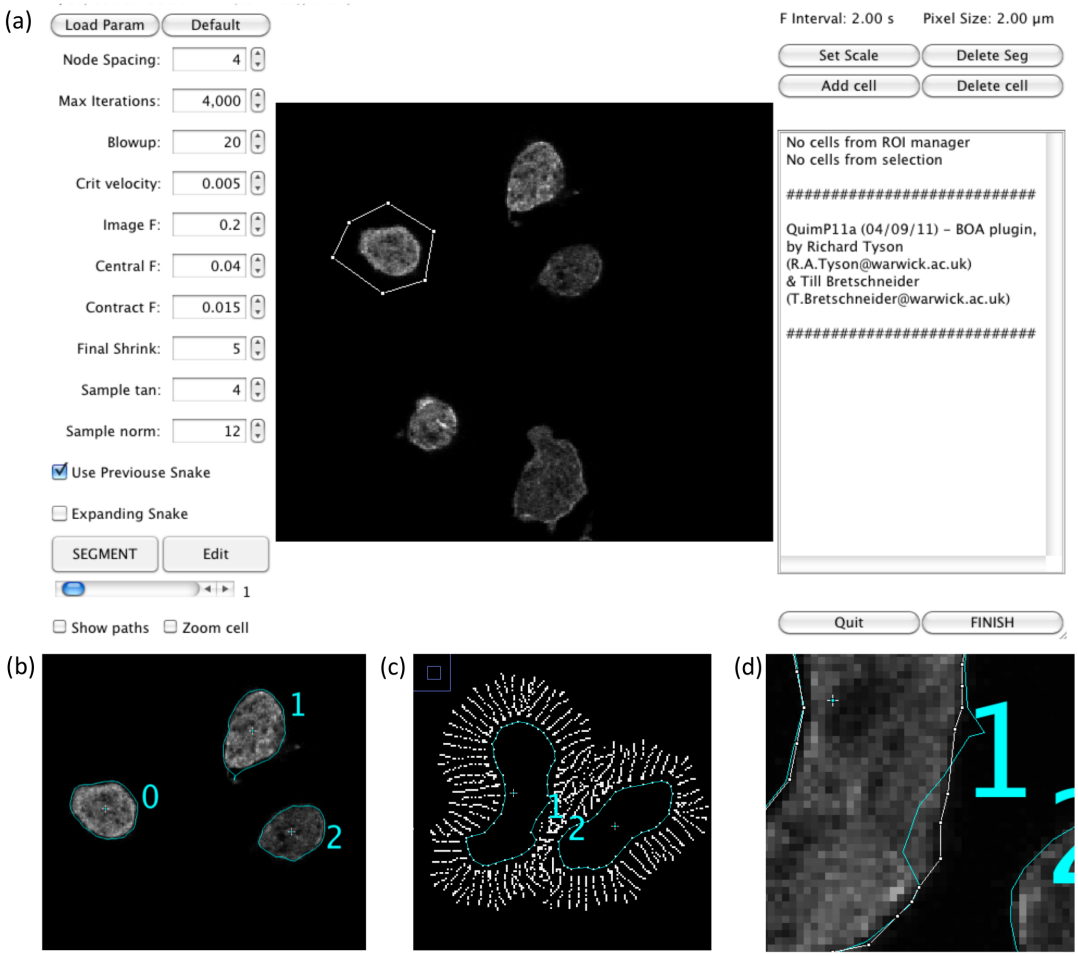

Figure 5.8: **The BOA segmentation window.** (a) ImageJ canvas with embedded controls. (b) Segmentation of multiple cells in parallel. (c) Intermediate solutions resulting from interacting active contours. (d) Manual correction of solutions via the dragging of nodes (white outline).

5.5.2 ECMM Plug-in Output

ECMM parameters are generally unintuitive (for example charge magnitude), so for usability these are hidden from the user. ECMM uses a default set of parameters, suitable for all cases.

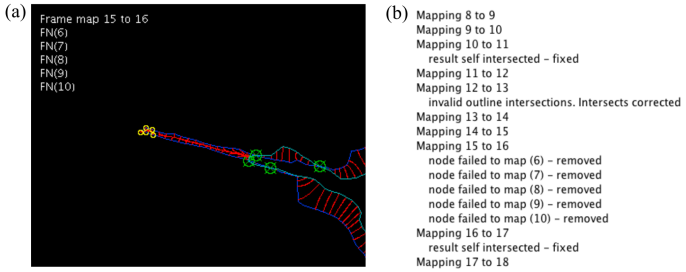

Figure 5.9: **ECMM output display.** (a) Marker mappings between frames 15 and 16. The blue outline represents Γ_{15}, the green Γ_{16}. Green circles denote valid intersection points utilised for calculating sectors. Red lines denote the paths taken by migrated nodes. Markers that fail to map are highlighted in yellow. In this instance, nodes failed to map because they exceeded the iteration limit for migration, set low for this purpose of this exmaple. Failed node (FN) warnings are displayed, along with a running total, in brackets, of the number of failed nodes in the whole sequence. (b) Log displaying progress and warnings.

ECMM outputs an image sequence displaying the mappings between outlines at each time point. Although a user can not interact with ECMM, visuals allow the user to identify problematic frames (caused by segmentation faults or numerical accuracy). For example, in the rare event that a marker fails to map correctly, it is marked in the output and recorded in the log (Figure 5.9b).

5.5.3 ANA and QAnalysis Parameter Settings

ANA requires the user to open and select an image sequence they wish to sample from. The ANA dialog, shown in Figure 5.10a, lets the user choose a data channel for storage, specify whether to normalise intensity measures, and whether to sample at previously recorded locations. Importantly, the user sets the required cortex width, aided by an instant preview (Figure 5.10b). Parameters may differ for each channel, including cortex width.

Similarly, the QAnalysis dialog (Figure 5.10c) provides control over the content of scalable vector graphics, aspects of curvature calculation, and horizontal map resolution. STMs are saved as both scaled images (aiding visualisation), and as text

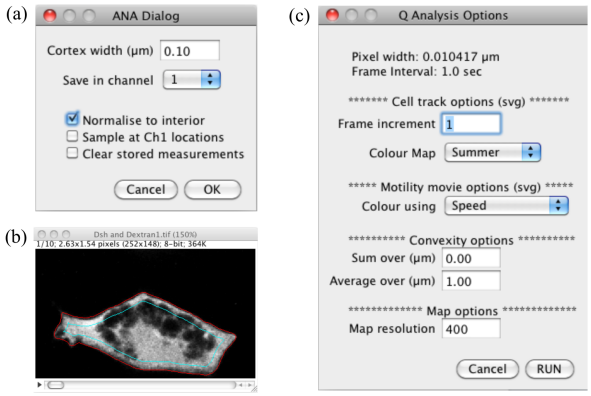

Figure 5.10: **ANA & QAnalysis input dialogs.** (a) ANA dialog. (b) Instant preview of user defined cortex width. (c) QAnalysis dialog.

files containing unscaled values. All files produced by QAnalysis can be imported into MATLAB, using the provided scripts.

5.5.4 Data Files and MATLAB Integration

It is common for users to want to output custom measures, specific for their needs. Previous version of QuimP produced tab delimited files to allow users to extend their analysis using personalised scripts, but this requires users to write code for loading data and performing simple tasks. We have significantly sped up the creation of custom analyses by including MATLAB scripts that generate data structures, draw common plots, and perform tracking through STMs.

To increase the speed of tracking though STMs, our MATLAB scripts compute two additional maps, tailored to matrix computations. Essentially, these allow tracking via discrete map pixels, rather than computing tracking using continuous values. These maps, along with all other data formats, are explained in the QuimP Guide (see disk file *QuimP_Software_QuimP11_Guide.pdf*), but are not required reading for the following chapters on the applications of QuimP.

Chapter 6

Automated Analysis of Blebbing in *Dictyostelium*

In this chapter we apply QuimP to develop an automated protrusion tracking algorithm, ECMM-APT, to produce a complete picture of the protrusive nature of *Dictyostelium* under agar. By doing so we avoid time consuming manual work, remove bias, inconsistencies, and subjectivity. ECMM tracking of decimal positions provides the perfect basis for building such an automated method.

Plots of protrusion measures are constructed using STMs, such as speed, curvature, and quantity of actin, which are used to characterise blebs in comparison to actin driven pseudopodia. ECMM-APT performance is evaluated with a manual analysis of wild type cells, and subsequently applied to automatically analyse motility of mutant strains.

Our data confirms findings in the literature, showing blebs are directed during chemotaxis, cannot be produced by myosin-II light chain mutants, and that they can reach a speed of $4.9\,\mu m/\,\mathrm{sec}$. Significantly, we show blebs emerge preferentially from concave regions at a cell's flanks. Furthermore, automated kymographs reveal a retrograde shift of the actin scar at sites of bleb nucleation.

6.1 Blebbing Assays in Resistive Environments (Experiments by Evgeny Zatulovskiy)

Laevsky and Knecht [2001] observed that cells migrating under 0.5% agarose migrate faster than those under 2%, and hence imaging under agar could be used as an assay for motility in resistive environments. Evgeny Zatulovskiy (MRC laboratory, Cambridge) performed a series of experiments using procedures adapted from Laevsky and Knecht

[2001], imaging *Dictyostelium discoideum* under 0.7% agar, and subsequently observed *Dictyostelium* to switch to a multimodal mechanism of movement, both extending pseudopodia and blebbing.

6.1.1 Imaging and Strains

Assayed strains include a myosin-II light chain KO (mlcE-KO), PI3K-KO quintuple mutant [Hoeller and Kay, 2007], and Pikl gene KO (the Pikl gene encodes a Type 1 PI(4)P5-kinase). For segmentation purposes, agar was stained with RITC-Dx so that cells appeared as shadows on a bright background.

Wild type cells expressed an F-actin labeller, GFP fused to the actin binding domain (ABD) of the actin binding protein (ABP), and were imaged at 2 fps using confocal microscopy, and at higher frames rates (4 to 5 fps) using spinning disk microscopy. Mutants were imaged with spinning disk microscopy only, and lacked the actin labeller. See Material and Methods, Section 2.5 for details.

6.2 Developing an Automated Protrusion Analysis

The quality of data and high velocity nature of blebs present significant challenges to developing an automated analysis. Protrusion tracking must be sensitive to both large and small deformations, highly variable speeds, and adapt to the chosen imaging frame rate. Morphology characteristics (e.g. curvature) can also vary hugely between protrusions.

The process of segmentation must not introduce false deformation of the cell outline, but retain subtle movements and small scale blebs. For example, parts of the cell body that exist transiently in the imaging plane will be recorded by ECMM as rapid deformation, and requires exclusion of offending cells. Vesicles resulting from the uptake of RITC-Dx may intermittently contact the cell surface, appear as background, and cause the segmented outline to fluctuate. Similarly, failure of the active contour to penetrate a concave region, successfully segmented on the previous frame, also causes fluctuations.

Image noise, combined with membrane fluctuations, becomes problematic given the high frame rates used for capturing fast deformation events. Noise in segmentation appears as a *shuddering* of the outline. Slow protrusions are seen to displace by only a few pixels between frames, and can become obscured by noise. Membrane speed at seemingly stationary locations can exceed $0.24\,\mu m/\,\text{sec}$ (Figure 6.1), potentially increasing measured speed of pseudopodia by 50% over one frame. Furthermore, the

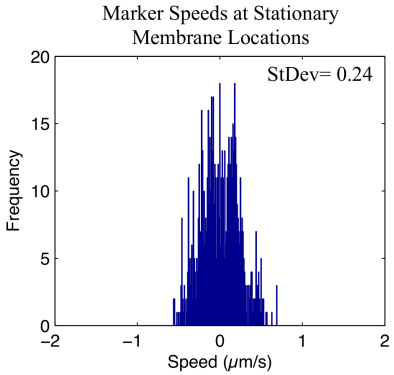

Figure 6.1: **Marker speeds at stationary membrane locations.** Marker speeds reveal noise in the segmentation with a standard deviation of 0.24, equivalent to approximately 2 pixels (the distribution is not normal ($P = 0.08$) as chosen stationary membrane moves subtly as a cell migrates.

effects of noise are greater at higher frame rates due to smaller displacement between images.

The chosen frame rate also limits the maximal measurable speed. For example, a deformation of $1\,\mu m$ in 0.5 seconds translates to a speed of $2\,\mu m/\,\text{sec}$. However, if imaging at 1 second intervals, the result of the deformation will only be visible a minimum of 1 second post initial extension, hence can be measured to a maximal speed of $1\,\mu m/\,\text{sec}$. Blebs are known to exceed $2\,\mu m/\,\text{sec}$ [Hoeller and Kay, 2007] over short displacements, hence analysis requires 0.5 second intervals or lower, which reduces image quality and increases the need for effective pre-processing.

6.2.1 Image Pre-Processing and Segmentation

Fluorescence images were pre-processed to remove fluctuations in intensity over the length of a sequence, shadows resulting from dirt in the optical path, and uneven illuminated background, also helping to minimise segmentation noise. See Material and Methods, Section 2.5.4 for details.

The BOA plug-in was used to segment cells from the RITC-Dx channel (and manually corrected in BOA if required). Contraction forces between nodes were lowered, and image resolution artificially increased, to facilitate segmentation of concave regions for problematic cells.

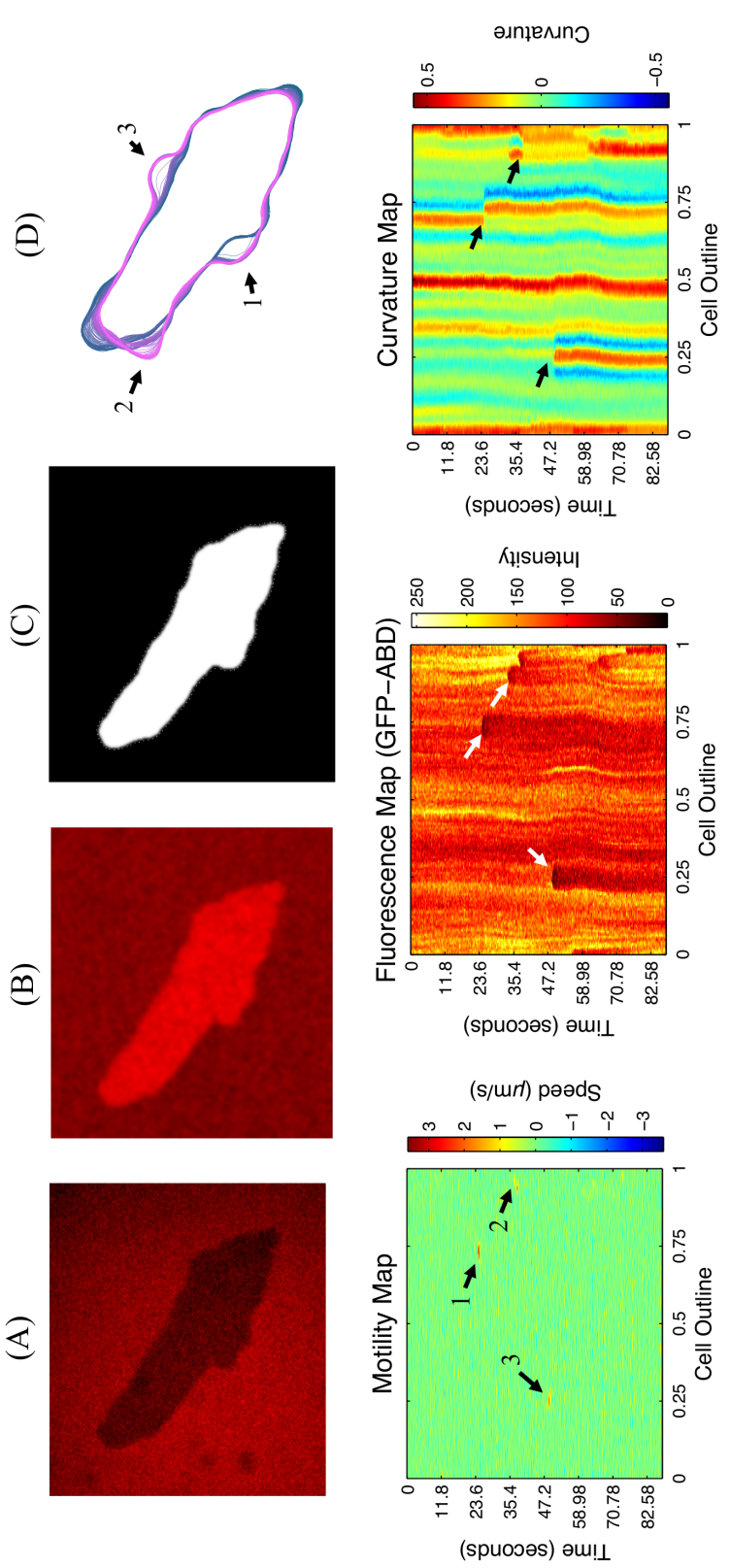

Figure 6.2: **Example QuimP analysis of a blebbing Ax2 cell under 0.7% agarose.** [Spinning disk microscopy, 4.45 fps, map resolution of 400 pixels, cortex width $0.7\mu m$, curvature smoothing over 1 μm, and summation over 1 μm]. (A) Raw image from RITC-Dx channel. (B) Pre-processed image used for segmentation; background removal and gaussian convolution applied ($\sigma = 1$ *pixel*) to smooth high frequency noise. (C) Thresholded image as an alternative for segmentation in cases where pre-processing fails to produce even illumination. (D) Cell track; overlaid cell outlines at all frames. Labels 1 and 3 indicate clearly identifiable, high speed blebs. Label 2 marks a slower occurring protrusion. Drops in GFP-ABD fluorescence are observed immediately following each protrusion, consistant with blebs being actin depleted.

6.2.2 QuimP Output

The cortex was typically set to a width of $0.7\,\mu m$ and STMs output from QAnalysis at a resolution of 400 $pixels$, with curvature averaging across $1\,\mu m$, and curvature summation across $1\,\mu m$. Figure 6.2 shows example input and output from QuimP demonstrating how blebs are visualised in the data. Blebs appear on motility maps as intense strips that can propagate over 1 to 4 frames, clearly contrasted against segmentation noise. Typically, the absence of actin is seen as a dark streak at a bleb's location in a cell's fluorescence map. Slower protrusions, of longer duration, are identifiable as broken streaks of seemingly heavy noise, running vertically down maps. QuimP output is used to profile characteristics of protrusions by overlaying protrusion paths onto STMs.

6.2.3 Defining Protrusion Paths and ECMM Tracks

A *protrusion path* is a series of 3D co-ordinates, two of which are spatial image co-ordinates (x, y), and the third being time (t). Each co-ordinate marks the centre position of the leading edge, estimated to be the position of highest velocity, at a specific point in time, hence encoding its movements. A protrusion path is interchangeable with an ECMM *track*, where spatial dimensions are replaced with DPs, allowing protrusions to be directly plotted onto STMs (conversion is performed using QuimP X-Map and Y-Map as described in Chapter 5, Section 5.4.1).

Data from QuimP analyses were imported into MATLAB using QuimP MATLAB scripts, and used to automatically extract quantitative data associated with each track. Tracks may be generated manually, but also automatically by ECM-APT. Both can be subjected to the same analysis pipeline.

6.2.4 Manual Generation of Protrusion Tracks

To create a *gold standard* for assessing automated methods, paths were manually traced by placing co-ordinates by eye with the aid of a composite image of both channels (actin labelling was found to be of particular importance for manually locating blebs and pseudopodia). Paths were converted to ECMM tracks and plotted over STMs, but also the original image sequence to verify position (Figure 6.3A). Tracks are assigned a width, $W_p = 0.8$ microns, forming a *track window* (Figure 6.3B). Tracks do not travel vertically down maps, but instead meander due to the cell displacing and changing in perimeter length, similar to ECMM tracking of DPs. In fact, we will later show that ECMM mapping can recreate protrusion paths given a starting point on the leading edge.

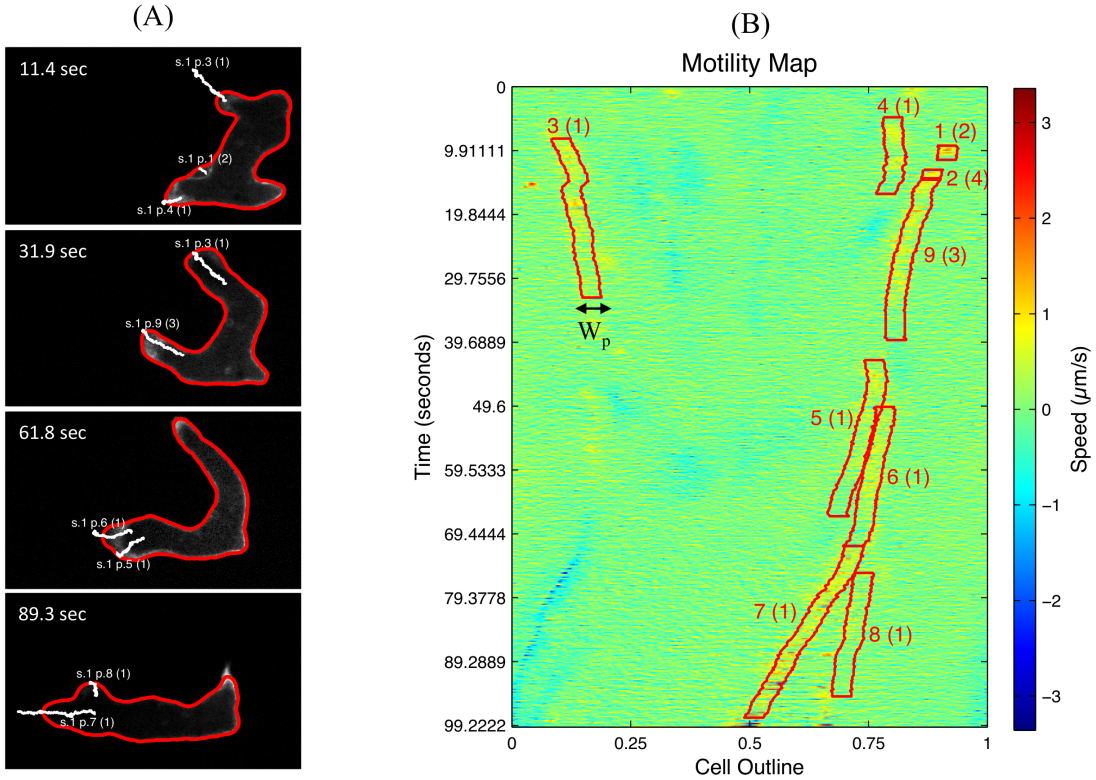

Figure 6.3: **Manual tracing of wild type Ax2 protrusions.** Protrusion paths are manually determined as a series of 3D image co-ordinates marking the centre of a protrusions edge, the point estimated to be of highest velocity, at a specific point in time. Paths are converted to protrusion tracks (replacing image co-ordinates with DP values). (A) Tracks are plotted back onto the original image sequence to verify correct conversion. (B) Given a protrusion width, W_p, tracks define protrusion widows within ST-maps. Protrusions are given an integer ID and categorised as in Table 6.1.

Label	Description	Key
1	Isolated actin driven protrusion	Actin D.
2	Isolated bleb	Bleb
3	Bleb immediately followed by an actin driven protrusion	Bleb-Actin D.
4	Multiple blebs occurring seamlessly on top of one another	Bleb-Bleb
-1	Unidentifiable	
-2	Incorrectly identified as a protrusion	

Table 6.1: **Protrusion categorisation.** Chosen to categorise protrusion tracks identified by our automated method, ECMM-APT.

Protrusions were labelled according to the categories listed in Table 6.1, predominantly by assessing the presence or absence of an actin scar. We describe protrusions other than blebs as being *actin driven*, although use the term pseudopod interchangeably. Categories were chosen to reflect those tracks identified by our automated method, ECMM-APT (see Section 6.2.7). Obviously, no manual tracks will be labelled as *incorrect*. Tracks are used to compile data on each protrusion.

6.2.5 Profiles and Measures of Protrusion

Using the cell in Figure 6.3 as an example, STMs specific to tracks were constructed from track windows, and profiles computed as averages across a window's width. A protrusion's direction is a unit vector of its initial extension over the first 0.3 μm. Figure 6.4 shows four protrusion profiles from our example. Motility profiles of the two blebs, 1(2) and 2(4), peak within 1 second and are short lived, in contrast to those which are actin driven. Bleb GFP-ABD maps contain distinctive arc shaped shadows due to drops in fluorescence, and spherical expansion (flanks move away from the actin scar at a slower rate).

Motility maps contain significant noise, despite image pre-processing, most noticeable as obscuring the profile of pseudopodia extension. In the next section, we circumvent noise by computing displacement profiles, and estimate protrusion speed.

6.2.5.1 Computing Peak Protrusion Speed from Displacement

Figures 6.5A and B, demonstrates measurement of peak speed ($\mu m/\,\mathrm{sec}$) either as the maximum speed within a raw motility profile, or the maximum of a 3 frame average. Noise artificially elevates the peak speed of pseudopodia, but smoothing blurs true peaks present in blebbing.

As an alternative, we compute displacement profiles by summing over speeds (and scaling by the frame interval), and define peak speeds as the maximal gradient (Figure 6.5C and D). Displacement profiles generally assume the shape of a sigmoid curve, featuring an acceleration phase, a constant speed phase (representative of peak speed), and a deceleration phase.

To attain a noise free measurement of the gradient we fit a generalised logistic sigmoid curve, as described in Material and Methods, Section 2.6.1.

6.2.5.2 Protrusion Displacement, Duration and Curvature

Displacement profiles are also utilised to define track displacement, as simply the maximal value in the profile (μm), and track duration as the time taken to reach the

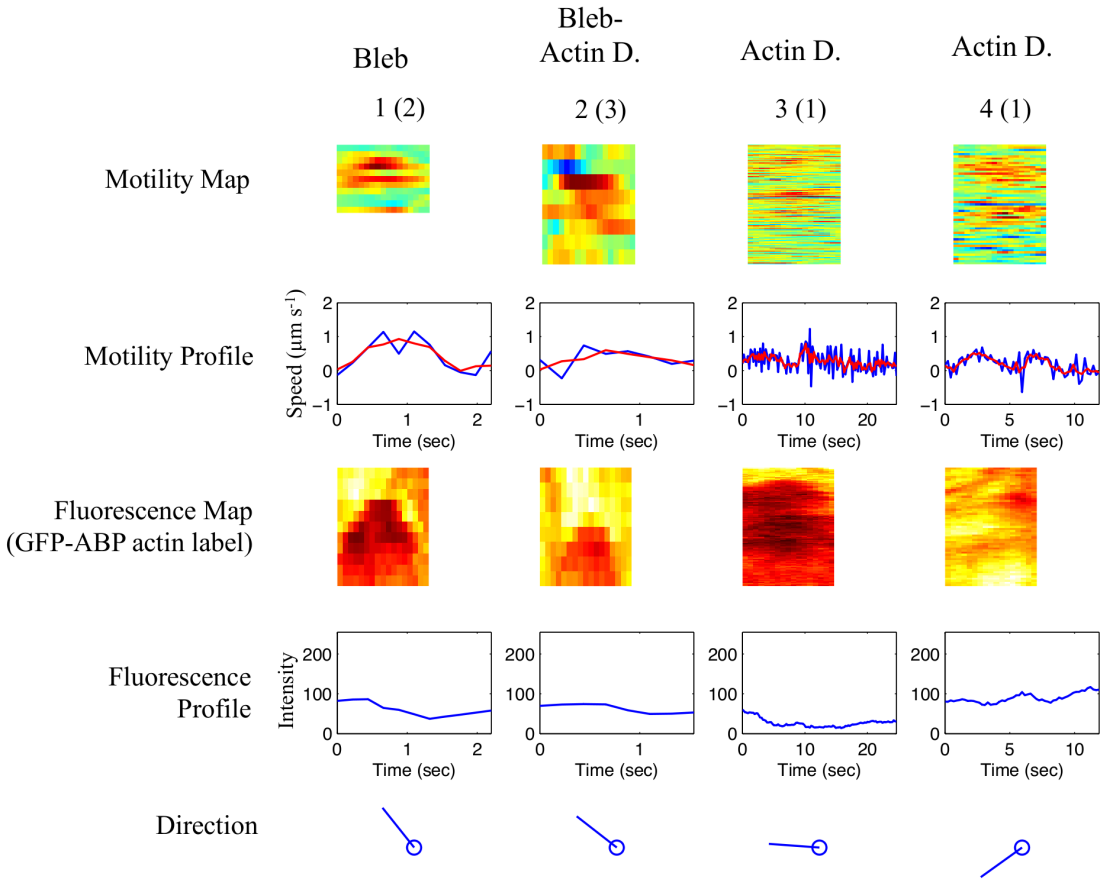

Figure 6.4: **Compiling data from tracks: example protrusions from Figure 6.3.** Maps are constructed from pixels enclosed by track windows, and were averaged at each time point to produce map profiles. Blebs show characteristic sharp peaks in speed over a short time period, and a drop in fluorescence, appearing arc shaped due to spherical expansion. Pseudopodia occur over longer periods. Marker speeds are on the same scale as noise resulting from segmentation. The drop in fluorescence seen in 3(1) is likely due to GFP-ABD becoming *diluted* during expansion. Direction indicates the initial unit vector of deformation over the first $0.3\,\mu m$.

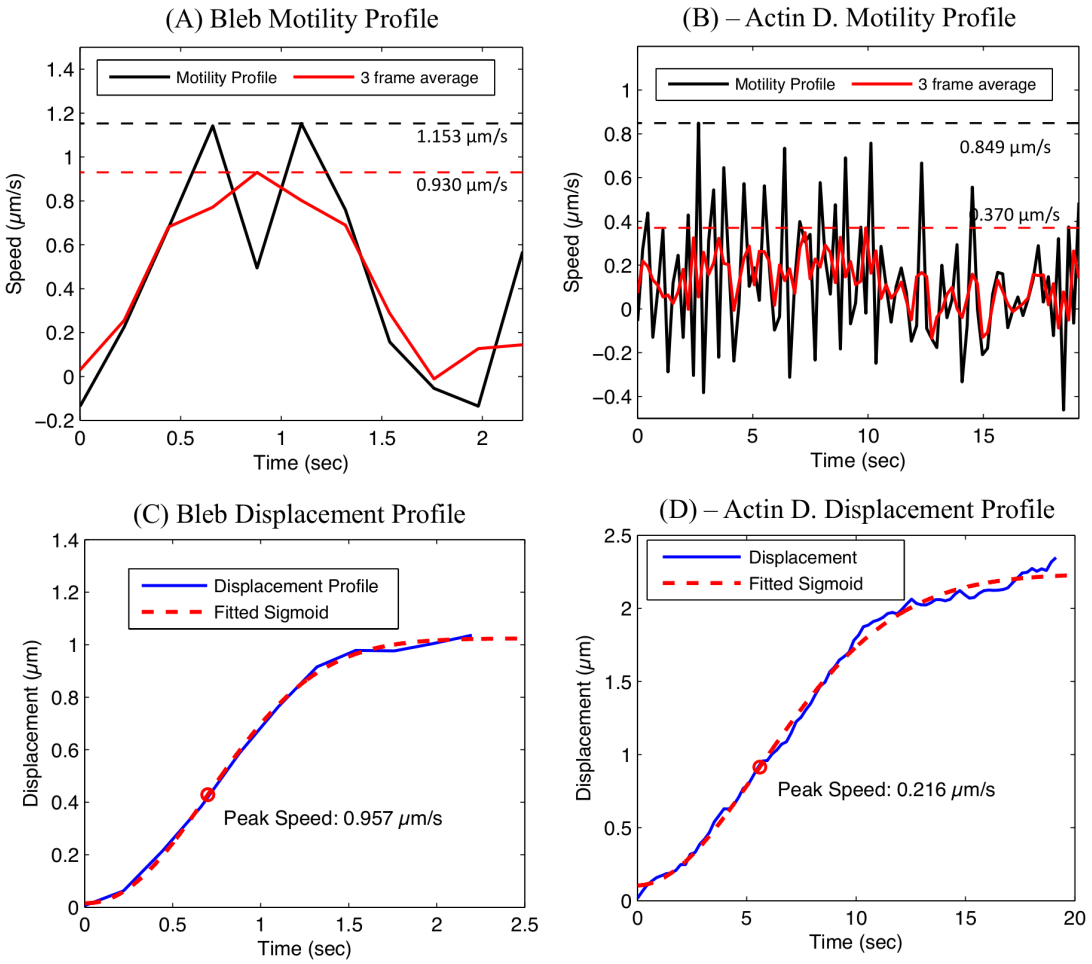

Figure 6.5: **Measuring peak protrusion speed from displacement profiles.** (A-B) Motility profiles of a bleb and pseudopodia respectively, with peak speed measured as either the maximal profile speed (black dashed line), or the maximal of a 3 frame average (red dashed line). (C-D) Peak speed estimated by fitting a sigmoid curve to displacement profiles (See Section 2.6.1, Equation 2.12), and computing the peak gradient. Using peak gradient of displacement circumvents issues associated with noise affecting speed measurements computed from motility profiles.

maximal displacement (seconds).

As with motility and fluorescence, curvature maps are extracted via track windows. Curvature is represented as normalised values in the range $[-1, 1]$ (negative being concave, as described in Section 5.4.1). With regard to protrusions, we refer to a protrusions *curvature* as being the membrane curvature prior to extension, and Δcurvature as the change in curvature up to the time of maximal displacement.

6.2.5.3 Quantifying Drop In GFP-ABD fluorescence

Given a protrusion's fluorescence profile, I^p, we compute a drop in membrane GFP-ABD fluorescence, I^p_{drop}, as the maximum percentage intensity reduction over the first 2 seconds of extension,

$$I_{drop} = 100 - \frac{I^p_0 - \min(I^p_{0\to 2})}{I^p_0} \cdot 100, \tag{6.1}$$

where I^p_0 is the membrane intensity at frame zero relative to a protrusions extension, and $\min(I^p_{0\to 2})$ is the minimum measured intensity within the first 2 seconds of extension.

Computing the minimum fluorescence is an effective method for avoiding the need to define a set time period, or displacement. As blebs vary in duration and displacement, it is unknown as to when the actin cortex will reassemble, hence we avoid computing I^p_{drop} with measurements resulting from the rebuilding of the cortex.

A period of 2 seconds is required to provide time for a bleb's displacement to match that of the cortex width set in ANA. Because ANA is designed to record maximum intensity values, a drop in intensity will not be apparent until a bleb has sufficiently displaced to *escape* the actin scar.

6.2.5.4 Location Relative to the Leading Edge

Assuming a DP value of zero at the leading edge, the position from which a protrusion emanates around the cell's circumference is normalised in the range $[0.5, -0.5)$, where negative values are anti-clockwise. For example, a value of 0.25 indicates that a protrusion emanated $\frac{1}{4}$ clockwise round the cell perimeter from the leading edge.

The leading edge is defined as the DP most advanced in the cAMP gradient. The gradient was oriented north-south or east-west, depending on the coverslip orientation during imaging, and was set manually).

6.2.5.5 Quantifying Protrusion Rate

The protrusion rate, PR, indicates the frequency of protrusions as a function of cell perimeter. To allow comparison over varying frame rates, we divide the number of observed protrusions by the integral of the cell perimeter over the length of the sequence (employing trapezoidal approximation). See Materials and Methods, Section 2.6.2 for details.

6.2.6 Kymograph Analysis and Quantifying Actin Scar Disassembly

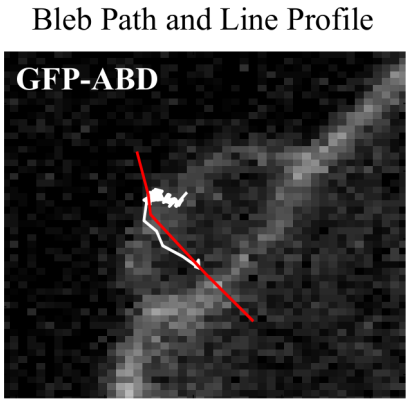

Figure 6.6: **Bleb path and kymograph line profile.** Overlay of manually tracked bleb path (white), and automated kymograph line profile, L^p (red) [see Section 2.6.3 for details].

To visualise cortex dynamics, and quantify disassembly of the actin scar, we automate the construction of protrusion kymographs. Because protrusions rarely extend in straight lines, we implemented multi-segment line profiles, L^p, for sampling GFP-ABD intensities. Intensities from each frame are *stacked* on top of one another to produce space-time plots.

Tracks were smoothed, and reduced in resolution, to attain L^p, as described in Materials and Methods, Section 2.6.3. Line profiles are extended in space and time (3 seconds prior, and 20 seconds post extension) relative to the path to ensure the capture of cortex dynamics. See Figure 6.6 for an example.

To investigate the disassembly rate of the actin scar, subsequent line profiles, L^s, are placed within bleb kymographs (an example is given later in Figure 6.14A, Section 6.3.7). Although kymograph generation is automated, no method has been conceived to automate the positioning of L^s, and therefore it must be done manually

for each bleb. Scar disassembly half-life is quantified as the time for intensity to drop to half that of the initial intensity, I_0^s, defined as the average intensity along L^s prior to extension.

In the next section we describe ECMM-APT for automatically generating tracks to which the same set of measures can be applied.

6.2.7 ECMM Automated Protrusion Tracking (ECMM-APT)

Experimental work presented in Chapter 4 showed that ECMM tracking gives a good approximation to membrane deformation at the centre of retracting membrane regions, and we presumed that ECMM would also give a good approximation in expanding regions. Here, we present how ECMM tracking can indeed be used to track the displacement of pseudopodia and blebs, as compared with manual tracking.

Motility maps are used to identify mid-extension co-ordinates associated with individual protrusions, and tracking data allows for automatic tracing of tracks from these points. To complete the processes, resulting tracks are post processed to remove spatial overlaps and join tracks representative of continuous protrusions.

In Section 6.2.5.1 we tackled segmentation noise by creating displacement profiles to measure peak speed. Similarly, we avoid issues raised by noise in motility maps by building *displacement maps*, which not only remove noise, but can be employed in a consistent manner across a range of different frame rates.

6.2.7.1 Constructing Displacement Maps

Unlike pixels in a motility map which represent membrane speed, pixels in a displacement map represent membrane displacement over a short time interval, δt. For example, for $\delta t = 1\,\text{sec}$, and a frame interval of $0.5\,\text{sec}$, displacement will be calculated over 2 frames, whereas at an interval of $0.25\,\text{sec}$ displacement will be calculated over 4 frames. The duration δt is defined independently of the frame rate, hence displacements are consistent across frame rates, as are noise levels.

At each pixel the associated DP is tracked forwards and backwards in time (totalling δt), as demonstrated in Figures 6.7A and B. The displacement along each track is computed in microns (Figures 6.7D), which are assigned to corresponding pixels in a displacement map (Figures 6.7C).

Computationally, building displacement maps is the most expensive operation in ECMM-APT. Figure 6.7C was computed in approximately 10 seconds in MATLAB, although this could be significantly accelerated if implemented in a lower level language.

Displacement maps remove noise to great affect. Mid points of protrusion ex-

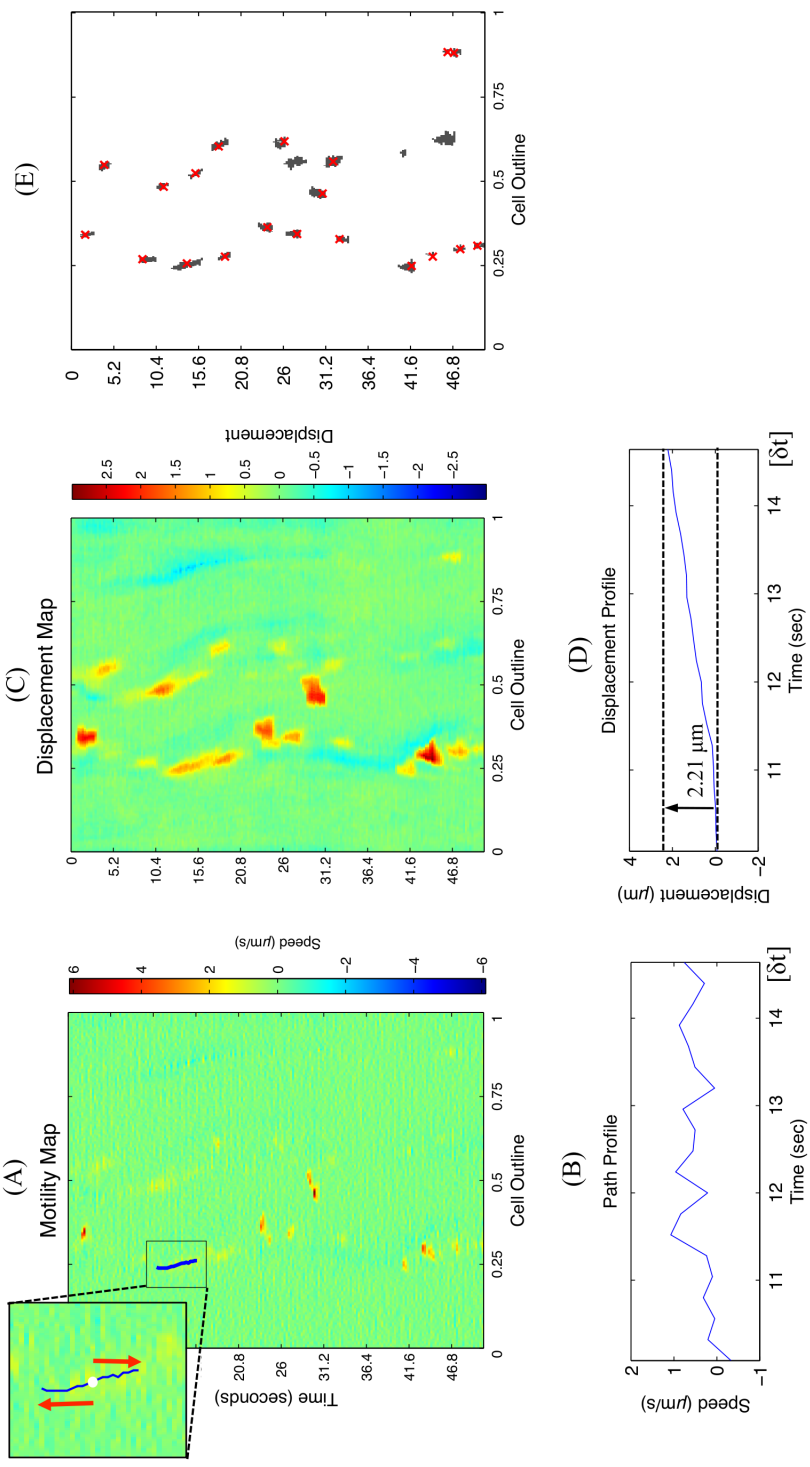

Figure 6.7: **Constructing displacement maps using ECMM tracking data.** (A) Motility map of migrating *Dictyostelium* (4.16 fps). Segmentation noise masks slower protrusions. At each pixel, ECMM data is used to track DPs forward and backward in time (blue trace), resulting in motility profiles. For example, that shown in (B). Profiles are of a duration δt (for illustrative purposes, δt has been set overly large). (C) Displacement map of A ($\delta t = 2.16$ sec). Pixels are valued in microns according to the calculate displacement within motility profiles, as shown in (D) for our example. (E) Result of the extended h-maxima transform ($h = 0.3\,\mu m$) applied to C. Protrusion mid-extension points (red crosses) are placed at the point of maximal displacement in each peak region. Regions with a mean displacement of less than $0.3\,\mu m$ were considered insignificant and excluded.

tension are assigned the largest displacement values, exposing protrusion locations to automated methods. Consequently, high velocity protrusions, such as blebs, appear *smudged* in time, but they are still characterised by a large, central peak in displacement, detectable by peak finding algorithms employed in the following section. Furthermore, we can easily refer to the original motility map for velocity data.

6.2.7.2 Locating Protrusion Mid-Extension Points

A mid-extension point is defined as the location of maximal displacement with in each peak region, as marked by red crosses in Figure 6.7E. Mid-extension points act as seeds for ECMM tracking.

Protrusions differ greatly in amount of displacement, and are rarely flat peaked on displacement maps. Therefore, an extended h-maxima transform [Soille, 2010] was applied (as implemented in Image Processing Toolbox). This suppresses all regional maxima whose height is less than a threshold h; regional maxima being connected pixels of intensity i, surrounded by pixels valued less than i. A value of $h = 0.3\,\mu m$ suppresses background peaks while separating consecutive protrusions, and does not need to be adjusted for analysis at different frame rates (assuming δt remains consistent). Regions with a mean displacement of less than $0.3\,\mu m$ were considered insignificant, and were excluded.

6.2.7.3 Extending Protrusion Tracks

Beginning at a mid-extension point, the associated DP is tracked both forward and backwards in time within the displacement map. Tracking is halted when the displacement value drops to 30% of that at the mid-extension point, creating protrusion tracks, as shown in Figure 6.8A.

Under most circumstances, the resulting tracks need no further adjustment, but occasionally they will overlap with one another if protrusions occur in quick succession. An overlap does not refer to protrusions crossing paths, as ECMM does not allow this, but to being in close proximity spatially and temporally (Figure 6.8D). Overlaps are corrected by trimming tracks, while maintaining mid-extension points (Figure 6.8E). Additionally, protrusions can be joined end-to-end if they occur sequentially (that is, their end points meet within a threshold distance). For details on correcting overlaps, see Materials and Methods, Section 2.6.4 (page 38).

The example given in Figure 6.8 reveals one drawback associated with displacement maps. Inspection shows that protrusion 12, a bleb, is in fact accompanied by a neighbouring bleb that occurs 3 frames earlier. These two neighbouring blebs become

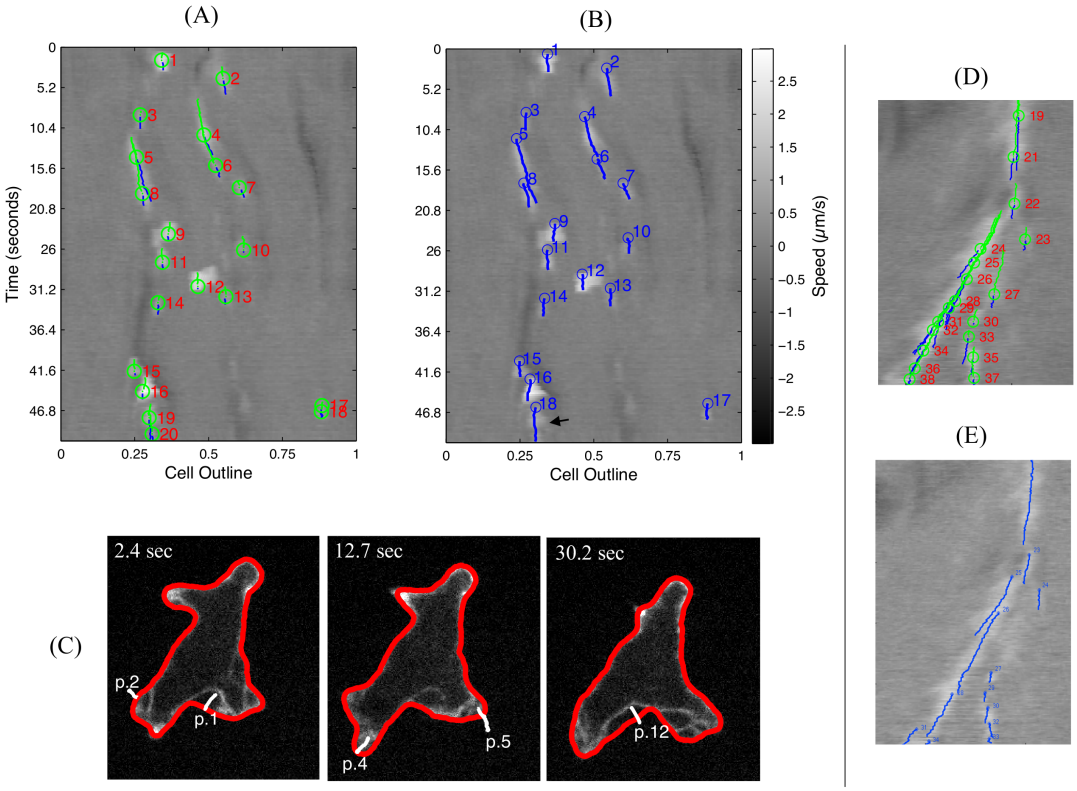

Figure 6.8: **ECMM automated protrusion tracking (ECMM-APT).** (A) Beginning at each mid-extension point, ECMM tracking data is used to track the associated DP backwards (green) and forwards (blue) until the displacement falls below 30% of that measured at the mid-extension point. (B) Resulting tracks are post-processed to remove overlaps between protrusions (*overlap* does not refer to tracks crossing paths, but being in close proximity). Overlaps are corrected by cutting either the forward or backward tracks according to the criteria defined in Section 2.6.4. (C) Tracks overlaid onto the GFP-ABD channel. (D) Complex protrusion pattern before overlap correction. (E) Tracks from D after overlap correction. [For the accompanying movie see disk file */Chapter*6/*Figure*6.8_*Ax*2_*seq*12_*auto_tracking.avi*]

merged together in the displacement map and are identified as a single peak region, and hence a single protrusion. However, this does not result in an incorrect tracking of protrusion 12 as we use only maximal displacement to determine mid-extension points (rather than peak region centres), and instead the neighbouring bleb is simply missed. This behaviour is key for avoiding potential false positives.

6.2.7.4 Removing False Positives

There are two dominant causes of false positives (incorrectly placed protrusion tracks), which we correct to some extent. Firstly, transient concavities caused by vesicles, containing RITC-Dx, are identified by looking for a characteristic retraction, just prior to a detected protrusion, that roughly cancels out the displacement of the protrusion. This method will fail if a vesicle remains at the surface for an extended period.

Secondly, displacing membrane structures during contraction are mostly seen at the cell's rear. As very few true protrusions nucleate at the rear of our chemotaxing cells, we assume protrusion tracks close to the rear (opposite the leading DP) are in fact displacements, and remove them from the analysis.

6.3 Analysis of Protrusion Tracks

This section outlines key observations from the analysis of wild type Ax2 and mutant strains of *Dictyostelium*, using both manual and ECMM-APT protrusion tracks. Complete tables of results are included in appendix A, and we provide some example tracked sequences on the accompanying disk.

6.3.1 Ax2 Manually Generated Protrusion Tracks

Experiment	Num. Cells	Frame Rate (fps)	Total Seq. Duration (sec)	Traced Protrusion Count
Ex.1.1-3 Ax2.	18	2	1613.50	Bleb: 59
Ex.2. Ax2	12	4.54, 4.16*	912.74	Actin D: 22 Bleb: 12 Bleb-Actin D.: 4 Bleb-Bleb: 5

* Sequences are either 4.54 fps or 4.16 fps

Table 6.2: **Ax2 manually generated protrusion tracks.** Protrusions were located manually in Ax2 cells, imaged at two sets of frame rates. Experiments 1.1-3 were imaged at 2 fps. Cells in experiment 2 were imaged at frame rates above 4 fps.

Table 6.2 summarises the number of manually generated protrusion tracks in Ax2 sequences (see Section 6.2.4 for how tracks are generated). Experiment 1.1-3 Ax2 consists of three experiments, conducted on separate days, imaged at 2 fps. Experiment 2 was imaged at frames rates above 4 fps (using spinning disk microscopy). For the full break down of tracks see Table A.1 (Appendix A.2.1, page 147) and for associated, averaged measures of protrusion, see Table A.2 (page 148).

Only protrusions which could be identified with little doubt over their category were included in this analysis, hence they are only a subset of all protrusions. This is done to attain a clear picture of how pseudopodia and blebs are arranged within the multidimensional space of protrusion measures, and to provide data for assessment of ECMM-APT. Only blebs were marked in the confocal image sequences (Ex.1.1-3) to allow for comparison of measured bleb speeds when imaged at different frame rates.

6.3.2 Ax2 ECMM-APT Generated Protrusion Tracks

Experiment	Num. Cells	Frame Rates (fps)	Total Seq. Duration (sec)	Protrusion Count	Protrusion Rates (prots $\mu m\ sec^{-1}$)
Ex.1.1-3. Ax2	18	2	1613.5	Actin D: 216 Bleb: 107 Bleb-Actin D.: 44 Bleb-Bleb: 1 Unidentifiable: 15 False Positive: 17 False Negative: 15	All Prot: 0.003518 Actin D.: 0.002388 Bleb: 0.001396
Ex.2. Ax2	12	4.54, 4.16	912.74	Actin D: 88 Bleb: 37 Bleb-Actin D.: 5 Bleb-Bleb: 0 Unidentifiable: 6 False Positive: 5 False Negative: 4	All Prot: 0.002141 Actin D.: 0.001464 Bleb: 0.000661

Table 6.3: **Ax2 ECMM-APT generated protrusion tracks.** Categories of protrusions tracked by ECMM-APT in sequences of wild type Ax2 cells.

ECMM-APT was applied to the same sequences as for manual analysis, and categorised as shown in Table 6.3. Unidentifiable protrusions were typically small and *bleb-like*, where the presence of an actin scar, as apposed to F-actin polymerisation, was indistinguishable.

For the full break down of tracks see Table A.3 (Appendix A.3.1, page 149) and for associated, averaged measures of protrusion, see Table A.4 (page 150). For example movies of ECMM-APT tracking, see folder */Chapter6/ecmm-apt_examples/* on the accompanying disk.

6.3.3 ECMM-APT Performance

We introduce false positives and negatives, representing counts of incorrectly positioned protrusions and missed protrusions respectively. Nineteen false negatives occurred for the following reasons (number of occurrences are given in brackets):

- Slow, short lived protrusions that fell below the displacement threshold (2).
- Protrusion emitted because it is incorrectly identified as being a rear displacement (1).
- Protrusions occurring in close proximity become merged on displacement maps. The majority are missed blebs (16).

Twenty two false positives were incurred for the following reasons:

- Segmentation faults, either as a result of noise, or RITCDx filled vesicles at the cell surface (2).
- Parts of the cell body move in and out of the imaging plane, mimicking rapid protrusions (3).
- Cell *swells* as the rear contracts, generally causing the cell's flanks to move outwards, as if protruding (8).
- Concave membrane regions displacing laterally as a cell contracts (7).
- Protrusions in close proximity merge within displacement maps, causing a track to be incorrectly placed (2).

The false positive rate was reduced from 44 (7.8% of all those detected) to 22 (4.1%) by omitting protrusions that occurred at the cell's rear at the expenses of incurring 1 false negative.

The protrusion rate (PR) for all protrusions includes those that were unidentifiable, but not those that were missed by ECMM-APT. Actin driven PR includes all categories in which actin driven protrusions occur (categories 1 & 2), and likewise for bleb PR (categories 2, 3 & 4).

Peak speeds computed by ECMM were compared with those determined manually (Figure 6.9). Points align at the diagonal with a relative error of 0.18 (SD: 0.23) [relative error calculated as in Appendix A.5], indicating good agreement. Automatically detected protrusions have higher peak speeds over their manual counterparts. This is likely the result of mid-extension points being placed precisely at displacement maxima, as opposed to being positioning *by eye*.

Of the 538 protrusions observed in sequences of Ax2 cells, 19 were missed, which equates to a sensitivity of $\approx 96.5\%$. (specificity can not be calculated as we have no quantity for *true negatives*). False positives occurred at a rate of 4.1%.

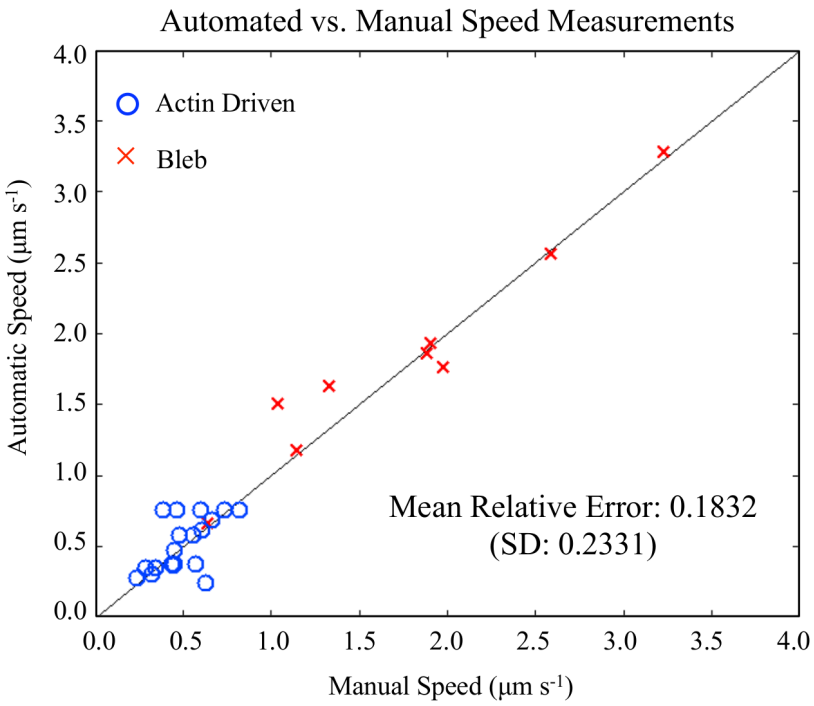

Figure 6.9: **Plot of manual versus ECMM-APT determined peak protrusion speeds in Ax2 cells (4.16 fps).** The closer a point lies to the diagonal the better the agreement between the two methods. Methods differ by a mean relative error of 0.1832 (SD=0.2331).

Generally speaking, ECMM-APT is able to located the vast majority of cellular protrusions, far exceeding the numbers realistically identifiable by eye, from an unbiased perspective, and at multiple frame rates. Throughout the rest of this section we show that the distributions of protrusion measures reflects those achieved manually, but provides an almost complete picture of cell protrusive behaviour. Furthermore, computation of tracks on our relatively modest hardware is a matter of seconds, even in its current MATLAB implementation.

6.3.4 Three Classes of Protrusion in Wild Type *Dictyostelium*

ECMM-APT reveals a top blebbing speed of $4.93\,\mu m/\,\text{sec}$ (typically speeds are between $0.5\,\mu m/\,\text{sec}$ and $2\,\mu m/\,\text{sec}$). Actin driven protrusions show an average peak speed of $0.51\,\mu m/\,\text{sec}$ (± 0.21), the fastest measured at $1.15\,\mu m/\,\text{sec}$. The proportion of blebs to actin driven protrusions were 0.58 and 0.45 for 2 fps and 4-5 fps respectively.

More importantly, scatter plots of peak speed versus displacement (Figure 6.10) describe the full spectrum of protrusions extended by Ax2 cells under agar. The manual analysis reveals a clear pattern of slow, high displacement protrusions that arrange vertically, and high speed blebs, with short displacement, aligning along a shallow, linear slope. ECMM-APT reproduces, and expands upon this picture by including all cellular protrusions, the majority being short in displacement and slow.

As data is available only at discrete time points, we might expect measured speeds to lie at discrete speeds, similar to discrete measures of duration (not shown). This is not the case as spatial displacement is measured at the sub-pixel level by BOA, and fitted curves are not limited to discrete slopes. A fitted slope may even exceed the maximal measurable speed, which accounts for some overly fast bleb speeds observed at 2 fps.

At a frame rate of 2 fps, we may conclude that the linear distribution of blebs is likely caused by the upper limit to the measurable peak speed at a certain displacement and frame rate. The fastest measured manual protrusion, $5.00\,\mu m/\,\text{sec}$, at a frame interval of 0.5 sec, displaces by $2.46\,\mu m$, almost exactly matching the maximal possible measurable speed, hence a requirement for higher frame rates.

Surprisingly, higher frame rates reveal a similar linear slope that does not approach the theoretical maximal, but the fastest bleb, measured at $4.93\,\mu m/\,\text{sec}$, does exceed the speed that could be measured at 2 fps. Although frame rate is limiting to the analysis at 2 fps, measurements at 4-5 fps suggest that the linear relationship is not simply the result of these limitations, but instead indicate that the mechanics behind blebbing (the magnitude of hydrostatic pressure available in generating a bleb and/or the adhesion forces between cortex and membrane) determine both bleb speed

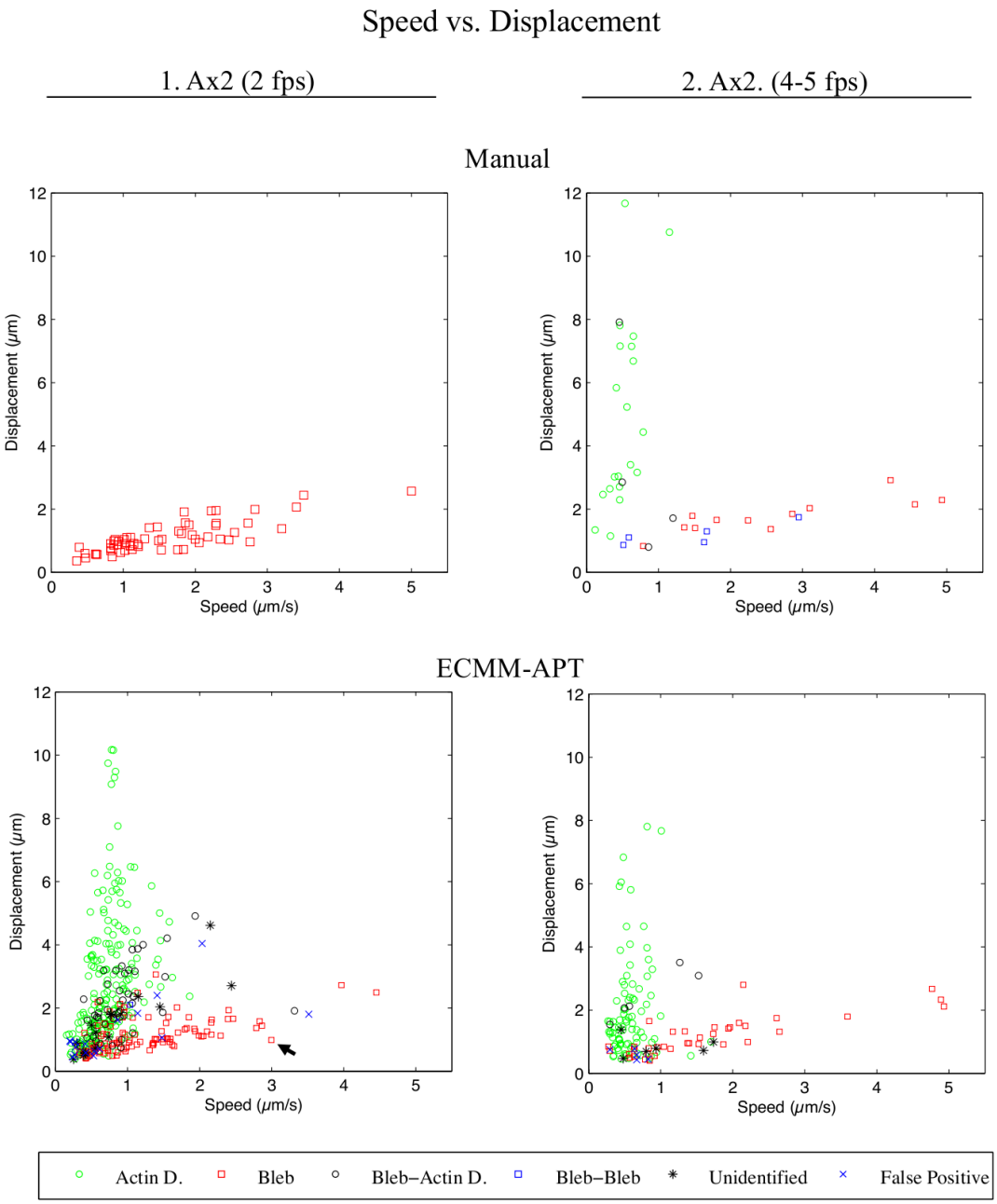

Figure 6.10: **Scatter plots of peak speed versus displacement in Ax2 cells.** Results are given for two frame rates, and both manual and ECMM-APT methods. ECMM-APT recreates well the patterns observed by manual analysis. Blebs (red) align linearly at a shallow gradient, distinct from pseudopodia (green). Increasing the frame rate allows for measuring faster blebbing speeds, but the linear relationship remains. Black arrow indicates an anomaly that exceeds the maximal measurable speed at 2 fps, caused by over-fitting. [For average data see Table A.2 and Table A.4].

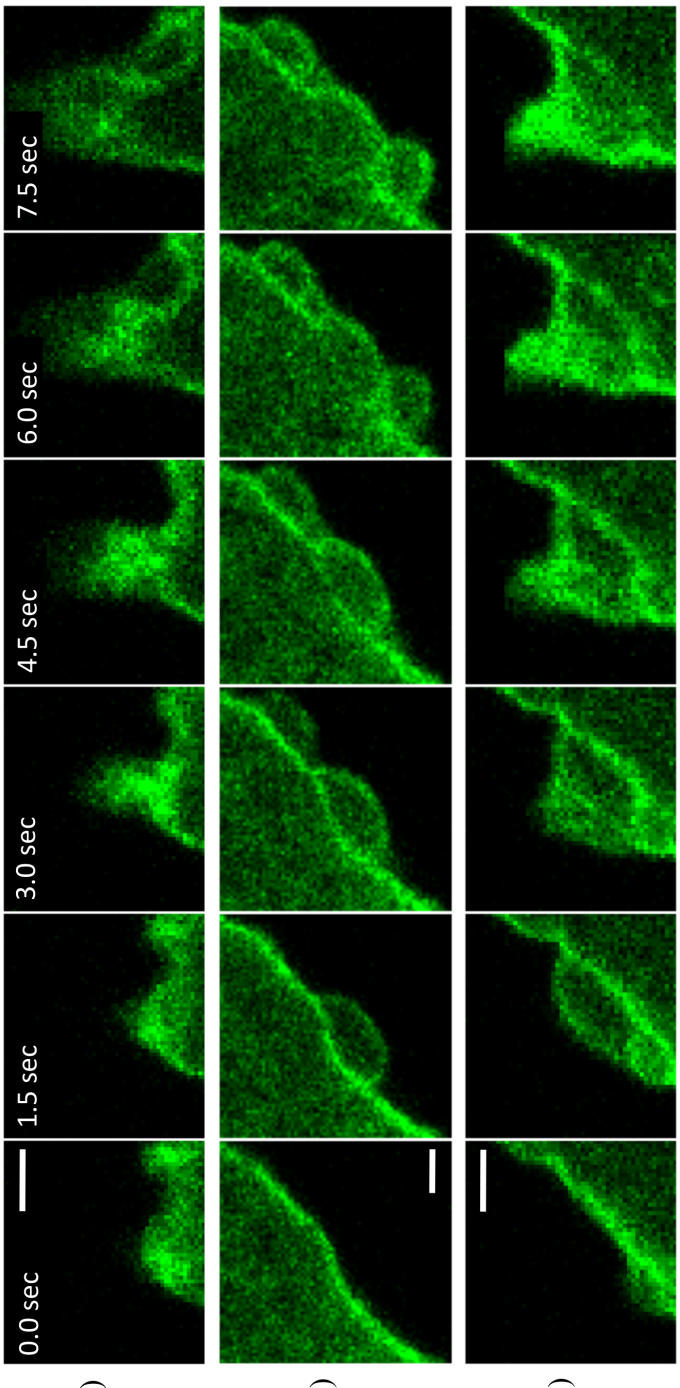

Figure 6.11: **Three classes of protrusion in Ax2 cells.** Image sequences of expanding protrusions in Ax2 cells expressing GFP-ABD. Scale bars are $2\,\mu m$ (images shown at 1.5 *sec* intervals). (A) Actin driven pseudopodium. (B) Consecutive series of three blebs. (C) Bleb, followed immediately by actin polymerisation at the site of cortex reassembly.

and displacement. This is as apposed to blebs always protruding at a set speed, but being terminated after different intervals.

In addition to distinct blebs and actin driven protrusions (Figure 6.11A and B) a third class of protrusion is present, extended by combining an initial bleb that is seamlessly followed (in terms of displacement) by actin polymerisation. Although a relatively rare event, the transition from bleb to pseudopodia is often seamless, hence ECMM-APT tracks it as a single protrusion (Figure 6.11C). Blebs may occur sequentially, but it is more likely that a drop in membrane speed will separate them, so they appear as typical blebs within the shallow gradient.

6.3.5 Convexity Correlates with Bleb Nucleation and Speed

Membrane convexity plays an important role in determining the location of blebs, and their speed of expansion, although blebs are not characterised by increased change in curvature.

Protrusion $\Delta curvature$ shows little discrimination between pseudopodia and blebs, averages measured at 0.347 ($\pm$0.117) and 0.318 ($\pm$0.073) respectively (4 fps). The distribution of $\Delta curvature$ (Figure 6.12) does however show that protrusions that emanate from highly convex regions cause less change in curvature, simply because the membrane is already curved. Although blebs are viewed as high velocity and spherical, actin driven protrusions that emanate from flat membrane regions alter curvature on par, or exceeding that of blebs.

In contrast, a clear separation is observed in initial curvature with average values of 0.100 ($\pm$0.100) and -0.124 ($\pm$0.104) for actin driven and blebs respectively. Blebs preferentially emanate from concave regions, which may occur due to expansion of neighbouring blebs or cell deformation via F-actin. Furthermore, visualisation of peak speed versus curvature, shows a trend in which a higher speed blebs emerge from regions of higher concavity.

6.3.6 Blebs are Devoid of Actin in Ax2 cells

Figure 6.13 shows plots of peak speed versus drop in GFP-ABD fluorescence. Measuring fluorescence drop post protrusion should, theoretically, be a reliable indicator of a protrusion being either a bleb or pseudopodia, given that blebs are well documented as being devoid of actin. As such, a clear segregation is observed in the manual tracks at 4-5 fps (blebs dropping by an average of 78% ($\pm$6.3), pseudopodium by 15.5% ($\pm$16.7)), but slower blebs at 2 fps do not register such large drops. Results from ECMM-APT show a similar pattern of overlap between blebs and actin driven protrusions. Medians

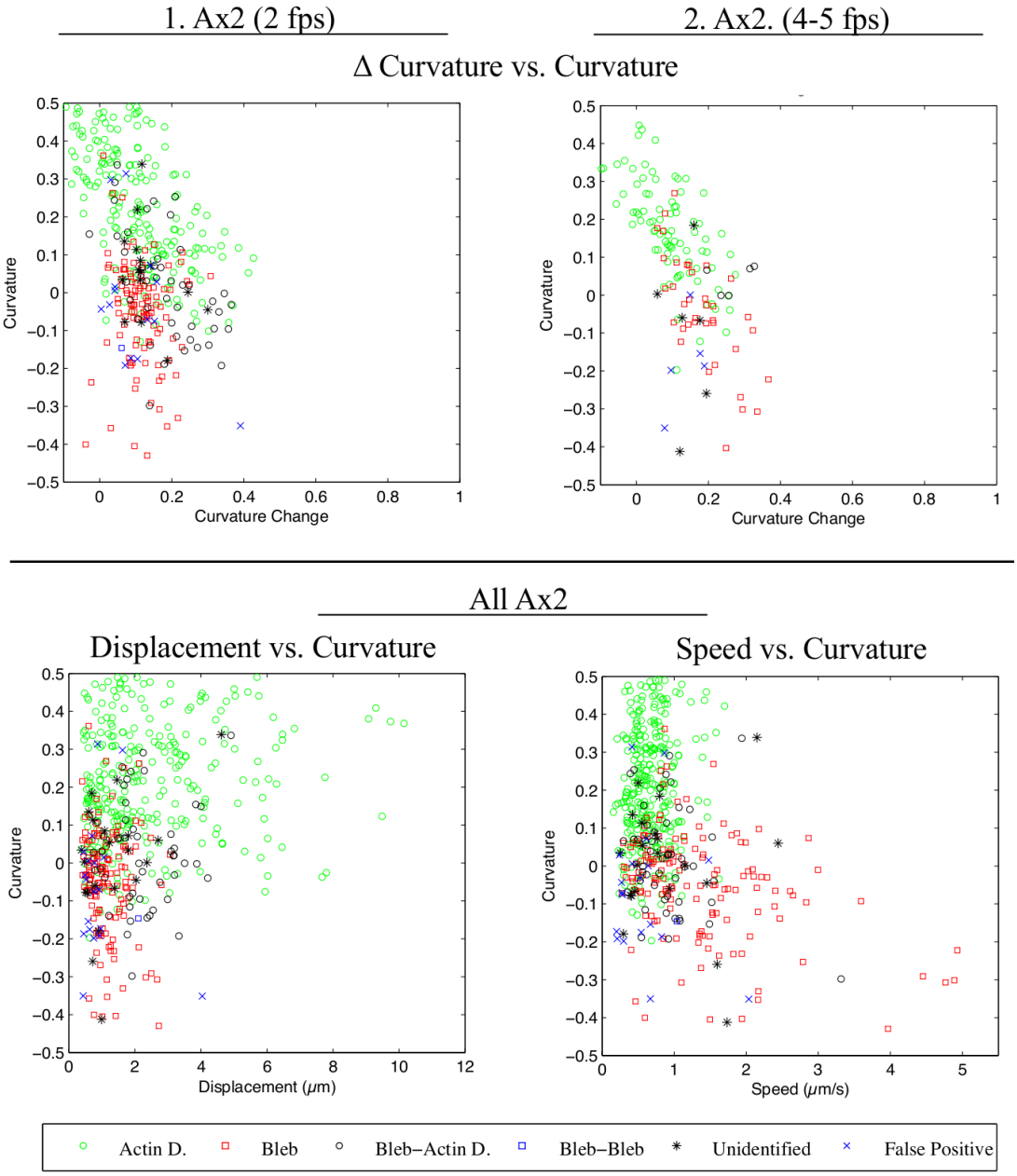

Figure 6.12: **Scatter plots of curvature in Ax2 cells.** Results are given for ECMM-APT only. The change in curvature ($\Delta curvature$) shows little discrimination between pseudopodia and blebs. Pseudopodia emanating from highly concave regions induce less curvature change. Blebs preferentially emanate from flat or concave regions, with a general trend for high speed blebs to be associated with highly negative curvature (concavities). Bleb displacement shows no such pattern. [For average data see Table A.2 and Table A.4].

of the distributions at 2 fps are significantly different (p-value of $1.33e10^{-14}$, determined using Mann-Whitney U test, applied in the case of non-normal distributions).

Inspection of sequences reveals that anomalies may exist for three reasons. Firstly, although we allow 2 seconds for a protrusion to sufficiently displace (see Section 6.2.5.3), blebs that displace by only short distances do not exceed the cortex width parameter set for fluorescent sampling by ANA. This is in agreement with slower blebs having a smaller recorded drop.

Secondly, pseudopodia that result in a large increase in area can record a large drop in fluorescence. This is likely because of the weak binding affinity of GFP-ABD (known to be much lower than that of ABP-120, due to only having a single actin-binding domain [Pang et al., 1998]). As a protrusion extends actin polymerises and as a result GFP-ABD quickly re-localises to newly formed F-actin [Pang et al., 1998], diminishing the measured intensity drop.

Thirdly, at slower fame rates, key points in the bleb expansion maybe missed, and measurement of the actin scar, or newly constructed cortex, prevents measurement of the true drop in fluorescence.

Alternatively, we may be seeing a real biological affect. L929 cells are observed to nucleate blebs by rupture of the cortex, and do not appear to be devoid of actin [Paluch et al., 2005]. Similarly, blebs may not be completely devoid of actin because of large ruptures in the cortex. This is unlikely, as fast blebs always recorded a large drop, suggesting anomalies are because of the issues raised above.

6.3.7 Actin Scar Disassembly and Retrograde Shift

Generally speaking, a bleb kymograph shows rapid expansion at time zero, is devoid of GFP-ABD, and is followed by assembly of a new cortex (to the right of the kymograph), and disassembly of the actin scar (Figure 6.14A). Of the 12 manually traced blebs we measured an average disassembly half-life of 24.92 ($\pm$22.71) seconds. Dis-assembly half-life varies greatly (Figure 6.14D).

Although our measurements are limited in describing the dynamics of disassembly, the variability indicates that the process is not simplistic. Plotting the intensity profile of disassembly, as in the example Figure 6.14C, shows two features; 1) there is a delay in the loss of intensity from the time of nucleation; 2) intensity decays with a curved profile, that is, it is non-linear, even when accounting for the delay (linear fitting is poor, data not shown).

At face value, we may interpret this as disassembly being non-linear, varying according to some set of factors, and initiating after a period of delay. However, our data is not sufficient to statistically validate these observations (predominantly due to

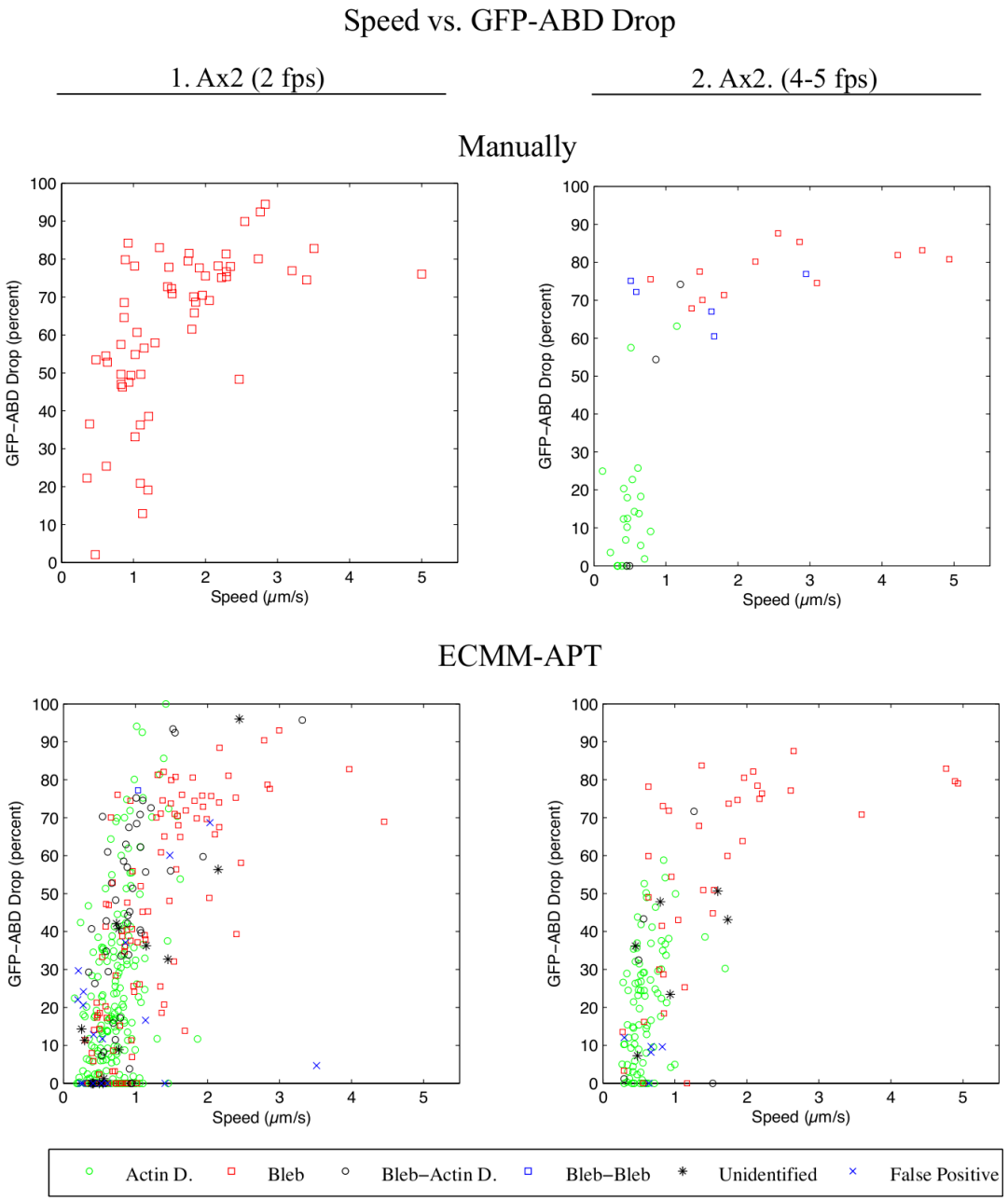

Figure 6.13: **Scatter plots of peak speed versus drop in GFP-ABD fluorescence in Ax2 cells.** Results are given for two frame rates, and both manual and ECMM-APT methods. Fast blebs, which displace by greater amounts, show a clear drop in F-actin. Slower blebs suffer from the influence of the actin scar during measurement. Furthermore, pseudopodia can show a large drop in fluorescence due to the mechanics of GFP-ABD labelling. [For average data see Table A.2, and Table A.4].

time constraints), and interpretation is affected by the dynamics of the label, GFP-ABD. We postpone the discussion of the validity of these results until Chapter 8, Section 8.3.2 (page 130).

In 9 of the 12 kymographs of manually tracked blebs ($4-5fps$) the actin scar is seen to shift to the left (a retrograde shift, towards the cell interior) by $\approx 0.35\,\mu m$, during the short period of expansion (Figure 6.14B). The image co-ordinates of kymograph profiles are not altered during bleb expansion, and are independent of segmentation, hence the shift is not the result of noise, or incorrect tracking data. Such a shift has not been reported in blebbing *Dictyostelium*, but has in the parasite *Entamoeba histolytica* by Maugis et al. [2010] (although no data is presented).

6.3.8 Blebs Nucleate at the Flanks During Chemotaxis

Circular plots (Figure 6.15) indicate the frequency of protrusions that emanate at DP increments of 0.055 around the cell perimeter. The complete tracking of protrusions by ECMM-APT shows that blebs are nucleated at membrane regions advanced in the gradient, as demonstrated by Langridge and Kay [2006] and Kay et al. [2008]. However, we also gain insight into the patterns of blebs in relation to pseudopodia, and show that blebs predominantly occur at the flanks of the leading edge.

Blebs appear to be distributed roughly equally either side of the leading edge, with pseudopodium leading the way during chemotaxis (in that they are the most advanced protrusions in the gradient).

6.3.9 Protrusion and Blebbing Deficiencies in Mutant Strains

Figure 6.16 shows plots resulting from the application of ECMM-APT to sequences of mutant strains. For sequence information and protrusion counts see Appendix A.6 (page 151); for averaged measure values see Appendix A.7 (page 151).

Although based on a relatively few number of cells, ECMM-APT analysis of the myosin-II mutant, mlcE, clearly demonstrates the dependence of blebbing on myosin-II action [Charras et al., 2005; Chen et al., 1995; Cheung et al., 2002]. The characteristic linear distribution of blebs within *peak speed vs. displacement* plots is completely absent, resulting in a 55% drop in average peak speed (which includes both blebs and pseudopodia) compared to wild type cells.

Myosin-II light chain mutants are able to undergo chemotaxis, reflected in mlcE cells maintaining their persistence in direction, and elongation, in comparison to Ax2 cells (see Appendix A.5 for mutant migration statistics). However, as reported by Kay et al. [2008], pseudopodia extend at reduced speeds, averaging $0.49\,\mu m/\,\text{sec}$ (± 0.23)

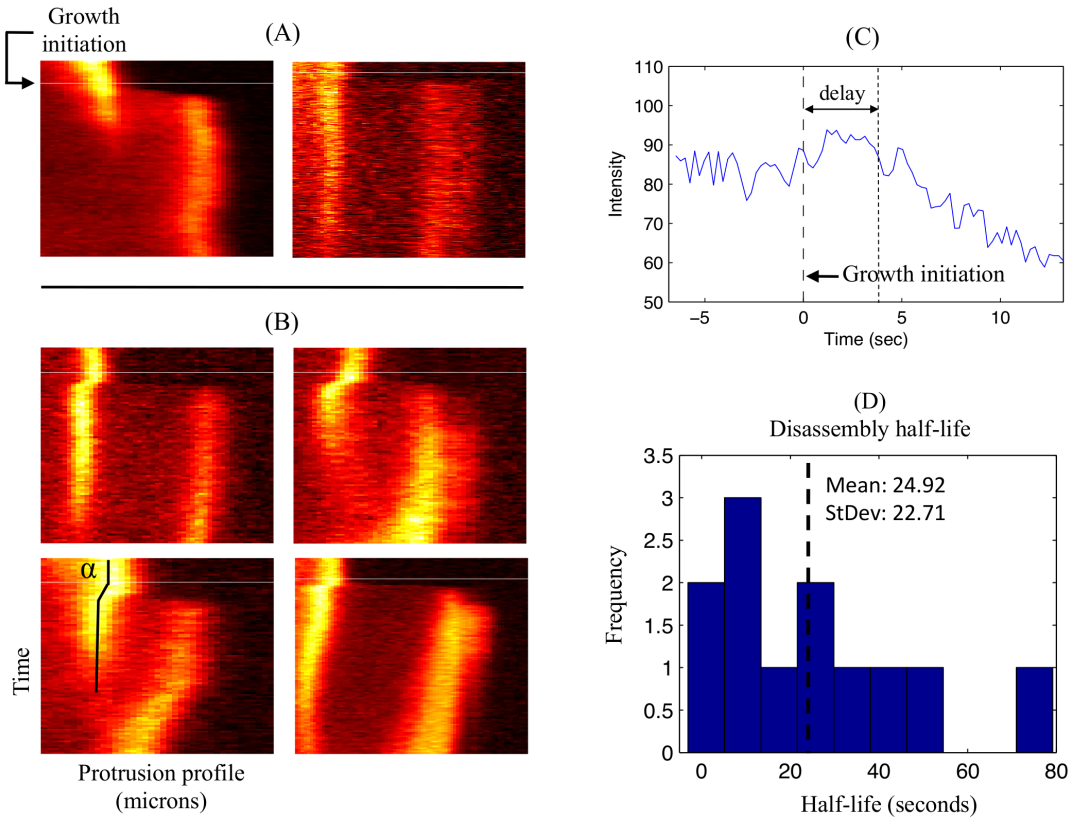

Figure 6.14: **Example bleb kymographs and scar disassembly half-life.** (A) Bleb kymographs; the horizontal axis represents positions along sampling profiles (see Section 6.2.6), with time points stacked vertically. Horizontal white lines indicate initiation of expansion, hence pixels above this line are *pre bleb*. (B) Bleb kymographs revealing a retrograde shift of the actin scar (to the left). (C) Kymograph intensity profile along sampling paths (example path, α). (D) Histogram of disassembly half-lives recorded from 12 manually traced blebs, computed from sampling paths. Half-life is the time (sec) taken to drop to half of the pre-bleb average fluorescence. Half-lives are highly variable.

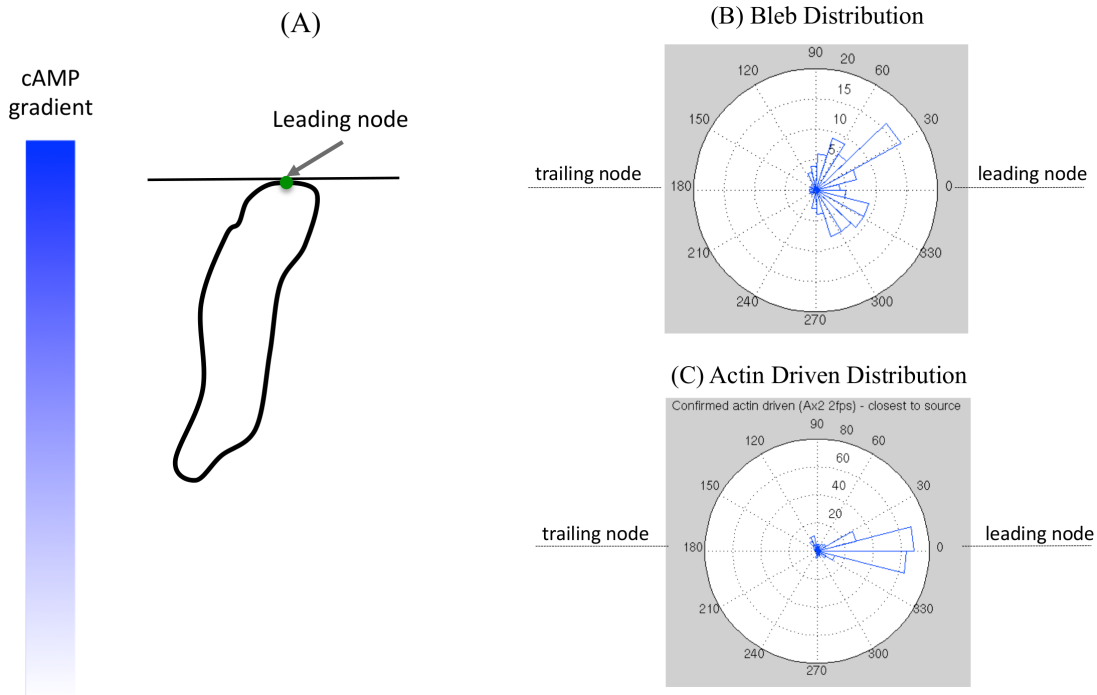

Figure 6.15: **Distribution of Ax2 protrusions relative to the leading edge.** (A) The leading edge is defined as the DP most advanced in the cAMP gradient. (B) Frequency distribution of 304 actin driven protrusions. (C) Distribution of 144 blebs. Expectedly, actin driven protrusions emerge at positions furthest advanced in the gradient. Blebs are clearly directed during chemotaxis, generally emerging high in the gradient, but distributed evenly either side of the most advanced membrane regions.

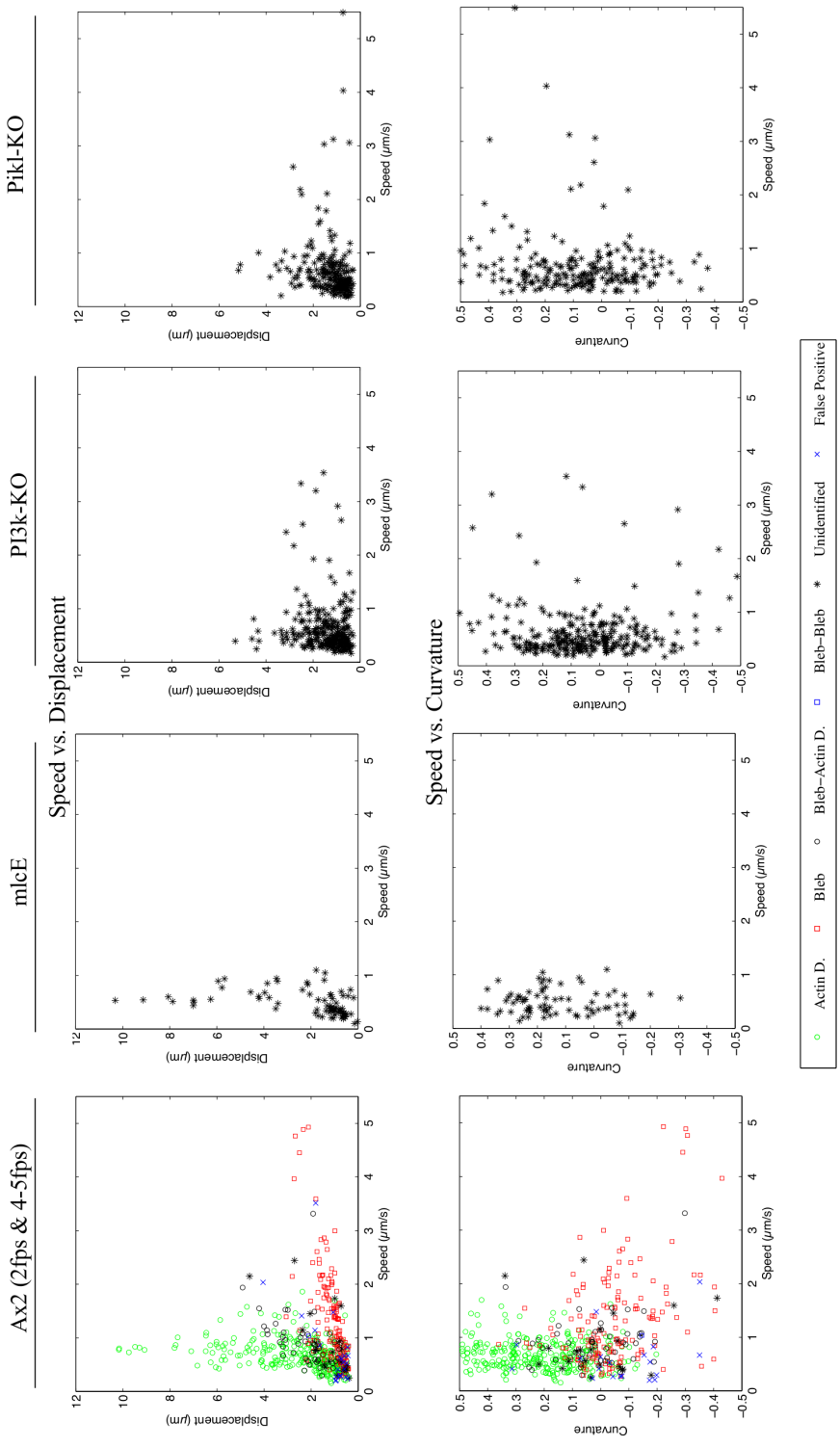

Figure 6.16: **Analysis of mutant strains using ECMM-APT.** Classifications of protrusions in mutant strains are not available due the lack of GFP-ABD labelling. The distribution of protrusions representative of blebbing is absent in the myosin-II mutant, mlcE, but pseudopodia maintain displacement, but at a slower rate. Analysis of PI3K and Pikl mutants suffered from poor quality images, but both show reduced protrusion displacement and little evidence of the blebbing behaviour seen in wild type cells. [For average data see Table A.7]

compared to an average Ax2 speed of $0.67\,\mu m/\,\text{sec}$ ($\pm 0.0.28$). This does not decrease the average displacement, which may have been expected if pseudopodia extend at a slower rate, hence reduced speeds seem to be compensated for by longer time periods of extension.

As blebs have been shown to emanate from concave regions, one would expect an increase in average initial curvature in mlcE cells, but we actually observed near identical values to Ax2 cells (≈ 0.117). As blebs have been shown to occur at half the rate of actin driven protrusions, and there is a large degree of overlap between curvature distributions, averaging curvature over all protrusions masks the contribution of blebbing, and therefore does not reveal the *blebbyness* of a strain (how much a strain utilises blebs for motility).

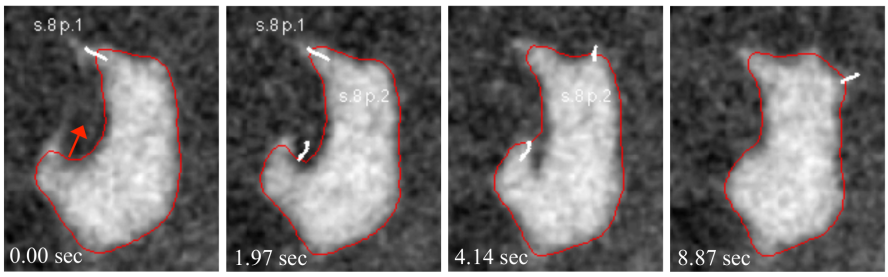

Figure 6.17: **ECMM-APT false positive resulting from movement through the z-axis.** Red arrow indicates the emergence of a false positive detected in segmentation of a Pikl mutant cell.

Analysis of PI3K and Pikl mutants suffered from poor segmentation, particularly problematic are pseudopodia entering and leaving the imaging plane (Figure 6.17), and falsely registering high speed, *bleb-like* extensions, causing skewing of average protrusion measures. However, it is often the case that these false protrusions do not show the concave nature of blebbing observed in Ax2 cells, or the linear distribution of speeds.

Based on the available evidence it appears highly likely that mutants are displaying severely hampered ability to bleb, but segmentation issues prevent us from determining if blebs are completely absent, or indeed if they differ in migration characteristics.

However, global measures show PI3K and Pikl mutants are less persistent in direction, and less morphologically elongated on average, but can successfully chemotax (as also reported by Hoeller and Kay [2007]), albeit at reduced rate. We see that protrusion rates are not hampered, and arguably increase, but the displacement of protrusions is reduced compared to both wild type and mlcE mutant strains.

Before discussing how these observations impact our view of blebbing in *Dictyostelium*, we present some other applications of the new QuimP software.

Chapter 7

QuimP Applications

In this chapter we present three examples in which the next generation QuimP software has contributed to collaborators work.

7.1 Study of Ras1 Signalling in *Schizosaccharomyces pombe*

The ras proteins are small GTPases involved in signal transduction [Masuda et al., 1995]. Modification of the C-terminal, and targeting to the plasma membrane, are key to ras functionality, but recent studies have shown signalling can also be initiated from intracellular membrane compartments, such as the Golgi apparatus. However, it has been suggested that these observations are largely a consequence of over-expression and that ras functionality still occurs exclusively at the membrane.

Schizosaccharomyces pombe has a single ras protein, Ras1, which regulates cell polarity and has a key role in the yeast phermone-induced mating response. Michel Bond (Graham Ladds' group, Clinical Sciences Research Institute, University of Warwick) utilised GFP-Ras1 mutants to demonstrate that localisation to the plasma membrane is required for ras activity.

QuimP was used to provide a quantitative measure of plasma membrane localisation. Palmitoylation/farnesylation deficient Ras1^{C215S} and Ras1^{C216S} fail to produce a mating response and were subsequently shown to have massively reduced plasma membrane fluorescence in comparison to functioning GFP-Ras1 (Figure 7.1), hence disrupted membrane localisation.

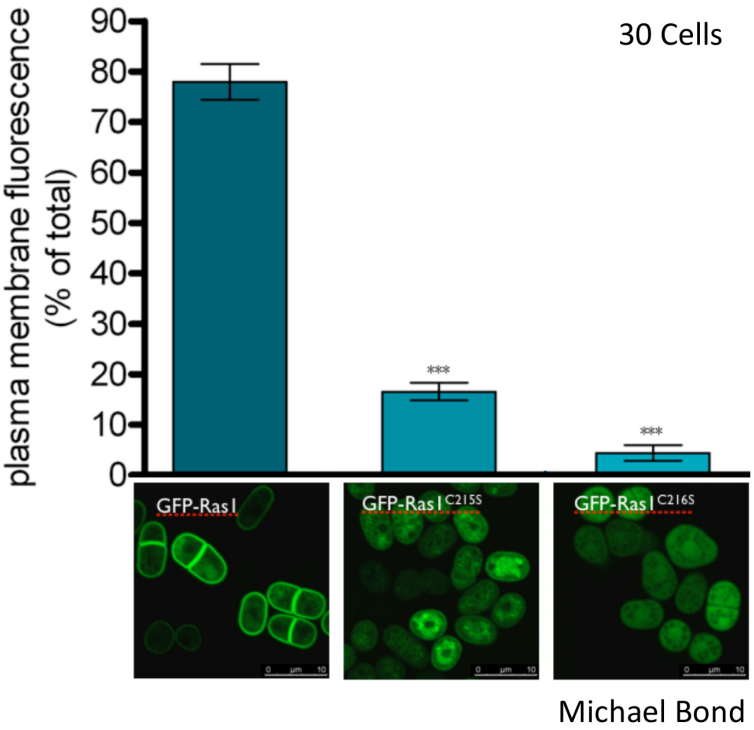

Figure 7.1: **Ras1 mutants show reduced percentage membrane fluorescence**. QuimP was used to segment the periphery of yeast cells expressing GFP-Ras1, palmitoylation/farnesylation deficient GFP-Ras1^{C215S}, or GFP-Ras1^{C216S}. The sum of pixel intensities within the periphery, and the whole cell, allows determination of the percentage membrane fluorescence, hence quantification of membrane localisation of Ras1 (average over 30 cells). Ras1 mutants show dramatic reduction in plasma membrane localisation (analysis and figures provided by Michael Bond [Clinical Sciences Research Institute, University of Warwick]).

7.2 Cycles of Protrusion/Retraction in Four Dimensional Data

As part as a joint grant proposal, submitted in collaboration with John Ferguson and Len Stephens (Babraham Institute, Inositide Laboratory, University of Cambridge), QuimP has been used to produce an example analysis of 4-dimensional data (each frame captured as a z-stack) to study the dynamics of cell protrusion and retraction as observed from a horizontal viewpoint. This allows for a new perspective on cell deformations during a response to stimulus, and aims to demonstrate potential usefulness of membrane tracking in full 3D. Although QuimP is limited to 2D image analysis, a 3D z-stack can be *re-sliced* along a vertical plane of interest, such as the direction of movement, to reveal a sequence of 2D images of a cell as viewed from a side angle.

Figure 7.2 provides an example analysis in which a cell transitions from an initial spherical shape into a flattened disc as it begins forward migration. By averaging the speed of markers located at the front and rear of the cell, ECMM reveals a quantifiable cyclic pattern of protrusion at the front, agreeing with cyclical bursts of actin polymerisation observed to be effected by PI3K signalling [Andrew and Insall, 2007]. By utilising similar analyses it will be possible to investigate the impact of PH domain PI3K effector knockouts, known to alter movement (such as SHIP1, ARAP3 and Prex1) on cycles of protrusion, and correlate with dynamics of actin reports or surface markers.

7.3 Localisation of Dishevelled in the Gastrulating Mesoderm of *Xenopus*

An early *Xenopus* embryo consists of a sphere of cells that divide and migrate, reshaping the embryo to form a head, elongated body, and tail. Much of this reorganisation is realised by chordamesodermal cells which polarise and then migrate towards the embryonic midline (medial-direction). This lengthens the body head-to-tail (anterio-posterior direction) in a process termed convergent extension [Keller et al., 1985].

In collaboration with Eleni Panousopoulou and Dr. Jeremy Green (Department of Craniofacial Development, Kings College London) we conclusively demonstrate that Dishevelled (Xdsh), implicated as a key protein in controlling cell polarity during convergent extension, does not convey polarity in chordamesodermal cells of *Xenopus*.

Observations in epithelial tissues of *Drosophila* show Dishevelled to polarise, accumulating at sites of actin enrichment, providing a direct means of regulating cell elongation [Jaglarz and Howard, 1995]. Localisation of Xdsh in chordamesodermal cells

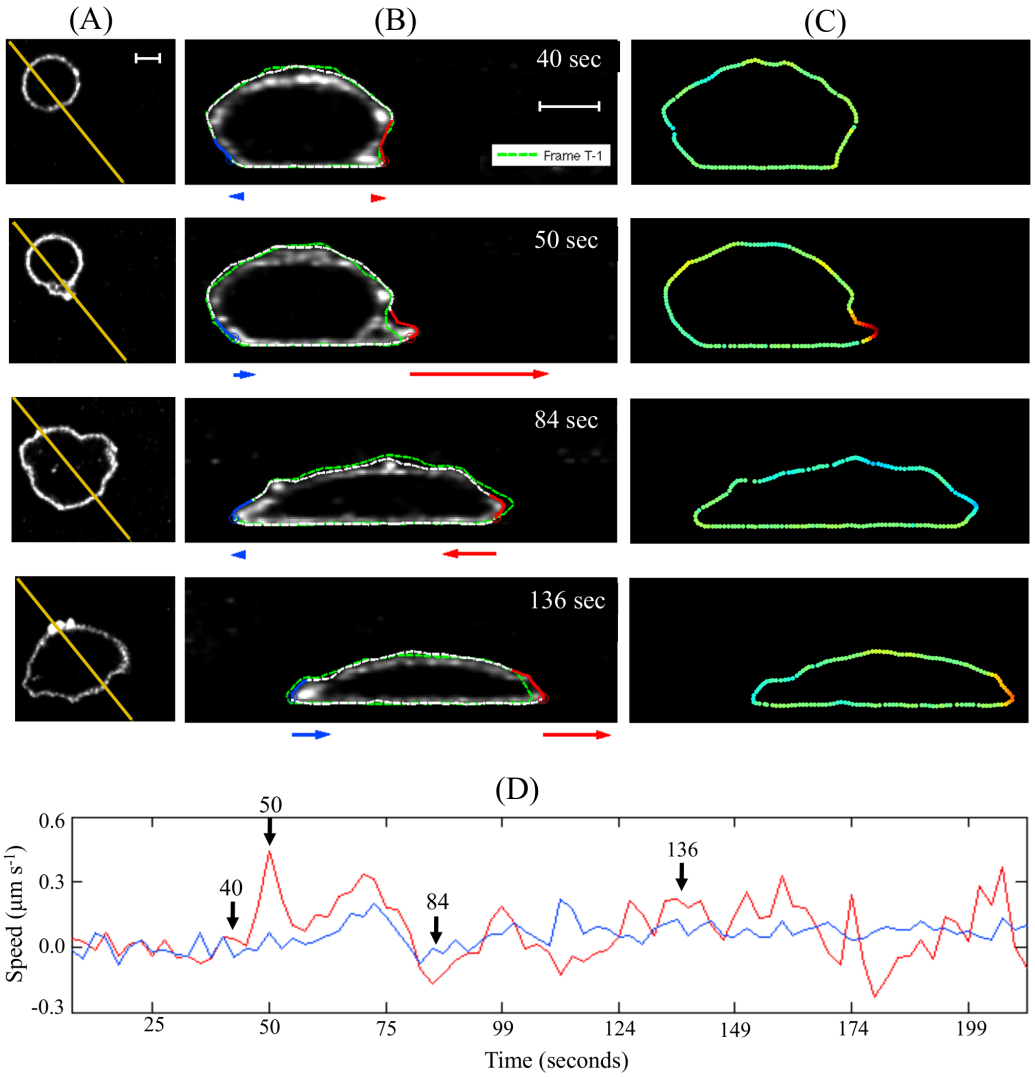

Figure 7.2: **QuimP analysis of motile cells using z-stack data.** Sequence is 85 frames in length and consists of 31 z-slices per frame. (A) cell as viewed from a single z-slice. Yellow lines represent the plane on which the z-stack has been re-sliced. (B) images resulting from the re-slice are subjected to QuimP analysis. The leading edge is highlighted in red, the rear in blue. Arrows are proportional to the average speed of membrane deformation at the highlighted regions. (C) heat map in which markers on the cell outline are coloured according to their speed. Red is representative of expansion, blue retraction. (D) plot shows the average speed of movement in the forward direction (left to right) of the front and rear highlighted regions. At frame 50 the cell begins protruding forward while the rear remains stationary, flattening the cell. Front and back then move in unity with the cell picking up speed. At frame 34, the front is seen to retract as the result of a protrusion not observable within the chosen plane. (Work in collaboration with Len Stephens, Phill Hawkins & John Ferguson, Babraham Institute, Inositide Laboratory).

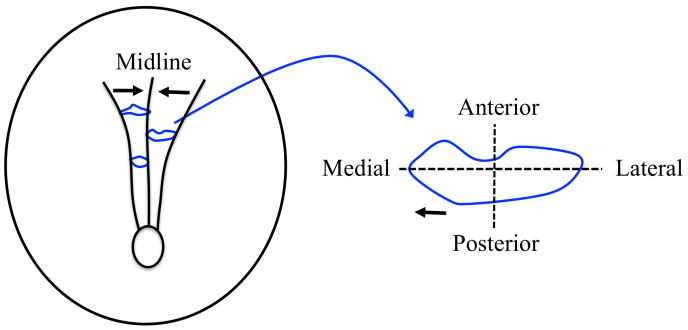

Figure 7.3: **Character of convergent extension in an *Xenopus* embryo.** Chordamesodermal cells polarise in the medial-direction and migrate towards the midline, elongating the embryo.

has not been quantified [Shook and Keller, 2003], but it assumed that Xdsh functions in an analogous way, localising to the membrane in the medial direction.

We disprove this hypothesis by extending an initial analysis conceived by our collaborators in which Xdsh fluorescence is quantified within four domains, defined by the axis of the embryonic midline. We utilise QuimP to increase the sensitivity of the analysis by restricting measurements to the membrane, and implementing an analysis of fluorescence maps to identify subtle clustering of Xdsh in membrane regions.

7.3.1 Data and Initial Analysis

All data was generated at the Department of Craniofacial Development by Eleni Panousopoulou. Tissue samples were prepared in which chordamesodermal cells co-expressed GFP-Xdsh and the cytoplasmic stain Rhodamine-Dextran. Dextran is required for distinguishing patterns in Xdsh localisation from that of heterogeneous fluorescence that naturally occurs in the cytoplasm (due to intracellular structures). A total of 64 cells were prepared for analysis, of which 49 were categorised according to their protrusive behaviour, as summarised in Table 7.1.

	Description	Num. Cells
ML Directed	Elongated in the medial-lateral axis	13
AP Directed	Elongated in the anterior-posterior axis	11
Bipolar	Elongated along both axes	16
Non Protruding	Not elongated	9
		49

Table 7.1: Cell categorisation by protrusive behaviour

Figure 7.4A-C shows some example cells and the results for an initial analysis performed by E. Panousopoulou (Figure 7.4D,E]). Each cell was manually segmented and the total fluorescence intensity of Xdsh and dextran calculated within four domains; Medial (M), Lateral (L), Posterior (P), Anterior (A) (Figure 7.4D). The proportion of fluorescence in each domain, for Xdsh and dextran, was computed across all cells but no significant localisation became apparent (Figure 7.4E).

However, because Xdsh has been shown to localise to the membrane, any preferential localisation to certain domains may be obscured by including cytoplasmic pixels. We therefore applied QuimP, and its MATLAB tools, to restrict the analysis to the membrane.

7.3.2 Measure of Proportional Membrane Fluorescence

Post QuimP analysis, we defined domains by diagonally connecting the corners of an outlines bounding box (Figure 7.5A). This better defines membrane boundaries, as domains are not required to be of equal area. From the inner boundary, computed by ANA, we created a binary image membrane mask for each domain, I_d (Figure7.5B), and computed the proportion of mean fluorescence in each domain, P_d,

$$P_d = \frac{\bar{F}_d}{\sum_4^{d=1} \bar{F}_d}, \tag{7.1}$$

$$F_d = \sum_{i=1}^{X} \sum_{j=1}^{Y} I(i,j) \cdot I_d(i,j), \tag{7.2}$$

where I is the image, i and j are image pixel co-ordinates, F_d is the total fluorescence in a domain, and $\bar{F}_d$ the mean. Comparing the P_d of Xdsh and Dextran across all cells (Figure 7.5C), reveals no significant differences, supporting the conclusion of the initial analysis. Similarly, separating cells by protrusive behaviour produces the same result (Figure 7.5D-G).

7.3.3 Peak Analysis of Fluorescence Profiles

To discover if Xdsh is in fact localising in specific domains, but by forming clusters that have little effect on the mean membrane intensity, we implemented an analysis sensitive to peaks in Xdsh fluorescence in membrane intensity profiles, output by ANA.

As data consists of a single frame, fluorescence maps contain only a single row of pixels, visualised as Xdsh and Dex fluorescence profiles, λ_{Xdsh} and λ_{Dex} (Figure 7.6A). The ratio of profiles, $\lambda_{Xdsh/Dex}$, identifies increases in Xdsh intensity relative to Dextran

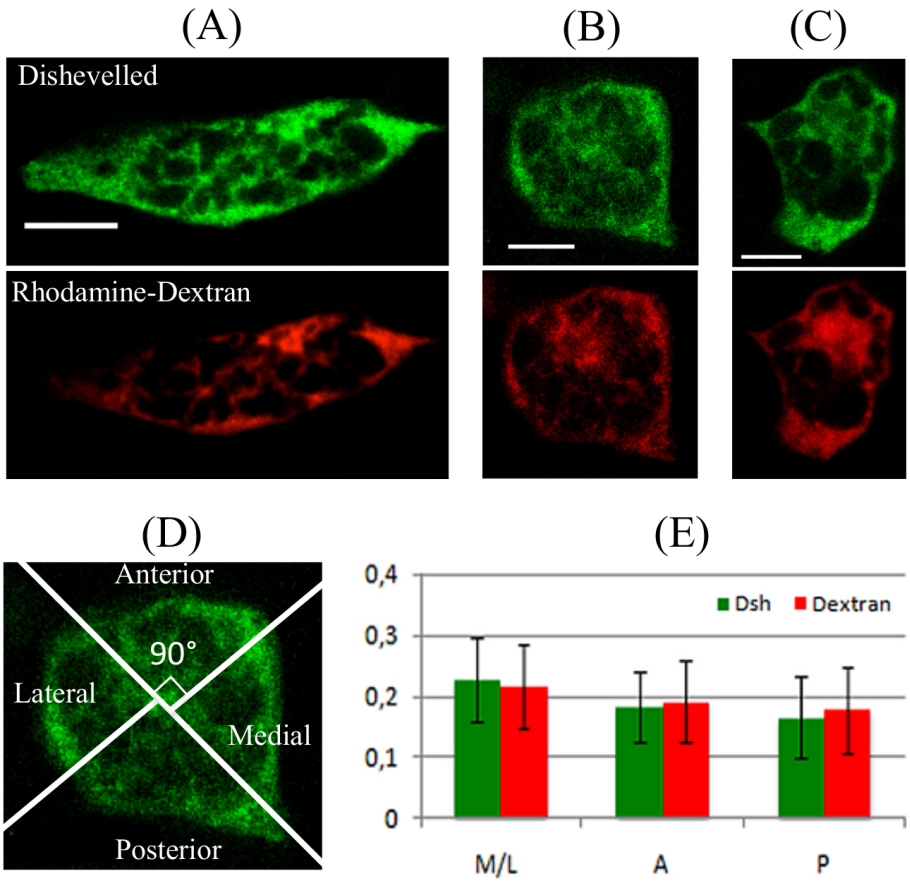

Figure 7.4: **Analysis of Xdsh localisation: domain proportional fluorescence.** Data is 2 channel z-stack through fixed tissue samples (1200×1200 *pixels*, 86 z slices spaced at 1.30 μm). Channel 1: labelled Xdsh (green). Channel 2: labelled Rhodamine-Dextran (red) used to visualise innate heterogeneous fluorescence. Centre slices were chosen for analysis. (D) Domain boundaries lie at 45 *degrees* to the vertical, and split the cell into four equal areas. (E) The proportion of fluorescence in each domain, across all cells. No significant difference is observed between Xdsh and Dextran, suggesting Xdsh does not localise within any particular domain.

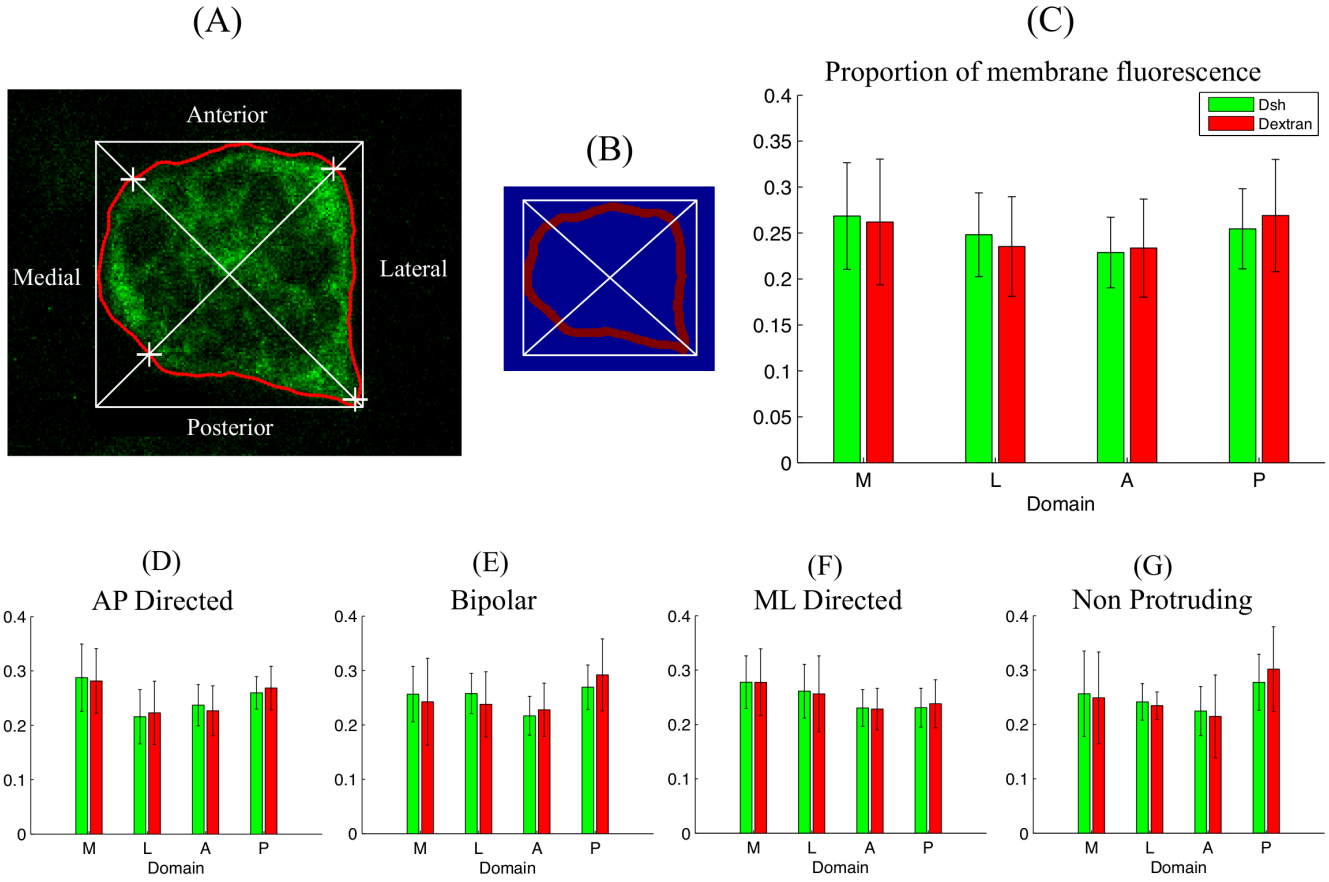

Figure 7.5: **Analysis of Xdsh localisation: proportional domain membrane fluorescence.** (A) The cell outline was computed by BOA and split into domains by diagonally connecting corners of the bounding box. White crosses indicate intersections with the outline and define the membrane boundaries. (B) Binary membrane mask, I_d (equating to a cortex of $\approx 1\ \mu m$ in width). (D) Proportion of mean membrane fluorescence (as computed in Equation 7.1), averaged across all cells. (E-G) Proportion of mean membrane fluorescence, averaged within cell categories of protrusive behaviour. All plots show comparable levels of Xdsh and Dex within all domains.

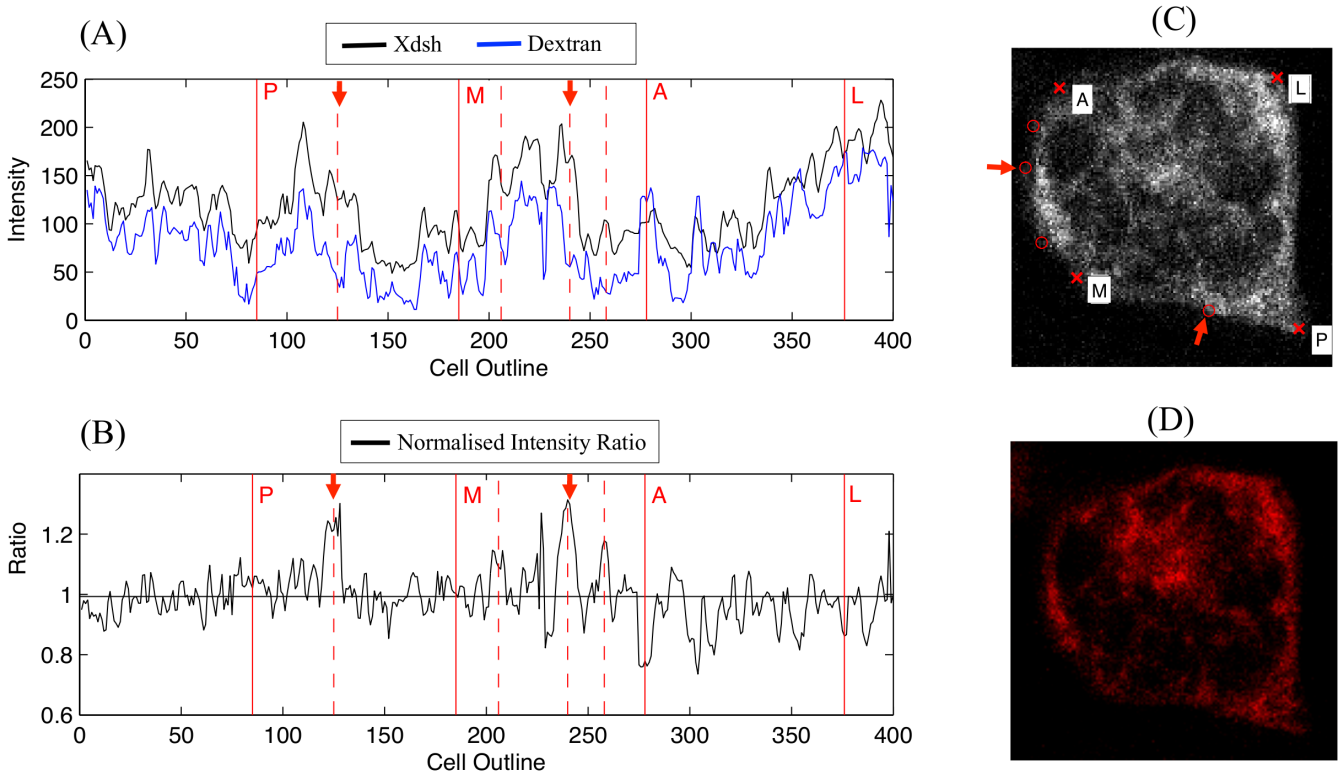

Figure 7.6: **Locating clusters of Xdsh within QuimP fluorescence maps.** (A) Cells are subject to QuimP analysis and the resulting fluorescence maps (that contain only a single frame of data) are visualised as Xdsh and Dex fluorescence profiles, λ_{Xdsh}(black) and λ_{Dex}(blue). Profiles are normalised to the range (1,2) and a ratio profile calculated, $\lambda_{Xdsh/Dex}$, as in Equation 7.3. (B) Continuous regions exceeding the mean ratio (vertical dashed lines) indicate heightened Xdsh intensity. The size of a region is defined by its approximate integral. Regions that exceed a threshold size, c, are counted as Xdsh clusters. Clusters are assigned to domains defined by boundaries (solid vertical lines). Two artificial clusters (20% rises in intensity) are present in this example (red arrows), and have been correctly identified. (C) Xdsh channel indicating the positions of domain boundaries and artificial clusters. (D) Dextran channel.

(Figure 7.6B). To ensure a true ratio we used ANA's option to sample at the same locations in each channel, and normalised profiles to the range $(1, 2)$.

$$\lambda_{Xdsh/Dex}(i) = \frac{\lambda^N_{Xdsh}(i)}{\lambda^N_{Dex}(i)}, \tag{7.3}$$

$$\lambda^N_{Xdsh}(i) = \frac{\lambda_{Xdsh}(i) - \min(\lambda_{Xdsh})}{\max(\lambda^N_{Xdsh}) - \min(\lambda_{Xdsh})} + 1, \tag{7.4}$$

$$\lambda^N_{Dex}(i) = \frac{\lambda_{Dex}(i) - \min(\lambda_{Dex})}{\max(\lambda_{Dex}) - \min(\lambda_{Dex})} + 1, \tag{7.5}$$

where i is a position along the cell outline (discreet map pixels, at a resolution of 400 pixels), and λ^N_{Xdsh} and λ^N_{Dex} are normalised profiles.

Clusters are identified by scanning $\lambda_{Xdsh/Dex}$ for continuous regions that exceed the mean ratio. We determine the size of a region as the integral of intensities (approximated by a sum), and define a cluster as any region that exceeds a threshold size of c (filtering out noise). It should be noted that the integral is scaled according to the length of the cell perimeter, therefore the value of c is fixed across all cells. Figure 7.6B shows example clusters (dotted lines), two of which are artificially inserted (arrows) to demonstrate the validity of the method.

Domains are defined as previously, and the number of clusters counted in each, across all cells, and cell categories. Results for $c = 1.8$ are displayed in Figure 7.7 (1.8 chosen to detect artificial clusters representing a 20% increase in Xdsh fluorescence).

7.3.4 Conclusion

Quantifying the proportion of fluorescence within four biologically significant domains revealed no preferential localisation of Xdsh within chordamesodermal cells. When sampling was restricted to membrane regions of these domains, where Xdsh has been shown to localise in epithelia tissue of *Drosophila*, Xdsh also shows almost identical proportional fluorescence to that of Rhodamine-Dextran, a control used to visualise naturally occurring heterogeneous cell fluorescence.

To investigate the possibility that Xdsh is forming clusters in the membrane, a process missed by proportional fluorescence analysis, peaks in Xdsh fluorescence within the membrane were scored utilising the STMs output by QuimP. The resulting cluster counts show no evidence for preferential localisation of Xdsh.

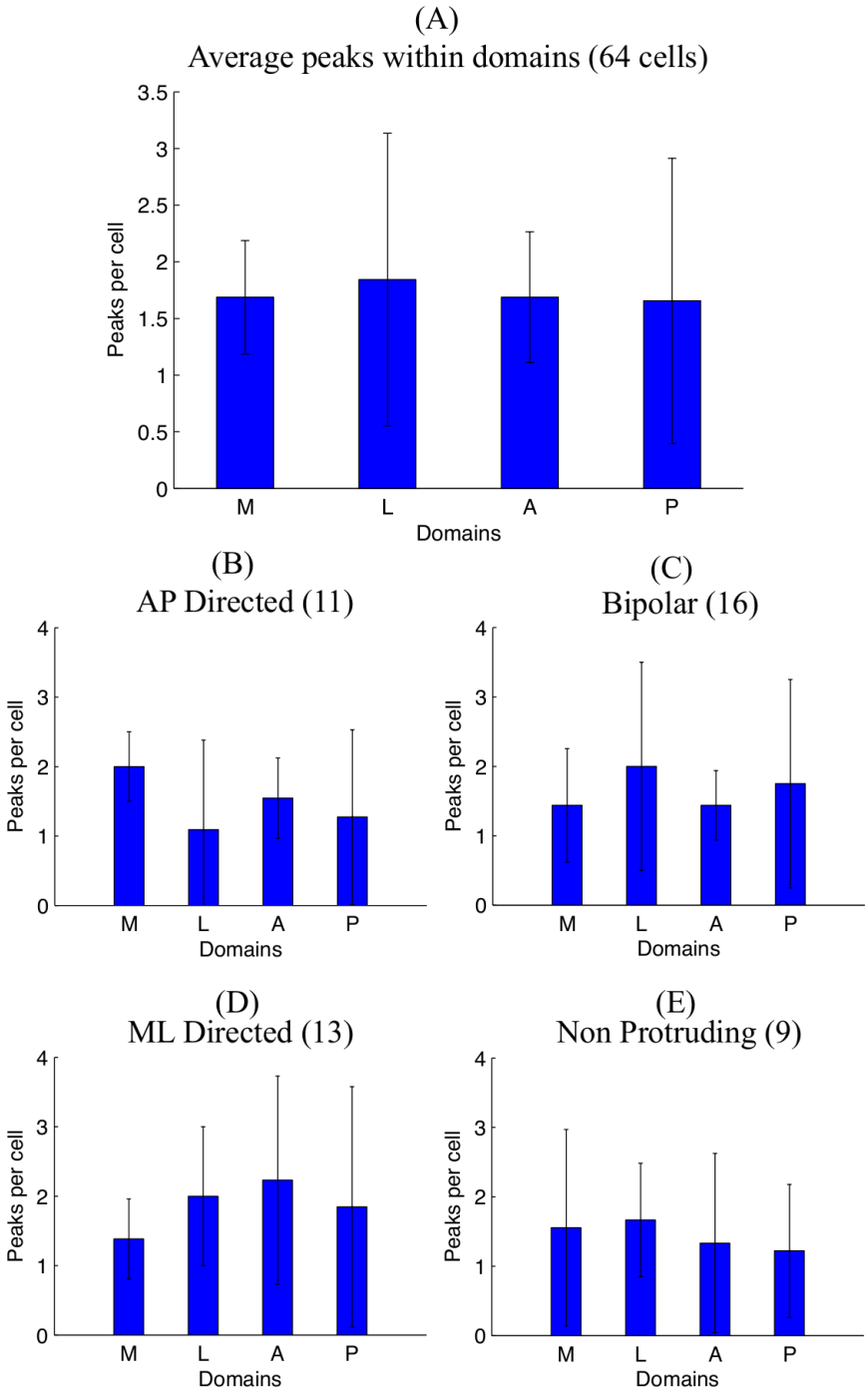

Figure 7.7: **Average number of Xdsh membrane clusters within domains.** The number of clusters were counted for each domains, and the mean computed for cells displaying the same directed elongation. (A) All 64 cells. (B-E) Breakdown of A into directed categories (as in Table 7.1).

Chapter 8

Discussion

8.1 ECMM: A Simple, High Speed Method for Quantifying Deformation

We have presented an improved version of the novel method for high resolution tracking of cell contours, ECMM, as published in our previous work [Tyson et al., 2009]. We reiterate that ECMM is computationally cheap compared to the level set method, solving the elliptical test case 16 times faster than the LSM with the simplest speed function. Furthermore, ECMM implementation in the Java language has achieved a further 30 fold increase in speed, and therefore allows long sequences of outlines to be mapped beyond real time, at high resolution.

The forward/reverse scheme prevents reduction of marker density in expanding sectors, and field strength can be used to tune marker paths without introducing complex speed functions. ECMM is therefore much better equipped for mapping large deformations, not encountered in applications of LSM by the Danuser lab Ji et al. [2008]; Machacek et al. [2009].

We enhance ECMM by replacing point charges with connected line charges, eliminating skewing of markers, improving stability, and allowing marker resolution to be increased beyond the field complexity with linear computational scaling. ECMM can now correct instances of invalid sectors, although the choice of solution may occasionally be inappropriate. Finally, we introduce a new co-ordinate system based on decimal position (DP) and marker origin (MO) which enables tracking of arbitrary positions on the outline, independently of marker position and resolution, throughout an entire sequence. Marker lineages always remain unbroken.

ECMM provides us with quantitative data that can be applied to rigorous testing of mathematical models. However, it is not a method that can currently be used to

model cell deformation by predicting movement. This is still the domain of the LSM which is extendable for use in mechanical models. For example, Yang et al. [2008] built a viscoelastic model to determine membrane forces, translated to membrane velocities by using a specialised LSM speed function.

8.2 ECMM in Light of Bleach Markers

Tracking of ECMM decimal positions as a cell migrates persistently in one direction, reveals that they gradually congregate to the cell's rear. To better understand the causes of this effect, and to validate mappings by ECMM, we created real life membrane markers in the form of bleach spots in the cAR labelled membrane of *Dictyostelium*.

Difficulties relating to imaging and photosensitivity of *Dictyostelium* limited the quality and quantity of data (similar issues were experienced by Traynor and Kay [2007] when attempting to bleach the tips of extensions), hence a gold standard for testing membrane tracking methods has not been fully realised.

Future attempts may consider the attachment of *sticky* fluorescent beads to the membrane which can be analysed using particle tracking [Godinez et al., 2007], although endocytosis of beads, and alterations in behaviour due to physical contact, would likely prove too problematic. A more promising approach maybe to correlate naturally occurring patterns of cAR fluorescence between images of neighbouring frames, eliminating the need for bleaching, or beads. This is similar to the approach of fluorescent speckle microscopy (FSM) Waterman-Storer et al. [1998], used to quantify cytoskeletal and adhesion protein turnover [Danuser and Waterman-Storer, 2006] and intracellular force from actin polymerisation [Ji et al., 2008]. FSM requires fluorescence images with a *speckled* appearance, achieved by having a very low fraction of labelled molecules relative to endogenous, unlabelled molecules. The translation of speckles can then be used to infer protein dynamics. Fluorescent cAR results in an intense, relatively evenly labelled membrane. Application of FSM would benefit from an alternative label that produces greater variability, for example Rac1A [Müller-Taubenberger et al., 2002].

Despite difficulties, several image sequences have provided useful insight into the true nature of membrane displacement during extension and retraction. Haastert and Bosgraaf [2009b] showed that pseudopodia occur at 90 degree angles to the cell surface. We can show that the centre point of a retraction behaves in a similar way, retracting along the inner normal direction. Yet, the nature of retraction causes tangential movement at the flanks. Similarly, bleach spots positioned within the flanking region of a pseudopodium showed the same tangential movement at the flanks, supporting results from Traynor and Kay [2007] (showing bleach spots move forward in

line with pseudopodia extension). If we assume that both flanks move at tangents, and that membrane within retracting regions behaves in a similar way to extending regions (both show tangential movement at the flanks), we are able to predict with some confidence, that if a bleach spot was successfully located at the focal point of a pseudopodia it would follow the outer normal direction.

Tangential movement is not unexpected considering the underlying structure of the membrane and cortex. Although membrane might be unfolded, or new membrane added by the active endocytic cycle, the increase in surface area during rapid expansion must (at least in part) come from membrane displacement. Neither ECMM or LSM are able to reproduce tangential movement, and this is highlighted by the existence of fixed points at the intersections of consecutive outlines. In ECMM, they form isolated sectors that can not flow into one another. In LSM, these are points where the speed function is zero, hence no movement occurs. The lack of tangential movement is the source of marker dilation in expanding regions, and compression in contracting regions. Ultimately, this results in the conjugating of decimal positions to a cell's rear as it moves persistently in one direction. Unlike LSM implementations, ECMM counters the loss of marker density by effectively inserting new markers using the F/R scheme while maintaing lineages.

In respect to simulation, a model by Neilson et al. [2010a] also suffered from being unable to produce tangential movement, disrupting the computation of PDEs at the membrane. Their solution was to use a parameterised finite element method Neilson et al. [2010b] which successfully produces tangential movement, but consequently introduces the same movement around the entire cell circumference. These shifts of markers in, for example, in the stationary rear would disrupt fluorescence measurements.

We stress that ECMM was not conceived to track the movements of specific molecules, or bundles of molecules, but to describe deformation for the purpose of making biologically relevant observations. For example, QuimP2 demonstrated that it is the ratio of myosin-II to F-actin that determines whether a pseudopodium will extend or retract [Bosgraaf et al., 2009]. We should also point out that all methods discussed here are computed in the 2D plane, within which we can only estimate the true to life movement.

8.3 Mechanisms of Blebbing in *Dictyostelium*

8.3.1 ECMM-APT Provides a Global View of Protrusion

ECMM-APT suffers from the presence of pseudo protrusions contained within motility maps. These emerge because of errors in image segmentation, which could be avoided

with better imaging technology and processing techniques. Cell displacements have proved equally difficult, particularly prolific at the rear due to global myosin-II contraction. This is where the body of the cell shifts as a whole, appearing as a retraction one side, and extension the other. Although these are true movements, ECMM can not yet distinguish between displacement and membrane extension.

Protrusion tracking is performed by following ECMM-tracking beginning at points of mid-extension, unlike Bosgraaf and Haastert [2009c] which relies on detecting patterns of curvature, or methods by Xiong et al. [2010] that use skeletonisation and changes in area, to compute protrusion location and speeds. The advantage of ECMM-APT, is that it is a fast, integrated method for both tracking and measuring membrane deformation, provides direct measurement of membrane velocity, and is sensitive deformations that may be very subtle, or exhibit odd patterns in curvature. Like pruning in skeletonisation methods, a certain amount of post-processing is needed to trim and join detected protrusions, but this is computationally inexpensive.

In spite of the non-trivial problems of segmentation and displacement (which hampers all current methods), ECMM-APT achieves a 96% true positive rate, and we have shown that the exhaustive approach by ECMM-APT can confirm, and expand upon, published findings.

The unbiased view presented in speed versus displacement plots clearly reveals that *Dictyostelium* migration is the result of two distinct mechanisms, identified as high speed, pressure driven blebs, and extension via actin polymerisation [Yoshida and Soldati, 2006]. ECMM-APT confirms low speeds for pseudopodia, and records a top blebbing speed of ($4.9\,\mu m/\,\mathrm{sec}$). This is greater than current values reported in *Dictyostelium*, perhaps due to cells responding to the resistive environment. The linear relationship seen between peak speed and displacement (consistent between frame rates) fits well with the idea of cortical and membrane tension simultaneously determining both these factors, as also suggested by laser ablation experiments by Tinevez et al. [2009], designed to induce blebs by damaging the cortex. These experiments revealed that the max size of a bleb strongly depends on tension. The combination of bleb kymographs and QuimP fluorescence measurements confirm the drop in F-actin in expanding blebs, the presence and degradation of an actin scar, and the rebuilding of a new cortex beneath a blebs surface.

We reproduced two observations of impeded migration in myosin-II essential light chain mutants, mlcE: 1) reduced speed of pseudopodia extension, supporting the hypothesis that hydrostatic pressure contributes significantly to pseudopodia extension speed, as well as blebbing [Chen et al., 1995; Kay et al., 2008]; 2) loss of the ability to produce high speed blebs [Cunningham, 1995; Kay et al., 2008].

Finally, as discussed by [Kay et al., 2008], we show blebs form at membrane regions most advanced in chemoattractant gradients during chemotaxis in *Dictyostelium*, and as discussed in subsequent sections, do so distinctly at the flanks.

8.3.2 Biological and Measurement Sources of Variability in Actin Scar Disassembly Half-Life

Kymographs of scar disassembly showed great variability, non-linear disassembly over time, and an apparent delay post nucleation. We might be able to account for these observations by considering the dynamics of, for example, the ADF/cofilin family (which disassemble actin filaments), and how the actin labeller, GFP-ABD, binds F-actin.

ADF/cofilin is thought to promote disassembly by binding filaments co-operatively (one cofilin per monomer) and lowering thermal stability by altering filament rigidity, leading to fracturing [Andrianantoandro and Pollard, 2006]. Fracturing exposes more pointed ends to disassembly. Fracturing probability is not only a function of cofilin concentration, but also filament length. As in the disassembly curve in Figure 6.14C, the relationship is non-linear, with number of severs decreasing as filaments shorten. This likely due to long filaments, and mechanics of an intact network, being needed to concentrate stress at flexing filaments [Cruz, 2009]. Cofilin also has a preference for older, ADP-actin, hence disassembly may be a function of filament age.

In relation to actin scars, varying degradation could therefore be the result of differences in F-actin density or filament length, cortex age, as well as the speed of recruitment of ADF/cofilin. However, our measure of half-life does not account for the apparent delay, and could easily be misinterpreted due to the dynamics of GFP-ABD.

F-actin cross-linking proteins, like fimbrin, contain two ABD domains that bind parallel filaments, forming a stable structure. A single ABD domain will still bind (interacting with only a single actin subunit), but with less affinity, ensuring cross-linking proteins are not *wasted* by binding single filaments. Hence GFP-ABD transiently labels F-actin. Importantly, fimbrin preferentially binds (or is incorporated) during polymerisation of ATP-actin [Volkmann et al., 2001], hence GFP-ABD may exhibit the same behaviour; preferentially binding newly polymerised filaments, but dissociating as they age, leading to a gradual loss of labelling, and possibly faster measured disassembly.

GFP-ABD dynamics may also explain the delay in disassembly, given that severing initially long, cross-linked filaments may not necessary cause their immediate translocation from the cortex, or dissociation of the label. However, the signals that promote scar disassembly are unknown, and may have a *built in delay*, perhaps to maintain structural rigidity during bleb expansion and/or cortex reassembly.

Our analysis of disassembly needs to be expanded to greater numbers, include

fitting of disassembly curves, and correlation with factors that may affect disassembly, such as curvature.

8.3.3 Retrograde Shift of the Actin Scar Caused by Cortex Contraction

We are yet to develop an automated approach to characterise actin scar dynamics. Correlation of the size of the shift with bleb speed, displacement, and volume would allow for much greater insight. It should also be noted that the kymograph represents only a central cross-section through a bleb, and as such does not indicate how the actin scar deforms along its entire length. Observation by eye, suggests the scar curves inwards at its centre, while the sides of the scar, close to where membrane is still attached, shift less. Measurement of this curve may provide data for modelling the mechanical properties of the cortex in terms of its lateral rigidity.

The porous nature of the cortex makes it improbable that the shift results from growing pressure within a bleb. The shift is more likely caused by force from actin-myosin cortex contraction, implicated in providing inward force to increasing tension on the cortex-membrane interface, and breaking tethers. This hypothesis was proposed by Maugis et al. [2010], whereby on tether breakage and release of tension, the cortex contracts inwards.

This hypothesis relies on the assumption that under normal conditions the membrane provides resistance to cortex contraction. However, it does not fully explain our observations on bleb nucleation in concave regions, as discussed in the next section.

8.3.4 Effects of Membrane Curvature on Blebbing

Blebs are thought to occur due to the weakening of membrane-cortex adhesion, which can then be overcome by the force of intracellular pressure. A weakening could result from the reduction in availability of ERM binding sites, via reduction in PtdIns(4,5)P_2 at the membrane, or local F-actin disassembly at the cortex. However, disassembly intensity profiles do not show any dramatic reduction in F-actin prior to bleb nucleation, and at the leading edge, where PtdIns(4,5)P_2 should be most depleted, we see a lower frequency of blebbing. Although weakening may exist, we show that blebs are more likely to occur in concave membrane regions, with larger blebs observed under greater concavity, suggesting that it is the building of tension which is of greater importance. Similarly, Maugis et al. [2010] observed that amoeba cellular blebs exhibit large velocities in concave regions, but could not test the effects of concavities experimentally, and as such excluded it from their model.

Our observations raise two questions for discussion; 1) How do concave regions promote the nucleation of blebs; 2) How may inward curvature influence bleb peak speed and displacement? We propose that both these questions can be addressed by considering how membrane and cortex tension may differ in concave regions, given theoretical models presented in current literature by Charras et al. [2008] and Brugués et al. [2010].

Brugués et al. [2010] present a theoretical model for the failure of cortex-membrane adhesion, guided by micropipette aspiration experiments. Cortex tension in a convex region results in an inward force, and is defined as a function of cortex thickness and positive curvature. Outward force, resulting from intracellular pressure, is experienced in its majority by the plasma membrane, rather than the permeable cortex. These opposing forces induce tension on the cortex-membrane interface. At some critical tension, which is proportional to surface curvature, membrane tethers rupture, and a bleb forms. Curvature in this case refers to convexity, but within concave regions these forces may be very different.

Let us first consider an isolated lipid bilayer, similar to a vesicle. The bilayer will assume the lowest energy state of a sphere, in which the surface is of uniform tension and positive curvature. Membrane tension in concavities will therefore act to push out the membrane and restore uniform curvature. Intra and extracellular pressure, assuming it is homogeneous, will also act uniformly and produce a spherical shape, pushing concave regions outwards. If we then introduce a contractile, actin-myo cortex, required for building intracellular pressure, it too will assume a spherical shape when contracting. This *rounding* effect is seen in the case of *Dictyostelium* undergoing initial contraction prior to movement [Dalous et al., 2008; Bosgraaf et al., 2009], and in the cringe response [Etzrodt et al., 2006]. Additionally, using adhesive micro-patterns, Théry et al. [2006] showed that epithelial cells placed on patterns containing concavities, shape themselves as to find the shortest distance between apices (by forming stress fibres), but inhibiting myosin function caused cell borders to follow the concave shapes. Although *Dictyostelium* does not form stress fibres, myosin contraction may similarly function to remove concavities.

A concave structure, given its inherent properties of expansion, therefore provides a much more favourable membrane configuration for blebbing, but also protrusion extension in general. However, as cortical tension also likely acts to remove concavities, creating a force imbalance to stress tethers requires cortex tension to oppose intracellular pressure and membrane tension. The scar retrograde shift we have observed, apparent in blebs nucleated in concave regions, implies significant inward force, which cannot result from cortex tension due to curvature, as this likely acts to push out-

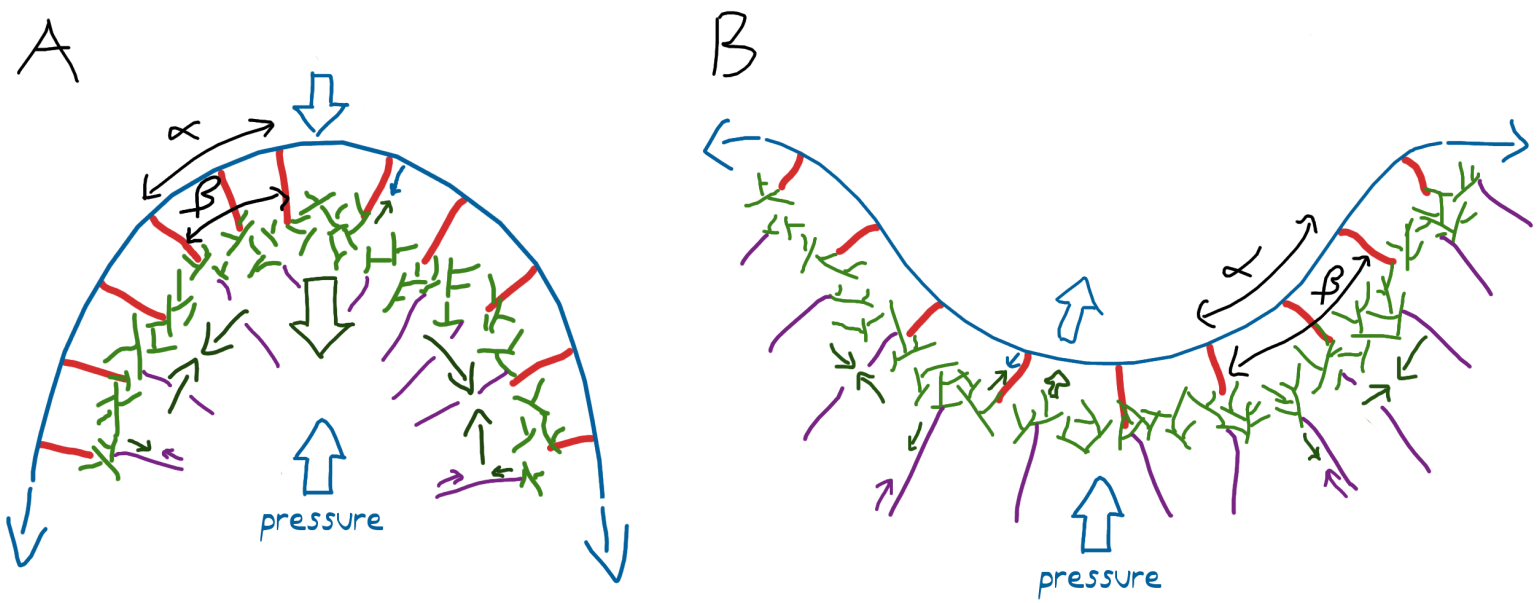

Figure 8.1: **Sketch comparing convex and concave membrane mechanics.** (A) Convex membrane (blue) supported by a branched actin cortex (green). The membrane is tethered by ERM homologues (red). Arrows indicate tension within the membrane, cortex, and links with the greater intracellular structure (purple), possibly focal adhesions. Membrane tension and extracellular pressure produces a net inward force, opposing bleb formation. Similarly, cortex tension results in inward force. This force arrangement reduces the likelihood of tether breakage. (α) and (β) demonstrate the difference in tether linkage density across the membrane and cortex, destiny being higher at the cortex. (B) Concave membrane and cortex structure. Membrane tension produces a net outward force, facilitating blebbing. Cortex tension also produces outward force, but this may be counteracted by tension with the greater intracellular structure, leading to a greater build up of tension on tethers. Notably, the tether density at (α) and (β) is reversed, although the significants of this on tether breakage is unclear.

wards (as opposed to inwards at convex membrane). To explain the retrograde shift, and stress in membrane-cortex tethering, we have to consider structures which hold concave regions inwards, preventing them from *popping* outwards.

The process of phagocytic cup formation must overcome similar outward cortical tension resulting from increased surface area as a particle is surrounded by membrane. The force to generate convexity, working against tension, is that of actin polymerisation, forcing membrane around the sides of a particle. There is a limit to the tension that can be worked against, and it is thought that the unfolding or addition of membrane at the site of engulfment is abel to relieve membrane tension [Clarke et al., 2010]. In a similar fashion, cortex tension must also be minimised.

We consider that the actin cytoskeleton is a relatively rigid structure that can store mechanical stress by transmitting force from the cortex to other regions of the cell, and to focal adhesions. For example, when extending a pseudopodium via actin polymerisation, links to the whole cortex are required to provide the rigidity to push against, and prevent actin retrograde flow (known not to occur in *Dictyostelium* pseudopodium extension). Focal adhesions, formed during extension, are also required for stabilisation, preventing the pseudopodium being retracted by cortex/membrane tension. Swimming cells are also able to form rigid pseudopodia which become backward moving *bumps*, and function as paddles [Haastert, 2011].

This force transition could play the same role in stabilising concave membrane regions, which are continually formed at the flanks of pseudopodia in both blebbing and non-blebbing cells. The scar retrograde shift would therefore result from elastic properties of the actin cytoskeleton storing tension from focal adhesions, or other regions of cortex, intended to hold concave regions stable. In fact, we may hypothesis that focal adhesions nearby concavities are a requirement for bleb nucleation, and hence would limit nucleation in the z-axis to regions of substrate contact. To investigate we would need z-stack data, or an otherwise sideways view (we may possibly be able to inferrer the 3D positioning of bleb nucleation using 2D DIC images, as in the DIAS system [Wessels et al., 2006]).

The sketches in Figure 8.1 compare forces in concave and convex regions, and although not intended to depict the precise mechanics, we intend to use the ideas they convey to build an *in silico* model to test our observation of increased bleb nucleation in concavities.

8.3.4.1 Determining Bleb Speed and Halting Expansion

During initial bleb expansion from a concave region, surface area does not increase, as would be the case if a bleb emerged form a convex region. Instead, surface area drops

following tearing from the cortex, lowing membrane tension. Less tension would allow a bleb to expand faster in proportion with greater convexity, precisely what we observe in curvature versus speed scatter plots. This is opposed to blebs emerging from convex regions, where expansion increases surface area, and therefore tension, lowering bleb speed and displacement.

Bleb expansion could be halted by either the rebuilding of the cortex, dissipation of pressure, or an increase in membrane tension that eventually exceeds the force of intracellular pressure. Because of the high speed nature of blebbing in *Dictyostelium*, compared to, for example M2 cells, it is unlikely that cortex reassembly halts expansion. Given the relationship between bleb speed and membrane curvature, it is probable that membrane tension is responsible, coupled with a drop in pressure. However, pressure is unlikely to drop significantly as blebs are seen to occur simultaneously, and in quick succession.

8.3.4.2 Regulation of Tether Strength

Although the mechanical aspects of curvature appears to be very important, we cannot rule out influences on tether strength. Reduction in PtdIns(4,5)P_2 may weaken ERM binding at the leading edge, but many membrane binding proteins are known to have a higher affinity for specific membrane curvatures (for example, the BinAmphiphysinRvs domain binds lipids closest to its intrinsic curvature [Peter et al., 2004]), and hence curvature is considered important for creating membrane domains [McMahon and Gallop, 2005]. Tethering could be one such an example, with ERM protein binding becoming less favourable in concave structures, lowering the tension required for breakage. During phagocytosis, actin polymerisation is directed actively to sites of curvature, so we cannot rule out an active response to curvature [Clarke et al., 2010].

We should also consider how tether density may change between convex and concave regions. Charras et al. [2006] showed that GFP tagged ezrin in M2 cells was absent from the membrane during expansion, suggesting it is the membrane link that is broken (as opposed to the cortex link) leaving ezrin behind a the site of nucleation. Ezrin was observed to be recruited before actin in rebuilding of the cortex, suggesting the amount of exposed membrane determines the density of linkages. In concave regions, tether density (links per square micron) may be higher at the membrane than those links to the cortex, and *vice versa* in convex regions (see lengths marked α and β in Figure 8.1). Potentially, linkage density could affect how tether tension is spread, becoming more concentrated at the membrane in concave regions, and more dispersed in convex regions.

Although changing tether density between curvatures could be a factor in nucle-

ation, the ideas above would favour nucleation in concave regions. However, we are unaware of data that could shed light on tether density in these two cases, and are left to infer it from the ratio of cortex length to membrane length. Neither do we know how ezrin localises in blebbing in *Dictyostelium*.

As a final note on tethering, we might consider the links ERM proteins form as being transient, and created in a stochastic manner. Rather than have stable tethers, like a mechanical scaffold, we imagine a random process, where by chance the amount of linkages drops locally below a threshold required to counter outward forces. This may explain why we see blebs nucleate at very specific positions, rather than more haphazard tearing over longer stretches of membrane. Of course, blebs may simply nucleate at positions where cortex-membrane tension peaks (for example, the base of a concavity), but we make this point to acknowledge that we are not dealing with, say the scaffolding around a building, but a highly dynamic structure which is continually changing. Future models must keep this in mind, particularly if using mechanical rods and springs.

8.3.5 How Blebbing is Directed to the Flanks

The absence of blebbing at the rear can be well explained by the presence of dense actin filaments required for myosin-II contraction, and maintained levels of PIP2, both contributing to strong cortex-membrane adhesion as a result of ERM protein tethering Laevsky and Knecht [2003]. However, we have also observed blebbing to be absent at membrane regions most advanced in the gradient, which are typically where a pseudopodia is extending, or has extended previously.

We observed blebs seamlessly preceding actin driven protrusions, but never the reverse case, presumably because the curvature following a pseudopod creates high membrane tension due to the rapid remodelling of the cytoskeleton during actin polymerisation. Langridge and Kay [2006] demonstrated that a partially inactivated Arp2/3 complex in *Dictyostelium* leads to greatly increased blebbing, concluding that blebbing is inhibited by actin dynamics. This inhibition could be accounted for by pseudopod extension at the leading edge causing curvature that is detrimental to bleb formation, while new pseudopodia can formed and be maintained unhindered via splitting [Bosgraaf and Haastert, 2009b]Andrew and Insall [2007]. Contrary, pseudopodia extension, often generates concave membrane curvature either side of the site from which it emerged [Bosgraaf and Haastert, 2009c], which produces ideal conditions for bleb nucleation, as discussed above. In this case, pseudopodia extension would contribute to the energy for bleb expansion by being the driving force in creating negative membrane tension.

Counter to this idea, is that break down of the cortex prior to F-actin polymerisation (via the action of ADF/cofilins), should weaken cortex-membrane adhesion and promote blebbing [Bamburg et al., 1999; DesMarais et al., 2004]. In the same fashion, inhibiting filamin, or treating cells with drugs that promote depolymerisation of the cortex, can induce blebs [Cunningham et al., 1992; Keller et al., 2002]. We propose that these effects may contribute, enhancing the polarisation of blebs, but it requires Arp2/3 to be absent at the site of bleb formation, as was shown to be the case in M2 cells [Charras et al., 2006].

An important question is why directing blebbing to the flanks is an advantage in *Dictyostelium* chemotaxis. Because blebs generally extend normal to the membrane (membrane tears from the cortex evenly either side of the nucleation location), flanking blebs are not directed in the direction of the gradient, similarly to pseudopodia in *Dictyostelium* lacking the Diaphanous-related formin dDia2, or the proposition that membrane curvature dictates the direction of extension [Haastert and Bosgraaf, 2009b]. We hypothesise that blebs help provide *space* into which the cell body can advance by opening up resistive extracellular matrices, rather than contributing to ascend the gradient directly.

8.3.6 Reduced Blebbing in Pikl and PI3K Mutants Due to Disrupted Chemotaxis

Considering the role of PtdIns(4,5)P_2 in maintaining ERM cortex-membrane adhesion, we can make some predictions as to how blebbing would be effected in PI3K KO and Pikl mutant strains. A PI3K mutant is unable to generate a PtdIns(3,4,5)P_3 gradient [Hoeller and Kay, 2007], leaving PtdIns(4,5)P_2 levels unaltered. Therefore, cortex-membrane adhesion by ERM proteins should remain unaltered, and reduce blebbing [Bretscher et al., 2002]Hao et al. [2009]. Our observations support this prediction as there is little evidence for blebbing in comparison with data collected from wild type cells.

However, following the same argument, Pikl mutants would have reduced levels of PtdIns(4,5)P_2, given its role of PtdIns(4,5)P_2 production from the precursor PtdIns(4)P, but we observe almost identical results to the PI3K KO strain.

This may be due to the poor quality of data, but possibly cell damage and unfavourable experimental conditions. Mutant strains are visibly less healthy than the wild type, presumably because PtdIns(4,5)P_2 is important for many other cellular processes (Hoeller and Kay [2007] showed that careful treatment of mutant strains is required to observe true activity). As such, reduced blebbing in both mutants could be the direct result of hindered ability to polarise, effecting the amount of pressure

build up, and the maintenance of pseudopodia, hypothesised to create concavities to promote blebbing. Our results show reduced elongation and shorter protrusions, in line with the results by Hoeller and Kay [2007] showing 42% reduced chemotaxis rate in PI3K KO, and observations by the Kay lab of impaired chemotaxis in Pikl mutants (unpublished).

The relative levels of PtdIns(4,5)P_2 in these mutants may be negligible in terms of its effect on blebbing, in comparison to failure in building pressure and forming concave curvature. We must also consider that there are other redundant pathways for PtdIns(4,5)P_2 production, such as the Type II PI(5)P-kinase, which may compensate for low PtdIns(4,5)P_2 levels in the Pikl KO strain [Rameh et al., 1997], making interpretation of data much more complex.

8.3.7 Furthering the Analysis of Blebbing

Given the magnitude of data we can obtain on protrusions using QuimP there are numerous other avenues for analysis. There are several examples in the literature where the pattern of protrusions have been studied, suggesting an ordered splitting of pseudopodia during random amoeboid movement [Bosgraaf and Haastert, 2009b; Xiong et al., 2010], and biased maintenance of random protrusions in shallow gradients [Andrew and Insall, 2007]. Maugis et al. [2010] demonstrated periodic bleb formation, although at random locations. Similarly, we may discover that blebs are produced following a integrated pattern with actin driven protrusions, or are dependant on events at other times and locations [Charras et al., 2008].

Patterns in bleb size may become apparent, for example, due to the requirement to re-elevate hydrostatic pressure, the size of concurrent blebs might be reduced [Tinevez et al., 2009]. If a dependence on bleb separation is seen, it may reveal if pressure can be localised within *Dictyostelium* as described by the poro-elasticity model of the cytoplasm [Charras et al., 2005].

Most significantly data from ECMM-APT can be used to inform quantitative models. For example, Tinevez et al. [2009] modeled how cortex tension drives blebs in L929 cells, the cortex modelled as an active elastic material. Similarly, Maugis et al. [2010] developed a quantitative model of intracellular pressure, containing parameters for membrane-cytoskeletal stress, actin turnover time, and myosin contraction, and was able to correctly predict the periodic extension of blebs in *Entamoeba histolytica*. Applying the same modelling techniques to study membrane tension in concave regions would likely demonstrate increased probability of blebbing, predict how curvature might affect bleb speed, size, and breadth. We could attempt to demonstrate how blebbing is restricted to the cell flanks based solely on mechanical stresses resulting from curvature,

and incorporate this model of blebbing with those of pseudopodia (for example, the model by Neilson et al. [2011]).

ECMM-APT will benefit from improvements in detecting and/or incorporating displacement into ECMM tracking, greatly reducing false positives. Curvature maps could be used to improve detection of protrusions occurring simultaneously in close proximity as demonstrated in Figure 8.2.

Finally, real benefit could be made by creating an automated classifier that can identify blebs, removing the analysis bottle neck. A simple classifier, based on support vector machines, was applied to measures of bleb speed, drop in GFP-ABD fluorescence, and curvature, but failed to reach a usable accuracy because of the strong overlap of bleb and pseudopodia measures.

8.4 QuimP Software Applications and Outlook

The version of QuimP presented in Chapter 5 has been downloaded by over 50 parties worldwide. The active contour, although relatively simple in comparison to other implementations in the literature, has performed consistently well in the past, but now boasts an interactive GUI for supervised segmentation and manual correction. This greatly improves the ease at which a good segmentation can be attained. ECMM is fully incorporated in the ImageJ implementation, and provides an improved method for sampling fluorescence intensities. QuimP is accompanied by a set of Matlab based scripts that were utilised in all the example applications presented in Chapter 7.

Attaining true high through-put analysis with QuimP is still somewhat limited by segmentation and lack of 'batch analysis' options. Although parallel segmentation is possible, the current implementation can introduce distortions at cell boundaries that need manual correction, and QuimP must be run separately for each cell once segmented.

The need for additional software to aid analysis by users unfamiliar with the details of QuimP's implementation, has proved imperative due to the wide range of applications. This remains a drawback because of the quantity of data output by QuimP, the apparent complexity of the tracking data, and need for scripting ability. We hope to tackle this issue by providing more example analyses, and expanding on scripts already available, making them simpler, and in open source languages. We also recognise the need for efficient exploration of data analysis to discern general trends, features of interest, and assess data quality. This is particularly challenging when viewing large quantities of high-throughput data, as output by QuimP. The QuimP Explorer (QE), developed by Ingrid Tigges (PhD student, Warwick Systems Biology

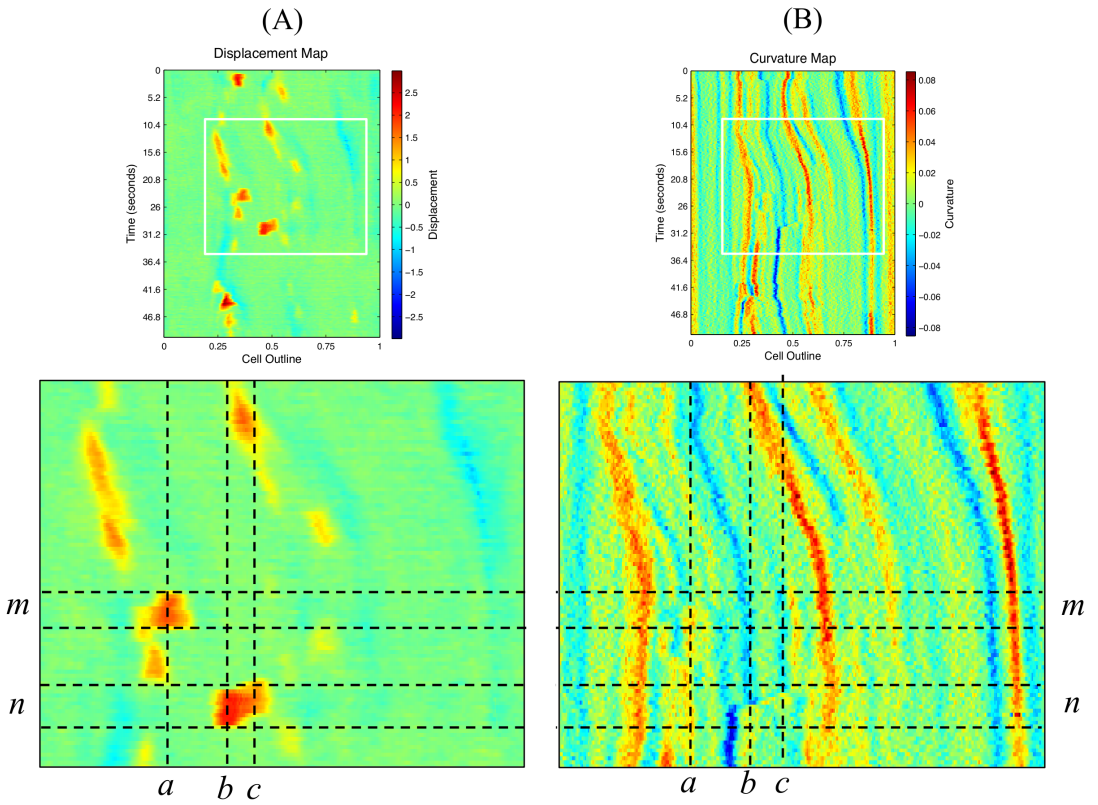

Figure 8.2: **Complex patterns of curvature during blebbing.** (A) Displacement map and close up. Vertical lines *a, b* and *c*, mark the centre of blebs, *b* and *c* occurring in close proximity, and becoming merged. Horizontal lines *m* and *n* are a guides to bleb start points. The pattern of spatial-temporal pattern of convexity reveal *b* and *c* to be separate protrusion events, while regional maxima transforms will identify only a single protrusion.

DTC), is an interactive MATLAB graphical user interface that facilitates manipulation and visualisation of methods and data structures, and will be made available for the next release.

Regrettably, the current release is missing an ECMM-APT implementation due to time constraints, but the current MATLAB prototype will be converted into an ImageJ plug-in in the near future.

A significant avenue for development is in expansion to three dimensions. As technology improves, 3D data will become more common, and is already key for studying motility in *in vivo*, such as the cancer invasion [Decaestecker et al., 2007; Gadea et al., 2007]. This will require a 3D active contour, like that of Dufour et al. [2005], and extension of ECMM to 3D. Because ECMM is based on real world 3D electric fields, conversion to 3D is very feasible, on condition that field forces resulting from triangular planes can be efficiently computed.

We also propose that ECMM has the potential to evolve past the use of intersection points, and towards altering forces to simulate translational effects. For example, placing a large charge in the direction of movement would *drag* markers, within flanking regions, in the general direction of the extension. This could be made proportional to the speed at which an extension is moving at its very tip. Alternatively, we could mechanically couple neighbouring markers (akin to an active contour) and allow fast moving markers greater ability to drag their neighbours along with them. Ultimately, we envision the possibility of using ECMM as a boundary propagation method for simulation purposes, that is faster than LSM, applicable to 3D, and can re-create tangential movement.

Chapter 9

Conclusions

The primary aim of this thesis was to fundamentally alter how QuimP quantifies local cell membrane deformation to study the mechanics of blebbing in chemotaxing *Dictyostelium* cells.

The novel Electrostatic Contour Migration Method has been improved over the version published during the course of this PhD project, and now uses lines of charge for fast, even mapping of markers between cell outlines. It completely fulfils the brief of surpassing the drawbacks and computational complexity of the level set method, which is typically used in the literature.

Bleaching experiments, designed to validate mapping methods, clearly demonstrates that membrane displaces tangentially during deformation, highlighting issues with purely mathematical methods containing fixed points during boundary propagation. However, examples of retraction events allow the inference that membrane moves perpendicular to the surface at a protrusion's centre, and as such match tracks computed by ECMM.

ECMM is now fully integrated into a new version of QuimP (QuimP11), rewritten from the ground up for better speed, stability, and inclusion of new features. QuimP11 is freely available for download, with accompanying analysis scripts. Paper preparation with collaborators in London and Cambridge is ongoing, in which analyses from Quim11 (and ECMM-APT) are key for assembling complete stories for publication.

Decimal position tracking allows cell protrusions to be traced fully automatically, based purely on local membrane speed characteristics, rather than curvature, or other bias features. ECMM-APT correctly identified 96% of cellular protrusions. Furthermore, the conception of ECMM displacement maps permits comparable tracking at different frame rates using very few algorithm parameters, all directly relevant to real

world measures (microns and seconds).

Hundreds of protrusions can be tracked, and measures made by QuimP compiled together to build a picture of global cell protrusion characteristics. Two distinct groups of protrusions were identified within *speed versus displacement* scatter plots, pseudopodia and blebs, revealing a linear relationship of bleb speed with displacement. Significantly, blebs emerge predominately from concave membrane, and attain the highest speeds of expansion within highly concave regions. From this data we have learned about possible mechanisms that couple the membrane and cortex, and have generated hypothesise concerning the importance of concave curvature in increasing tension on tethering proteins at the membrane-cortex interface.

From protrusion tracks, one can easily create plots of protrusion distributions around a cell, and in relation to chemical sources. Blebbing is directed to positions flanking the leading edge highest in a cAMP gradient. This distribution provides a role for pseudopodia in driving changes in curvature via local membrane extension, suggesting actin polymerisation might be equally important for bleb nucleation in *Dictyostelium* as intracellular pressure. These observations highlight the advantages of having access to a variety of measures from the same data source, putting observations into global context without having to invest many hours into manual analysis. For example, tracks were also used to automatically extract kymographs, which led to the discovery of unexpected retrograde shift of actin scars.

Although data regarding mutants was limited, ECMM-APT made plainly apparent the inability to bleb, and reduction in pseudopodia speed, known to hamper myosin-II KO strains, and did so using only negative stain image sequences.

We have not completely exhausted the possible avenues for analysis for the current data, and have raised many questions for further study throughout our discussion. In parallel with this continued analysis, we want to further develop ECMM for mapping in 3D, and investigate methods to simulate tangential movement, while also improving QuimP's segmentation (particularly parallel segmentation), and provide the community with improved tools for analysis of QuimP data.

Appendix A

Automated Protrusion Analysis

A.1 Protrusion Tracking

A.1.1 Path Resolution Reduction

Given a path, P, composed of N two-dimensional image co-ordinates, a new path, $P^n \subset P$, is determined by implementing the following algorithm:

$P_0^n = P_0$
$i \leftarrow 1$
while $i \leq N - 1$ **do**
  $j = i + 2$
  while $j \leq N - 1$ **do**
    $a =$ Area of the polygon formed by$[P_i, P_{i-1}...P_{i-k}]$
    if $a >$ threshold **then**
      Add P_{j-1} to P^n
    end if
    $j \leftarrow j + 1$
  end while
  $i \leftarrow i + 1$
end while

A.1.2 Decision Tree Determining the Cutting of Protrusion Paths

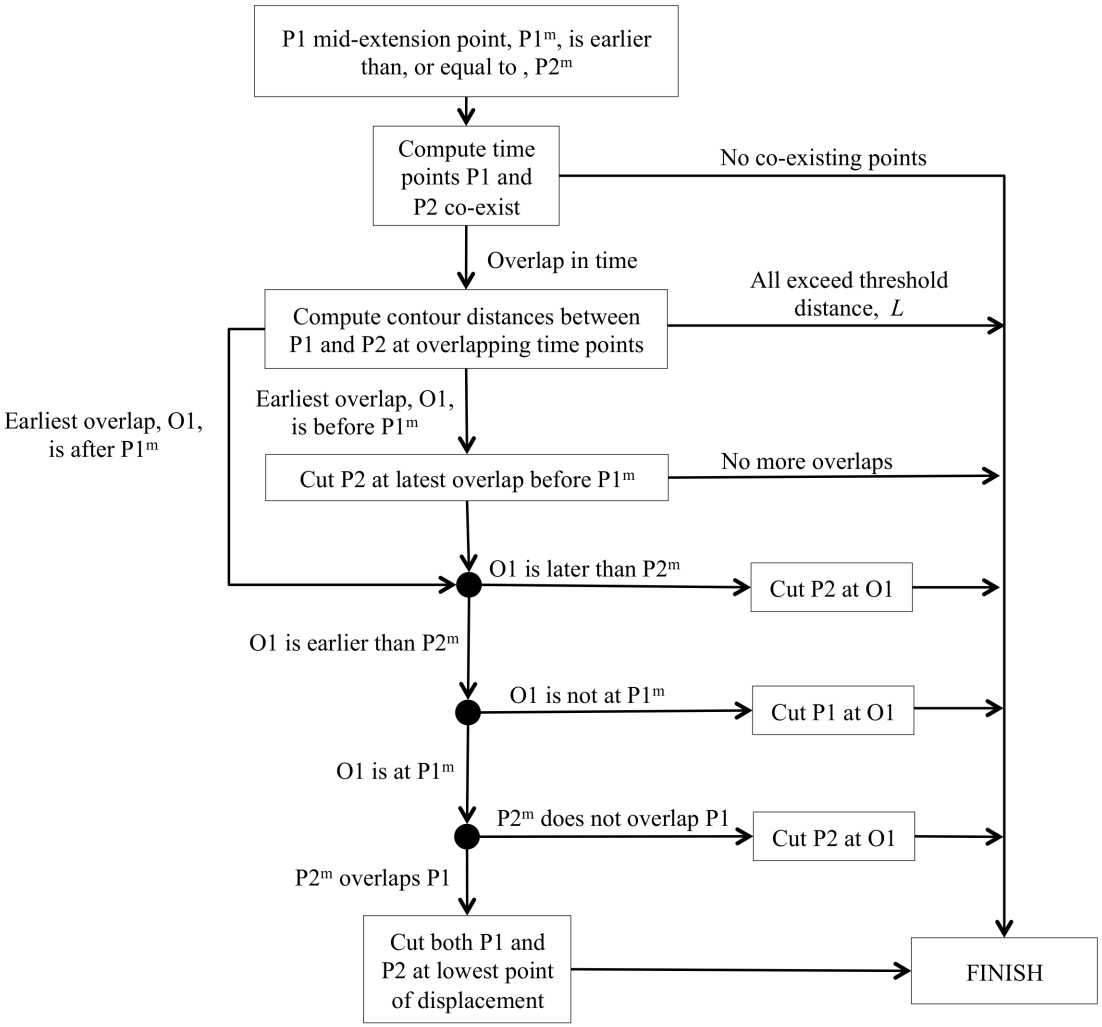

Figure A.1: **Decision tree determining the cutting of ECMM-APT protrusion tracks P1 and P2.** Protrusion mid-extension points for P1 and P2 are labelled P1^m and P2^m respectively. A position in P1 is defined as overlapping with position in P2 if they exist at the same time point (aligned horizontally on ST-maps) and are within a threshold distance of L along the cell's outline (vertical alignment). The earliest such overlap is represented as O1. When *cutting* a track, only the part containing the mid-extension point is retained. Figure 2.4 (page 39) provides three diagrammatic examples of overlap correction.

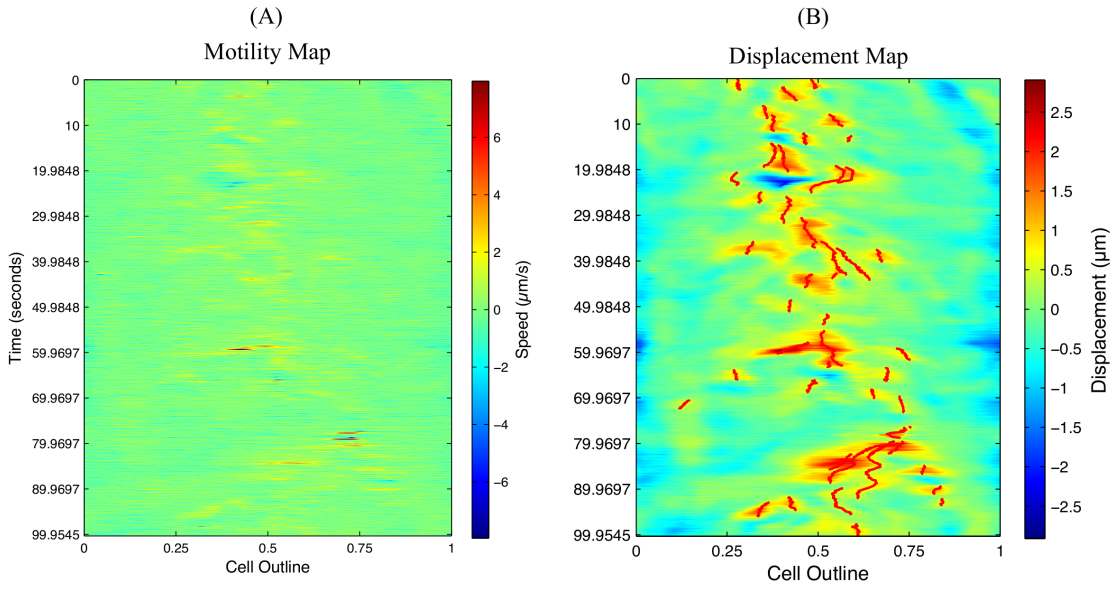

Figure A.2: **Protrusions resulting from ECMM-APT applied to a Pikl mutant cell.** (A) Motility map of Pikl mutant cell. (B) Protrusions computed by from ECMM-APT. In cases where segmentation is poor, either due to low contrast or the cell leaving/re-entering the plane of view, and noise is high, ECMM-APT is still able to identify cell protrusions, although false positives may occur.

A.2 Results Tables: Ax2 Manually Generated Protrusion Tracks

A.2.1 Protrusion Counts: Manual

Experiment	Num. Cells	Frame Rate (fps)	Total Seq. Duration (sec)	Traced Protrusion Count
1.1 Ax2	7	2	676.00	Bleb: 20
1.2 Ax2	6	2	549.00	Bleb: 21
1.3 Ax2	5	2	388.50	Bleb: 18
1.1-3 Ax2.	18	2	1613.50	Bleb: 59
2. Ax2	12	4.54, 4.16*	912.74	Actin D: 22 Bleb: 12 Bleb-Actin D.: 4 Bleb-Bleb: 5

* Sequences are either 4.54 fps or 4.16 fps

Table A.1: **Manually traced protrusions in Ax2 cells.** Contains the number of protrusions manually traced in all Ax2 sequences (*Bleb-Actin D* represents blebs followed immediately by deformation by actin polymerisation. Similarly, *Bleb-Bleb*, are multiple blebs occurring on top of one another).

A.2.2 Protrusion Measures: Manual

Experiment	Prot. Type	Peak Speed (μm/ sec)	Max Peak Speed (μm/ sec)	Displacement (μm)	Curvature (normalised)	ΔCurvature (normalised)	GFP-ABD drop (%)
1.1 Ax2							
	Bleb	1.44 (±0.77)	3.20	0.99 (±0.40)	-0.010 (±0.080)	0.231 (±0.085)	54.6 (±24.3)
1.2 Ax2							
	Bleb	1.45 (±0.76)	3.40	1.12 (±0.47)	-0.057 (±0.082)	0.256 (±0.069)	58.4 (±18.5)
1.3 Ax2							
	Bleb	1.93 (±1.12)	5.00	1.21 (±0.58)	-0.081 (±0.151)	0.245 (±0.075)	73.3 (±15.6)
1.1-3 Ax2							
	Bleb	1.52 (±0.90)	5.00	1.10 (±0.48)	-0.048 (±0.108)	0.244 (±0.076)	61.6 (±21.1)
2. Ax2							
	Actin D.	0.51 (±0.21)	1.15	5.66 (±3.63)	0.100 (±0.100)	0.347 (±0.117)	15.5 (±16.7)
	Bleb	2.62 (±1.36)	4.93	1.78 (±0.53)	-0.124 (±0.104)	0.318 (±0.073)	78.0 (±6.3)

Table A.2: **Measures from manually traced protrusions in Ax2 cells.** See Table A.1 for counts.

A.3 Results Tables: Ax2 ECMM-APT Generated Protrusion Tracks

A.3.1 Protrusion Counts: ECMM-APT

Experiment	Num. Cells	Frame Rates (fps)	Total Seq. Duration (sec)	Protrusion Count	Protrusion Rates
1.1. Ax2	7	2	676.00	Actin D: 90 Bleb: 30 Bleb-Actin D.: 15 Bleb-Bleb: 0 Unidentifiable: 7 False Positive: 5 False Negative: 4	All Prot: 0.003320 Actin D.: 0.002455 Bleb: 0.001052
1.2. Ax2	6	2	549.00	Actin D: 73 Bleb: 45 Bleb-Actin D.: 19 Bleb-Bleb: 1 Unidentifiable: 5 False Positive: 10 False Negative: 8	All Prot: 0.003742 Actin D.: 0.002408 Bleb: 0.001701
1.3. Ax2	5	2	388.50	Actin D: 53 Bleb: 32 Bleb-Actin D.: 10 Bleb-Bleb: 0 Unidentifiable: 3 False Positive: 2 False Negative: 3	All Prot: 0.003516 Actin D.: 0.002260 Bleb: 0.001507
1.1-3. Ax2	18	2	1613.5	Actin D: 216 Bleb: 107 Bleb-Actin D.: 44 Bleb-Bleb: 1 Unidentifiable: 15 False Positive: 17 False Negative: 15	All Prot: 0.003518 Actin D.: 0.002388 Bleb: 0.001396
2. Ax2	12	4.54, 4.16	912.74	Actin D: 88 Bleb: 37 Bleb-Actin D.: 5 Bleb-Bleb: 0 Unidentifiable: 6 False Positive: 5 False Negative: 4	All Prot: 0.002141 Actin D.: 0.001464 Bleb: 0.000661

Table A.3: **ECMM-APT protrusions in Ax2 cells.** Contains the number of protrusions detected automatically by ECMM-APT in all Ax2 sequences (*Bleb-Actin D* represents blebs followed immediately by deformation by actin polymerisation. Similarly, *Bleb-Bleb*, are multiple blebs occurring on top of one another).

A.3.2 Protrusion Measures: ECMM-APT

Experiment	Prot. Type	Peak Speed (μm/ sec)	Max Peak Speed (μm/ sec)	Displacement (μm)	Curvature (normalised)	ΔCurvature (normalised)	GFP-ABD drop (%)
1.1 Ax2.	Actin D.	0.67 (±0.28)	1.86	2.42 (±2.09)	0.246 (±0.179)	0.076 (±0.121)	19.3 (±19.1)
	Bleb	1.17 (±0.67)	2.86	1.12 (±0.44)	-0.050 ±0.124)	0.126 (±0.060)	40.6 (±31.6)
	Bleb-Actin D.	0.78 (±0.21)	1.06	1.83 (±0.71)	0.030 (±0.155)	0.201 (±0.092)	38.7 (±25.0)
	Bleb-Bleb	NA	NA	NA	NA	NA	NA
	Unidentifiable	0.81 (±0.66)	2.15	1.46 (±1.55)	0.060 (±0.143)	0.118 (±0.060)	21.3 (±23.4)
	False Positive	0.94 (±1.44)	3.52	0.94 (±0.53)	0.021 (±0.301)	0.044 (±0.033)	11.3 (±13.7)
1.2 Ax2.	Actin D.	0.70 (±0.28)	1.46	3.09 (±2.39)	0.267 (±0.174)	0.078 (±0.129)	15.6 (±18.4)
	Bleb	1.17 (±0.64)	2.83	1.05 (±0.48)	-0.054 ±0.123)	0.113 (±0.057)	34.4 (±28.1)
	Bleb-Actin D.	0.79 (±0.29)	1.49	1.98 (±0.85)	0.003 (±0.116)	0.176 (±0.079)	39.6 (±23.4)
	Bleb-Bleb	1.04 (±0.00)	1.04	2.10 (±0.00)	-0.146 ±0.000)	0.061 (±0.000)	77.2 (±0.0))
	Unidentifiable	0.72 (±0.44)	1.45	1.48 (±0.45)	0.016 (±0.146)	0.164 (±0.083)	10.8 (±13.2)
	False Positive	0.80 (±0.63)	2.03	1.34 (±1.11)	0.092 (±0.280)	0.083 (±0.178)	22.3 (±25.6)
1.3 Ax2.	Actin D.	0.77 (±0.29)	1.58	2.77 (±1.68)	0.221 (±0.168)	0.126 (±0.128)	31.0 (±30.0)
	Bleb	1.40 (±0.98)	4.45	1.23 (±0.65)	-0.049 ±0.170)	0.109 (±0.059)	50.4 (±28.7)
	Bleb-Actin D.	1.43 (±0.76)	3.32	3.21 (±1.12)	0.029 (±0.186)	0.176 (±0.138)	62.1 (±29.3)
	Bleb-Bleb	NA	NA	NA	NA	NA	NA
	Unidentifiable	1.21 (±1.08)	2.44	1.70 (±1.05)	0.089 (±0.040)	0.106 (±0.037)	45.6 (±48.2)
	False Positive	0.84 (±0.42)	1.14	1.23 (±0.85)	0.175 (±0.495)	0.170 (±0.092)	14.2 (±3.5))
1.1-3 Ax2.	Actin D.	0.71 (±0.28)	1.86	2.73 (±2.12)	0.247 (±0.175)	0.089 (±0.127)	20.9 (±22.7)
	Bleb	1.24 (±0.77)	4.45	1.13 (±0.53)	-0.051 ±0.137)	0.116 (±0.059)	40.9 (±29.8)
	Bleb-Actin D.	0.93 (±0.49)	3.32	2.21 (±1.02)	0.018 (±0.144)	0.185 (±0.098)	44.4 (±26.6)
	Bleb-Bleb	1.04 (±0.00)	1.04	2.10 (±0.00)	-0.146 ±0.000)	0.061 (±0.000)	77.2 (±0.0))
	Unidentifiable	0.86 (±0.67)	2.44	1.52 (±1.12)	0.051 (±0.126)	0.131 (±0.066)	22.7 (±27.9)
	False Positive	0.85 (±0.87)	3.52	1.21 (±0.92)	0.081 (±0.290)	0.082 (±0.142)	18.1 (±21.1)
2. Ax2.	Actin D.	0.59 (±0.23)	1.7	2.00 (±1.63)	0.172 (±0.131)	0.089 (±0.091)	20.5 (±15.7)
	Bleb	1.66 (±1.21)	4.93	1.18 (±0.60)	-0.043 ±0.148)	0.183 (±0.082)	55.3 (±26.6)
	Bleb-Actin D.	0.83 (±0.53)	1.53	2.47 (±0.81)	0.042 (±0.039)	0.266 (±0.055)	29.7 (±30.2)
	Bleb-Bleb	NA	NA	NA	NA	NA	NA
	Unidentifiable	1.00 (±0.55)	1.73	0.84 (±0.31)	-0.102 (±0.208)	0.139 (±0.049)	34.7 (±16.6)
	False Positive	0.62 (±0.19)	0.82	0.60 (±0.16)	-0.178 (±0.125)	0.138 (±0.049)	7.9 (4±.6))

Table A.4: **Measures from ECMM-APT protrusions in Ax2 cells.** See Table A.3 for counts.

A.4 Results Tables: Mutant ECMM-APT Tracks

A.4.1 Average Global Measures

Experiment	Persistence	Speed ($\mu m/$ sec)	Elongation
1.1-3 Ax2 (2 fps)	0.842 ($\pm$0.173)	0.284 ($\pm$0.107)	3.925 ($\pm$1.615)
2. Ax2 (4-5 fps)	0.314 ($\pm$0.248)	0.183 ($\pm$0.074)	2.507 ($\pm$0.964)
3. Pi3K-KO	0.594 ($\pm$0.245)	0.277 ($\pm$0.062)	1.945 ($\pm$0.610)
4. pikl-KO	0.463 ($\pm$0.194)	0.264 ($\pm$0.099)	1.663 ($\pm$0.413)
5. mlcE	0.808 ($\pm$0.215)	0.306 ($\pm$0.124)	2.441 ($\pm$1.189)

Table A.5: **Average global measures for Ax2 and mutant cells.** These measures are as described in Chapter 2 Materials and Methods, Section 2.4.1.

A.4.2 Mutant ECMM-APT Protrusion Measures

Strain	Num. Cells	Frame Rate (FPS)	Total Seq. Time (sec)	Num. Prots.*
Ax2 (all)	30	2, 4.54, 4.16	2526.24	550
3. Pi3K-KO	19	6.67 , 5.08	1026.51	285
4. pikl-KO	12	4.16	730.8	226
5. mlcE	6	4.55	454.58	77

*Number of protrusions

Table A.6: **Mutant ECMM-APT protrusion counts.** Sequence information and ECMM-APT protrusion counts for mutant strains, as compared to Ax2 wild type cells.

Peak Speed ($\mu m/$ sec)	Max Peak Speed ($\mu m/$ sec)	Displacement (μm)	Curvature (normalised)	ΔCurvature (normalised)	Protrusion Rate
0.89 ($\pm$0.64)	4.93	2.02 ($\pm$1.71)	0.116 ($\pm$0.206)	0.112 ($\pm$0.108)	0.002945
0.63 ($\pm$0.58)	3.54	1.43 ($\pm$0.87)	0.054 ($\pm$0.176)	0.150 ($\pm$0.128)	0.005949
0.71 ($\pm$0.70)	5.49	1.32 ($\pm$0.83)	0.099 ($\pm$0.195)	0.148 ($\pm$0.134)	0.008187
0.49 ($\pm$0.23)	1.1	2.24 ($\pm$2.35)	0.117 ($\pm$0.163)	0.190 ($\pm$0.091)	0.002244

Table A.7: **Mutant ECMM-APT protrusion measures.** Average measured parameters determined by ECMM-APT mutant strains compared to Ax2 wild type cells.

A.5 Relative Error

Let x be the true value measure, then the relative error an approximation, x_0, is given by

$$\delta x = \frac{x_0 - x}{x}. \tag{A.1}$$

A.6 Coefficient of Determination

For the data set (y_i, x_i), where y_i are the observed values, and f is a fitted curve, the proportion of variation explained by f in the data, R^2, is

$$R^2 = 1 - \frac{SS_{error}}{SS_{total}}, \tag{A.2}$$

$$SS_{total} = \sum_{i=0}^{N} (y_i - \bar{y})^2, \tag{A.3}$$

$$SS_{error} = \sum_{i=0}^{N} (y_i - f(x_i))^2, \tag{A.4}$$

where N is the number of observed values.

Bibliography

Abràmoff, M., Magalhães, P. and Ram, S. (2004). Image processing with imagej. *Biophotonics international* **11**, 36–42.

Aguilar, H. N. and Mitchell, B. F. (2010). Physiological pathways and molecular mechanisms regulating uterine contractility. *Hum Reprod Update* **16**, 725–44.

Aizawa, H., Fukui, Y. and Yahara, I. (1997). Live dynamics of dictyostelium cofilin suggests a role in remodeling actin latticework into bundles. *Journal of Cell Science* **110 (Pt 19)**, 2333–44.

Al-Kofahi, O., Radke, R. J., Goderie, S. K., Shen, Q., Temple, S. and Roysam, B. (2006). Automated cell lineage construction: a rapid method to analyze clonal development established with murine neural progenitor cells. *Cell Cycle* **5**, 327–35.

Andrew, N. and Insall, R. (2007). Chemotaxis in shallow gradients is mediated independently of ptdins 3-kinase by biased choices between random protrusions. *Nature cell biology* **9**, 193–200.

Andrianantoandro, E. and Pollard, T. D. (2006). Mechanism of actin filament turnover by severing and nucleation at different concentrations of adf/cofilin. *Mol Cell* **24**, 13–23.

Applegate, K. T., Besson, S., Matov, A., Bagonis, M. H., Jaqaman, K. and Danuser, G. (2011). plustiptracker: Quantitative image analysis software for the measurement of microtubule dynamics. *J Struct Biol* **176**, 168–84.

Arai, Y., Shibata, T., Matsuoka, S., Sato, M. J., Yanagida, T. and Ueda, M. (2010). Self-organization of the phosphatidylinositol lipids signaling system for random cell migration. *Proceedings of the National Academy of Sciences of the United States of America* **107**, 12399–12404.

Atilgan, E., Wirtz, D. and Sun, S. (2006). Mechanics and dynamics of actin-driven thin membrane protrusions. *Biophysical Journal* **90**, 65–76.

Balla, T. (2005). Inositol-lipid binding motifs: signal integrators through protein-lipid and protein-protein interactions. *Journal of Cell Science* **118**, 2093–104.

Bamburg, J. R., McGough, A. and Ono, S. (1999). Putting a new twist on actin: Adf/cofilins modulate actin dynamics. *Trends in cell biology* **9**, 364–70.

Baum, B. and Kunda, P. (2005). Actin nucleation: spire - actin nucleator in a class of its own. *Curr Biol* **15**, R305–8.

Bear, J. E., Rawls, J. F. and Saxe, C. L. (1998). Scar, a wasp-related protein, isolated as a suppressor of receptor defects in late dictyostelium development. *The Journal of cell biology* **142**, 1325–35.

Bernheim-Groswasser, A., Prost, J. and Sykes, C. (2005). Mechanism of actin-based motility: a dynamic state diagram. *Biophysical Journal* **89**, 1411–9.

Blaser, H., Reichman-Fried, M., Castanon, I., Dumstrei, K., Marlow, F., Kawakami, K., Solnica-Krezel, L., Heisenberg, C. and Raz, E. (2006). Migration of zebrafish primordial germ cells: a role for myosin contraction and cytoplasmic flow. *Developmental cell* **11**, 613–627.

Bollobas, B. (1998). Modern graph theory. *Springer Verlag* **184**.

Bolourani, P., Spiegelman, G. B. and Weeks, G. (2006). Delineation of the roles played by rasg and rasc in camp-dependent signal transduction during the early development of dictyostelium discoideum. *Mol Biol Cell* **17**, 4543–50.

Bonner, J. (1947). Evidence for the formation of cell aggregates by chemotaxis in the development of the slime mold dictyostelium discoideum. *J Exp Zool* **106**, 1–26.

Bosgraaf, L. and Haastert, P. J. M. V. (2009a). The ordered extension of pseudopodia by amoeboid cells in the absence of external cues. *PLoS One* **4**, e5253.

Bosgraaf, L., Haastert, P. J. M. V. and Bretschneider, T. (2009). Analysis of cell movement by simultaneous quantification of local membrane displacement and fluorescent intensities using quimp2. *Cell motility and the cytoskeleton* **66**, 156–65.

Bosgraaf, L. and Haastert, P. V. (2009b). Navigation of chemotactic cells by parallel signaling to pseudopod persistence and orientation. *PLoS One* **4**, 6842.

Bosgraaf, L. and Haastert, P. V. (2009c). Quimp3, an automated pseudopod-tracking algorithm. *Cell adhesion and migration* **4**.

Bosgraaf, L., Keizer-Gunnink, I. and Haastert, P. V. (2008). Pi3-kinase signaling contributes to orientation in shallow gradients and enhances speed in steep chemoattractant gradients. *Journal of Cell Science* **121**, 3589.

Bosgraaf, L., Russcher, H., Smith, J. L., Wessels, D., Soll, D. R. and Haastert, P. J. M. V. (2002). A novel cgmp signalling pathway mediating myosin phosphorylation and chemotaxis in dictyostelium. *The EMBO Journal* **21**, 4560–70.

Bosgraaf, L., Waijer, A., Engel, R., Visser, A. J. W. G., Wessels, D., Soll, D. and Haastert, P. J. M. V. (2005). Rasgef-containing proteins gbpc and gbpd have differential effects on cell polarity and chemotaxis in dictyostelium. *Journal of Cell Science* **118**, 1899–910.

Bovellan, M., Fritzsche, M., Stevens, C. and Charras, G. (2010). Death-associated protein kinase (dapk) and signal transduction: blebbing in programmed cell death. *FEBS J* **277**, 58–65.

Bretscher, A., Edwards, K. and Fehon, R. G. (2002). Erm proteins and merlin: integrators at the cell cortex. *Nat Rev Mol Cell Biol* **3**, 586–99.

Bretscher, M. S. (1984). Endocytosis: relation to capping and cell locomotion. *Science* **224**, 681–6.

Bretschneider, T., Diez, S., Anderson, K., Heuser, J., Clarke, M., Müller-Taubenberger, A., Köhler, J. and Gerisch, G. (2004). Dynamic actin patterns and arp2/3 assembly at the substrate-attached surface of motile cells. *Curr Biol* **14**, 1–10.

Bretschneider, T., Jonkman, J., Köhler, J., Medalia, O., Barisic, K., Weber, I., Stelzer, E. H. K., Baumeister, W. and Gerisch, G. (2002). Dynamic organization of the actin system in the motile cells of dictyostelium. *Journal of muscle research and cell motility* **23**, 639–49.

Brugués, J., Maugis, B., Casademunt, J., Nassoy, P., Amblard, F. and Sens, P. (2010). Dynamical organization of the cytoskeletal cortex probed by micropipette aspiration. *Proceedings of the National Academy of Sciences of the United States of America* **107**, 15415–20.

Cameron, L. A., Svitkina, T. M., Vignjevic, D., Theriot, J. A. and Borisy, G. G. (2001). Dendritic organization of actin comet tails. *Curr Biol* **11**, 130–5.

Carpenter, A. E., Jones, T. R., Lamprecht, M. R., Clarke, C., Kang, I. H., Friman, O., Guertin, D. A., Chang, J. H., Lindquist, R. A., Moffat, J., Golland, P. and Sabatini, D. M. (2006). Cellprofiler: image analysis software for identifying and quantifying cell phenotypes. *Genome Biol* **7**, 100.

Carrin, I., Murgia, I., McLachlan, A. and Kay, R. (1996). A mutational analysis of dictyostelium discoideum multicellular development. *Microbiology* **142**, 993–1003.

Chalhoub, N. and Baker, S. J. (2009). Pten and the pi3-kinase pathway in cancer. *Annual review of pathology* **4**, 127–50.

Chan, F., Lam, F. and Zhu, H. (1998). Adaptive thresholding by variational method. *IEEE Transactions on Image Processing* **7**, 468–473.

Charest, P. G., Shen, Z., Lakoduk, A., Sasaki, A. T., Briggs, S. P. and Firtel, R. A. (2010). A ras signaling complex controls the rasc-torc2 pathway and directed cell migration. *Developmental cell* **18**, 737–49.

Charras, G. and Paluch, E. (2008). Blebs lead the way: how to migrate without lamellipodia. *Nature Reviews Molecular Cell Biology* **9**, 730–736.

Charras, G. T., Coughlin, M., Mitchison, T. J. and Mahadevan, L. (2008). Life and times of a cellular bleb. *Biophysical Journal* **94**, 1836–53.

Charras, G. T., Hu, C.-K., Coughlin, M. and Mitchison, T. J. (2006). Reassembly of contractile actin cortex in cell blebs. *The Journal of cell biology* **175**, 477–90.

Charras, G. T., Yarrow, J. C., Horton, M. A., Mahadevan, L. and Mitchison, T. J. (2005). Non-equilibration of hydrostatic pressure in blebbing cells. *Nature* **435**, 365–9.

Chen, L., Iijima, M., Tang, M., Landree, M. A., Huang, Y. E., Xiong, Y., Iglesias, P. A. and Devreotes, P. N. (2007). Pla2 and pi3k/pten pathways act in parallel to mediate chemotaxis. *Developmental cell* **12**, 603–14.

Chen, M. Y., Insall, R. H. and Devreotes, P. N. (1996). Signaling through chemoattractant receptors in dictyostelium. *Trends Genet* **12**, 52–7.

Chen, T. L., Kowalczyk, P. A., Ho, G. and Chisholm, R. L. (1995). Targeted disruption of the dictyostelium myosin essential light chain gene produces cells defective in cytokinesis and morphogenesis. *Journal of Cell Science* **108 (Pt 10)**, 3207–18.

Cheung, A., Dantzig, J. A., Hollingworth, S., Baylor, S. M., Goldman, Y. E., Mitchison, T. J. and Straight, A. F. (2002). A small-molecule inhibitor of skeletal muscle myosin ii. *Nat Cell Biol* **4**, 83–8.

Clarke, M., Engel, U., Giorgione, J., Müller-Taubenberger, A., Prassler, J., Veltman, D. and Gerisch, G. (2010). Curvature recognition and force generation in phagocytosis. *BMC Biol* **8**, 154.

Coleman, M. L., Sahai, E. A., Yeo, M., Bosch, M., Dewar, A. and Olson, M. F. (2001). Membrane blebbing during apoptosis results from caspase-mediated activation of rock i. *Nature cell biology* **3**, 339–45.

Cooper, J. A. (1991). The role of actin polymerization in cell motility. *Annual review of physiology* **53**, 585–605.

Cooper, J. A. and Schafer, D. A. (2000). Control of actin assembly and disassembly at filament ends. *Current opinion in cell biology* **12**, 97–103.

Cruz, E. M. D. L. (2009). How cofilin severs an actin filament. *Biophys Rev* **1**, 51–59.

Cunningham, C. C. (1995). Actin polymerization and intracellular solvent flow in cell surface blebbing. *The Journal of cell biology* **129**, 1589–99.

Cunningham, C. C., Gorlin, J. B., Kwiatkowski, D. J., Hartwig, J. H., Janmey, P. A., Byers, H. R. and Stossel, T. P. (1992). Actin-binding protein requirement for cortical stability and efficient locomotion. *Science* **255**, 325–7.

Dai, J. and Sheetz, M. P. (1999). Membrane tether formation from blebbing cells. *Biophysical Journal* **77**, 3363–70.

Dalous, J., Burghardt, E., Müller-Taubenberger, A., Bruckert, F., Gerisch, G. and Bretschneider, T. (2008). Reversal of cell polarity and actin-myosin cytoskeleton reorganization under mechanical and chemical stimulation. *Biophysical journal* **94**, 1063–1074.

Daly, K. E., Huang, K. C., Wingreen, N. S. and Mukhopadhyay, R. (2011). Mechanics of membrane bulging during cell-wall disruption in gram-negative bacteria. *Phys Rev E Stat Nonlin Soft Matter Phys* **83**, 041922.

Danuser, G. and Waterman-Storer, C. M. (2006). Quantitative fluorescent speckle microscopy of cytoskeleton dynamics. *Annu. Rev. Biophys. Biomol. Struct.* **35**, 361–87.

Debeir, O., Camby, I., Kiss, R., Ham, P. V. and Decaestecker, C. (2004). A model-based approach for automated in vitro cell tracking and chemotaxis analyses. *Cytometry A* **60**, 29–40.

Decaestecker, C., Debeir, O., Ham, P. V. and Kiss, R. (2007). Can anti-migratory drugs be screened in vitro? a review of 2d and 3d assays for the quantitative analysis of cell migration. *Medicinal Research Reviews* **27**, 149–76.

Dellas, C. and Loskutoff, D. J. (2005). Historical analysis of pai-1 from its discovery to its potential role in cell motility and disease. *Thromb Haemost* **93**, 631–40.

Delorme, V., Machacek, M., DerMardirossian, C., Anderson, K. L., Wittmann, T., Hanein, D., Waterman-Storer, C., Danuser, G. and Bokoch, G. M. (2007). Cofilin activity downstream of pak1 regulates cell protrusion efficiency by organizing lamellipodium and lamella actin networks. *Developmental cell* **13**, 646–62.

DesMarais, V., Ghosh, M., Eddy, R. and Condeelis, J. (2005). Cofilin takes the lead. *Journal of Cell Science* **118**, 19–26.

DesMarais, V., Macaluso, F., Condeelis, J. and Bailly, M. (2004). Synergistic interaction between the arp2/3 complex and cofilin drives stimulated lamellipod extension. *Journal of Cell Science* **117**, 3499–510.

Devreotes, P. and Janetopoulos, C. (2003). Eukaryotic chemotaxis: distinctions between directional sensing and polarization. *J Biol Chem* **278**, 20445–8.

Dickinson, R. B., Caro, L. and Purich, D. L. (2004). Force generation by cytoskeletal filament end-tracking proteins. *Biophysical Journal* **87**, 2838–54.

Dormann, D., Libotte, T., Weijer, C. and Bretschneider, T. (2002). Simultaneous quantification of cell motility and protein-membrane-association using active contours. *Cell Motil Cytoskeleton* **52**, 221–30.

Dormann, D. and Weijer, C. (2006). Imaging of cell migration. *The EMBO Journal* **25**, 3480–3493.

Dormann, D., Weijer, G., Dowler, S. and Weijer, C. J. (2004). In vivo analysis of 3-phosphoinositide dynamics during dictyostelium phagocytosis and chemotaxis. *Journal of Cell Science* **117**, 6497–509.

Downey, G. P. (1994). Mechanisms of leukocyte motility and chemotaxis. *Curr Opin Immunol* **6**, 113–24.

Downey, M. J., Jeziorska, D. M., Ott, S., Tamai, T. K., Koentges, G., Vance, K. W. and Bretschneider, T. (2011). Extracting fluorescent reporter time courses of cell lineages from high-throughput microscopy at low temporal resolution. *PLoS One* , 1–21.

Du, C.-J., Marcello, M., Spiller, D. G., White, M. R. H. and Bretschneider, T. (2010). Interactive segmentation of clustered cells via geodesic commute distance and constrained density weighted nyström method. *Cytometry A* **77**, 1137–47.

Dufour, A., Shinin, V., Tajbakhsh, S., Guillén-Aghion, N., Olivo-Marin, J.-C. and Zimmer, C. (2005). Segmenting and tracking fluorescent cells in dynamic 3-d microscopy with coupled active surfaces. *IEEE Trans Image Process* **14**, 1396–410.

Etzrodt, M., Ishikawa, H. C. F., Dalous, J., Müller-Taubenberger, A., Bretschneider, T. and Gerisch, G. (2006). Time-resolved responses to chemoattractant, characteristic of the front and tail of dictyostelium cells. *FEBS letters* **580**, 6707–13.

Ferguson, G. J., Milne, L., Kulkarni, S., Sasaki, T., Walker, S., Andrews, S., Crabbe, T., Finan, P., Jones, G., Jackson, S., Camps, M., Rommel, C., Wymann, M., Hirsch, E., Hawkins, P. and Stephens, L. (2007). Pi(3)kgamma has an important context-dependent role in neutrophil chemokinesis. *Nature cell biology* **9**, 86–91.

Fischer, M., Cox, J., Davis, D. J., Wagner, A., Taylor, R., Huerta, A. J., Money, N. P. and Huerta, A. J. (2004). New information on the mechanism of forcible ascospore discharge from ascobolus immersus. *Fungal Genet Biol* **41**, 698–707.

Frangogiannis, N., Smith, C. and Entman, M. (2002). The inflammatory response in myocardial infarction. *Cardiovascular Research* **53**, 31.

Friedl, P. and Wolf, K. (2003). Proteolytic and non-proteolytic migration of tumour cells and leucocytes. *Biochem Soc Symp* , 277–85.

Frischknecht, F., Moreau, V., Röttger, S., Gonfloni, S., Reckmann, I., Superti-Furga, G. and Way, M. (1999). Actin-based motility of vaccinia virus mimics receptor tyrosine kinase signalling. *Nature* **401**, 926–9.

Fujiwara, I., Takahashi, S., Tadakuma, H., Funatsu, T. and Ishiwata, S. (2002). Microscopic analysis of polymerization dynamics with individual actin filaments. *Nature cell biology* **4**, 666–73.

Funamoto, S., Meili, R., Lee, S., Parry, L. and Firtel, R. A. (2002). Spatial and temporal regulation of 3-phosphoinositides by pi 3-kinase and pten mediates chemotaxis. *Cell* **109**, 611–23.

Gadea, G., de Toledo, M., Anguille, C. and Roux, P. (2007). Loss of p53 promotes rhoa-rock-dependent cell migration and invasion in 3d matrices. *The Journal of Cell Biology* **178**, 23.

Gerisch, G. (1982). Functions of chemotaxis in dictyostelium development. *Annual review of physiology* , 535–552.

Gerisch, G., Albrecht, R., Heizer, C., Hodgkinson, S. and Maniak, M. (1995). Chemoattractant-controlled accumulation of coronin at the leading edge of dictyostelium cells monitored using a green fluorescent protein-coronin fusion protein. *Curr Biol* **5**, 1280–5.

Gerisch, G. and Keller, H. U. (1981). Chemotactic reorientation of granulocytes stimulated with micropipettes containing fmet-leu-phe. *Journal of Cell Science* **52**, 1–10.

Godinez, W., Lampe, M., Wörz, S., Müller, B., Eils, R. and Rohr, K. (2007). Tracking of virus particles in time-lapse fluorescence microscopy image sequences. *Biomedical Imaging: From Nano to Macro, 2007. ISBI 2007. 4th IEEE International Symposium on* , 256–259.

Goley, E. and Welch, M. (2006). The arp2/3 complex: an actin nucleator comes of age. *Nat Rev Mol Cell Biol* **7**, 713–26.

Gottwald, U., Brokamp, R., Karakesisoglou, I., Schleicher, M. and Noegel, A. A. (1996). Identification of a cyclase-associated protein (cap) homologue in dictyostelium discoideum and characterization of its interaction with actin. *Mol Biol Cell* **7**, 261–72.

Haastert, P. J. M. V. (2010). A model for a correlated random walk based on the ordered extension of pseudopodia. *PLoS Computational Biology* **6**, e1000874.

Haastert, P. J. M. V. (2011). Amoeboid cells use protrusions for walking, gliding and swimming. *PLoS ONE* **6**, e27532.

Haastert, P. J. M. V., Keizer-Gunnink, I. and Kortholt, A. (2007). Essential role of pi3-kinase and phospholipase a2 in dictyostelium discoideum chemotaxis. *The Journal of cell biology* **177**, 809–16.

Haastert, P. J. M. V. and Veltman, D. M. (2007). Chemotaxis: navigating by multiple signaling pathways. *Sci STKE* **2007**, pe40.

Haastert, P. V. and Bosgraaf, L. (2009a). Food searching strategy of amoeboid cells by starvation induced run length extension. *PLoS One* **4**, e6814.

Haastert, P. V. and Bosgraaf, L. (2009b). The local cell curvature guides pseudopodia towards chemoattractants. *HFSP Journal* **3**, 282–286.

Hagmann, J., Burger, M. M. and Dagan, D. (1999). Regulation of plasma membrane blebbing by the cytoskeleton. *J Cell Biochem* **73**, 488–99.

Hao, J., Liu, Y., Kruhlak, M., Debell, K., Rellahan, B. and Shaw, S. (2009). Phospholipase c–mediated hydrolysis of pip2 releases erm proteins from lymphocyte membrane. *The Journal of Cell Biology* **184**, 451.

Haston, W. and Shields, J. (1984). Contraction waves in lymphocyte locomotion. *Journal of cell science* **68**, 227.

Hernandez, O. M., Jones, M., Guzman, G. and Szczesna-Cordary, D. (2007). Myosin essential light chain in health and disease. *Am J Physiol Heart Circ Physiol* **292**, H1643–54.

Hill, T. L. (1981). Microfilament or microtubule assembly or disassembly against a force. *Proceedings of the National Academy of Sciences of the United States of America* **78**, 5613–7.

Hoeller, O. and Kay, R. (2007). Chemotaxis in the absence of pip3 gradients. *Current Biology* **17**, 813–817.

Hou, Z. and Han, C. (2005). Force field analysis snake: an improved parametric active contour model. *Pattern Recognition Letters* **26**, 513–526.

Huang, L. and Helmke, B. P. (2011). A semi-automatic method for image analysis of edge dynamics in living cells. *Cellular and molecular bioengineering* **4**, 205–219.

Iglesias, P. and Devreotes, P. (2008). Navigating through models of chemotaxis. *Current opinion in cell biology* **20**, 35–40.

Iijima, M. and Devreotes, P. (2002). Tumor suppressor pten mediates sensing of chemoattractant gradients. *Cell* **109**, 599–610.

Ilic, D., Furuta, Y., Kanazawa, S., Takeda, N., Sobue, K., Nakatsuji, N., Nomura, S., Fujimoto, J., Okada, M. and Yamamoto, T. (1995). Reduced cell motility and enhanced focal adhesion contact formation in cells from fak-deficient mice. *Nature* **377**, 539–44.

Inoué, S. and Salmon, E. D. (1995). Force generation by microtubule assembly/disassembly in mitosis and related movements. *Mol Biol Cell* **6**, 1619–40.

Insall, R., Kuspa, A., Lilly, P. J., Shaulsky, G., Levin, L. R., Loomis, W. F. and Devreotes, P. (1994). Crac, a cytosolic protein containing a pleckstrin homology domain, is required for receptor and g protein-mediated activation of adenylyl cyclase in dictyostelium. *J Cell Biol* **126**, 1537–45.

Insall, R. H. (2010). Understanding eukaryotic chemotaxis: a pseudopod-centred view. *Nat Rev Mol Cell Biol* **11**, 453–8.

Insall, R. H. and Weiner, O. D. (2001). Pip3, pip2, and cell movement–similar messages, different meanings? *Developmental Cell* **1**, 743–7.

Jaglarz, M. and Howard, K. (1995). The active migration of drosophila primordial germ cells. *Development* **121**, 3495.

Janetopoulos, C., Jin, T. and Devreotes, P. (2001). Receptor-mediated activation of heterotrimeric g-proteins in living cells. *Science* **291**, 2408–11.

Janson, L. W. and Taylor, D. L. (1993). In vitro models of tail contraction and cytoplasmic streaming in amoeboid cells. *The Journal of cell biology* **123**, 345–56.

Ji, L., Lim, J. and Danuser, G. (2008). Fluctuations of intracellular forces during cell protrusion. *Nature cell biology* **10**, 1393. Specular.

Jilkine, A. and Edelstein-Keshet, L. (2011). A comparison of mathematical models for polarization of single eukaryotic cells in response to guided cues. *PLoS Computational Biology* **7**, e1001121.

Jones, T. R., Carpenter, A. E., Lamprecht, M. R., Moffat, J., Silver, S. J., Grenier, J. K., Castoreno, A. B., Eggert, U. S., Root, D. E., Golland, P. and Sabatini, D. M. (2009). Scoring diverse cellular morphologies in image-based screens with iterative feedback and machine learning. *Proceedings of the National Academy of Sciences of the United States of America* **106**, 1826–31.

Kae, H., Kortholt, A., Rehmann, H., Insall, R. H., Haastert, P. J. M. V., Spiegelman, G. B. and Weeks, G. (2007). Cyclic amp signalling in dictyostelium: G-proteins activate separate ras pathways using specific rasgefs. *EMBO reports* **8**, 477–82.

Kaksonen, M., Toret, C. P. and Drubin, D. G. (2006). Harnessing actin dynamics for clathrin-mediated endocytosis. *Nature Reviews Molecular Cell Biology* **7**, 404–14.

Kamimura, Y., Xiong, Y., Iglesias, P. A., Hoeller, O., Bolourani, P. and Devreotes, P. N. (2008). Pip3-independent activation of torc2 and pkb at the cell's leading edge mediates chemotaxis. *Curr Biol* **18**, 1034–43.

Kass, M., Witkin, A. and Terzopoulos, D. (1988). Snakes: Active contour models. *International Journal of Computer Vision* **1**, 321–331.

Kay, R., Langridge, P., Traynor, D. and Hoeller, O. (2008). Changing directions in the study of chemotaxis. *Nature Reviews Molecular Cell Biology* **9**, 455–463.

Keller, H. and Eggli, P. (1998). Protrusive activity, cytoplasmic compartmentalization, and restriction rings in locomoting blebbing walker carcinosarcoma cells are related to detachment of cortical actin from the plasma membrane. *Cell motility and the cytoskeleton* **41**, 181–93.

Keller, H., Rentsch, P. and Hagmann, J. (2002). Differences in cortical actin structure and dynamics document that different types of blebs are formed by distinct mechanisms. *Experimental cell research* **277**, 161–72.

Keller, R. E., Danilchik, M., Gimlich, R. and Shih, J. (1985). The function and mechanism of convergent extension during gastrulation of xenopus laevis. *J Embryol Exp Morphol* **89 Suppl**, 185–209.

Kesbeke, F., Snaar-Jagalska, B. E. and Haastert, P. J. V. (1988). Signal transduction in dictyostelium fgd a mutants with a defective interaction between surface camp receptors and a gtp-binding regulatory protein. *J Cell Biol* **107**, 521–8.

Kim, J., McKinnis, V., Nawrocki, A. and White, S. (1998). Stimulation of migration and wound repair of guinea-pig airway epithelial cells in response to epidermal growth factor. *American Journal of Respiratory Cell and Molecular Biology* **18**, 66–74.

King, J. S. and Insall, R. H. (2009). Chemotaxis: finding the way forward with dictyostelium. *Trends in cell biology* **19**, 523–30.

Konijn, T. M. (1972). Cyclic amp as a first messenger. *Adv Cyclic Nucleotide Res* **1**, 17–31.

Korn, E. D. and Hammer, J. A. (1988). Myosins of nonmuscle cells. *Annu Rev Biophys Biophys Chem* **17**, 23–45.

Koshland, D. E. (1977). A response regulator model in a simple sensory system. *Science* **196**, 1055–63.

Kovar, D. R. (2006). Molecular details of formin-mediated actin assembly. *Current opinion in cell biology* **18**, 11–7.

Kreitmeier, M., Gerisch, G., Heizer, C. and Müller-Taubenberger, A. (1995). A talin homologue of dictyostelium rapidly assembles at the leading edge of cells in response to chemoattractant. *J Cell Biol* **129**, 179–88.

Laevsky, G. and Knecht, D. (2003). Cross-linking of actin filaments by myosin ii is a major contributor to cortical integrity and cell motility in restrictive environments. *Journal of Cell Science* **116**, 3761.

Laevsky, G. and Knecht, D. A. (2001). Under-agarose folate chemotaxis of dictyostelium discoideum amoebae in permissive and mechanically inhibited conditions. *BioTechniques* **31**, 1140–2, 1144, 1146–9.

Langridge, P. and Kay, R. (2006). Blebbing of dictyostelium cells in response to chemoattractant. *Experimental cell research* **312**, 2009–2017.

Lee, S., Comer, F. I., Sasaki, A., McLeod, I. X., Duong, Y., Okumura, K., Yates, J. R., Parent, C. A. and Firtel, R. A. (2005). Tor complex 2 integrates cell movement during chemotaxis and signal relay in dictyostelium. *Mol Biol Cell* **16**, 4572–83.

Li, L., Cox, E. C. and Flyvbjerg, H. (2011). 'dicty dynamics': Dictyostelium motility as persistent random motion. *Physical Biology* **8**, 046006.

Libotte, T., Kaiser, H., Alt, W. and Bretschneider, T. (2001). Polarity, protrusion–retraction dynamics and their interplay during keratinocyte cell migration. *Experimental Cell Research* **270**, 129–137.

Lilly, P. J. and Devreotes, P. N. (1994). Identification of crac, a cytosolic regulator required for guanine nucleotide stimulation of adenylyl cyclase in dictyostelium. *J Biol Chem* **269**, 14123–9.

Lilly, P. J. and Devreotes, P. N. (1995). Chemoattractant and gtp gamma s-mediated stimulation of adenylyl cyclase in dictyostelium requires translocation of crac to membranes. *J Cell Biol* **129**, 1659–65.

Lorentzen, A., Bamber, J., Sadok, A., Elson-Schwab, I. and Marshall, C. J. (2011). An ezrin-rich, rigid uropod-like structure directs movement of amoeboid blebbing cells. *Journal of Cell Science* **124**, 1256–67.

Machacek, M. and Danuser, G. (2006). Morphodynamic profiling of protrusion phenotypes. *Biophysical Journal* **90**, 1439–1452.

Machacek, M., Hodgson, L., Welch, C., Elliott, H., Pertz, O., Nalbant, P., Abell, A., Johnson, G., Hahn, K. and Danuser, G. (2009). Coordination of rho gtpase activities during cell protrusion. *Nature* **461**, 99–103.

Maeda, Y., Inose, J., Matsuo, M., Iwaya, S. and Sano, M. (2008). Ordered patterns of cell shape and orientational correlation during spontaneous cell migration. *PLoS ONE* **3**, e3734.

Manahan, C., Iglesias, P., Long, Y. and Devreotes, P. (2004). Chemoattractant signaling in dictyostelium discoideum. *Annu. Rev. Cell Dev. Biol.* **20**, 223–53.

Marcy, Y., Prost, J., Carlier, M.-F. and Sykes, C. (2004). Forces generated during actin-based propulsion: a direct measurement by micromanipulation. *Proceedings of the National Academy of Sciences of the United States of America* **101**, 5992–7.

Masuda, T., Kariya, K., Shinkai, M., Okada, T. and Kataoka, T. (1995). Protein kinase byr2 is a target of ras1 in the fission yeast schizosaccharomyces pombe. *Journal of Biological Chemistry* **270**, 1979.

Maugis, B., Brugués, J., Nassoy, P., Guillen, N., Sens, P. and Amblard, F. (2010). Dynamic instability of the intracellular pressure drives bleb-based motility. *Journal of Cell Science* **123**, 3884–92.

McGrath, J. L., Eungdamrong, N. J., Fisher, C. I., Peng, F., Mahadevan, L., Mitchison, T. J. and Kuo, S. C. (2003). The force-velocity relationship for the actin-based motility of listeria monocytogenes. *Curr Biol* **13**, 329–32.

McMahon, H. T. and Gallop, J. L. (2005). Membrane curvature and mechanisms of dynamic cell membrane remodelling. *Nature* **438**, 590–6.

Medalia, O., Weber, I., Frangakis, A. S., Nicastro, D., Gerisch, G. and Baumeister, W. (2002). Macromolecular architecture in eukaryotic cells visualized by cryoelectron tomography. *Science* **298**, 1209–13.

Meijering, E., Dzyubachyk, O., Smal, I. and van Cappellen, W. A. (2009). Tracking in cell and developmental biology. *Seminars in Cell & Developmental Biology* **20**, 894–902.

Meili, R., Ellsworth, C., Lee, S., Reddy, T., Ma, H. and Firtel, R. (1999). Chemoattractant-mediated transient activation and membrane localization of akt/pkb is required for efficient chemotaxis to camp in dictyostelium. *The EMBO Journal* **18**, 2092–2105.

Mitchell, I. (2008). The flexible, extensible and efficient toolbox of level set methods. *J Sci Computing* **35**, 300–29.

Miura, K. (2005). Tracking movement in cell biology. *Advances in Biochemical Engineering Biotechnology* **95**, 267–296.

Mogilner, A. (2006). On the edge: modeling protrusion. *Current opinion in cell biology* **18**, 32–9.

Mogilner, A. and Oster, G. (1996). Cell motility driven by actin polymerization. *Biophysical journal* **71**, 3030–45.

Mooseker, M. S., Pollard, T. D. and Wharton, K. A. (1982). Nucleated polymerization of actin from the membrane-associated ends of microvillar filaments in the intestinal brush border. *J Cell Biol* **95**, 223–33.

Mooseker, M. S. and Tilney, L. G. (1975). Organization of an actin filament-membrane complex. filament polarity and membrane attachment in the microvilli of intestinal epithelial cells. *J Cell Biol* **67**, 725–43.

Müller-Taubenberger, A., Bretschneider, T., Faix, J., Konzok, A., Simmeth, E. and Weber, I. (2002). Differential localization of the dictyostelium kinase dpaka during cytokinesis and cell migration. *Journal of muscle research and cell motility* **23**, 751–63.

Mullins, R. D., Kelleher, J. F., Xu, J. and Pollard, T. D. (1998). Arp2/3 complex from acanthamoeba binds profilin and cross-links actin filaments. *Mol Biol Cell* **9**, 841–52.

Murray, J., Vawter-Hugart, H., Voss, E. and Soll, D. R. (1992). Three-dimensional motility cycle in leukocytes. *Cell motility and the cytoskeleton* **22**, 211–23.

Neilson, M., Mackenzie, J., Webb, S. and Insall, R. (2010a). Modelling cell movement and chemotaxis using pseudopod-based feedback. *SIAM Journal on Scientific Computing* **33**.

Neilson, M. P., Mackenzie, J. A., Webb, S. D. and Insall, R. H. (2010b). Use of the parameterised finite element method to robustly and efficiently evolve the edge of a moving cell. *Integr Biol (Camb)* **2**, 687–95.

Neilson, M. P., Veltman, D. M., Haastert, P. J. M. V., Webb, S. D., Mackenzie, J. A. and Insall, R. H. (2011). Chemotaxis: a feedback-based computational model robustly predicts multiple aspects of real cell behaviour. *PLoS biology* **9**, e1000618.

Osher, S. and Sethian, J. (1988). Fronts propagating with curvature dependent speed: algorithms based on hamilton-jacobi formulations. *Journal of computational physics* **79**, 12–49.

Paluch, E., Piel, M., Prost, J., Bornens, M. and Sykes, C. (2005). Cortical actomyosin breakage triggers shape oscillations in cells and cell fragments. *Biophysical Journal* **89**, 724–33.

Pang, K. M., Lee, E. and Knecht, D. A. (1998). Use of a fusion protein between gfp and an actin-binding domain to visualize transient filamentous-actin structures. *Curr Biol* **8**, 405–8.

Pantaloni, D., Boujemaa, R., Didry, D., Gounon, P. and Carlier, M. F. (2000). The arp2/3 complex branches filament barbed ends: functional antagonism with capping proteins. *Nature cell biology* **2**, 385–91.

Parent, C. (2004). Making all the right moves: chemotaxis in neutrophils and dictyostelium. *Current opinion in cell biology* , 4–13.

Parent, C. A., Blacklock, B. J., Froehlich, W. M., Murphy, D. B. and Devreotes, P. N. (1998). G protein signaling events are activated at the leading edge of chemotactic cells. *Cell* **95**, 81–91.

Parent, C. A. and Devreotes, P. N. (1999). A cell's sense of direction. *Science* **284**, 765–70.

Peter, B. J., Kent, H. M., Mills, I. G., Vallis, Y., Butler, P. J. G., Evans, P. R. and McMahon, H. T. (2004). Bar domains as sensors of membrane curvature: the amphiphysin bar structure. *Science* **303**, 495–9.

Pletjushkina, O. J., Rajfur, Z., Pomorski, P., Oliver, T. N., Vasiliev, J. M. and Jacobson, K. A. (2001). Induction of cortical oscillations in spreading cells by depolymerization of microtubules. *Cell motility and the cytoskeleton* **48**, 235–44.

Pollard, T. and Borisy, G. (2003). Cellular motility driven by assembly and disassembly of actin filaments. *Cell* **112**, 453–465.

Pollard, T. D. and Weihing, R. R. (1974). Actin and myosin and cell movement. *CRC Crit Rev Biochem* **2**, 1–65.

Proseus, T. E., Zhu, G. L. and Boyer, J. S. (2000). Turgor, temperature and the growth of plant cells: using chara corallina as a model system. *J Exp Bot* **51**, 1481–94.

Rakic, P., Cameron, R. and Komuro, H. (1994). Recognition, adhesion, transmembrane signaling and cell motility in guided neuronal migration. *Curr Opin Neurobiol* **4**, 63–9.

Rameh, L. E., Tolias, K. F., Duckworth, B. C. and Cantley, L. C. (1997). A new pathway for synthesis of phosphatidylinositol-4,5-bisphosphate. *Nature* **390**, 192–6.

Raucher, D., Stauffer, T., Chen, W., Shen, K., Guo, S., York, J., Sheetz, M. and Meyer, T. (2000). Phosphatidylinositol 4, 5-bisphosphate functions as a second messenger that regulates cytoskeleton-plasma membrane adhesion. *Cell* **100**, 221–228.

Ray, N., Acton, S. T. and Ley, K. (2002). Tracking leukocytes in vivo with shape and size constrained active contours. *IEEE Transactions on Medical Imaging* **21**, 1222–35.

Ridley, A., Schwartz, M., Burridge, K., Firtel, R., Ginsberg, M., Borisy, G., Parsons, J. and Horwitz, A. (2003). Cell migration: Integrating signals from front to back. *Science* **302**, 1704–1709.

Riemann, B. and Wilkins, D. (1851). Grundlagen für eine allgemeine theorie der functionen einer veränderlichen complexen grösse. *Inaugural dissertation, Gottingen, 1851* .

Rivero, F. and Somesh, B. P. (2002). Signal transduction pathways regulated by rho gtpases in dictyostelium. *Journal of muscle research and cell motility* **23**, 737–49.

Rowley, R. (2006). Finite line of charge. *American Journal of Physics* **74 SP -**, 1120.

Sahai, E. and Marshall, C. (2003). Differing modes of tumour cell invasion have distinct requirements for rho/rock signalling and extracellular proteolysis. *Nature cell biology* **5**, 711–719.

Saraste, M. and Hyvönen, M. (1995). Pleckstrin homology domains: a fact file. *Curr Opin Struct Biol* **5**, 403–8.

Sarti, A., de Solorzano, C. O., Lockett, S. and Malladi, R. (2000). A geometric model for 3-d confocal image analysis. *IEEE Transactions on Biomedical Engineering* **47**, 1600–1609.

Sasaki, A. T., Chun, C., Takeda, K. and Firtel, R. A. (2004). Localized ras signaling at the leading edge regulates pi3k, cell polarity, and directional cell movement. *The Journal of cell biology* **167**, 505–18.

Sasaki, A. T., Janetopoulos, C., Lee, S., Charest, P. G., Takeda, K., Sundheimer, L. W., Meili, R., Devreotes, P. N. and Firtel, R. A. (2007). G protein-independent ras/pi3k/f-actin circuit regulates basic cell motility. *The Journal of cell biology* **178**, 185–91.

Servant, G., Weiner, O. D., Neptune, E. R., Sedat, J. W. and Bourne, H. R. (1999). Dynamics of a chemoattractant receptor in living neutrophils during chemotaxis. *Mol Biol Cell* **10**, 1163–78.

Shen, L., Farid, H. and Mcpeek, M. A. (2009). Modeling three-dimensional morphological structures using spherical harmonics. *Evolution* **63**, 1003–1016.

Shen, S., Sandham, W., Granat, M. and Sterr, A. (2005). Mri fuzzy segmentation of brain tissue using neighborhood attraction with neural-network optimization. *Ieee T Inf Technol B* **9**, 459–467.

Shook, D. and Keller, R. (2003). Mechanisms, mechanics and function of epithelial-mesenchymal transitions in early development. *Mechanisms of development* **120**, 1351–83.

Shutt, D. C., Wessels, D., Wagenknecht, K., Chandrasekhar, A., Hitt, A. L., Luna, E. J. and Soll, D. R. (1995). Ponticulin plays a role in the positional stabilization of pseudopods. *The Journal of cell biology* **131**, 1495–506.

Small, J. V., Herzog, M. and Anderson, K. (1995). Actin filament organization in the fish keratocyte lamellipodium. *J Cell Biol* **129**, 1275–86.

Small, J. V., Isenberg, G. and Celis, J. E. (1978). Polarity of actin at the leading edge of cultured cells. *Nature* **272**, 638–9.

Soille, P. (2010). Morphological image analysis: Principles and applications. *Springer-Verlag* , 391.

Soll, D. (1995). The use of computers in understanding how animal cells crawl. *International review of cytology* **163 SP -**, 43.

Soll, D. and Voss, E. (1997). Two-and three-dimensional computer systems for analyzing how animal cells crawl. *Motion analysis of living cells* , 25–52.

Sundd, P., Gutierrez, E., Pospieszalska, M. K., Zhang, H., Groisman, A. and Ley, K. (2010). Quantitative dynamic footprinting microscopy reveals mechanisms of neutrophil rolling. *Nat Methods* **7**, 821–4.

Svitkina, T. M. and Borisy, G. G. (1999). Arp2/3 complex and actin depolymerizing factor/cofilin in dendritic organization and treadmilling of actin filament array in lamellipodia. *J Cell Biol* **145**, 1009–26.

Taminato, A., Bagattini, R., Gorjão, R., Chen, G., Kuspa, A. and Souza, G. M. (2002). Role for yaka, camp, and protein kinase a in regulation of stress responses of dictyostelium discoideum cells. *Molecular biology of the cell* **13**, 2266–75.

Théry, M., Pépin, A., Dressaire, E., Chen, Y. and Bornens, M. (2006). Cell distribution of stress fibres in response to the geometry of the adhesive environment. *Cell motility and the cytoskeleton* **63**, 341–55.

Tilney, L. G. (1975). The role of actin in nonmuscle cell motility. *Soc Gen Physiol Ser* **30**, 339–88.

Tilney, L. G., DeRosier, D. J., Weber, A. and Tilney, M. S. (1992). How listeria exploits host cell actin to form its own cytoskeleton. ii. nucleation, actin filament polarity, filament assembly, and evidence for a pointed end capper. *J Cell Biol* **118**, 83–93.

Tinevez, J.-Y., Schulze, U., Salbreux, G., Roensch, J., Joanny, J.-F. and Paluch, E. (2009). Role of cortical tension in bleb growth. *Proceedings of the National Academy of Sciences of the United States of America* **106**, 18581–6.

Torgerson, R. R. and McNiven, M. A. (1998). The actin-myosin cytoskeleton mediates reversible agonist-induced membrane blebbing. *Journal of Cell Science* **111 (Pt 19)**, 2911–22.

Traynor, D. and Kay, R. R. (2007). Possible roles of the endocytic cycle in cell motility. *Journal of Cell Science* **120**, 2318–27.

Trinkaus, J. (1973). Surface activity and locomotion of fundulus deep cells during blastula and gastrula stages* 1. *Developmental Biology* **30**, 68–103.

Tsujioka, M., Yoshida, K., Nagasaki, A., Yonemura, S., Müller-Taubenberger, A. and Uyeda, T. Q. P. (2008). Overlapping functions of the two talin homologues in dictyostelium. *Eukaryotic Cell* **7**, 906–16.

Tsukada, Y., Aoki, K., Nakamura, T., Sakumura, Y., Matsuda, M. and Ishii, S. (2008). Quantification of local morphodynamics and local gtpase activity by edge evolution tracking. *PLoS Computational Biology* **4**, e1000223.

Tuxworth, R. I., Cheetham, J. L., Machesky, L. M., Spiegelmann, G. B., Weeks, G. and Insall, R. H. (1997). Dictyostelium rasg is required for normal motility and cytokinesis, but not growth. *J Cell Biol* **138**, 605–14.

Tyson, R., Epstein, D., Anderson, K. and Bretschneider, T. (2009). High resolution tracking of cell membrane dynamics in moving cells: An electrifying approach. *Mathematical Modelling of Natural Phenomena* **3**, 1–3.

Upadhyaya, A., Chabot, J. R., Andreeva, A., Samadani, A. and van Oudenaarden, A. (2003). Probing polymerization forces by using actin-propelled lipid vesicles. *Proceedings of the National Academy of Sciences of the United States of America* **100**, 4521–6.

Vallotton, P., Ponti, A., Waterman-Storer, C., Salmon, E. and Danuser, G. (2003). Recovery, visualization, and analysis of actin and tubulin polymer flow in live cells: a fluorescent speckle microscopy study. *Biophysical journal* **85**, 1289–1306.

Vartiainen, M. K. and Machesky, L. M. (2004). The wasp-arp2/3 pathway: genetic insights. *Current opinion in cell biology* **16**, 174–81.

Veltman, D., Keizer-Gunnik, I. and Haastert, P. V. (2008). Four key signaling pathways mediating chemotaxis in dictyostelium discoideum. *Journal of Cell Biology* **180**, 747–753.

Vicente, S., Kolmogorov, V. and Rother, C. (2008). Graph cut based image segmentation with connectivity priors. *Computer Vision and Pattern Recognition, 2008* , 1 – 8.

Vicker, M. G. (2002). Eukaryotic cell locomotion depends on the propagation of self-organized reaction-diffusion waves and oscillations of actin filament assembly. *Experimental cell research* **275**, 54–66.

Volkmann, N., DeRosier, D., Matsudaira, P. and Hanein, D. (2001). An atomic model of actin filaments cross-linked by fimbrin and its implications for bundle assembly and function. *The Journal of cell biology* **153**, 947–56.

Waterman-Storer, C. M., Desai, A., Bulinski, J. C. and Salmon, E. D. (1998). Fluorescent speckle microscopy, a method to visualize the dynamics of protein assemblies in living cells. *Curr Biol* **8**, 1227–30.

Watts, D. J. and Ashworth, J. M. (1970). Growth of myxameobae of the cellular slime mould dictyostelium discoideum in axenic culture. *Biochem J* **119**, 171–4.

Wei, L., Yang, Y., Nishikawa, R. M. and Jiang, Y. (2005). A study on several machine-learning methods for classification of malignant and benign clustered microcalcifications. *IEEE Transactions on Medical Imaging* **24**, 371–80.

Wessels, D., Kuhl, S. and Soll, D. R. (2006). Application of 2d and 3d dias to motion analysis of live cells in transmission and confocal microscopy imaging. *Methods Mol Biol* **346**, 261–79.

Wessels, D., Soll, D. R., Knecht, D., Loomis, W. F., Lozanne, A. D. and Spudich, J. (1988). Cell motility and chemotaxis in dictyostelium amebae lacking myosin heavy chain. *Developmental Biology* **128**, 164–77.

Wessels, D., Titus, M. and Soll, D. R. (1996). A dictyostelium myosin i plays a crucial role in regulating the frequency of pseudopods formed on the substratum. *Cell motility and the cytoskeleton* **33**, 64–79.

Wessels, D., Voss, E., Bergen, N. V., Burns, R., Stites, J. and Soll, D. (1998). A computer-assisted system for reconstructing and interpreting the dynamic three-dimensional relationships of the outer surface, nucleus and pseudopods of crawling cells. *Cell motility and the cytoskeleton* **41**, 225–246.

Wolf, K., Mazo, I., Leung, H., Engelke, K., Andrian, U. V., Deryugina, E., Strongin, A., Bröcker, E. and Friedl, P. (2003). Compensation mechanism in tumor cell migration. *The Journal of cell biology* **160**, 267.

Wu, K., Gauthier, D. and Levine, M. (1995a). Live cell image segmentation. *IEEE Transactions on Biomedical Engineering* **42**, 1–12.

Wu, L., Valkema, R., Haastert, P. J. V. and Devreotes, P. N. (1995b). The g protein beta subunit is essential for multiple responses to chemoattractants in dictyostelium. *J Cell Biol* **129**, 1667–75.

Xia, X., Yang, J., Li, F., Li, Y., Zhou, X., Dai, Y. and Wong, S. T. C. (2010). Image-based chemical screening identifies drug efflux inhibitors in lung cancer cells. *Cancer research* **70**, 7723–33.

Xiao, Z., Zhang, N., Murphy, D. B. and Devreotes, P. N. (1997). Dynamic distribution of chemoattractant receptors in living cells during chemotaxis and persistent stimulation. *J Cell Biol* **139**, 365–74.

Xiong, Y. and Iglesias, P. A. (2010). Tools for analyzing cell shape changes during chemotaxis. *Integr Biol (Camb)* **2**, 561–7.

Xiong, Y., Kabacoff, C., Franca-Koh, J., Devreotes, P., Robinson, D. and Iglesias, P. (2010). Automated characterization of cell shape changes during amoeboid motility by skeletonization. *BMC Systems Biology* **4**, 33.

Xu, C. and Prince, J. (1998). Snakes, shapes, and gradient vector flow. *IEEE Transactions on image Processing* **7**, 359–369.

Yamaguchi, H. and Condeelis, J. (2007). Regulation of the actin cytoskeleton in cancer cell migration and invasion. *Biochim Biophys Acta* **1773**, 642–52.

Yang, L., Effler, J., Kutscher, B., Sullivan, S., Robinson, D. and Iglesias, P. (2008). Modeling cellular deformations using the level set formalism. *BMC Systems Biology* **2**, 68.

Yang, S.-A., Carpenter, C. L. and Abrams, C. S. (2004). Rho and rho-kinase mediate thrombin-induced phosphatidylinositol 4-phosphate 5-kinase trafficking in platelets. *J Biol Chem* **279**, 42331–6.

Yoshida, K. and Inouye, K. (2001). Myosin ii-dependent cylindrical protrusions induced by quinine in dictyostelium: antagonizing effects of actin polymerization at the leading edge. *Journal of Cell Science* **114**, 2155–65.

Yoshida, K. and Soldati, T. (2006). Dissection of amoeboid movement into two mechanically distinct modes. *Journal of Cell Science* **119**, 3833.

Zimmer, C., Labruyère, E., Meas-Yedid, V., Guillén, N. and Olivo-Marin, J.-C. (2002). Segmentation and tracking of migrating cells in videomicroscopy with parametric active contours: a tool for cell-based drug testing. *IEEE Transactions on Medical Imaging* **21**, 1212–21.